

# **Hydroelastic Interactions between Ocean Waves and Offshore Open-Net Fish Cages**



**Mingyuan Ma**

BEng, MEngSc

School of Engineering and Built Environment  
Griffith University

Submitted in fulfilment of the requirements of the degree of  
*Doctor of Philosophy*

February 2023



I would like to dedicate this thesis to my loving parents and friends . . .



## **Declaration**

I hereby declare that this thesis is submitted for the fulfillment of the Doctor of Philosophy degree at Griffith University. This work has not previously been submitted for a degree or diploma in any university. To the best of my knowledge and belief, the thesis contains no material previously published or written by another person except where due reference is made in the thesis itself.

Signed: \_\_\_\_\_



Mingyuan Ma  
February 2023



## **Acknowledgements**

First of all, I would like to show my utmost respect to the three persons in conducting my Ph.D. research. I would like to express my most heartfelt appreciation to my principal supervisor, Professor Hong Zhang. Thanks to her for introducing me to academia, and with her continuous encouragement and support, I was able to persevere in the long research journey. I am lucky and proud to have such an academically excellent, responsible and kind mentor. I would also like to extend my deepest gratitude to my associate supervisor, Professor Dong-Sheng Jeng. Prof. Jeng is also a very accomplished scholar academically and humor person. He provided many insight techniques and perspectives in my research, which enabled me to improve a lot in academia. I am extremely grateful to Professor Chien Ming Wang. Prof. Wang is a senior expert in the field offshore fish farming. With his professional advice, I have a deeper level of thinking and understanding of the related knowledge and skills.

Special and sincere thanks to Griffith University and Blue Economy CRC for providing scholarships to support my Ph.D. studies. Griffith University is one of my alma maters for undergraduate studies and also gave me the opportunity to the doctoral career. Thanks to BECRC for giving me the opportunity to join a big family with other excellent scholars.

Also, I cannot begin to express my thanks to my beloved parents for their understanding and support for my doctoral study, and my friends for their company and care. The period with them is my happiest moment.

Finally, I hope that the epidemic will end soon, and the world is peaceful forever.





## Acknowledgements of Published Papers

This thesis includes co-authored papers with other scholars in Chapters 4, 5, and 6. My contributions to each co-authored article are listed at the beginning of the relevant chapters. The detailed bibliography of these publications are as follows:

Chapter 4:

**Ma, M.**, Zhang, H., Jeng, D.-S., and Wang, C.M. (2021). A semi-analytical model for studying hydroelastic behaviour of a cylindrical net cage under wave action. *Journal of Marine Science and Engineering*, 9:1445.

Chapter 5:

**Ma, M.**, Zhang, H., Jeng, D.-S., and Wang, C.M. (2022). Analytical solutions of hydroelastic interactions between waves and submerged open-net fish cage modeled as a porous cylindrical thin shell. *Physics of Fluids*, 34:017104.

Chapter 6:

**Ma, M.**, Zhang, H., Jeng, D.-S., and Wang, C.M. (2022). Hydroelastic interactions between waves and an array of submersible flexible fish cages. *Ocean Engineering*, 266:113035.

Signed: \_\_\_\_\_

Date: 02/02/2023

Mingyuan Ma

Countersigned: \_\_\_\_\_

Date: 02/02/2023

Prof. Hong Zhang (Principal Supervisor, School of Engineering and Built Environment, Griffith University)

Countersigned: \_\_\_\_\_

Date: 2/2/2023

Prof. Dong-Sheng Jeng (Associate Supervisor, School of Engineering and Built Environment, Griffith University)

Countersigned: \_\_\_\_\_

Date: 02/02/2023

Prof. Chien Ming wang (Co-author, School of Civil Engineering, University of Queensland)



## List of Publications

Refereed journal articles:

**Ma, M.**, Zhang, H., Jeng, D.-S., and Wang, C.M. (2021). A semi-analytical model for studying hydroelastic behaviour of a cylindrical net cage under wave action. *Journal of Marine Science and Engineering*, 9:1445.

**Ma, M.**, Zhang, H., Jeng, D.-S., and Wang, C.M. (2022). Analytical solutions of hydroelastic interactions between waves and submerged open-net fish cage modeled as a porous cylindrical thin shell. *Physics of Fluids*, 34:017104.

**Ma, M.**, Zhang, H., Jeng, D.-S., and Wang, C.M. (2022). Hydroelastic interactions between waves and an array of submersible flexible fish cages. *Ocean Engineering*, 266:113035.

Refereed conference articles:

**Ma, M.**, Zhang, H., and Jeng, D.-S. (2020). Hydrodynamic analysis of wave and cylinder fish cage interactions. In the *22nd Australasian Fluid Mechanics Conference (AFMC 2020)*.

**Ma, M.**, Zhang, H., Jeng, D.-S., and Wang, C.M. (2021). Hydro-elastic interactions between wave and cylindrical flexible porous net array. In the *5th Australasian Conference on Computational Mechanics (ACCM 2021)*.

**Ma, M.**, Zhang, H., Jeng, D.-S., and Wang, C.M. (2022). A closed-form solution for interactions between waves and an array of fish net cages. In the *37th International Conference on Coastal Engineering (ICCE 2022)*.



## Abstract

Marine aquaculture is playing an increasingly important role in the global food supply chain. Data from the Food and Agriculture Organization of the United Nations (FAO, 2020b) indicates that harvested fish account for at least 20% of the animal protein intake of 3.3 billion people, and global marine aquatic products are expected to grow by 155% from 2020 to 2050 according to the Marine Aquatic Forecast Report of DNV (2021). As the scale of mariculture grows in nearshore areas, severe environmental pollution and resource utilisation conflicts with competing users such as shipping, tourism, fishing and conservation are inevitable. Therefore, some companies or organisations, for example, Blue Economy Cooperative Research Centre in Australia, are considering moving the fish farms to offshore areas. Because of the lack of theoretical research and empirical practise, such as the determination of environmental loads and the mechanism of hydroelastic interactions between waves and flexible net structures, offshore fish farming still faces tremendous risks and challenges. This also means that cutting-edge science and technology in this field are gaining research traction from both academia and industry. At offshore sites, aquatic facilities exposed to high-energy environments will be subjected to more significant wave loads. Therefore, it is one of the core design considerations for engineers to effectively and accurately predict the hydroelastic behaviour of fish cages under the action of ocean waves.

Based on this background, the present Ph.D. thesis will investigate the hydroelastic interaction between ocean waves and open-net fish cages. The specific objectives include: 1. Undertaking a systematic literature review to identify research trends and gaps in this field; 2. Establishing an innovative semi-analytical solution for the research question; 3. Simulating and analysing the hydroelastic behaviour of the net cage under wave action; 4. Conducting parametric studies on the mechanical characteristics of the cages. These tasks provide references and experience for engineers when designing offshore aquaculture systems. To achieve these objectives, the Ph.D. research is divided into three phases.

In Study I, a preliminary closed-loop solution for the interaction between waves and net cages is proposed. The wave field is described by the potential flow theory, and

---

the motion of the net cage is governed by the string vibration equation. Based on the eigenfunction expansion in the frequency domain, the general solution of this physical problem is written as a Fourier-Bessel series, and the corresponding particular solution can be obtained by boundary value conditions and a least squared approximation. Convergence and comparative studies are to validate the reliability of the models. The simulation results indicate that a significant wave-induced response appeared on the top of the cage, especially for short waves, so a submersible fish cage is recommended to avoid strong surface waves. The porous effect of the fish cage net can generate disturbances to the wave surface. Also, the ratio of incident wavelength to cage diameter is an important parameter affecting the wave force and overturning moment acting on the cage.

To overcome the oversimplification in modelling the structural component in Study I, the flexible net is equivalent to a perforated thin cylindrical shell that cannot provide bending stiffness, and the shell-membrane theory from Flügge (1973) is applied to describe the motion behaviour and constitutive relationship of the net cage. The corresponding method of solutions is proposed in Study II, where a more realistic dynamic behaviour of the cage is illustrated compared to the conventional model. Due to the porous effect of the net, the wave amplitude around the cage is distributed in a “wake” shape, which causes the dissipation of wave energy inside the cage and behind its leeward side. Increasing the porosity and flexibility of the net facilitates suppressing the scattering effect of the wave. Notably, when the ratio of cage diameter to incident wavelength is around 0.59 and 1.70, the wave force and overturning moment acting on the cage are zero.

A theoretical extension to wave interference among multiple cages is exhibited in Study III. According to the Kagemoto and Yue (1986) interaction theory, the interference phenomenon of the wave field can be regarded as the superposition of scattered waves produced by each individual cage, and Graf’s addition theorem can express the coordinate transformation of the velocity potential. In addition, the mean wave drift force acting on the fish cage can be deduced by the time-averaged operation of the nonlinear term in the Bernoulli equation. In this study, an array of cages laid in two rows by three columns is discussed. The results indicate that by increasing the wavenumber, spacing of the cages and porosity of the net, the amplitude variation of the free water surface elevation caused by the interference effect can be suppressed. In the direction of the incident wave, the rear cages are imposed with opposite mean wave loads compared to the front cages. The parametric study still shows that the wave force on the cage is zero when the ratio of cage diameter to incident wavelength is 0.59, but the maximum magnitude of the wave force occurs in the low-frequency range of incident waves.

---

These studies provide scientific and technical contributions to the engineering application of offshore fish farming. The theoretical implication of wave-cage interaction includes the introduction of shell-membrane theory and wave interference. In view of practical implications, the developed semi-analytical model provides an effective tool for engineers to predict the wave response of fish cages, and the research conclusions provide reference and experience in engineering design. In future work, more complex hydrodynamic phenomena and marine aquaculture systems are expected to be explored.





# Table of Contents

<b>List of Figures</b>	<b>xxi</b>
<b>List of Tables</b>	<b>xxix</b>
<b>Nomenclatures</b>	<b>xxxii</b>
<b>1 Introduction</b>	<b>1</b>
1.1 Research Background . . . . .	1
1.2 Aims and objectives . . . . .	5
1.3 Outline of the thesis . . . . .	6
<b>2 Literature Review</b>	<b>9</b>
2.1 Introduction . . . . .	9
2.2 Hydrodynamic actions and analysis in marine aquaculture . . . . .	10
2.2.1 Hydrodynamic responses . . . . .	10
2.2.2 Empirical equations of hydrodynamic loads . . . . .	19
2.2.3 Potential flow models . . . . .	24
2.2.4 Computational fluid dynamic models . . . . .	33
2.3 Structural reliability and modelling of a fish cage system . . . . .	37
2.3.1 Structural reliability . . . . .	37
2.3.2 Modelling of fish cages . . . . .	41
2.4 Summary and research gaps . . . . .	43
2.4.1 Summary of the literature review . . . . .	43

## Table of Contents

---

2.4.2	Existing research gaps . . . . .	44
<b>3</b>	<b>Research Question and Methodologies</b>	<b>45</b>
3.1	Research question . . . . .	45
3.2	Methodologies . . . . .	46
3.2.1	Study I: A theoretical framework for the hydroelastic interaction between waves and submersible flexible fish cages . . . . .	46
3.2.2	Study II: Innovative analytical schemes by practising the shell- membrane theory in modelling net chambers . . . . .	49
3.2.3	Study III: Theoretical extensions to the wave interference effects in the multi-cage system . . . . .	50
<b>4</b>	<b>Closed-Form Solutions to Interactions between Waves and Net Cages</b>	<b>55</b>
4.1	Introduction . . . . .	57
4.2	Problem definition, assumption and theoretical formulation . . . . .	59
4.2.1	Governing equations . . . . .	59
4.2.2	Boundary conditions . . . . .	60
4.3	Derivation of the solutions . . . . .	63
4.4	Convergence studies and model validation . . . . .	67
4.4.1	Convergence studies . . . . .	67
4.4.2	Model validation . . . . .	69
4.5	Results and discussions . . . . .	69
4.5.1	Hydrodynamic behaviours . . . . .	70
4.5.2	Structural dynamic responses . . . . .	73
4.5.3	Parametric studies . . . . .	77
4.6	Conclusions . . . . .	84
<b>5</b>	<b>Analytical Schemes by Practicing the Shell-Membrane Theory</b>	<b>89</b>
5.1	Introduction . . . . .	91
5.2	Problem definition, assumption and theoretical formulation . . . . .	94

5.2.1	Governing equations . . . . .	94
5.2.2	Boundary conditions . . . . .	97
5.3	Derivation of the solutions . . . . .	99
5.3.1	Fluid domain . . . . .	99
5.3.2	Structural domain . . . . .	101
5.3.3	Fluid-structure interaction . . . . .	103
5.4	Convergence studies and model validation . . . . .	105
5.4.1	Convergence studies . . . . .	105
5.4.2	Model validation . . . . .	106
5.5	Results and discussions . . . . .	107
5.5.1	Wave surface profiles . . . . .	108
5.5.2	Structural dynamic responses . . . . .	113
5.5.3	Parametric studies . . . . .	114
5.6	Conclusions . . . . .	120
<b>6</b>	<b>Theoretical extension to wave interference effects in multi-cage systems</b>	<b>123</b>
6.1	Introduction . . . . .	125
6.2	Problem definition, assumption and theoretical formulation . . . . .	128
6.2.1	Governing equations . . . . .	128
6.2.2	Boundary conditions . . . . .	131
6.3	Derivation of the solutions . . . . .	132
6.3.1	Fluid domain . . . . .	132
6.3.2	Structural domain . . . . .	136
6.3.3	Fluid-structure interactions . . . . .	137
6.4	Convergence studies and model validation . . . . .	140
6.4.1	Convergence studies . . . . .	140
6.4.2	Model validation . . . . .	141
6.5	Results and discussions . . . . .	144
6.5.1	Wave interference effects . . . . .	144

## Table of Contents

---

6.5.2	Structural dynamic responses . . . . .	146
6.5.3	Parametric studies . . . . .	149
6.6	Conclusions . . . . .	158
<b>7</b>	<b>Conclusions</b>	<b>161</b>
7.1	Research restatement . . . . .	161
7.2	General discussions and key findings . . . . .	162
7.2.1	An establishment for the semi-analytical solution . . . . .	162
7.2.2	Model updating by introducing the shell-membrane theory . . . . .	163
7.2.3	Wave interference effects in an array of fish cages . . . . .	164
7.3	Scientific contributions . . . . .	165
7.3.1	Implications in theoretical developments . . . . .	165
7.3.2	Implications in engineering practice . . . . .	166
7.4	Research limitations and future work . . . . .	166
7.4.1	Research limitations . . . . .	167
7.4.2	Future work lines . . . . .	167
	<b>References</b>	<b>171</b>

# List of Figures

1.1	Global statistics and predictions: (a) Marine aquaculture production; (b) Installed finfish production capacity (DNV, 2021). . . . .	2
1.2	The schematic diagram of a basic fish cage system (Zhao et al., 2019b). . . . .	5
2.1	Configuration of a typical net structure. . . . .	12
2.2	Range of application of different wave theories (Méhauté, 1976). . . . .	16
2.3	Sketch of the method when utilising the Morison-type equation: $F_1$ is the drag force when the net twine is inclined with respect to the incoming flow velocity vector, and $F_2$ is the drag force when the net twine is orthogonal with the incoming flow velocity vector. . . . .	20
2.4	Sketch of the screen-type method. . . . .	23
2.5	Deformed net chambers with different current velocities and sinker weights (Lader and Enerhaug, 2005). . . . .	39
2.6	Mooring system types: spread moorings: (a) Taut; (b) Taut spread; (c) Catenary; (d) Multi-catenary; and single point moorings: (e) SALM; (f) CALM; (g) Lazy-S (Davidson and Ringwood, 2017). . . . .	40
3.1	Methodological framework for the existing research. . . . .	47
3.2	Theoretical framework of the simulation model in Study I. . . . .	48
3.3	Theoretical framework of the simulation model in Study II. . . . .	50
3.4	Theoretical framework of the simulation model in Study III. . . . .	51
3.5	Numerical execution flow chart for the eventual simulation model to analyse the wave-net cage interaction. . . . .	53

## List of Figures

---

4.1	A sketch of a cylindrical net cage submerged in a finite water depth: (a) Plan view; (b) Isometric view. . . . .	60
4.2	The fish cage net is modelled as a porous membrane. . . . .	61
4.3	Convergence curves of control errors versus truncated terms for different wave frequencies: (a) $\Delta E_r(N)$ versus $N$ ; (b) $\Delta E_r(M)$ versus $M$ . . . . .	68
4.4	Model validations: (a) Horizontal wave force $ F $ ; (b) Cage deflection amplitude $ \eta $ . . . . .	69
4.5	Free water surface elevations $\xi$ around a cylindrical net cage with different opening ratios at $t/T = n$ , $n = 0, 1, 2, \dots, \infty$ , Cases B1 to B4: (a) $\tau_0 = 0$ ; (b) $\tau_0 = 0.1$ ; (c) $\tau_0 = 0.2$ ; (d) $\tau_0 = 0.3$ . . . . .	72
4.6	Amplitude distributions of pressure drop $\Delta p_a$ on the net interface, Cases A1 to A4: (a) $T = 4$ s; (b) $T = 6$ s; (c) $T = 8$ s; (d) $T = 10$ s. . . . .	73
4.7	(a) Nondimensional transverse deflection amplitudes of cage $ \eta /d_2$ ; (b) Nondimensional horizontal wave load amplitudes per unit length $K_f$ along cage height for various wave periods $T$ , Cases A1 to A4. . . . .	75
4.8	(a) Nondimensional transverse deflection amplitudes of cage $ \eta /d_2$ ; (b) Nondimensional horizontal wave load amplitudes per unit length $K_f$ along cage height for various net opening ratios $\tau_0$ , Cases B5 to B8. . . . .	75
4.9	(a) Nondimensional transverse deflection amplitudes of cage $ \eta /d_2$ ; (b) Nondimensional horizontal wave load amplitudes per unit length $K_f$ along cage height for various dimensionless mooring spring constants $\alpha$ , Cases C1 to C4. . . . .	76
4.10	(a) Nondimensional transverse deflection amplitudes of cage $ \eta /d_2$ ; (b) Nondimensional horizontal wave load amplitudes per unit length $K_f$ along cage height for various dimensionless axial tensile forces $\gamma$ in the net, Cases D1 to D4. . . . .	76
4.11	(a) Nondimensional transverse deflection amplitudes of cage $ \eta /d_2$ ; (b) Nondimensional horizontal wave load amplitudes per unit length $K_f$ along cage height for various relative diving depths $d_1/h$ of the cage, Cases E1 to E4. . . . .	77
4.12	3D shapes of a net cage at different submerged depths with the maximum deformation in an exaggerated scale of 5 times: (a) $d_1/h = 0$ ; (b) $d_1/h = 0.05$ ; (c) $d_1/h = 0.15$ ; (d) $d_1/h = 0.25$ . . . . .	78

4.13 Effect of wave-effect parameter $C_w$ on (a) Nondimensional amplitude of horizontal hydrodynamic force $K_F$ ; (b) Nondimensional amplitude of horizontal overturning moment $K_M$ for various net opening ratios $\tau_0$ , $H = 7$ m, $h = 200$ m, $a = 50$ m, $d_1 = 0$ , $d_2 = 50$ m, $\alpha = 20$ , $\gamma = 1$ and $\beta = 0.001$ .	80
4.14 Effect of wave steepness $H/L$ on (a) Nondimensional amplitude of horizontal hydrodynamic force $K_F$ ; (b) Nondimensional amplitude of horizontal overturning moment $K_M$ for various net opening ratios $\tau_0$ , $T = 8$ s, $h = 200$ m, $a = 50$ m, $d_1 = 0$ , $d_2 = 50$ m, $\alpha = 20$ , $\gamma = 1$ and $\beta = 0.001$ .	80
4.15 Effect of relative water depth $h/L$ on (a) Nondimensional amplitude of horizontal hydrodynamic force $K_F$ ; (b) Nondimensional amplitude of horizontal overturning moment $K_M$ for various net opening ratios $\tau_0$ , $T = 8$ s, $H = 7$ m, $a = 50$ m, $d_1 = 0$ , $d_2 = 50$ m, $\alpha = 20$ , $\gamma = 1$ and $\beta = 0.001$ .	81
4.16 Effect of relative cage diameter $2a/L$ on (a) Nondimensional amplitude of horizontal hydrodynamic force $K_F$ ; (b) Nondimensional amplitude of horizontal overturning moment $K_M$ for various net opening ratios $\tau_0$ , $T = 8$ s, $H = 7$ m, $h = 200$ m, $d_1 = 0$ , $d_2 = 50$ m, $\alpha = 20$ , $\gamma = 1$ and $\beta = 0.001$ .	82
4.17 Effect of relative cage diving depth $d_1/h$ on (a) Nondimensional amplitude of horizontal hydrodynamic force $K_F$ ; (b) Nondimensional amplitude of horizontal overturning moment $K_M$ for various net opening ratios $\tau_0$ , $T = 8$ s, $H = 7$ m, $h = 200$ m, $a = 50$ m, $d_2 = 50$ m, $\alpha = 20$ , $\gamma = 1$ and $\beta = 0.001$ .	82
4.18 Effect of relative cage height $d_2/h$ on (a) Nondimensional amplitude of horizontal hydrodynamic force $K_F$ ; (b) Nondimensional amplitude of horizontal overturning moment $K_M$ for various net opening ratios $\tau_0$ , $T = 8$ s, $H = 7$ m, $h = 200$ m, $a = 50$ m, $d_1 = 0$ , $\alpha = 20$ , $Q/(m_s g a) = 1$ and $m_s/(\rho a^2) = 0.001$ .	83
4.19 Effect of nondimensional mooring spring constant $\alpha$ on (a) Nondimensional amplitude of horizontal hydrodynamic force $K_F$ ; (b) Nondimensional amplitude of horizontal overturning moment $K_M$ for various net opening ratios $\tau_0$ , $T = 8$ s, $H = 7$ m, $h = 200$ m, $a = 50$ m, $d_1 = 0$ , $d_2 = 50$ m, $\gamma = 1$ and $\beta = 0.001$ .	84
4.20 Effect of nondimensional axial tensile force $\gamma$ in the net on (a) Nondimensional amplitude of horizontal hydrodynamic force $K_F$ ; (b) Nondimensional amplitude of horizontal overturning moment $K_M$ for various net opening ratios $\tau_0$ , $T = 8$ s, $H = 7$ m, $h = 200$ m, $a = 50$ m, $d_1 = 0$ , $d_2 = 50$ m, $\alpha = 20$ and $\beta = 0.001$ .	85

## List of Figures

---

4.21	Effect of nondimensional net mass per unit length $\beta$ on (a) Nondimensional amplitude of horizontal hydrodynamic force $K_F$ ; (b) Nondimensional amplitude of horizontal overturning moment $K_M$ for various net opening ratios $\tau_0$ , $T = 8$ s, $H = 7$ m, $h = 200$ m, $a = 50$ m, $d_1 = 0$ , $d_2 = 50$ m, $\alpha = 20$ and $\gamma = 1$ . . . . .	85
4.22	Effect of net opening ratio $\tau_0$ on (a) Nondimensional amplitude of horizontal hydrodynamic force $K_F$ ; (b) Nondimensional amplitude of horizontal overturning moment $K_M$ for various nondimensional axial tensile forces $\gamma$ in the net, $T = 8$ s, $H = 7$ m, $h = 200$ m, $a = 50$ m, $d_1 = 0$ , $d_2 = 50$ m, $\alpha = 20$ and $\beta = 0.001$ . . . . .	86
4.23	Effect of fluid inertia effect parameter $\tau_i$ on (a) Nondimensional amplitude of horizontal hydrodynamic force $K_F$ ; (b) Nondimensional amplitude of horizontal overturning moment $K_M$ for various nondimensional axial tensile forces $\gamma$ in the net, $T = 8$ s, $H = 7$ m, $h = 200$ m, $a = 50$ m, $d_1 = 0$ , $d_2 = 50$ m, $\tau_0 = 0.7$ , $\alpha = 20$ and $\beta = 0.001$ . . . . .	86
5.1	Submerged cylindrical fish net cage in a constant water depth and under wave action: (a) Plan view; (b) Isometric view. . . . .	95
5.2	Sketch of a cylindrical shell: (a) Displacement components; (b) Membrane stress resultants in a shell element. . . . .	96
5.3	The fish cage net is modelled as a porous membrane. . . . .	98
5.4	Convergence analysis for truncated terms of $N$ and $M$ : (a) Variations of $\Delta E_r(N)$ versus $N$ ; (b) Variations of $\Delta E_r(M)$ versus $M$ . . . . .	106
5.5	Model validations: (a) Normalised free water surface elevation variations $\xi/H$ ; (b) Normalised horizontal wave force $ F /[\rho g(H/2)a^2]$ . . . . .	107
5.6	Variations of free water surface elevations $\xi$ around a cylindrical net cage over time: (a) $t/T = 0$ ; (b) $t/T = 1/4$ ; (c) $t/T = 1/2$ ; (d) $t/T = 3/4$ , Case A3. . . . .	109
5.7	Variations of normalized free water surface elevations $\xi/H$ with time series for different positions in zones 1 and 2, Case A3. . . . .	110
5.8	Amplitudes of free surface elevations $\xi_a$ around a cylindrical net cage with various wave-effect parameters $C_w$ : (a) $C_w = 0.04$ ; (b) $C_w = 0.06$ ; (c) $C_w = 0.08$ ; (d) $C_w = 0.12$ , Cases A1–A4. . . . .	110



5.9	Amplitudes of free surface elevations $\xi_a$ around a cylindrical net cage with various porous effect parameters $\tau$ : (a) $\tau = 1 + 1i$ ; (b) $\tau = 2 + 2i$ ; (c) $\tau = 3 + 3i$ ; (d) $\tau = 4 + 4i$ , Cases B1–B4. . . . .	111
5.10	Amplitudes of free surface elevations $\xi_a$ around a cylindrical net cage with various nondimensional elastic modulus $\eta$ : (a) $\eta = 0.5 \times 10^3$ ; (b) $\eta = 1 \times 10^3$ ; (c) $\eta = 2 \times 10^3$ ; (d) $\eta = 4 \times 10^3$ , Cases C1–C4. . . . .	112
5.11	Free surfaces and dynamic responses of a cylindrical net cage over time: (a) $t/T = 0$ ; (b) $t/T = 1/4$ ; (c) $t/T = 1/2$ ; (d) $t/T = 3/4$ , Case A3. . . . .	113
5.12	Spatial contours of (a) Axial displacement amplitude $U_a$ ; (b) Circumferential displacement amplitude $V_a$ ; (c) Radial displacement amplitude $W_a$ ; (d) Pressure drop amplitude $\Delta p_a$ , Case A3. . . . .	114
5.13	Pressure drops $\Delta p$ on a cylindrical net cage and corresponding deformations with various wave-effect parameters $C_w$ at $t = T/2$ : (a) $C_w = 0.04$ ; (b) $C_w = 0.06$ ; (c) $C_w = 0.08$ ; (d) $C_w = 0.12$ , Cases A1–A4. . . . .	115
5.14	Pressure drops $\Delta p$ on a cylindrical net cage and corresponding deformations with various porous effect parameters $\tau$ at $t = T/2$ : (a) $\tau = 1 + 1i$ ; (b) $\tau = 2 + 2i$ ; (c) $\tau = 3 + 3i$ ; (d) $\tau = 4 + 4i$ , Cases B1–B4. . . . .	115
5.15	Pressure drops $\Delta p$ on a cylindrical net cage and corresponding deformations with various nondimensional elastic modulus $\eta$ at $t = T/2$ : (a) $\eta = 0.5 \times 10^3$ ; (b) $\eta = 1 \times 10^3$ ; (c) $\eta = 2 \times 10^3$ ; (d) $\eta = 4 \times 10^3$ , Cases C1–C4. . . . .	116
5.16	Pressure drops $\Delta p$ on a cylindrical net cage and corresponding deformations with various relative diving depths $d_1/h$ at $t = T/2$ : (a) $d_1/h = 0$ ; (b) $d_1/h = 0.05$ ; (c) $d_1/h = 0.10$ ; (d) $d_1/h = 0.15$ , Cases D1–D4. . . . .	117
5.17	Influences of wave effect parameters $C_w$ on nondimensional amplitudes of (a) Horizontal wave forces $K_F$ ; (b) Overturning moments $K_M$ under various porous effect parameters $\tau$ , $t_s/a = 10^{-4}$ , $d_1/h = 0$ , $d_2/(2a) = 0.5$ and $\eta = 10^3$ . . . . .	117
5.18	Influences of relative diameters $2a/L$ of the cage on nondimensional amplitudes of (a) Horizontal wave forces $K_F$ ; (b) Overturning moments $K_M$ under various porous effect parameters $\tau$ , $C_w = 0.08$ , $d_1/h = 0$ , $d_2/(2a) = 0.5$ and $\eta = 10^3$ . . . . .	118

## List of Figures

---

5.19	Influences of relative diving depths $d_1/h$ of the cage on nondimensional amplitudes of (a) Horizontal wave forces $K_F$ ; (b) Overturning moments $K_M$ under various porous effect parameters $\tau$ , $C_w = 0.08$ , $t_s/a = 10^{-4}$ , $d_2/(2a) = 0.5$ and $\eta = 10^3$ . . . . .	119
5.20	Influences of slenderness ratios $d_2/(2a)$ of the cage on nondimensional amplitudes of (a) Horizontal wave forces $K_F$ ; (b) Overturning moments $K_M$ under various porous effect parameters $\tau$ , $C_w = 0.08$ , $t_s/a = 10^{-4}$ , $d_1/h = 0$ and $\eta = 10^3$ . . . . .	119
5.21	Influences of nondimensional elastic modulus $\eta$ of the cage on nondimensional amplitudes of (a) Horizontal wave forces $K_F$ ; (b) Overturning moments $K_M$ under various porous effect parameters $\tau$ , $C_w = 0.08$ , $t_s/a = 10^{-4}$ , $d_1/h = 0$ and $d_2/(2a) = 0.5$ . . . . .	120
5.22	Influences of porous resistance parameters $\tau_r$ of the cage on nondimensional amplitudes of (a) Horizontal wave forces $K_F$ ; (b) Overturning moments $K_M$ under various fluid inertia parameters $\tau_i$ , $C_w = 0.08$ , $t_s/a = 10^{-4}$ , $d_1/h = 0$ , $d_2/(2a) = 0.5$ and $\eta = 10^3$ . . . . .	121
5.23	Influences of fluid inertia parameters $\tau_i$ of the cage on nondimensional amplitudes of (a) Horizontal wave forces $K_F$ ; (b) Overturning moments $K_M$ under various porous resistance parameters $\tau_r$ , $C_w = 0.08$ , $t_s/a = 10^{-4}$ , $d_1/h = 0$ , $d_2/(2a) = 0.5$ and $\eta = 10^3$ . . . . .	121
6.1	Sketches and parameter definitions of multiple cylindrical net cages: (a) Plan view; (b) Isometric view. . . . .	129
6.2	A sketch and parameter definitions of a cylindrical shell. . . . .	130
6.3	Layout of an array of cylindrical net cages with two rows by three columns. . . . .	141
6.4	Convergence studies for the truncated terms $N$ and $M$ : (a) $\sum_{j=1}^{NC} K_{F_x}^j$ versus $N$ ; (b) $\sum_{j=1}^{NC} \overline{K_{F_x}}^j$ versus $M$ , $N = 40$ . The other constant parameters are $H = 7$ m, $\beta = \pi/4$ , $h = 200$ m, $a^j = 50$ m, $t_s^j/a^j = 10^{-4}$ , $d_1^j/h = 0.05$ , $d_2^j/h = 0.25$ , $\tau^j = 1+1i$ , $\nu^j = 0.3$ , $\rho_s^j/\rho = 1.2$ , $E^j/(\rho_s^j gh) = 10^3$ and $s_x/h = s_y/h = 0.1$ . . . . .	142
6.5	Comparison of the free water surface elevation amplitude $\xi_a$ around four porous cylinders. The other constant parameters are $H = 1$ , $\beta = \pi/4$ , $a^j = 0.2$ , $\kappa_0 a^j = \pi/2$ , $h/a^j = 5$ , $d_1^j/h = 0$ , $d_2^j/h = 1$ , $\tau^j = 1$ , $\nu^j = 0.3$ , $\rho_s^j/\rho = 1.2$ , $E^j/(\rho_s^j gh) = 10^9$ and $s_x/h = s_y/h = 0.4$ . . . . .	143

6.6	Comparison of the total wave force on four floating porous cages. The other constant parameters are $H = 1$ , $a^j = 8.44$ m, $h = 200$ m, $d_1^j/h = 0$ , $d_2^j/h = 0.175$ , $v^j = 0.3$ , $\rho_s^j/\rho = 1.2$ , $E^j/(\rho_s^jgh) = 10^9$ and $s_x/h = s_y/h = 0.347$ .	143
6.7	Comparison of the normalised wave forces $K_{F_x}^j$ on an array of flexible porous cages and a single flexible porous cage. The other constant parameters are $H = 7$ m, $\beta = 0$ , $h = 200$ m, $a^j = 50$ m, $t_s^j/a^j = 10^{-4}$ , $d_1^j/h = 0$ , $d_2^j/h = 0.25$ , $v^j = 0.3$ , $\rho_s^j/\rho = 1.2$ , $E^j/(\rho_s^jgh) = 10^3$ and $s_x/h = s_y/h = 10^5$ .	144
6.8	Contour plots of the free water surface elevation amplitude $\xi_a$ around a $2 \times 3$ array of net cages under different incident wave angles, (a) to (d): Cases A1 to A4. . . . .	146
6.9	Contour plots of the free water surface elevation amplitude $\xi_a$ around a $2 \times 3$ array of net cages under different incident wavelengths, (a) to (d): Cases B1 to B4. . . . .	147
6.10	Contour plots of the free water surface elevation amplitude $\xi_a$ around a $2 \times 3$ array of net cages under different cage spacings, (a) to (d): Cases C1 to C4. . . . .	147
6.11	Contour plots of the free water surface elevation amplitude $\xi_a$ around a $2 \times 3$ array of net cages under different net porous effect parameters, (a) to (d): Cases D1 to D4. . . . .	148
6.12	First-order pressure drop $\Delta p^j$ on a $2 \times 3$ array of net cages with an exaggerated deformation of twice the scale and the nearby free water surface (purple shaded), Case B2. . . . .	149
6.13	Spatial contour plots of the amplitude of first-order pressure drop $\Delta p_a^j$ on the interface of each cage, Case B2. . . . .	150
6.14	Spatial contour plots of the amplitude of time-averaged pressure drop $\overline{\Delta p_a^j}$ on the interface of each cage, Case B2. . . . .	150
6.15	Spatial contour plots of the amplitude of axial displacement $U_a^j$ of each cage, Case B2. . . . .	151
6.16	Spatial contour plots of the amplitude of circumferential displacement $V_a^j$ of each cage, Case B2. . . . .	151
6.17	Spatial contour plots of the amplitude of axial displacement $W_a^j$ of each cage, Case B2. . . . .	152

## List of Figures

---

- 6.18 Normalised first-order wave forces: (a) Component  $K_{F_x}^j$ ; (b) Component  $K_{F_y}^j$  and normalised mean wave drift forces: (c) Component  $\overline{K_{F_x}^j}$ ; (d) Component  $\overline{K_{F_y}^j}$  on each cage versus varied nondimensional incident wave angles  $\beta/(2\pi)$ . The other constant parameters are  $\kappa_0 h = 12$ ,  $t_s^j/a^j = 10^{-4}$ ,  $\tau^j = 1+1i$  and  $s_x/h = s_y/h = 0.1$ . . . . . 153
- 6.19 Normalised first-order wave forces: (a) Component  $K_{F_x}^j$ ; (b) Component  $K_{F_y}^j$  and normalised mean wave drift forces: (c) Component  $\overline{K_{F_x}^j}$ ; (d) Component  $\overline{K_{F_y}^j}$  on each cage versus varied nondimensional incident wavelengths  $\kappa_0 h$ ,  $\beta = \pi/4$ ,  $t_s^j/a^j = 10^{-4}$ ,  $\tau^j = 1+1i$  and  $s_x/h = s_y/h = 0.1$ . 153
- 6.20 Normalised first-order wave forces: (a) Component  $K_{F_x}^j$ ; (b) Component  $K_{F_y}^j$  and normalised mean wave drift forces: (c) Component  $\overline{K_{F_x}^j}$ ; (d) Component  $\overline{K_{F_y}^j}$  on each cage versus varied relative diameters of the cages  $2a^j/L$ ,  $\beta = \pi/4$ ,  $\kappa_0 h = 12$ ,  $\tau^j = 1+1i$  and  $s_x/h = s_y/h = 0.1$ . . . . . 154
- 6.21 Normalised first-order wave forces: (a) Component  $K_{F_x}^j$ ; (b) Component  $K_{F_y}^j$  and normalised mean wave drift forces: (c) Component  $\overline{K_{F_x}^j}$ ; (d) Component  $\overline{K_{F_y}^j}$  on each cage versus varied porous resistance effect parameters of the net  $\tau_r^j$ ,  $\beta = \pi/4$ ,  $\kappa_0 h = 12$ ,  $t_s^j/a^j = 10^{-4}$ ,  $\tau_i^j = 1$  and  $s_x/h = s_y/h = 0.1$ . . . . . 155
- 6.22 Normalised first-order wave forces: (a) Component  $K_{F_x}^j$ ; (b) Component  $K_{F_y}^j$  and normalised mean wave drift forces: (c) Component  $\overline{K_{F_x}^j}$ ; (d) Component  $\overline{K_{F_y}^j}$  on each cage versus varied fluid inertial effect parameters of the net  $\tau_i^j$ ,  $\beta = \pi/4$ ,  $\kappa_0 h = 12$ ,  $t_s^j/a^j = 10^{-4}$ ,  $\tau_r^j = 1$  and  $s_x/h = s_y/h = 0.1$ . 156
- 6.23 Contour plots of the normalised first-order wave force component  $K_{F_x}^j$  on each cage as a function versus relative cage spacings  $s_x/L$  and  $s_y/L$ ,  $\beta = \pi/4$ ,  $\kappa_0 h = 12$ ,  $t_s^j/a^j = 10^{-4}$  and  $\tau^j = 1+1i$ . . . . . 156
- 6.24 Contour plots of the normalised first-order wave force component  $K_{F_y}^j$  on each cage as a function versus relative cage spacings  $s_x/L$  and  $s_y/L$ ,  $\beta = \pi/4$ ,  $\kappa_0 h = 12$ ,  $t_s^j/a^j = 10^{-4}$  and  $\tau^j = 1+1i$ . . . . . 157
- 6.25 Contour plots of the normalised mean wave drift force component  $\overline{K_{F_x}^j}$  on each cage as a function versus relative cage spacings  $s_x/L$  and  $s_y/L$ ,  $\beta = \pi/4$ ,  $\kappa_0 h = 12$ ,  $t_s^j/a^j = 10^{-4}$  and  $\tau^j = 1+1i$ . . . . . 157
- 6.26 Contour plots of the normalised mean wave drift force component  $\overline{K_{F_y}^j}$  on each cage as a function versus relative cage spacings  $s_x/L$  and  $s_y/L$ ,  $\beta = \pi/4$ ,  $\kappa_0 h = 12$ ,  $t_s^j/a^j = 10^{-4}$  and  $\tau^j = 1+1i$ . . . . . 158

# List of Tables

1.1	Classifications of coastal, off-coast and offshore farming (Chu et al., 2020).	4
2.1	Degree of exposure for waves and currents (NS9415, 2009). . . . .	10
2.2	The Douglas sea scale for wind-sea states and swells (Morrisey et al., 2015).	15
4.1	Case groups with different studied parameters (Study I). . . . .	71
5.1	Case groups with different studied parameters (Study II). . . . .	108
6.1	Case groups with different studied parameters (Study III). . . . .	145



# Nomenclatures

$A_s$	Area of the screen in the screen-type method
$C_w$	Wave effect parameters
$E$	Young's modulus
$ETI$	Wave transmission index
$F$	First-order wave force magnitude
$F_x$	First-order wave force component in $x$ direction
$F_y$	First-order wave force component in $y$ direction
$G$	Shear modulus
$H$	Incident wave height
$H_m$	Hankel functions of the first kind in $m$ th order
$H_s$	Significant wave height
$I_m$	Modified Bessel functions of the first kind in $m$ th order
$J_m$	Bessel functions of the first kind in $m$ th order
$K$	Discharge coefficient
$K_C$	Keulegan–Carpenter number
$K_m$	Modified Bessel functions of the second kind in $m$ th order
$L$	Incident wave length
$M_o$	First-order wave overturning moment magnitude
$N_z$	Axial membrane stress resultant in a micro shell element

## Nomenclatures

---

$N_\theta$	Circumferential membrane stress resultant in a micro shell element
$N_{\theta z}, N_{z\theta}$	Shear membrane stress resultant in a micro shell element
$Q$	Axial tension force in the net
$R_e$	Reynolds's number
$S$	Boundary of the fluid domain in the boundary element method
$S_i$	Source term in the RANS and VARANS equations
$S_n$	Net solidity ratio
$S_{gap}$	Gap region
$S_{net}$	Net region
$T$	Incident wave period
$T_p$	Peak energy wave period
$U$	Axial displacement of the cage
$U_a$	Axial displacement of the cage amplitude
$V$	Circumferential displacement of the cage
$V_{twine}$	Volume of the net twine
$V_a$	Circumferential displacement of the cage amplitude
$W$	Radial displacement of the cage
$W_a$	Radial displacement of the cage amplitude
$\Delta E_r$	Control error in convergence studies on the truncated terms
$\Delta p_a$	Pressure drop amplitude
$\Delta p$	Pressure drop
$\Phi$	Fluid velocity potential
$\Phi^D$	Diffracted wave velocity potential
$\Phi^I$	Incident wave velocity potential



$\Phi^R$	Rational wave velocity potential
$\Phi^S$	Scattered wave velocity potential
$\alpha$	Attack angle of flow
$\beta$	Incident wave angle
$F_D$	Fluid drag force in the screen-type method
$F_L$	Fluid lift force in the screen-type method
$F_N$	Normal force component in the screen-type method
$F_T$	Tangential force component in the screen-type method
$F_d$	Fluid drag force in the Morison equation
$F_i$	Fluid inertia force in the Morison equation
$n$	Unit normal vector
$u$	Flow velocity
$u_n$	Normal flow velocity
$u_r$	Relative flow velocity
$u_\infty$	Incoming flow velocity
$u_\tau$	Tangential flow velocity
$x$	Structural displacement relative to the mean position
$\eta$	Transverse deflection complex amplitude of the cage (Chapter 4); Nondimensional elastic modulus of the net (Chapter 5)
$\gamma$	Phase index in the volume of fluids method (Chapter 2); Nondimensional axial tensile force in net (Chapter 4)
$\kappa_0$	Incident wave number
$\mu$	Fluid dynamic viscosity
$\mu_s$	Material roughness
$\mu_t$	Eddy viscosity

## Nomenclatures

---

$\nu$	Poisson's ratio
$\omega$	Angular wave frequency
$\overline{F}_x$	Mean wave drift force component in $x$ direction
$\overline{F}_y$	Mean wave drift force component in $y$ direction
$\overline{\Delta p_a}$	Amplitude of the mean wave drift pressure drop
$\overline{\Delta p}$	Mean wave drift pressure drop
$\rho$	Fluid density
$\rho_s$	Solid density
$\tau$	Porous effect parameter of the net
$\tau_0$	Porosity of the net
$\tau_i$	Fluid inertia effect parameter of the net
$\tau_r$	Porous resistance effect parameter of the net
$\varepsilon$	Incident wave slope (Chapter 4)
$\varphi$	Velocity potential complex amplitude
$\varphi^I$	Complex amplitude of the incident wave velocity potential
$\varphi^S$	Complex amplitude of the scattered wave velocity potential
$\varphi_0$	Source function in the boundary element method
$\xi$	Free water surface elevation
$\xi_a$	Amplitude of the Free water surface elevation
$\zeta$	Transverse deflection (Chapter 4)
$a$	Radius of the cage
$d_1$	Cage height
$d_2$	Submerged depth of the cage
$d_{\text{twine}}$	Diameter of the net twine

$f(z)$	Horizontal wave load per unit length on the cage
$f_i$	Linearised fluid inertia coefficient
$f_r$	Linearised porous resistance coefficient
$h$	Water depth
$k_s$	Spring constant of the mooring cables
$l_{\text{twine}}$	Length of the net twine
$l_{\text{cube}}$	Side length of a cube cage
$m_s$	Uniform mass of the net per unit length
$p$	Fluid dynamic pressure
$p^*$	Fluid pressure
$s_x$	Spacing of the cage array in $x$ direction
$s_y$	Spacing of the cage array in $y$ direction
$t_s$	Shell thickness
$u_a$	Amplitude of the flow velocity
$C_D$	Drag force coefficient in the screen-type method
$C_L$	Lift force coefficient in the screen-type method
$C_N$	Normal force coefficient in the screen-type method
$C_T$	Tangential force coefficient in the screen-type method
$C_d$	Drag coefficient in the Morison equation
$C_m$	Added mass coefficient in the Morison equation
$c_m$	Added mass coefficient in the VARANS equation
$g$	Gravity acceleration



# Chapter 1

## Introduction

### 1.1 Research Background

Marine resource is an important supply chain of global prolificacy, with the aquaculture industry being one of the major suppliers of animal proteins for human beings. According to the report from the Food and Agriculture Organization (FAO, 2020b), harvested fish account for at least 20% of the animal protein intake for 3.3 billion people. Over recent years, the rapid development of fisheries has created considerable economic value due to population growth and increased food demand. The data from DNV (2021) demonstrates that from 1990 to 2020, the output from marine aquaculture increased 5.8 times to 29 million tons per year, and it is expected to grow to 74 million tons in 2050 as a dominant production sector, the same is true of capture fisheries, based on the fastest-growing tendency (Fig. 1.1a).

Nearshore fish farming has become increasingly attractive and has been the focus of international attention since the 1990s (Langan, 2009). However, along with the environmental deterioration and resource allocation conflicts with other ocean industries along coasts and inner bays, it is an inevitable challenge for the aquaculture industry to sustainably utilize marine resources and maintain the health of marine ecosystems simultaneously, i.e., the blue economy.

At offshore sites, a deeper water column will reduce waste deposit concentrations around the fish cage and give fish more movement space by increasing the cage height (Chu et al., 2020). In addition, it is helpful to move the fish cage into a deeper and safer water layer to avoid storms (Chu et al., 2020). Cardia and Lovatelli (2015) also suggested that the water depth is preferably more than three times that of the depth of the fish cage. Therefore, some countries such as Ireland, Scotland, the Faroe Islands, Canada,

Image Removed

**(a)**

Image Removed

**(b)**

**Fig. 1.1** Global statistics and predictions: (a) Marine aquaculture production; (b) Installed finfish production capacity (DNV, 2021).

the Canary Islands, Australia, the Mediterranean, and Mexico, have begun offshore fish farming operations (Fredheim and Langan, 2009). In addition, DNV (2021) predicted that the capacity of global offshore finfish production will continue to increase and exceed that of sheltered fish farming as Fig. 1.1b.

Holmer (2010) defined 3 classes for fish farming sites: Class 1 – coastal farming, Class 2 off-coast farming and Class 3 - offshore farming, based on the geographical and hydrodynamical settings as shown in Table 1.1, reviewed by Chu et al. (2020). It can be found that the classification is mainly determined by the distance from shore, water depth, and wave conditions. Chu et al. (2020) also defined some practised restrictions on conditions for offshore fish cages:

- i) The offshore fish cage should be located in an exclusive economic zone, which is at least 3 km away from the coastline;
- ii) The water depth of the site should be greater than 50 m or at least three times the fish cage height, and the distance between the cage bottom and the seabed should not be less than 15 m;
- iii) The current velocity at the site is within the range of 0.1 to 1 m/s;
- iv) The significant wave height of 1 year return period at the site is greater than 3 m.

Nevertheless, offshore fish farming still faces difficulties and challenges. Compared with sheltered water, the sea conditions in deep sea are more complicated and the environmental loads are more severe. Under extreme weather conditions, the destruction, collapse or sinking of cages cause fishes to escape and die, resulting in significant economic losses, which inevitably lead to supernumerary difficulties and costs in the design, manufacturing and installation. Therefore, new technologies for offshore aquaculture cage systems, such as innovative concepts of ultra-large offshore fish cages, advanced engineering analysis models and data monitoring systems, et cetera, will gain traction and market share. For example, Ocean Farm I is a pioneering large-scale offshore cage system. Its design, manufacturing and installation incorporate a large number of advanced scientific technologies and require high levels of industrial manufacturing capabilities. As a result, extensive theoretical knowledge and technical support are demanded for the feasibility investigation of offshore fish farming based on the perspective of engineering research.

The marine facilities exposed offshore are bound to be affected by complex environmental factors, including wind, waves, currents, ice and other hydrological and meteorological elements. Earthquakes may also cause submarine landslides and high-density turbidity currents, with velocities of up to 25 m/s (Faltinsen, 2014). However, there are few requirements in existing standards for the determination of extreme environmental conditions.

**Table 1.1** Classifications of coastal, off-coast and offshore farming (Chu et al., 2020).

Image Removed

The forces generally experienced by cage chambers include gravity, hydrostatic pressure, fluid drags, fluid inertial forces, internal forces caused by other structural components and impact forces due to fish (the loads provided by a sudden impact due to fish movement). The vortex-induced vibration caused by viscous flows can also cause fatigue damage to the mooring cables. Therefore, the mechanistic study of hydrodynamics is crucial for the design of fish cages. Furthermore, the knowledge of the flow field is important for analysing the ecological environment inside and around the cages. This will facilitate the modelling of oxygen concentration and effluent transport inside or through the cage by capturing the flow field around the cage (Patursson, 2008).

An aquaculture cage system generally comprises of floating collars, net chambers, mooring systems, and sinkers (Fig. 1.2), and some novel concepts of offshore cage type are also proposed, such as hull-structure farms, semi/fully submersible cages, closed-containment tanks, et cetera. Severe structural dynamic responses can result in safety risks, and cage volume reductions also impact fish welfare under large deformations. Therefore, the simulation and monitoring of structural behaviours are commonly employed with the development of computational mechanics techniques. Notably, because of the motions and deformations of the net cage under hydrodynamic actions, the flow characteristics are significantly influenced due to fluid-structure interactions (FSI). The coupling theory of



Image Removed

**Fig. 1.2** The schematic diagram of a basic fish cage system (Zhao et al., 2019b).

FSI links the hydrodynamics to the structural analysis, which is essential for establishing a completed numerical framework for the cage system.

## 1.2 Aims and objectives

To date, the technology of nearshore fish cages has been developed and widely applied. However, the sheltered water areas are approaching its capacities, and many problems caused by nearshore aquaculture, such as the environmental issues and limited feeding capacities, indicate that offshore fish farming will become an inevitable trend for high productivity and low pollution in the future. For the offshore fish cage system, there are some technical challenges that need to be overcome. First, there are limited information and references about the feasibility of fish farming sited in deep seas due to the more complex sea conditions. Secondly, stronger waves, currents and other environmental loads will lead to more stringent requirements on the types, materials and robustness of the cage structure. Finally, traditional numerical methods usually require a huge amount of computation for hydroelastic analysis, which cannot be effectively applicable in the cases with actual scales in practising.

The aim of the present research is to develop a more efficient model for the hydroelastic analysis of fish cages, which can be employed by engineers and managers for the development of fish farms. The specified objectives include:

1. Presenting a systematic literature review to identify the major challenges associated with the development of offshore fish farming;

2. Developing a hydroelastic model of the open-net cages from single cages to cage arrays based on semi-analytical solutions, which can quickly and effectively simulate flow field information and structural dynamic responses, so it provides possible practice for the research of real-scale cages in the large wave domain;
3. Characterising the scattered or interfered wave fields in the presence of the cage and its corresponding wave responses;
4. Conducting parametric studies of the factors affecting the mechanical properties in the fish cage design, including hydrodynamic conditions (wave heights, wave periods, water depths, current velocities, etc.) and structural parameters (dimensions, strengths, net porosity, etc.). By the optimisation analysis to the relevant design parameters, it is beneficial to ensure the safety of aquatic facilities in a more economical design.

By accomplishing the four objectives, the hydroelastic mechanism of the flexible fish pen structure can be determined and along with some important findings assist engineers in designing offshore aquaculture systems through the developed model.

### 1.3 Outline of the thesis

This Ph.D. thesis is composed of the following parts:

Chapter 1 is an introduction to the research topic and background, and the research objectives are outlined.

Chapter 2 is an literature review, which critically reviews: i) the hydrodynamic actions and relevant evaluation approaches in marine aquaculture; ii) the structural dynamic performances and modelling techniques of cage systems. Finally, some significant research gaps are summarized.

Chapter 3 defines the research questions and establishes a research methodology for the Ph.D. research by assessing the literature available on the hydroelastic modelling methods and design considerations of fish cages. The scope and hypotheses of the current Ph.D. research are elucidated, and the whole research outcome of the Ph.D. thesis is divided into three study elements based on the development stage of the hydroelastic model of open-net fish cages.

Chapter 4 proposes a semi-analytical solution to describe the interaction between waves and open net cages. The results demonstrate that the proposed modelling framework could

give reasonable predictions for the hydroelastic behaviours of submersible flexible fish cages.

Chapter 5 improves the developed solution by introducing the membrane theory of shells for the governing equation of the cage structure. The improved model provides a more realistic solution to the wave response of cage structures. The characteristics of the scattered waves surrounding the cage and its corresponding dynamic response were identified.

Chapter 6 extends the model presented in Chapter 5 into the case with multiple net cages. Fish farming usually consists of multiple aquaculture pens. This study leads to a more general simulation model, and the properties of the wave interference phenomenon and mean wave drift effect in the fish cage array are implied.

Finally, Chapter 7 elaborates on some significant conclusions about the Ph.D. research. A general discussion is presented about the research outcomes, and this thesis is concluded by highlighting some key research findings. The significance, novelty and scientific contributions of the present studies are summarised, and the research limitations and future work lines are outlined as well.



# Chapter 2

## Literature Review

### 2.1 Introduction

An optimal fish cage design should provide adequate and suitable living spaces for fish under limited environmental conditions. Furthermore, the structures should be sufficiently strong to resist environmental loads as well as easy to maintain. In the design of fish farms, it is essential to understand the mechanisms of hydrodynamic actions and structural dynamic response for fish cages exposed to marine environments. This chapter reviews relevant studies on fish cages from the perspectives of fluid dynamics and structural and elastic dynamics, which provides theoretical foundations for the establishment of this Ph.D. study's hydroelastic analysis model.

Simulation techniques related to fish cage systems have always been a topic worthy of research attention. Laboratory tests or field measurements are the most direct and effective methods of hydroelastic analysis. However, physical simulations are limited by the design dimensions, equipment conditions, and laboratory costs. Moreover, it is relatively difficult to monitor and measure in-field experiments, which are susceptible to complex external factors and disturbances. Therefore, numerical modelling is an effective and flexible tool, but challenges exist when establishing the numerical model of a fish cage. Chen (2016) highlighted the following three main aspects in which such challenges manifest:

- i) A net is a complex structure composed of numerous twines, and the design scale of fish cages in practice is usually greater than 10 m in diameter; therefore, detailed modelling is not feasible for the cages with actual scales in practising;
- ii) The hydrodynamic modelling of fish cages is a multiscale problem. Microscopically, the diameter of normal net twine is approximately 2-5 mm, and determining the

**Table 2.1** Degree of exposure for waves and currents (NS9415, 2009).

Image Removed

effects of viscosity and turbulence in the boundary layer requires a relatively small scale for spatial discretisation. However, a macroscopic analysis of the fish cage system requires a relatively large computational domain with millions or even billions of computing grids, which is also extremely difficult and expensive;

- iii) The net material is a relatively flexible structure. In real sea conditions, considering the interaction of the flow field influenced by the structural deformation is essential.

These aspects imply that the most appropriate modelling techniques should be developed for this complex system. In reviewing the relevant literature, various rational methods were found to have been proposed for the hydroelastic analysis of net cages. The remainder of this chapter comprehensively elaborates on these methods for the simulation modelling of fish cages.

## **2.2 Hydrodynamic actions and analysis in marine aquaculture**

### **2.2.1 Hydrodynamic responses**

When marine structures are exposed offshore, the environmental factors will naturally be more complex. They mainly include the actions of currents, waves and winds, among others. The Norwegian aquaculture standard NS9415 (2009) defines the degree of exposure for waves and currents, as presented in Table 2.1. The hydrodynamic conditions have five exposure levels - namely small, moderate, medium, high and extreme, according to the ranges of wave conditions and current velocities.

## 2.2 Hydrodynamic actions and analysis in marine aquaculture

---

### I. Current

Ocean currents refer to the movements of seawater caused by various environmental actions. They can be divided into the following components (Faltinsen, 1993):

$$\mathbf{u}_c = \mathbf{u}_t + \mathbf{u}_w + \mathbf{u}_s + \mathbf{u}_m + \mathbf{u}_{\text{set-up}} + \mathbf{u}_d, \quad (2.1)$$

in which:

$\mathbf{u}_t$  is the tidal current component;

$\mathbf{u}_w$  is the wind-generated current component;

$\mathbf{u}_s$  is the Stokes drift current component;

$\mathbf{u}_m$  is the major ocean circulation component;

$\mathbf{u}_{\text{set-up}}$  is the component due to set-up phenomenon and surge;

$\mathbf{u}_d$  is the local density-driven current component.

Furthermore, several other factors can also contribute to the effect of currents on fish cages. For example, since the characteristic time of internal waves is 20 minutes, they are considered a stable current within a depth of 300 m, and the maximum horizontal velocity may reach up to 3 m/s during a 100-year return period (Faltinsen, 2014). This may also be a factor that cannot be ignored for aquatic facilities that are located extremely far away from the coastline with quite deep water depth, such as Shenlan No. 1 in China.

Drag forces caused by excessive current velocities can cause severe deformation to as well as reduce the volume of the net cage and critical mooring loads (Lader and Fredheim, 2006). The reduction in cage volume leads to a reduction in swimming space and increased living stress on farmed fish, resulting in a decline in growth (Conte, 2004). Additionally, the intensity and period of turbulence inside the net cage can also affect the manoeuvring of fish while swimming (Kim, 2012). In practice, current velocities in the range of 0.1 - 0.6 m/s are most suitable for salmon farming, but breeding salmon in environments where current velocities exceed 1 m/s is also not recommended (reviewed by Chu et al. (2020)). However, currents also have several positive effects: First, they can accelerate the transport of deposited wastes to purify the water around the fish cage. Helsley and Kim (2005) conducted a field test in the wake region of a submerged biconical fish cage. Ammonia ( $\text{NH}_4^+$ ) was used as a tracer to measure the mixing in the wake stream. Significant dilution occurred in the first two diameters downstream of the cage, and the concentration of  $\text{NH}_4^+$  was reduced 10-fold. This indicated that the water in the wake region was replaced by

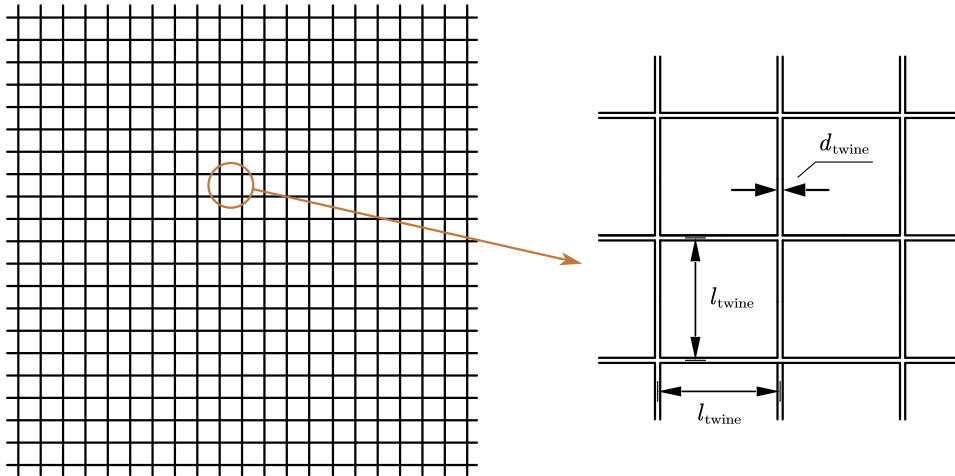


**Fig. 2.1** Configuration of a typical net structure.

fresh water from the outer region. In addition, because of the current action, the slack in the net was also reduced (Lader and Fredheim, 2006).

The flow drag force is composed of the pressure difference and viscous stress. The drag force acting on the net is generally believed to be determined by the angle of flow attack, the solidity ratio, the Reynolds number, and material properties, among others. The solidity ratio  $S_n$  is to indicate the density of the net mesh instead of the porosity, which is defined as the net projected area divided by the outline area (Fredheim, 2005):

$$S_n = \frac{2d_{\text{twine}}}{l_{\text{twine}}} - \left( \frac{d_{\text{twine}}}{l_{\text{twine}}} \right)^2, \quad (2.2)$$

where  $d_{\text{twine}}$  is the diameter of the net twines, and  $l_{\text{twine}}$  is the distance between the net twines, as illustrated in Fig. 2.1. The Reynolds number  $R_e$  has been proposed to describe the ratio of inertial forces to viscous forces within the fluid, which is defined for the net structure as follows:

$$R_e = \frac{\rho |\mathbf{u}_\infty| d_{\text{twine}}}{\mu}, \quad (2.3)$$

where  $\mathbf{u}_\infty$  is the incoming current velocity,  $\rho$  is the density of the fluid, and  $\mu$  is the dynamic viscosity of the fluid.

The experimental investigation by Tang et al. (2017) illustrated that, for an inclined net panel in the current, the drag force increases with the greater angle between the incoming flow velocity vector and the tangential vector of the screen, but the lift force reaches its peak at an angle of  $50^\circ$ . Tang et al. (2018) conducted extensive physical water tank tests for the fluid resistance effect of net panels. Their results clearly demonstrated that the drag force increases with a greater solidity ratio  $S_n$ . When  $S_n$  was low (0.190), the



## 2.2 Hydrodynamic actions and analysis in marine aquaculture

---

relationship between the fluid resistance coefficients of the net panel and the Reynolds numbers  $R_e$  was similar to that of a cylinder. Therefore, for fish cage nets with a high solidity ratio, the interactions between the net twines cannot be ignored. The measured data indicated that the effect of the net knot was also negligible under a flow condition with low Reynolds numbers. Additionally, the discrepancy in the fluid resistance of nylon and steel is explained by the material hydrophilicity and surface roughness, while it is independent of the Reynolds number (Tang et al., 2018).

The consideration of FSI is also necessary when estimating the drag force in fluids. Through experimental investigations of the geometry of fish pens in a uniform flow, Lader and Enerhaug (2005) found that the simple drag calculation formula exhibited a large error with the experimental results; by contrast, a numerical model that considered the dependency between force and deformation provided a more accurate estimation. Yao et al. (2016) compared their simulated results between numerical models with and without FSI, wherein a notable deviation manifested under high current velocities.

In addition, the topic of wakes caused by the blocking effect of fish cage nets has received much attention in engineering. Neglecting the flow velocity reduction at the rear of the cage will result in an overestimation of the mooring force by up to 22% (Faltinsen and Shen, 2018). Moreover, in an array of net cages, those further downstream might experience less water exchange; thus, there would be lower concentrations of dissolved oxygen and increased waste pressure compared with the upstream cages, and the interaction of the wakes due to each cage would result in stronger combined water blockage (Klebert et al., 2013). Cheng et al. (2020) concluded that the wake effects around a cage can be classified as twine-to-twine, net-to-net or cage-to-cage interactions. Normally, velocity reduction is a function determined by the Reynolds number, solidity ratio and incoming flow angle (Cheng et al., 2020). Some empirical evaluations of the velocity reduction through a net panel can be found in the experimental tests and calculations of Løland (1991), Patursson (2008) and Kristiansen and Faltinsen (2012).

The impact of the drag effects of twines on the flow field can be captured through experimental measurements and numerical simulations as the water flows through the net. Bouhoubeiny et al. (2011) used the time-resolved PIV method to conduct flow field measurements around trawl nets for cod, and they also extracted large-scale energy vortices using the proper orthogonal decomposition method. Based on an analysis of the vortex shedding frequency, the authors found that the vortex shedding near the wake was synchronised with the vibration of the net structure. Through numerical simulations, Shim et al. (2009) found that nets with low porosities (i.e., fouling leads to serious net blockage)

## Literature Review

---

might cause flow recirculation, while Helsley and Kim (2005) indicated that the tilt angle of the fish cage could generate additional turbulence and cause large-scale vortices.

Generally, finer nets can increase the lateral flow velocity around the cage and significantly reduce the flow velocity in the wake region (Gansel et al., 2010). Gansel et al. (2010) defined the following three regimes for describing the flow around the cylindrical net cage (reviewed by Klebert et al. (2013)):

- i)  $0 < S_n \leq 0.25$ : At this time, a large amount of water can pass through the net and will evoke a clear vortex street in the wake region;
- ii)  $0.25 < S_n \leq 0.75$ : The interaction of the wakes causes an additional blocking effect as well as more water to be compressed around the cage;
- iii)  $S_n > 0.75$ : The porous cage is currently similar to a solid cylindrical shell, and more water blockage and vortex shedding occur around it.

Therefore, different solidity ratios or porosities of the net significantly determine the flow condition's characteristics around the fish cage.

## II. Waves

Waves are a common form of energy transfer in the sea. Excessive hydrodynamic loads caused by waves may not only damage cages and mooring systems but also injure fish (the cage is over squeezed or the fish is rammed) (Chu et al., 2020). Different from the long-term deformation caused by a steady flow, the wave excitation force will cause periodic motions of the cage, which are collectively known as the structural dynamic response. When the wave frequency is close to the natural frequency of the structure causing the resonance, the structure will have a significant dynamic response. Therefore, in the design of offshore floating structures, it is essential to avoid the occurrence of resonance.

Higher waves can easily cause serious destruction and the collapse of floating fish cages, leading fish to escape, which would result in tremendous economic losses. The Douglas sea scale is a standard for describing the wave intensity of wind seas and swells. Table 2.2 presents the classification of wind-sea states and swells from Morrissey et al. (2015). Moreover, oceanic freak or rogue waves are characterised by an unusually large ratio between the maximum wave height and the significant wave height (i.e., greater than two; Faltinsen (2014)).

Because of the nonlinear effects of surface waves, the applicable wave theory can be determined using the normalised wave height  $H/(gT^2)$  and the normalised water depth  $h/(gT^2)$  according to Méhauté (1976), as illustrated in Fig. 2.2. The linear wave and

**Table 2.2** The Douglas sea scale for wind-sea states and swells (Morrisey et al., 2015).

Image Removed

Image Removed

**Fig. 2.2** Range of application of different wave theories (Méhauté, 1976).

Stokes wave theory are found to be applicable to the deep water region, but the shallow water condition is mainly suitable for the conoidal wave and solitary wave theory. The waves in the intermediate depth region can be described using a variety of wave models. Song et al. (2005) indicated a greater calculation error between the second-order Stokes wave theory and the linear wave theory for estimating the wave forces acting on a cubic cage as the wave height increases or the water depth decreases. The mean wave drift load is also a nonlinear phenomenon caused by the first-order potential, wherein the second-order components do not contribute (Faltinsen, 1993), so the mean drift force can be directly estimated by the small-amplitude wave theory. Moreover, if the studied case is in irregular waves, the different wave spectrums could have an obvious influence on the motion of the cage (Qin et al., 2020).

Different from constant currents, since the wave-generated flows are unsteady, the inertial effect of the fluid cannot be ignored. The Keulegan–Carpenter ( $K_C$ ) number is a dimensionless number used to describe the relationship between the viscous and inertial forces on an object in an oscillating flow field. For net structures, it is defined as follows:

$$K_C = \frac{u_a T}{d_{\text{twine}}}, \quad (2.4)$$

## 2.2 Hydrodynamic actions and analysis in marine aquaculture

---

where  $u_a$  is the velocity amplitude of the water particle, and  $T$  is the oscillatory period of the fluid.

Dong et al. (2019) investigated the hydrodynamic forces on the net panel in a wave flume. Their experimental results revealed that the horizontal component of the wave force was greater than the vertical component, while the horizontal component significantly depended on the  $K_C$  number. On the other hand, a frequency domain analysis revealed that the high-frequency nonlinear effect was more obvious when the ratio of wavelength to water depth increased. The fitting of experimental data by Hamelin et al. (2013) indicated that the hydrodynamic drag coefficient of the slatted screen in an oscillatory flow was close to the results in a steady flow when  $K_C > 100$ . This implies that the fluid inertial force is minor in this case. Furthermore, calculations performed by Zhao et al. (2008) proved that the inertia effect can be ignored when the  $K_C$  number of the net exceeds 150. Furthermore, Lader et al. (2007a) experimentally demonstrated that high-wave energy environments (i.e., greater wave steepness and longer wave period) and nets with high solidity ratios  $S_n$  lead to an increase in wave force.

Usually, the cage being immersed under the free water surface is beneficial for reducing the imposed wave loads. The theoretical analyses of Su et al. (2015) and Mandal and Sahoo (2016) have demonstrated that the peak of the wave loads appeared near the top of the net chamber. Moreover, the experimental results of Liu et al. (2019) illustrated that the tension of the mooring cables and the movement of the floating collar were significantly weakened as the diving depth of the cage increased. However, when the fish cage reached a certain depth, the attenuation trend tended to stabilise. Based on the results of Liu et al. (2019), one-third of the water depth was determined to be the optimal submergence depth for the fish cage. Additionally, the numerical modelling of Xu et al. (2013a) revealed that the wave steepness had a minor effect on the mooring tension under the submerged condition compared with the floating condition.

The blocking effect and motion of the net cage cause certain perturbations to the surface waves. Based on the potential flow theory, the hydrodynamic force exerted on the floating structure can be divided into the following two parts (Faltinsen, 1993):

- i) The Froude–Kriloff force due to the incident waves and the force generated by wave diffraction due to the presence of the structure. These two forces are collectively referred to as the wave excitation force;
- ii) The added mass and damping effect as a result of wave radiation, as well as the restoring force of the static water due to the floating body deviating from the equilibrium position.

## Literature Review

---

Lader et al. (2007b) analysed the damping effect of nets on passing waves. For longer waves, nets with higher solidity ratios provided more effective damping of wave energy, while wave damping was related to the length of the twine for shorter waves. Furthermore, a more obvious influence of the net on the geometry of the wave occurred as the wave steepness increased. Selvan et al. (2021) derived analytical solutions for surface wave scattering around multiple circular net cages, and some of the regulations are summarised as follows:

- i) Wave amplitude attenuation occurs on the leeward side of the cage, and the attenuation is more pronounced under high-frequency wave conditions;
- ii) Constructive interference occurs for an array of cages with small spacings, and the scattering of waves is intense when the number of cages is increased.

To quantify these effects, Gharechae and Ketabdari (2022) introduced the energy transmission index (*ETI*) to represent the transmitted portion of incident wave energy:

$$ETI = \int_0^a \int_0^{2\pi} \xi_a^2 r d\theta dr \left/ \left[ \left( \frac{H}{2} \right)^2 \pi a^2 \right] \right., \quad (2.5)$$

where  $\xi_a$  is the amplitude of the free water surface elevation,  $H$  is the incident wave height, and  $a$  is the cage diameter.

For closed fish cages, the motion of the cage under wave excitation can cause an obvious water-sloshing phenomenon inside it. Because of the relatively large excitation amplitudes involved in marine applications, resonant sloshing may involve critical nonlinear free water surface effects (Faltinsen and Shen, 2018). Furthermore, the sloshing response is predicted to be infinite at the eigenfrequencies of the cage system through the linear potential flow theory instead of the finite amplitude in reality; thus, viscous damping and nonlinear free water surface effects should be included (Strand and Faltinsen, 2017).

Faltinsen and Timokha (2009) developed a nonlinear multimodal method for describing global sloshing loads in a time-efficient manner without considering wave breaking in deep water. Severe sloshing originates from the lowest sloshing mode with nonlinear energy transfer; therefore, some strategies for avoiding the excitation of the lowest mode by moving the cage in an elastic manner are as follows (Faltinsen and Timokha, 2009):

- i) A control system for body motion monitoring;
- ii) An air-turbine absorbing the sloshing energy;
- iii) The assembly of a compartment to prevent swirling.

## 2.2 Hydrodynamic actions and analysis in marine aquaculture

---

Wiegerink et al. (2022) also proposed the novel concept of slosh suppression blocks assembled on floating collars and validated their efficiency using water tank tests. Notably, a considerable change might occur in the motion response of a flexible cage compared with a rigid cage (Strand and Faltinsen, 2019).

In the ocean, another common form of seawater motion is the interaction between waves and currents. Currents can significantly affect the load caused by waves (Lader and Fredheim, 2006). In a numerical investigation, Xu et al. (2013b) found that the cage suffered the most critical hydrodynamic forces when the angle between the incident wave and the incoming current was less than  $30^\circ$ . The dominant mean hydrodynamic loads increase significantly under long and steep waves relative to currents only (Kristiansen and Faltinsen, 2015).

Kristiansen and Faltinsen (2015) simply superposed the current velocity and the wave water particle velocity in estimating the hydrodynamic force on a fish cage net. Zhao et al. (2007) and Xu et al. (2013a,b) have adopted the theory of Hedges and Lee (1992) to equvalate the combined waves and currents to new waves with interacted frequencies, wave heights and wavelengths for the cases with single or multiple cages, respectively. Moreover, Liu et al. (2021) introduced currents to the analytical solution for the interaction between waves and circular net cages, but they did not consider the potential for structure-induced disturbance to the current field.

Considering the aforementioned research comprehensively, the influence of waves is highly significant to the safety of fish cage systems. Therefore, floating breakwaters are essentially considered to attenuate the impacts of waves (Dai et al., 2018).

### 2.2.2 Empirical equations of hydrodynamic loads

Empirical formulas based on theoretical analyses and experimental investigations are usually simple and practical, so they are often applied for estimating hydrodynamic forces on fish cage nets. This section discusses two commonly applied empirical formulas, namely the Morison-type equation and the screen-type methods.

#### I. Morison-type equation

The net structure can be treated as consisting of mesh bars (as seen in Fig. 2.3). The Morison equation (Morison et al., 1950) is an empirical formula that is commonly used to evaluate the hydrodynamic force acting on slender bars, where the force is divided into

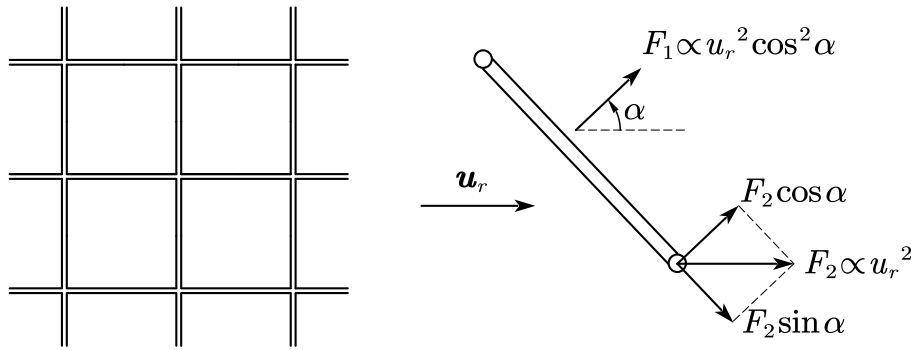


**Fig. 2.3** Sketch of the method when utilising the Morison-type equation:  $F_1$  is the drag force when the net twine is inclined with respect to the incoming flow velocity vector, and  $F_2$  is the drag force when the net twine is orthogonal with the incoming flow velocity vector.

two components, namely the drag forces  $\mathbf{F}_d$  and the inertial forces  $\mathbf{F}_i$ :

$$\mathbf{F} = \mathbf{F}_d + \mathbf{F}_i = \frac{1}{2}\rho C_d d_{\text{twine}} |\mathbf{u}| \mathbf{u} + \rho(1 + C_m) V_{\text{twine}} \frac{d\mathbf{u}}{dt}, \quad (2.6)$$

where  $\mathbf{u}$  is the flow velocity,  $d_{\text{twine}}$  is the diameter of the twine,  $V_{\text{twine}}$  is the volume of the twine,  $C_d$  is the drag coefficient, and  $C_m$  is the added mass coefficient. In Eq. (2.6) the first term on the right-hand side represents the drag force due to viscous effects and pressure differences, while the second term is the inertial force due to unsteady flow. According to Brebbia and Walker (1979), for movable members, the Morison equation can be generalised as follows:

$$\mathbf{F} = \frac{1}{2}\rho C_d d_{\text{twine}} |\mathbf{u}_r| \mathbf{u}_r + \rho V_{\text{twine}} \frac{d\mathbf{u}}{dt} - \rho(C_m - 1) V_{\text{twine}} \frac{d\mathbf{u}_r}{dt}, \quad (2.7)$$

where  $\mathbf{u}_r$  is the velocity of the flow relative to the net twine. If the net twine is inclined relative to the incoming flow, the drag force can be decomposed into a normal component and a tangential component following Haritos and He (1992):

$$\mathbf{F} = \frac{1}{2}\rho C_{dn} d_{\text{twine}} |\mathbf{u}_n| \mathbf{u}_n + C_{d\tau} \mathbf{u}_\tau + \rho C_m V_{\text{twine}} \frac{d\mathbf{u}_n}{dt} + \rho V_{\text{twine}} \frac{d\mathbf{u}}{dt}, \quad (2.8)$$

where  $\mathbf{u}_n$  and  $\mathbf{u}_\tau$  are the normal and tangential velocity components, and  $C_{dn}$  and  $C_{d\tau}$  are the drag coefficients in the normal and tangential direction, respectively.

The drag coefficient  $C_d$  is usually considered to be related to the Reynolds number  $R_e$ , where plotting curves of  $C_d$  versus  $R_e$  can be found in the book of Hoerner (1965). From the empirical formula of Choc and Casarell (1971), the drag coefficient of the slender bar



## 2.2 Hydrodynamic actions and analysis in marine aquaculture

---

is as follows:

$$C_{dn} = \begin{cases} \frac{8\pi}{Re_n^s} (1 - 0.87s^{-7}) & (0 < Re_n \leq 1) \\ 1.45 + 8.55Re_n^{-0.90} & (1 < Re_n \leq 30) \\ 1.1 + 4Re_n^{-0.50} & (30 < Re_n \leq 10^5) \end{cases}, \quad (2.9)$$

$$s = -0.077215665 + \ln(8/Re_n).$$

For the knot part of the net, Fredheim (2003) suggested a drag coefficient  $C_d$  in the range of 1.0 - 2.0 when it is modelled as a sphere. Furthermore, under unsteady currents, an added mass coefficient  $C_m$  of 1 is suggested for the circular cross-section (Wang and Liang, 2013). Nevertheless, under wave actions, the effects of  $K_C$  numbers are also significant. Sarpkaya and Isaacson (1981) demonstrated the factors that determine  $C_d$  and  $C_m$  through a nondimensional analysis as follows:

$$(C_d, C_m) = f\left(K_C, \frac{K_C}{Re}, \frac{\mu_s}{d_{twine}}\right), \quad (2.10)$$

where  $\mu_s$  is the material roughness coefficient of the net twine. The experimental measurements of Dong et al. (2019) indicated that the horizontal wave force heavily depends on the  $K_C$  number, where  $C_d$  decreases but  $C_m$  increases as the  $K_C$  number increases. Furthermore, the net solidity ratio  $S_n$  might be the fourth factor influencing these hydrodynamic coefficients (Fredheim, 2003).

The deformation of net panels and cages under the action of currents have been simulated using Morison-type equations, producing reasonable results (Bris and Marichal, 1998; Chen et al., 2021; Li et al., 2006; Myrli and Khawaja, 2019; Tsukrov et al., 2003). For the wave action, the Morison equation is valid for twine elements with a diameter much smaller than the wavelength, and the diffraction effect on the free water surface is also ignored (Tsukrov et al., 2003). Zhao et al. (2008) compared the calculated results of the Morison equation with experimental data for net panels in a wave flume, where there were no significant discrepancies. The authors highlighted that, when evaluating the wave force, the influence of the  $K_C$  number and inertial force can be ignored, and that it is feasible to use only the drag coefficient  $C_d$  related to the Reynolds number  $Re$ . However, as the conclusions of Zhao et al. (2008) are not consistent with the experimental results of Dong et al. (2019), further studies are required to clarify the effects of the  $K_C$  number and inertial force still.

The Morison-type equation provides a simple method of calculating the hydrodynamic load on the net cage, and the aforementioned experimental and numerical results indicate that it is feasible in engineering practice. However, the Morison equation still has some

drawbacks: First, the interaction between the net twines is ignored (e.g., twine-to-twine wake interaction effects). The flow around the twine elements is usually assumed not to be disturbed by the interaction with other twines (Tsukrov et al., 2003). Notably, Berstad et al. (2012) suggested that the corrected flow velocity surrounding the net mesh could be determined by conservation of momentum. On the other hand, the influences of  $R_e$  and  $K_C$  still require further discussion. When a vortex street is formed in the wake behind the twine cylinder, the cylinder will also impose a periodic lift excitation force perpendicular to the incoming flow direction, which is related to  $R_e$  and  $K_C$  ( $K_C$  is only for oscillating flow) (Wang and Liang, 2013).

## II. Screen-type method

Another hydrodynamic force empirical model for fish cage nets is the screen-type method. Kristiansen and Faltinsen (2012) presented a detailed expression for this method.

The net structure can be regarded as the composition of several super elements (the shading area in Fig. 2.4), whose centres are consistent with the knot centres. Each super element can be divide into four planar screens. The drag force  $\mathbf{F}_D$  and lift force  $\mathbf{F}_L$  acting on each screen can be decomposed into a normal force  $\mathbf{F}_N$  perpendicular to the plane and a tangential force  $\mathbf{F}_T$  tangential to the plane. The force magnitude can be described as follows:

$$\begin{aligned} F_D &= \frac{1}{2} C_D \rho A_s u_r^2, & F_L &= \frac{1}{2} C_L \rho A_s u_r^2, \\ F_N &= \frac{1}{2} C_N \rho A_s u_r^2, & F_T &= \frac{1}{2} C_T \rho A_s u_r^2, \end{aligned} \quad (2.11)$$

where  $A_s$  is the area of the screen, and the coefficients  $C_D$ ,  $C_L$ ,  $C_N$  and  $C_T$  satisfy the following relations:

$$C_D = C_N \cos \alpha + C_T \sin \alpha, \quad C_L = C_N \sin \alpha - C_T \cos \alpha. \quad (2.12)$$

$C_D$  and  $C_L$  can be expanded in Fourier series dependent on the attack angle of flow  $\alpha$ :

$$\begin{aligned} C_D(\alpha) &= C_D(0) \sum_{n=1}^{\infty} a_{2n-1} \cos(2n-1)\alpha, \\ C_L(\alpha) &= C_L\left(\frac{\pi}{4}\right) \sum_{n=1}^{\infty} b_{2n} \sin 2n\alpha, \end{aligned} \quad (2.13)$$

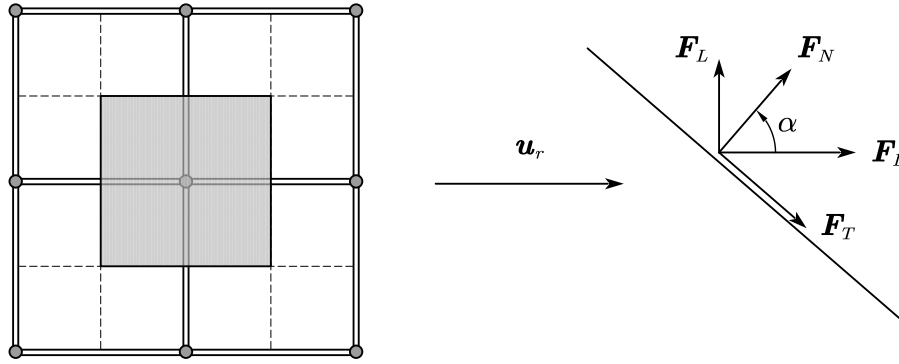


**Fig. 2.4** Sketch of the screen-type method.

and  $C_N$  and  $C_T$  are functions determined by the Reynolds number  $R_e$  and solidity ratio  $S_n$ :

$$\begin{aligned} C_N(\alpha) &= \frac{C_d S_n (2 - S_n)}{2(1 - S_n)^2} \cos^2 \alpha, \quad 0 \leq \theta \leq \pi/4, \\ C_T(\alpha) &= \frac{4C_N(\alpha)}{8 + C_N(\alpha)}, \quad 0 \leq \theta \leq \pi/4, \end{aligned} \quad (2.14)$$

where  $C_d$  is dependent on  $R_e$  from Eq. (2.9). Furthermore, from the experimental investigation of Tang et al. (2018), the effects of net knots and net materials on the coefficient  $C_D$  are relatively minor, and the influence of knots can be ignored when  $R_e \leq 400$ .

In Eq. (2.13), the unknown constants can be calibrated using experimental data, and it is usually an acceptable approximation to retain two or three truncation terms. Some calibrated parameters or empirical formulas about the coefficients  $C_D$  and  $C_L$  has been proposed (Cheng et al., 2022; Kristiansen and Faltinsen, 2012; Løland, 1991; Martin et al., 2020; Yao et al., 2016).

The screen-type model greatly compensates for the drawback of the Morison-type equation, ignoring the interaction between net twines, and it has been proven to be a reasonable approximation when evaluating the hydrodynamic loads on nets (Kristiansen and Faltinsen, 2012, 2015; Lader and Fredheim, 2006; Løland, 1991). In structural modelling, its principle is to replace the bar elements with equivalent super elements, and it can be coupled with computational fluid dynamics (CFD) models (Lader and Fredheim, 2006), as discussed in the subsequent section.

However, few researchers currently consider the effect of inertial forces and the  $K_C$  number under waves in the screen-type model; therefore, this method only performs more reasonably for constant current actions. For the net panel, Lader et al. (2007a) compared the measured wave forces in a water tank with the results calculated using the Morison equation and screen-type model. By contrast, the screen-type model only provided a

favorable evaluation for the net with high solidity ratios. Alternatively, Eq. (2.6) predicts the horizontal wave force more accurately, while Eq. (2.8) provides the best result for the vertical wave force. Therefore, the Morison equation still has potential in the evaluation of wave forces. Actually, the accuracy of the Morison-equation model and screen-type model in predicting the hydrodynamic loads should be both highly dependent on the accurate selection of the hydrodynamic coefficients.

Most researchers directly adopt the water particle velocity of incoming currents or incident waves when applying empirical formulas to assess hydrodynamic loads on the net. However, in actual conditions, the flow velocity would be significantly reduced in the wake behind the net (i.e., the flow field is disturbed by the net), and the diffraction effect of waves cannot be ignored because a fish cage is a large-scale structure relative to the wavelength macroscopically. In addition, the influence of rigid body motions or elastic deformations of the structure on the flow field is an issue in need of attention. Therefore, establishing a hydrodynamic simulation model is essential.

### 2.2.3 Potential flow models

As previously mentioned, for fish cages with large dimensions, the presence of the structure will have a negligible perturbation on the wavefield. On the other hand, waves in the ocean are gravity waves, which can be regarded as a kind of potential motion (Wang and Liang, 2013). Therefore, solving the interactions between waves and fish cages using the potential flow theory is feasible.

At present, in the potential flow model, the net plane is usually treated as the boundary of the fluid domain governed by the porous medium theory. On the other hand, the methods for solving the Laplace equation include the eigenfunction expansion method, boundary element method (BEM), finite element method (FEM) and scaled boundary FEM (SBFEM). This section elaborates on these methods as well as related applications of the potential flow models in detail.

#### I. Governing equation

If the fluid is assumed to be irrotational and inviscid, the fluid velocity vector  $\mathbf{u}(x, y, z, t)$  can be expressed as the gradient of the velocity potential  $\Phi(x, y, z, t)$ , that is,  $\mathbf{u} = \nabla\Phi$ . In this scenario, the flow field can be governed by the Laplace equation due to mass conservation:

$$\nabla^2\Phi = \frac{\partial\Phi^2}{\partial x^2} + \frac{\partial\Phi^2}{\partial y^2} + \frac{\partial\Phi^2}{\partial z^2} = 0. \quad (2.15)$$

## 2.2 Hydrodynamic actions and analysis in marine aquaculture

---

For large floating offshore structures, the velocity potential satisfies the linear superposition of the incident potential, diffraction potential and radiation potential, namely  $\Phi = \Phi^I + \Phi^D + \Phi^R$ , while they all satisfy the Laplace equation. Therefore, by solving the Laplace equation with known boundary conditions, the velocity potential and the corresponding fields of flow velocity, pressure and free water surface elevation can be obtained.

### II. Boundary conditions

For a mathematical physics equation, in addition to the governing equation, the initial value conditions and boundary value conditions corresponding to the specific problem should also be determined. Because the wave motion is assumed to be a harmonic oscillation, the difficulty of deriving its solution depends on the processing of the boundary conditions.

According to Dean and Dalrymple (1991), at the free water surface elevation  $z = \xi$ , the kinematic boundary condition is

$$\frac{\partial \Phi}{\partial z} \Big|_{z=\xi} = \frac{\partial \xi}{\partial t} + \frac{\partial \xi}{\partial x} \frac{\partial \Phi}{\partial x} \Big|_{z=\xi}, \quad (2.16)$$

and the dynamic boundary condition is

$$\frac{\partial \Phi}{\partial t} \Big|_{z=\xi} + \frac{1}{2} (\nabla \Phi \cdot \nabla \Phi) \Big|_{z=\xi} + g\xi = 0. \quad (2.17)$$

Because the viscosity of the fluid is ignored in the potential flow theory, the slippery condition is invoked on the seabed boundary with a constant water depth:

$$\frac{\partial \Phi}{\partial z} \Big|_{z=-d} = 0. \quad (2.18)$$

The perturbation theory assumes that the solution of the wave motion can be expanded by a power series with a small parameter  $\varepsilon$ :

$$\begin{aligned} \Phi &= \sum_{n=1}^{\infty} \varepsilon^n \Phi_n = \varepsilon \Phi_1 + \varepsilon^2 \Phi_2 + \dots, \\ \xi &= \sum_{n=1}^{\infty} \varepsilon^n \xi_n = \varepsilon \xi_1 + \varepsilon^2 \xi_2 + \dots, \end{aligned} \quad (2.19)$$

and the velocity potential  $\Phi$  at  $z = \xi$  can be expanded in a Taylor series:

$$\Phi \Big|_{z=\xi} = \Phi \Big|_{z=0} + \xi \frac{\partial \Phi}{\partial z} \Big|_{z=0} + \frac{\xi^2}{2!} \frac{\partial^2 \Phi}{\partial z^2} \Big|_{z=0} + \dots \quad (2.20)$$

By substituting Eqs. (2.16) and (2.17) into Eq. (2.20), one obtains the following:

$$\begin{aligned} \varepsilon \left( \frac{\partial \Phi_1}{\partial z} - \frac{\partial \xi_1}{\partial t} \right) + \varepsilon^2 \left( \frac{\partial \Phi_2}{\partial z} - \frac{\partial \xi_2}{\partial t} + \xi_2 \frac{\partial \Phi_2}{\partial z} - \frac{\partial \xi_1}{\partial x} \frac{\partial \Phi_1}{\partial x} \right) + \dots = 0, \\ \varepsilon \left( \frac{\partial \Phi_1}{\partial t} + g \xi_1 \right) + \varepsilon^2 \left\{ \begin{array}{l} \frac{\partial \Phi_2}{\partial t} + g \eta_2 + \frac{\partial}{\partial t} \left( \xi_1 \frac{\partial \Phi_1}{\partial z} \right) \\ + \frac{1}{2} \left[ \left( \frac{\partial \Phi_1}{\partial x} \right)^2 + \left( \frac{\partial \Phi_1}{\partial z} \right)^2 \right] \end{array} \right\} + \dots = 0. \end{aligned} \quad (2.21)$$

In Eq. (2.21), only when the coefficient corresponding to  $\varepsilon^n$  is 0, the left-hand sides of the equations are equal to zero, which represents the kinematic and dynamic boundary conditions for the  $n$ th-order velocity potential. In addition, the first-order scatter potential  $\Phi^S{}_1 = \Phi^D{}_1 + \Phi^R{}_1$  satisfies Sommerfeld's radiational condition (Sommerfeld, 1949) at infinity, whose form in a cylindrical coordinate system  $(r, \theta, z)$  is as follows:

$$\lim_{r \rightarrow \infty} \sqrt{r} \left( \frac{\partial \Phi^S}{\partial r} \pm i \kappa_0 \Phi^S \right) = 0, \quad (2.22)$$

where  $\kappa_0$  is the wavenumber.

According to the Bernoulli equation, the pressure  $p^*$  is:

$$p^* = -\frac{\partial \Phi}{\partial t} - \frac{1}{2} \rho (\nabla \Phi \cdot \nabla \Phi) - \rho g z, \quad (2.23)$$

and its linearised form is

$$p^* = -\frac{\partial \Phi}{\partial t} - \rho g z. \quad (2.24)$$

The mean wave pressure in a wave period can be obtained by substituting the first-order solution into Eq. (2.23) and the time-averaged operation.

Because the thickness of the net panel is quite small relative to the flow scale, it is often treated as a domain boundary and governed by the porous medium flow model, which mainly includes the linear model and the quadratic model.

**i. Linear porous flow model** The linear model implies that the flow through the perforated structure satisfies Darcy's law, where the pressure drop linearly depends on the normal velocity of the permeation flow. According to Yu and Chwang (1994), the momentum equation of the flow within the porous medium under wave action is as follows:

$$f_i \frac{\partial \mathbf{u}_n}{\partial t} = -\frac{\nabla p^*}{\rho} - f_r \omega \mathbf{u}_n, \quad (2.25)$$

where the constants  $f_r$  and  $f_i$  are the linearised coefficients of the porous resistance effect and fluid inertial effect, respectively.

## 2.2 Hydrodynamic actions and analysis in marine aquaculture

For a thin-walled structure, assuming the pressure across its thickness is approximated linearly and considering the structural motions, Eq. (2.25) can be rewritten on its cross-section equation  $S(r, \theta) = 0$  as follows:

$$\nabla\Phi \cdot \mathbf{n} = ik_0\tau(\Phi^- - \Phi^+) + \frac{\partial \mathbf{x}}{\partial t} \cdot \mathbf{n} \Big|_{S(r, \theta=0)}, \quad (2.26)$$

where  $\Phi^-$  and  $\Phi^+$  represent the velocity potential on the leeward and windward sides of the porous structure, respectively;  $\mathbf{n}$  is the unit normal vector on the structural body surface;  $\mathbf{x}$  is the structural displacement relative to the mean position; and the porous effect parameter  $\tau$  is

$$\tau = \frac{\tau_0(f_r + if_i)}{\kappa_0 t_s (f_r^2 + f_i^2)} = \tau_r + i\tau_i, \quad (2.27)$$

where  $\tau_0$  is the porosity of the porous medium and  $t_s$  is its thickness. In Eq. (2.27), the real part  $\tau_r$  represents the porous resistance effect of the medium, while the imaginary part  $\tau_i$  means the fluid inertia effect. Eq. (2.26) also means that the flow velocity is equal to the permeation velocity plus the velocity of the structural motion in the normal direction of the interface  $S(r, \theta) = 0$ . Notably, Eq. (2.26) is only a linear approximation on the structural body surface, as the boundary condition cannot be satisfied at the instantaneous position of the wet surface. This requires the deformation amplitude of the structure to be relatively small compared with its cross-sectional dimension by preserving the linear terms in the Taylor expansion (Faltinsen, 1993).

Ito et al. (2014) offered another set of empirical formulas for  $\tau_r$  and  $\tau_i$  as follows:

$$\begin{aligned} \tau_r &= \frac{1}{2\pi} \frac{[27.73/(\kappa_0 H/2)] \tau_0^2}{1 + [0.5510 - 0.01998/(\kappa_0 H/2)] \tau_0}, \\ \tau_i &= \frac{1}{2\pi} \frac{0.002579 [27.73/(\kappa_0 H/2)] (\kappa_0 l_{\text{cube}}/2) (\kappa_0 H/2)^{-1.547} \tau_0^2}{1 + [0.5510 - 0.01998/(\kappa_0 H/2)] \tau_0}. \end{aligned} \quad (2.28)$$

However, the formula of  $\tau_i$  is only for the cube cage with a side length  $l_{\text{cube}}$ , and the added mass effects are considered due to the acceleration of the net.

As the linear model is relatively simple to derive an analytical solution, it has been adopted in studies on the interaction between waves and flexible net cages by Su et al. (2015), Mandal and Sahoo (2016) and Selvan et al. (2021). Nevertheless, Darcy's law might be not applicable to problems where the openings are large and sharp enough to separate the flow, and the frictional force is negligible compared with the pressure difference force (Molin, 2011).

**ii. Quadratic porous flow model** Another theory considers the pressure drop acting on the perforated structure to have a quadratic relationship with the normal velocity of the penetration flow:

$$\Delta p = \frac{1}{2} K \rho |\mathbf{u}_n| \mathbf{u}_n |_{S(r,\theta)=0}. \quad (2.29)$$

Molin (2011) believed that the quadratic model should satisfy the following assumptions:

- i) The structural thickness can be negligible;
- ii) Flow separation occurs through the openings, resulting in a quadratic discharge;
- iii) The openings are infinitely small and numerous.

The discharge coefficient  $K$  can be calibrated using the screen-type method. Gjøsund and Enerhaug (2010) presented the following empirical formula of  $K$  for the net panel in a steady flow with an attack angle  $\alpha$ :

$$K(\alpha) = \left[ \frac{7.0}{R_e} + \frac{0.9}{\log(R_e + 1.25)} + 0.005 \log(R_e) \right] \frac{1 - \beta^2}{\beta^2} \sin 2\alpha. \quad (2.30)$$

The formulas based on the experiments in steady flow conditions may be applicable to the scenario in an unsteady flow as well when the  $K_C$  number is large enough, because  $C_D/C_D^{\text{steady}} \approx 1$  at this time (Hamelin et al., 2013).

By substituting Eq. (2.24) into Eq. (2.29), one obtains the following:

$$\Phi^- - \Phi^+ = \frac{1}{2} K \rho |\nabla \Phi^- \cdot \mathbf{n}| (\nabla \Phi^- \cdot \mathbf{n}) |_{S(r,\theta=0)}. \quad (2.31)$$

The nonlinear term in Eq. (2.31) can be solved through iterations. Molin (2011) suggested introducing a relaxation to accelerate the convergence:

$$\Phi^{-(j)} - \Phi^{+(j)} = \frac{1}{2} K \rho |\nabla \Phi^{-(j-3/2)} \cdot \mathbf{n}| (\nabla \Phi^{-(j)} \cdot \mathbf{n}) |_{S(r,\theta=0)}, \quad (2.32)$$

where  $(j - 3/2)$  means the averaged value between the previous two iterations  $(j - 1)$  and  $(j - 2)$ .

The quadratic model may be more realistic than the linear model because it accounts for the flow separation due to large openings. However, according to the experimental investigation from Ito et al. (2014), the linear model can still predict the flow through the net reasonably in specific circumstances. Furthermore, in practical situations, the viscous forces should be considered due to the increased porosity, roughness and thickness of the net due to bio-retention.



## 2.2 Hydrodynamic actions and analysis in marine aquaculture

---

In Eqs. (2.26) and (2.31), the unit normal vector  $\mathbf{n}$  of the curve equation  $S(r, \theta) = 0$  for the structural cross-section is required, which was given by Zheng et al. (2019) in a cylindrical coordinate system as follows:

$$\mathbf{n} = \frac{1}{\sqrt{1 + \left(\frac{1}{r} \frac{\partial S}{\partial \theta}\right)^2}} \left(1, \frac{1}{R} \frac{\partial S}{\partial \theta}, 0\right). \quad (2.33)$$

### III. Methods of solutions

Once the governing equation and boundary conditions of the research problem have been determined, the corresponding particular solution can be obtained using analytical or numerical methods. Analytical solutions usually have a higher precision and are not limited by the scale of the studied domain; however, numerical solutions may offer better generality, especially for cases with relatively complex geometries.

**i. Eigenfunction expansion methods** The Laplace equation is a homogeneous linear partial differential equation; thus, it is easy to obtain its general solution form. Herein, we mainly talk about the solving method in the cylindrical coordinate system  $(r, \theta, z)$  (most fish cages are usually designed with a circular cross-section) and only consider the first-order wave theory.

Assuming that the oscillation system has reached a harmonic state, the velocity potential can be expressed by separating the variables:

$$\Phi(r, \theta, z, t) = \text{Re} \left[ \varphi(r, \theta, z) e^{-i\omega t} \right] = \text{Re} \left[ R(r) g(\theta) f(z) e^{-i\omega t} \right]. \quad (2.34)$$

By substituting Eq. (2.34) into Eq. (2.15), the complex amplitude  $\varphi(r, \theta, z)$  is also governed by the Laplace equation, and the form in the cylindrical coordinate system is as follows:

$$\nabla^2 \varphi = \frac{\partial^2 \varphi}{\partial r^2} + \frac{1}{r} \frac{\partial \varphi}{\partial r} + \frac{1}{r^2} \frac{\partial^2 \varphi}{\partial \theta^2} + \frac{\partial^2 \varphi}{\partial z^2} = 0. \quad (2.35)$$

By substituting Eq. (2.34) into Eq. (2.35), an ordinary differential equation system is obtained:

$$\begin{cases} r \frac{d}{dr} \left( r \frac{dR}{dr} \right) + (\kappa_n^2 r^2 - m^2) R = 0 \\ \frac{1}{g} \frac{d^2 g}{d\theta^2} = -m^2 \\ \frac{1}{f} \frac{d^2 f}{dz^2} = \kappa_n^2 \end{cases}. \quad (2.36)$$

When  $\kappa_n$  is a real number, the first equation in Eq. (2.36) is the Bessel equation, whose linearly independent solutions have the first kind of Bessel function  $J_m(\kappa_n r)$ , the second kind of Bessel function  $Y_m(\kappa_n r)$ , the first kind of Hankel function  $H_m^{(1)}(\kappa_n r)$  and the second kind of Hankel function  $H_m^{(2)}(\kappa_n r)$ . If  $\kappa_n$  is an imaginary number, the linearly independent solutions are the first kind of modified Bessel function  $I_m(\kappa_n r)$  and the second kind of modified Bessel function  $K_m(\kappa_n r)$ . In addition, only  $H_m^{(1)}(\kappa_n r)$  and  $K_m(\kappa_n r)$  satisfy the radiational condition in Eq. (2.22), and only the values of  $J_m(\kappa_n r)$  and  $I_m(\kappa_n r)$  are not infinite when  $r = 0$ . The solution to the second equation is  $g(\theta) = e^{im\theta}$ , and the third equation also has two linearly independent solutions  $e^{\kappa_n z}$  and  $e^{-\kappa_n z}$  in Eq. (2.36).

The unknown constants  $\kappa_n$  and  $m$  are called eigenfunction values, which are determined by the boundary conditions. According to the linear superposition principle, the general form of  $\varphi(r, \theta, z)$  is

$$\varphi(r, \theta, z) = \sum_m \sum_n R_{mn}(\kappa_n r) f_n(z) e^{im\theta}, \quad (2.37)$$

where  $R_{mn}(\kappa_n r)$  and  $f_n(z)$  are linear combinations of the aforementioned fundamental solutions. Since  $\varphi$  is a periodic function of  $\theta$  with a period of  $2\pi$ , Eq. (2.37) is also the Fourier expansion of  $\varphi$  in the complex domain. As Eq. (2.37) is an infinite series, it is necessary to analyse the convergence of the solution.

**ii. Boundary element method** The BEM is often used in the hydrodynamic simulation of marine structures. Because only the boundary of the studied domain is required to be discretised, it has higher computational efficiency than the numerical methods based on volume discretisation.

According to Green's second identity, the boundary integral equation on the boundary of the fluid domain  $S$  is as follows:

$$\iint_S \left( \varphi_0 \frac{\partial \varphi}{\partial n} - \varphi \frac{\partial \varphi_0}{\partial n} \right) dS = 0, \quad (2.38)$$

where  $\varphi_0$  is the source function.

The difficulty of the BEM lies in constructing the source function. As presented by Sheng et al. (2022), in a finite water depth,  $\varphi_0$  is

$$\varphi_0 = \frac{1}{r} + \frac{1}{\hat{r}} + 2 \int_0^{+\infty} \frac{(\sigma + K) \cosh[\sigma(z+h)] \cosh[\sigma(z_0+h)]}{\sigma \sinh(\sigma h) - K \cosh(\sigma h)} e^{-\sigma H} J_0(\sigma R) d\sigma, \quad (2.39)$$

in which

$$\begin{aligned}
 r &= \sqrt{(x-x_0)^2 + (y-y_0)^2 + (z-z_0)^2}, \\
 \hat{r} &= \sqrt{(x-x_0)^2 + (y-y_0)^2 + (z+z_0+2h)^2}, \\
 R &= \sqrt{(x-x_0)^2 + (y-y_0)^2}, \\
 K &= \omega^2/g.
 \end{aligned} \tag{2.40}$$

Eq. (2.39) satisfies the boundary condition at the free water surface, seabed and infinity, on which the integral in Eq. (2.38) is zero. Therefore, it only needs to discretise the boundary of the body surface.

Ito et al. (2014) used a hybrid method to analyse the cube net cage under waves. The far-field wave is expressed in the eigenfunction method, and the domain near and inside the cage is solved using the BEM. Therefore, the source function  $\varphi_0$  does not need to satisfy the radiational condition at infinity; that is:

$$\varphi_0 = \frac{1}{r} + \frac{1}{\hat{r}}. \tag{2.41}$$

Nevertheless, discretisation is required at the free water surface and the boundary between the far-field and ambient waves, as the source function cannot satisfy those boundary conditions.

Gharechae and Ketabdari (2022) developed an analytical solution based on the BEM for an array of aquaculture cages. If the wave amplitude and steepness are small, the source function  $\varphi_0$  is as follows:

$$\varphi_0 = i/4H_0(k_0r). \tag{2.42}$$

Eq. (2.42) also satisfies the boundary conditions at the free wave surface, seabed and infinity; therefore, Eq. (2.38) is only limited to the body surface. By expanding the velocity potential as an eigenfunction series and substituting it into the boundary integral equation on the cage interface, the particular solution can be obtained.

Some scholars have also adopted a hybrid numerical model to determine the hydrodynamic loads on large rigid fish cages. Liu et al. (2020) analysed wave scattering due to the floating steel frame and pontoon using the BEM, while they modelled the net using the Morison element.

**iii. Finite element method** The FEM is a volume-discretised method for the whole fluid domain, which is enclosed by the free water surface, seabed, structural wet surface and

outer boundary. Different from the abovementioned method of solutions, which can handle the radiation boundary condition Eq. (2.22) at infinity, the FEM requires the construction of a damping region to absorb the wave. Here, a damping term is added to the kinematic free surface boundary condition.

Its principle is to express the velocity potential in each element as the superposition of the product of the corresponding nodal velocity potential and shape function. By applying the Galerkin method and the corresponding boundary conditions, a linear equation system is finally obtained. In addition, discretised schemes for the time steps are required, including multiple-step and single-step methods. Compared with multiple-step methods, such as the Adams-Bashforth scheme, single-step methods such as the Runge-Kutta scheme require a smaller time interval, but they can be applied to dynamic grids because only the values from the last time step are required (Wang and Wu, 2007).

A detailed description of FEM-based analysis for second-order wave diffraction around an array of vertical cylinders can be found in Wang and Wu (2007). Yang and Wang (2020) extended the work into a case with wave–current interaction. However, there is currently no application of the FEM in wave–porous structure interactions, including fish cages.

The advantage of the FEM is that it can handle complex unstructured grids and achieve high numerical accuracy. However, compared with the BEM and the SBFEM, the FEM requires higher computational power due to the discretisation of the whole volume space. Nevertheless, with the development of computer technology, optimisation of algorithms, and improvement of computing power in the future, this method still has the potential to be employed.

**iv. Scaled finite element method** The SBFEM has also recently been used for the wavefield solution. Its technical principle is similar to that of the FEM, but the discretisation is only processed on the domain boundary, which significantly reduces the required computation. According to Li et al. (2013b), The modelling concepts mainly include the following:

- i) Separating the variables for the velocity potential and writing the vertical component as an eigenfunction, such that the three-dimensional Laplace equation is converted into a two-dimensional Helmholtz equation;
- ii) Establishing a local scaled boundary coordinate system at the domain or subdomain and scaling the studied boundary;
- iii) Reformulating the gradient operator with the geometric mapping and expressing the velocity potential using the shape function and the nodal velocity potential;

- iv) Applying the weighted residual technique with a weighting function and Green's theorem to obtain a linear equation system.

Li et al. (2013b) applied the SBFEM to express the wave run-up around multiple cylinders, and the structural response could also be solved using the SBFEM. Meng and Zou (2012) developed an SBFEM model for the interaction between waves and a porous cylinder with arbitrary cross-sections, where a virtual porous cylinder was established to envelop the studied object. In addition, Liu and Lin (2013) analysed the wave response of arcuate or circular porous structures based on the SBFEM.

### 2.2.4 Computational fluid dynamic models

CFD is an interdisciplinary technique that combines fluid mechanics, numerical analysis, and computer science. It uses discretised mathematical theories to conduct numerical simulations on various problems of fluid mechanics. Due to the development of computing science, CFD has been widely applied in the fields of aerospace, automotive, petrochemical, biomedical, semiconductor design and marine and ocean engineering, among others, and it compensates for the shortcomings of analytical methods and physical experiments. This section discusses the basic control equations, discretisation methods, FSI and related applications in the hydrodynamic simulation of fish cages for CFD models in detail.

#### I. Governing equations

CFD models are usually based on the Navier-Stokes (N-S) equations to solve the flow field. The governing equation can also be modified to meet engineering requirements. The action of the net to the flow field is usually equivalent to a source term added to the governing equation, including the Reynolds-averaged N-S (RANS) equation and the volume-averaged RANS (VARANS) equation.

**i. RANS equation** Under flow conditions with high Reynolds numbers, turbulence occurs in the wake due to the net, as Bouhoubeiny et al. (2011), Pichot et al. (2009) and Kim (2012) have proven. When using the laminar flow model, the transition between the wake and the outer area behind the net is very sharp, which is unreasonable (Chen, 2016). Therefore, it is essential to introduce a turbulence model. The main turbulence models include the RANS equation simulation, large eddy simulation (LES) and direct numerical simulation (DNS). First, the principle of the RANS model is to time-average the fluctuations caused by turbulence, and an eddy-viscosity model was proposed by

## Literature Review

---

Boussinesq (1903) to simplify the Reynolds stress term. Second, LES directly simulates large-scale vortices, while small-scale vortices are calculated using the RANS through filtering. Third, the DNS method directly solves the N-S equation, but only with extremely small spatial grid lengths and time steps can the detailed turbulence characteristics be observed and distinguished. Therefore, this method requires extremely high computational power. Compared with LES and DNS, the RANS method requires less computational power; therefore, it is the most widely practised in engineering.

The governing equations of RANS for a two-phase incompressible flow, adopting the volume of fluid (VOF) method, are as follows:

$$\begin{cases} \frac{\partial \gamma}{\partial t} + \frac{\partial}{\partial x_i} (u_i \gamma) = 0 \\ \frac{\partial u_i}{\partial x_j} = 0 \\ \frac{\partial \rho u_i}{\partial t} + \frac{\partial \rho u_i u_j}{\partial x_j} = -\frac{\partial p}{\partial x_j} + (\mu + \mu_t) \frac{\partial}{\partial x_j} \left( \frac{\partial u_i}{\partial x_j} + \frac{\partial u_j}{\partial x_i} \right) + \rho g_i + S_i \end{cases}, \quad (2.43)$$

where the phase index  $\gamma$  indicates

$$\begin{aligned} 1, & \quad \text{control volume is filled only with liquid phase,} \\ 0, & \quad \text{control volume is filled only with gas phase,} \\ 0 < \gamma < 1, & \quad \text{interface present,} \end{aligned} \quad (2.44)$$

and  $S_i$  is the source term due to the effect of the fish cage net.

The turbulence viscosity  $\mu_t$  is related to the corresponding turbulence model. At present, the models commonly applied in engineering are two-equation models. These include the standard  $k - \varepsilon$  model and its improved versions, such as the RNG  $k - \varepsilon$  model and realisable  $k - \varepsilon$  model, and the  $k - \omega$  model and its improved versions, such as the  $k - \omega$  SST model. Based on the RANS equation, Chen (2016) compared the differences between the abovementioned turbulence models and found them not to be apparent. However, Zhao et al. (2013) believed that the realisable  $k - \varepsilon$  model is more suitable. Because of the blocking effect, a strong pressure gradient exists near the fish net.

**ii. VARANS equation** A fish cage net can also be modelled as a porous medium in CFD simulation. Nevertheless, Higuera (2015) indicated that the resistance source term  $S_i$  cannot fully represent the flows through regular porous materials, since the fluid is a constraint and able to pass only through the voids left by the solid matrix of the material. Therefore, the N-S equations require some modifications (averaging process) to account

## 2.2 Hydrodynamic actions and analysis in marine aquaculture

for low-porosity materials (0.35 - 0.65). The VARANS equation is described as follows:

$$\begin{cases} \frac{\partial \gamma}{\partial t} + \frac{1}{\tau_j} \frac{\partial \gamma \langle u_i \rangle}{\partial x_i} + \frac{1}{\tau_0} \frac{\partial \gamma (1-\gamma) \langle u_i \rangle}{\partial x_i} = 0 \\ \frac{\partial \langle u_i \rangle}{\partial x_j} = 0 \\ (1 + c_m) \frac{\partial}{\partial t} \frac{\rho \langle u_i \rangle}{\tau_0} + \frac{1}{\tau_0} \frac{\partial}{\partial x_j} \frac{\rho \langle u_i \rangle \langle u_j \rangle}{\tau_0} = - \frac{\partial \langle p \rangle^f}{\partial x_j} - g_j x_j \frac{\partial \rho}{\partial x_j} \\ + \frac{1}{\tau_0} \frac{\partial}{\partial x_j} \mu \left( \frac{\partial \langle u_i \rangle}{\partial x_j} + \frac{\partial \langle u_j \rangle}{\partial x_i} \right) - \frac{1}{\tau_0} \frac{\partial}{\partial x_j} \rho \langle \overline{u_i' u_j'} \rangle + S_i \end{cases} \quad (2.45)$$

Nakayama and Kuwahara (1999) also introduced the volume averaging operation of the  $k - \varepsilon$  and  $k - \omega$  SST models, but the extra terms generated through volume averaging need to be calibrated through experimental data to close the system.

The VARANS equation additionally introduces an added mass coefficient  $c_m$  to involve the fluid inertial effect for an unsteady flow. Chen (2016) applied the VARANS equation to simulate the waves and currents passing through a fish net cage, obtaining results that are similar to experimental data.

## II. Discretisation methods

Traditionally employed discretisation methods in CFD mainly include the finite difference method (FDM), FEM and finite volume method (FVM). In addition, there are some grid-free-based methods, including the Lattice-Boltzmann method (LBM) and the smooth particle hydrodynamic (SPH) method.

The FDM approximates the derivatives in differential equations by finite differences to obtain numerical solutions. Constructing higher-order-difference schemes is relatively easy, but handling complex unstructured grids is difficult. However, the effect of the fish cage can be equivalent to the source term added in the governing equations; thus, only simple rectilinear grids are feasible, as presented by Martin et al. (2021).

The principle of the FVM is to discretise the space into finite cells, convert the volume integral of the differential equations to the surface integral using Gauss's divergence theorem for each control volume (cell) and derive a set of discrete equations through the discrete scheme. The advantage of the FVM is that it can handle complex unstructured grids, and the conservation is better because of the integral processing of the governing equations; however, the higher-order difference schemes are difficult to construct. Some scholars have used the FVM to simulate the flow field distribution around the fish cage through the commercial software Fluent (Bi et al., 2014; Patursson et al., 2010; Zhao et al., 2013) or the open-source code OpenFOAM (Chen, 2016; Cheng et al., 2022).

Moreover, Tu et al. (2020) adopted the LBM to simulate the flow through the net panel, in which the net structure is directly modelled as a series of slender cylinders from the mesoscopic view, and simulated turbulence using LES.

### III. Fluid-structure interaction

It is essential to couple the hydrodynamic and structural solvers together, which is usually a two-way coupling; therefore, FSI algorithms are required.

One of the methods involves equivalating the effect of the net to a porous resistance source term governed by the quadratic porous flow model in the CFD solver (Bi et al., 2014; Chen, 2016; Patursson et al., 2010). The coefficients in said model are calibrated using the Morison equation (Bi et al., 2014; Chen, 2016) or the screen-type method (Patursson et al., 2010). The porous medium zone representing the net interface is generally divided into some planar elements on which different flow velocities are distributed. In the algorithm of Chen (2016), the position of the source term is updated in a static grid instead of a dynamic grid to represent the movement of the porous zone. Nonetheless, during the deformation of the net, the cells in adjacent porous zones overlap. To avoid this issue, Cheng et al. (2022) introduced an improved topological method.

Several other FSI algorithms have also been developed. Yao et al. (2016) proposed a hybrid-volume method. The source term or reaction force due to a net is equal to the sum of the products of the weight coefficients and the equivalent hydrodynamic force vectors of the net mesh bars, in which the weight coefficient of each mesh bar can be determined by its spatial location. Martin et al. (2021) adopted a Lagrangian–Eulerian coupling algorithm to directly introduce the structural response into the fluid solver. A series of Lagrangian points are distributed in the centres of some triangular elements, which is achieved by splitting the net structure’s macro elements. Then, the external forces acting on the triangular areas are directly integrated and the momentum loss at each fluid point is calculated (Eulerian grid).

Furthermore, Devilliers et al. (2016) proposed an algorithm for adaptive grid refinement near the net interface when interacting with the flow, which efficiently optimises the computational costs of the CPU and memory.



## 2.3 Structural reliability and modelling of a fish cage system

### 2.3.1 Structural reliability

In the design of a fish cage, the most critical procedure is structural reliability to guarantee the safety of life and property. Under the hydrodynamic action, excessive deformation or fatigue caused by long-term vibrations will lead to the failure of structural strength. A reliable quality of materials and facilities can avoid potential safety hazards to the aquaculture system. Moreover, a key part of sustainable development involves balancing safety and engineering costs.

#### I. Floating collar

The floating collar or frame has the function of supporting the cage and generating buoyancy. It is usually made of high-density polyethylene, steel or light concrete according to different applications, such as flexible floating circular rings, hull shape rigid floaters, and polygon rigid frames. Regarding the floating collar made of elastic high-density polyethylene (HDPE), its motion can be divided into rigid body motion with six degrees of freedom and elastic deformation. The rigid body motion of a floating structure includes three translational motions, namely surge, sway and heave, and three rotational motions, namely roll, pitch and yaw.

Besides the rigid body motion of floating collars in waves, their elastic deformation cannot be ignored. Through Euler's law of motion and elastic beam theory, Dong et al. (2010) found that a small elastic deformation occurs when the mooring cable is assembled symmetrically along the incident wave direction. They suggested that the out-of-plane stiffness should be enhanced to diminish the deformation. Using the lumped mass method, Huang et al. (2016) also demonstrated that the maximum deformation of the collar occurred when the wave propagated in the direction of the mooring line; furthermore, increasing the cross-section of the collar suppressed the maximum strain, but the effect of its circumference was relatively small. Based on a FEM analysis in the frequency domain, the results suggested that the rigid motion mode would dominate the dynamic response of floating in head seas, but that the flexibility of the collar would contribute more to the structural response in oblique seas (Fu and Moan, 2012).

By contrast, the experimental and analytical investigation of Gharechae et al. (2020) indicated that the upstream floaters in an array had more significant responses than a single

floater in head sea waves. The shape of the floating ring may affect the wave excitation, but the added mass, damping and response amplitude operator are not significantly different according to the analytical solution of Park and Wang (2022). If the cage is under the action of irregular waves, the motion of the floating collar satisfies the Gaussian distribution through time-frequency transformation (Qin et al., 2020). Moreover, a comparison between the experimental and numerical results indicated that the high-order wave effect cannot be ignored for the motion of the floating ring, especially for phenomena above the third-order that cannot be explained by the perturbation theory; thus, the N-S equation might be required (Li et al., 2016).

Bai et al. (2018) studied the fatigue life of the floating collar using FEM models and probabilistic analysis methods under irregular wave actions. Their results indicated that the fatigue estimations based on the short-term stress generalized extreme value distribution and gamma distributions were more accurate than the Rayleigh and Weibull distributions. Furthermore, long-term distributions are more conservative in estimating the fatigue life of floater systems.

## II. Net chamber

The net structure can be made of nylon wires with or without nodes and steel wires without nodes. The bending stiffness is usually considered negligible when deformed.

Through the experimental investigation of the geometry of fish pen cages in a uniform flow by Lader and Enerhaug (2005), a deformed net chamber with increased current velocities can be distinctly observed in Fig. 2.5. The maximum transverse displacement of the chamber occurs at the bottom. Adding a bottom sinker weight can suppress the deformation but will increase the net tension and fluid drag. Furthermore, in an FEM analysis, Moe et al. (2010) identified the net seam at the bottom of the cage as a potential hazard area because the internal forces could reach the design capacity.

Different from the quasistatic deformation under a constant flow, the net will generate a frequency-dependent dynamic response under wave actions. The transverse motion of the net is much smaller than its inline motion towards wave propagation (Zhao et al., 2008). In the analytical solution of Su et al. (2015) and Mandal and Sahoo (2016), the maximum deflection amplitude of the net cylinder occurs near the top restraint. Nevertheless, limited research exists on how to determine the resonance frequency for the net chamber. It is also essential to consider the fatigue failure of the net structure when exposed to long-term wave excitation. The Rayleigh distribution and the two-parameter Weibull distribution can achieve a reasonable fit for the stress range (Thomassen and Leira, 2012).

Image Removed

**Fig. 2.5** Deformed net chambers with different current velocities and sinker weights (Lader and Enerhaug, 2005).

According to the aforementioned literature review, a crucial design indicator is to avoid the excessive volume reduction of the net chamber caused by deformation. Chen et al. (2021) suggested that increasing the stiffness of the net twine rather than the diameter and adopting an elliptical cross-section cage and a uniform sinker weight distribution are both beneficial for suppressing the volume reduction of the cage. Regular cleaning of biofouling on the net is also necessary. Lader et al. (2008) considered it essential to develop an “early warning” system for detecting any significant deformation of fish cage nets.

### III. Mooring system

The function of a mooring system is to restrict the movement of the cage. Davidson and Ringwood (2017) presented categories of some commonly employed mooring systems, which are described as follows and depicted in Fig. 2.6:

- i) Spread moorings: catenary mooring, multi-catenary mooring and taut spread mooring;
- ii) Single point moorings: catenary anchor leg mooring (CALM) and single anchor leg mooring (SALM).

The strength of the mooring cable must be guaranteed to avoid cable breakage; therefore, it is critical to perform a reliability analysis of the uncertainty quantification system for the allowable strength (Hou et al., 2019). The numerical case studies of Hou et al.

Image Removed

**Fig. 2.6** Mooring system types: spread moorings: (a) Taut; (b) Taut spread; (c) Catenary; (d) Multi-catenary; and single point moorings: (e) SALM; (f) CALM; (g) Lazy-S (Davidson and Ringwood, 2017).

(2018b) indicated that zero initial preload (the mooring cable is in a relaxed state initially) can effectively improve the fatigue reliability of the mooring cables.

In addition to the excitation caused by the drag and inertial effect of the flow, the mooring cables can also generate vortex-induced responses. When the vortex release frequency is close to the natural frequency of the structure, the lock-in phenomenon will occur, where the structure responds violently. The condition for vortex-included resonance to occur is usually when the Strouhal number (the reciprocal form of the  $K_C$  number) is approximately 0.16 (Chaplin et al., 2005). Moreover, the negligence of the effect of embedded chains in the seabed may also lead to unreasonable predictions of the static and dynamic response of the mooring system (Hou et al., 2018a).

#### IV. Coupling of structural components

The abovementioned review only focused on studies of single structural components in aquaculture systems. However, the fish cage system is a comprehensive system that combines the floating collar, net chamber and mooring system, and it is usually designed as a multi-cage system. The interaction among the structural components is a noteworthy issue.

The numerical simulations of Li et al. (2013a) indicated that displacements of the floating collar coupled with a net chamber are obviously different from the results obtained with only the floater. In particular, the interaction between the floating collar and the

## 2.3 Structural reliability and modelling of a fish cage system

---

net has a large impact on the horizontal motions of the system. For frame-type fish net cages, the existence of frame cylinders leads to a 9.2% increase in the fluid drag coefficient when the solidity ratio  $S_n > 0.347$  (Wang et al., 2023). The maximum local stress occurs where the net connects to the floater; thus, this is a critical element of the structural design of fish cages (Lader et al., 2008). The gravity cage system exhibits small responses to high frequencies, which is characteristic of highly damped systems (Xu et al., 2011). Furthermore, the stiffness of the heave, roll and pitch provided by the mooring system is small compared with the hydrostatic stiffness, but the coupling stiffness of surge–pitch or sway–roll is considerable when the weight of the mooring cable or the wave drift force is not negligible (Kim et al., 2013).

In multi-cage systems, each cage is not in an isolated state but rather has a mutual interaction. For an array of net cages under wave actions, the maximum response does not necessarily occur in the upstream direction, and their frequent rolling and swaying will cause the mooring tension to be redistributed (Zhang et al., 2021). The numerical simulations of Xu et al. (2013a,b) have revealed that the dynamic response of each cage has a significant phase difference, and that the mooring tension and cage volume reduction of multiple cage systems is much greater than those in single cage systems and is related to the number of cages. In most cases, two adjacent ropes do not pull the cage together because the mooring force in one is usually much greater than that in the other; thus, two adjacent ropes are not always effective at reducing stress concentrations (Liu et al., 2022).

### 2.3.2 Modelling of fish cages

#### I. Floating collar

Dong et al. (2010) regarded the circular floating collar as a slender curved beam and used Euler's law of motion and elastic beam theory to solve its rigid displacement and elastic deformation, respectively. The elastic deformation solutions could be expanded in a series of eigenmodes. For such initial value problems, the Runge–Kutta method is a popular time-discretised method. However, the mechanism of damping is not negligible for the initial vibration state of structures. Zhao et al. (2015) introduced a viscous damping model assuming the structure to have a low velocity. They found that the undamped case was not consistent with the realistic system, and that the structural deformation tended to be the same for arbitrarily different damping rates when the time was sufficiently long. Huang et al. (2016) established a discretised lumped mass model to obtain the dynamic response of the floating collar. A four-node shell element was used to model the floating collar to

## Literature Review

---

simulate a more realistic stress distribution in the FEM model of Zhao et al. (2019a). The Morison equation has been applied for the hydrodynamic load evaluation in these studies.

Notably, the wave scattering effect due to the structure is neglected. Fu and Moan (2012) established a coupled model connecting the FEM model of the cage collar and the BEM model of the wave based on potential flow theory. Li et al. (2016) and Gharechae et al. (2020) have coupled the Euler–Bernoulli curved beam theory with the wave field solutions in the BEM, only considering the vertical motion of the collar, but the latter directly provided the analytical solutions. Additionally, Park and Wang (2022) derived the analytical solution of rigid body motions for a floating ring with arbitrary shapes in waves.

## II. Net chamber

The discretised models of fish cage nets mainly include the lumped mass model (Bi et al., 2014; Chen et al., 2021; Li et al., 2006; Martin et al., 2021; Yao et al., 2016; Zhao et al., 2008) and the truss element model (Kristiansen and Faltinsen, 2015; Moe et al., 2010; Tsukrov et al., 2003). The former equates the knots and twines of the net as several massed nodes connected by massless springs. The latter are directly analysed through the FEM. In the commercial software AquaSim, a four-node membrane element is adopted to model the net (Aquastructures, 2022). These discretised models are usually based on time domain analysis. Nevertheless, for these discretised approaches, a simplification of the calculation model relative to the original net pattern is usually necessary to avoid excessive computations. In addition, this type of structural modelling is often coupled with CFD models to achieve FSI; thus, the amount of computation will also increase.

Some researchers (Mandal and Sahoo, 2016; Selvan et al., 2021; Su et al., 2015) have also adopted continuum vibration equations to describe the net motion in analytical solutions, such as the lateral deflection equations of strings or elastic beams or the membrane vibration equation. By analysing the motion and elastic constitutive relationship of the micro-element segment, the governing equations of the structural displacement can be derived. This structural modelling is commonly coupled with potential flow models based on eigenfunction expansion methods to achieve FSI. Because of the application of frequency domain analysis, the response of the system can be predicted simply and quickly. However, this approach is based on some unreasonable assumptions: First, the cross-section of the cage retains a constant circular shape, and second, the stress variation due to structural deformation is assumed to be ignored. Therefore, modelling fish cage nets with the continuum model still requires a much additional theoretical research.

In addition to the numerical model, machine learning is also an effective and accurate approach for predicting the dynamic behaviour of aquaculture cage systems, such as the application of artificial neural networks by Zhao et al. (2019b).

### III. Mooring system

In most analyses of floating structures, the mooring system is equivalent to linear springs, which are simple to be included in the rigid body motion equation of the floating structure as constant stiffnesses. Liu et al. (2021) and Selvan et al. (2021) tried to calculate the mooring restoring forces on fish cages as provided by springs of constant stiffness along the transverse direction in their analytical solutions as well.

Another method is to directly model the mooring cables in the FEM, where the drag forces induced by waves and currents and the motions of the mooring lines are considered, and the tension information of the mooring line is directly given (Kim et al., 2013). By comparing the two methods, Kim et al. (2013) demonstrated that the FEM is more realistic because the complex nonlinear behaviour can be solved, but this is time-consuming.

## 2.4 Summary and research gaps

### 2.4.1 Summary of the literature review

The findings of the literature review presented in this chapter can be summarised as follows:

- The actions of currents and waves are crucial parameters in the design of a fish cage system and can cause complex hydrodynamic phenomena;
- In hydroelastic analysis, the perturbation effect on the flow field due to the presence of the fish cage and its motion is significant;
- Approaches to hydrodynamic analysis for fish cages mainly include empirical methods (the Morison equation and screen-type method), potential flow models and CFD models; the net structure is usually equivalent to a porous medium in the last two models;
- Lumped mass models, FEM models and continuum vibration equations are commonly used for the structural modelling of fish cage systems.

### 2.4.2 Existing research gaps

The literature review has revealed that research on offshore fish cages is still in its infancy. Flexible HDPE fish cages exposed to high-energy environments might not provide sufficient strength to resist environmental loads. High-strength rigid cages are considered to have excellent development potential and can achieve higher incoming value due to the tremendous breeding capacity that they provided; however, the expensive manufacturing costs may prevent some companies from choosing them as the optimal solutions. Therefore, the conceptual design of an affordable fish cage is an critical part of feasibility studies of offshore fish farming. On the other hand, although the developed hydroelastic analysis method based on traditional numerical techniques can achieve excellent approximation, the computational costs are still considerable, which makes it impractical to employ for a full-scale fish cage. Advanced calculation models are one of the research priorities for simulating the hydroelastic behaviours of fish cages. From the perspective of the long-term development of novel offshore fish cages, the conceptual design and relevant studies on theories, calculation models and experiments related to hydroelastic performance are required. Doing so will provide a wealth of technical reserves for the further engineering design, product construction and practical application of the new marine aquaculture platforms of the future.

From the aforementioned two points of view, the following research gaps and questions can be summarised:

- Which types of aquacultural systems are suitable for offshore fish farming?
- Which techniques can be improved to more efficiently predict the hydroelastic behaviours of net cages?
- In terms of the simulations of net cages in waves, the two-way coupling of fluids and structures is less well understood and difficult to be incorporated into the models.
- What are the characteristics of the wave field distribution in presence of a fish farm?
- What is the influence of hydrodynamic and structural conditions on the wave responses of net cages?

The aforementioned research gaps and questions indicate that the theoretical mechanism of the hydroelastic interaction between waves and fish net cages still requires further work; furthermore, innovative analysis methods are necessary for the engineering practice of offshore fish farming. This will lead to subsequent Ph.D. research.



# Chapter 3

## Research Question and Methodologies

### 3.1 Research question

The research background and literature review emphasise the importance of developing the offshore fish cage system and the relevant studies and technologies to investigate the hydroelastic characteristics of such marine structures. The research scope of this thesis focuses on the hydroelastic interaction between waves and flexible net chambers. For fish farms exposed to high-energy environments, waves are an important environmental load. Although fluids in the real ocean environment exhibit irregular oscillations, irregular waves can usually be decomposed into the superposition of infinite monochromatic waves. Also, diffracted and radiated waves caused by the cages can cause additional variations in the wavefield around the fish farm. The determination of the wave actions on structures can guarantee the robustness of offshore aquaculture systems and, ultimately, minimise engineering risks. Additionally, analysis of the distribution of wave amplitudes around the cages prevents fish damage caused by strong fluid oscillations and creates a favourable low-energy environment for fish survival. As a result, an understanding of this phenomenon is essential to both theoretical and engineering practice.

Therefore, this Ph.D. thesis proposes to answer the following question:  
“Under the incidence of an array of monochromatic waves in extreme conditions, what are the hydroelastic behaviours of the offshore open-net fish cage?”.

Based on this broad research question, several specific research questions are proposed:

- What are the characteristics of the wavefield distributions around a single fish cage or a fish cage array?

- What are the dominant factors that determine the wave response of net cages (such as hydrodynamic loads, structural motions, etc.), and what correlations may manifest between them?
- How do the elastic deformations of cages affect the hydrodynamic characteristics of waves?

## 3.2 Methodologies

The research methodologies involve analytical derivation and verification of coupled hydrodynamic and elasticity models, which are further combined with wave interference interaction theory. Compared to traditional numerical methods, analytical solutions limit intensive numerical computation by directly determining the smooth solution of the studied problem, but some complex nonlinear problems do not have a particular analytical form in real engineering problems. Therefore, some reasonable assumptions are essential. In the present study, the development of the theoretical models applies the assumptions of small-amplitude wave theory, Darcy's law and linear elasticity; these assumptions are achieved by neglecting the higher-order terms in the Taylor series of the relevant physical quantities.

The purpose of this model is to predict the wavefield distribution surrounding open-net fish cages and their corresponding dynamic behaviours. Specifically, the main activities conducted to answer the research question and achieve the research objectives are divided into three study elements, I, II and III, in the subsequent three chapters, respectively. A detailed methodological framework is included in Fig. 3.1. Furthermore, this chapter contains some important analytical techniques used for the mathematical modelling of each study element.

### 3.2.1 Study I: A theoretical framework for the hydroelastic interaction between waves and submersible flexible fish cages

The purpose of Study I is to establish a theoretical framework for the analytical solution to wave-cage interaction. Therefore, it is necessary to understand the mechanisms and governing equations in this physical problem and the corresponding approach to solutions. A schematic diagram of the preliminary theoretical framework is presented in Fig. 3.2. The following sections briefly describe the tasks required for this stage; a detailed discussion is presented in Chapter 4.

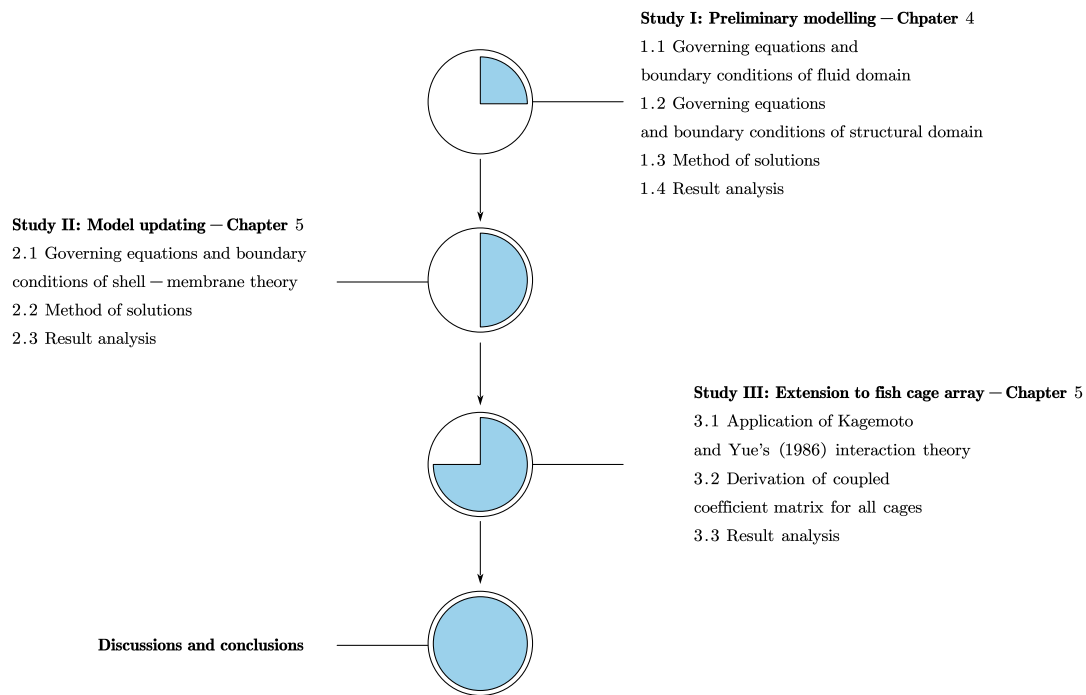


**Fig. 3.1** Methodological framework for the existing research.

### Stage 1.1: Governing equation and boundary condition of the fluid domain

Assuming that fluid is inviscid, irrotational and incompressible, the flow velocity can be expressed as a gradient of the velocity potential, which satisfies the Laplace equation. In small-amplitude wave theory, the free surface satisfies the linearised kinematic boundary conditions and dynamic conditions. Due to the assumption that the fluid is inviscid, slip-conditions are applied to the seabed. The first-order scattered wave potential satisfies the Sommerfeld (1949) radiation condition. At the interface of the cage, in addition to the continuity of flow velocity, the kinematic boundary conditions combined with the porous medium model must also be satisfied, for which the flow velocity is equal to the penetrated flow velocity plus the movement speed of the cage interface.

### Stage 1.2: Governing equation and boundary condition of the structural domain

From the analytical solutions developed by Su et al. (2015) and Mandal and Sahoo (2016), the transverse deflection of the net chamber can be approximately described by the vibration equation of a one-dimensional string. Next consider the constraint condition of the net chamber: its top end is tugged by the mooring load, wherein the mooring system is equivalent to a linear spring, and the lateral traction is free at the bottom end of the net chamber.

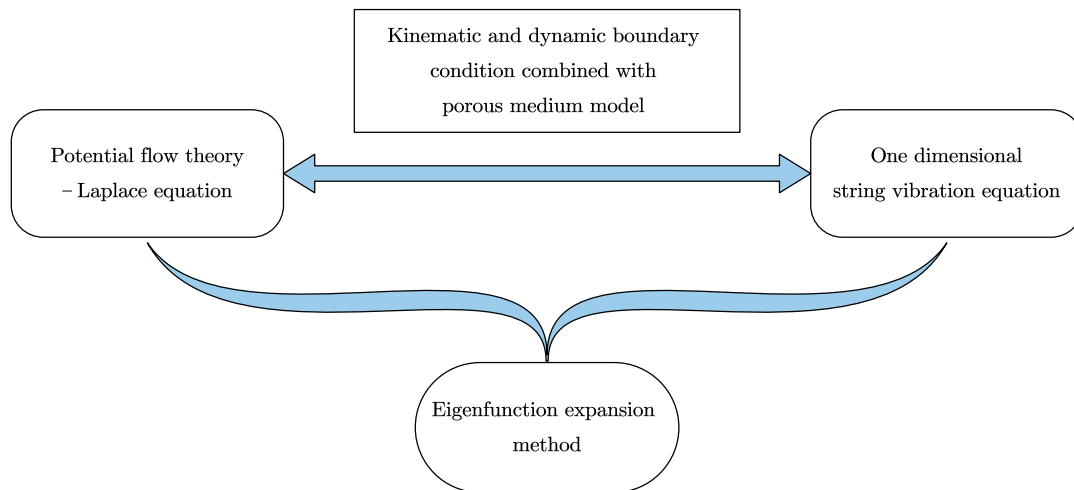


**Fig. 3.2** Theoretical framework of the simulation model in Study I.

### Stage 1.3: Method of solutions

Both the Laplace equation and the one-dimensional string vibration equation are linear differential equations. According to the superposition principle, its general solution can be expanded to a series of eigenfunctions in which the eigenvalues can be determined by the dispersion relation. To obtain the closed-form solution to this physical problem, a system of linear algebraic equations corresponding to the unknown constants in the general solution may be obtained by substituting the general solution into the boundary conditions and applying a least squared approximation. In the derivation, complex analysis is an effective tool to solve fluctuation problems.

### Stage 1.4: Analysis of results

The aforementioned governing equations can be solved to determine the velocity potential of the fluid domain and the transverse displacement of the fish cage. Convergence studies and model validation are completed to demonstrate the reasonableness of the solution. The free water surface elevation and dynamic pressure can be calculated according to the linearised Bernoulli equation, and the wave force and overturning moment acting on the cage are obtained by integrating the pressure drops on the cage interface. The characteristics of the parameters that significantly affect the wave forces and overturning moments acting on the cage are explained by parametric studies.

### 3.2.2 Study II: Innovative analytical schemes by practising the shell-membrane theory in modelling net chambers

In the first study phase, the net cage is over-simplified as a string, but it usually deforms differently in front and back. To overcome this issue, the purpose of Study II is to determine a more appropriate governing equation to describe the motions of the cage and provide more advanced solutions to the structural domain and the fluid-structure interaction. Chapter 5 presents a detailed discussion of these methods.

#### Stage 2.1: Governing equation and boundary condition for shell structures in the membrane theory

Fish cage nets are generally considered unable to provide bending resistance, so equations of their motion and constitutive relations can be approximately described by the membrane theory of thin shells proposed by Flügge (1973). The displacement of a cylindrical shell in the cylindrical coordinate system can be decomposed into the axial displacement, circumferential displacement and radial displacement, and the radial motion of the shell can be considered a forced vibration with the wave pressure acting as the excitation load. By substituting the constitutive relation into the motion equation, one obtains the governing equations for the displacements of the shell. The mathematical expression of the edge constraint conditions for cylindrical shells can be found in Belubekyan et al. (2017), including the traction-free condition, clamped condition, sliding contact constraint and Navier constraint. The traction-free condition and clamped condition are normally applicable to the restrained state at the edge of the net chamber.

#### Stage 2.2: Method of solutions to the structural domain and fluid-structure interaction

Under the excitation vibrations of waves, the governing equations of the shell displacements are a set of inhomogeneous linear partial differential equations (PDEs). If the variables are separated, these PDEs can be transformed into a system of ordinary differential equations (ODEs) with respect to the axial variables, and the corresponding general solution can be derived by determining the roots of the characteristic equation belonging to these ODEs.

The particular solution of these displacement components may be derived by introducing the boundary value conditions. For FSI, only the radial displacement of the shell affects the flow condition on the cage interface due to the assumption that the fluid is inviscid in the potential flow theory. Therefore, by repeating the technique used in Study I,

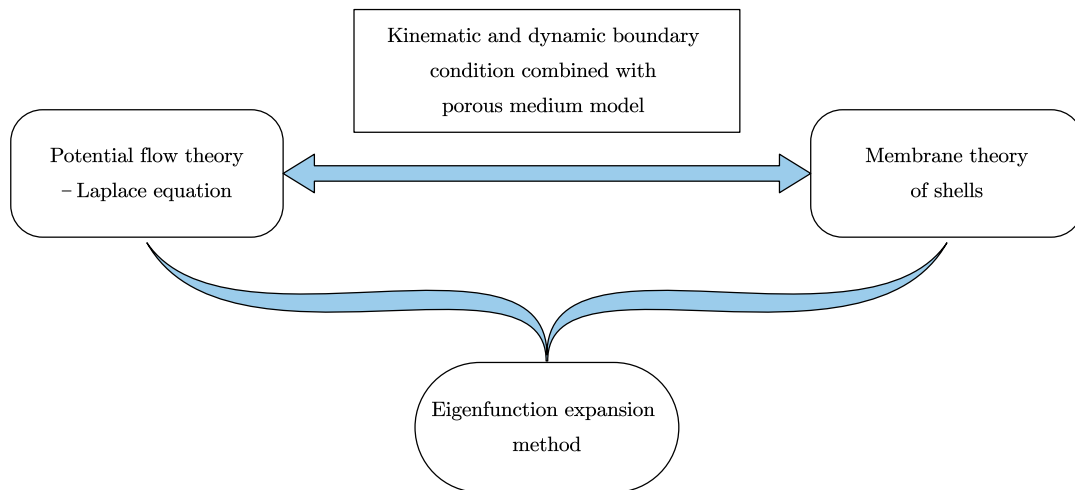


**Fig. 3.3** Theoretical framework of the simulation model in Study II.

a closed-form solution to the updated model can be obtained. The modified theoretical framework is presented in Fig. 3.3.

### **Stage 2.3: Analysis of results**

The results analysis of this study phase is similar to that of Study I. However, a more realistic dynamic response of the cage structure may be simulated. By contour plotting the pressure drop and structural displacement, one can identify the area with critical wave responses on the cage surface.

### **3.2.3 Study III: Theoretical extensions to the wave interference effects in the multi-cage system**

The objective of Study III is to extend the developed model to a more generalisable tool for predicting the hydroelastic behaviours of an array of fish cages with arbitrary numbers, dimensions and layouts. The superposition of scattered waves produced by each individual cage is the wave interference effect, which is the research focus in the third study phase. Limited literature has discussed the mean wave drift load acting on the fish cage, so this phenomenon is also explored at this stage. A detailed description of these methods can be found in Chapter 6.

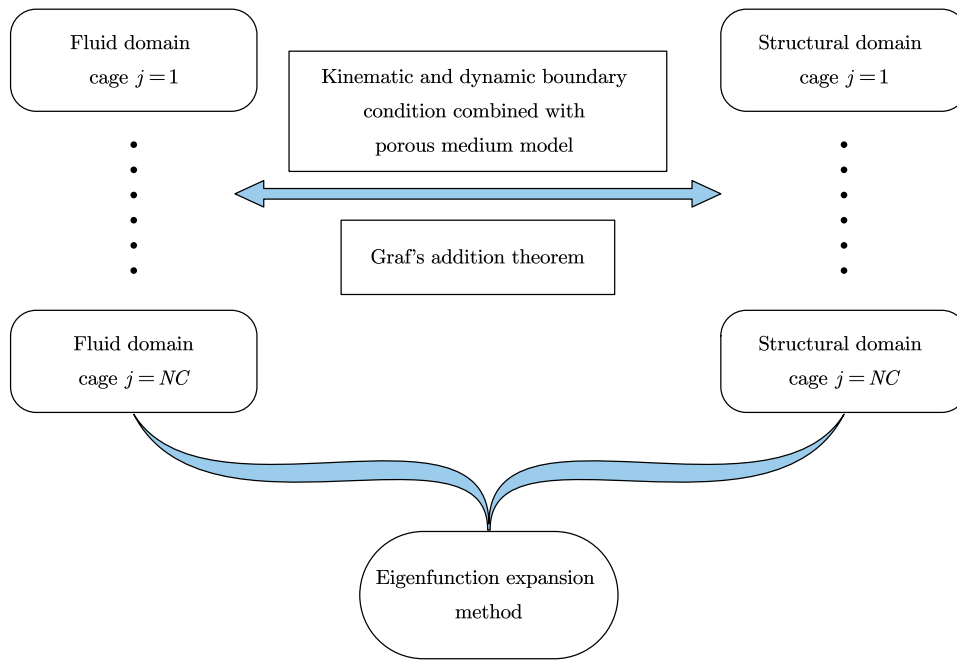


**Fig. 3.4** Theoretical framework of the simulation model in Study III.

### Stage 3.1: Application of the Kagimoto and Yue (1986) interaction theory

The Kagimoto and Yue (1986) interaction theory can provide an exact solution to describe the wavefield around multiple columnar structures. In the local coordinates of each cage, the scattering potential generated by that cage is written as an eigenfunction expansion, as in Studies II and III, and the coordinates can be transformed into the local coordinate systems belonging to other cages by employing Graf's addition theorem.

### Stage 3.2: Derivation of the coupled coefficient matrix for all cages

A series of fish cages numbered from  $j = 1, \dots, NC$  (number of cages) is considered. The analytical form of the nearby velocity potential is expressed in the local coordinate system of the  $k$ th cage according to Stage 3.1. By substituting the solution of the wavefield and structural displacement, which can be calculated directly using the developed FSI solver in Study II, into the kinematic boundary conditions of the cage interface, linear algebraic equations for the unknown constants in the general solution for this cage can be derived. The eventual coupled matrix system is obtained by simultaneously assembling the linear algebraic equations for all cages. The theoretical framework of Study III is illustrated in Fig. 3.4.

### Stage 3.3: Analysis of results

By contour plotting the wave amplitude distribution around the fish cage array, the characteristics of the wave interference effect can be effectively identified. However, the second-order wave potential does not contribute to the mean wave drift effect (Faltinsen, 1993). Therefore, by substituting the current first-order solution into the nonlinear Bernoulli equation and performing time-averaged operations, the mean wave drift load can be calculated. Additionally, some parametric studies on the wave forces acting on the cages in the array are discussed under the varied parameters that determine the wave interference phenomena. These findings are compared with the results of the single cage case.

According to the theoretical frameworks in the three study elements, the numerical execution flow chart for the eventual simulation model used to analyse the wave-net cage interaction is presented in Fig. 3.5.



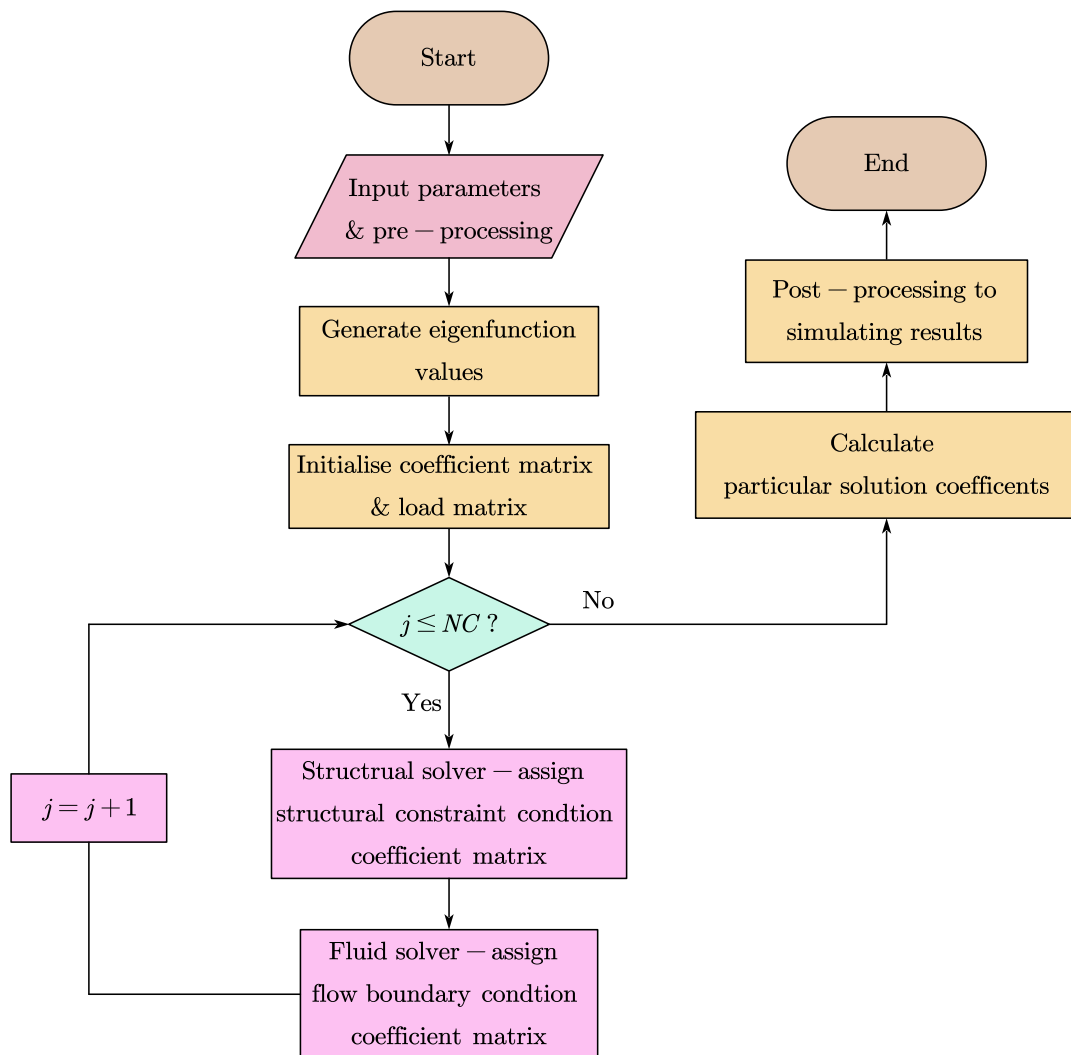


**Fig. 3.5** Numerical execution flow chart for the eventual simulation model to analyse the wave-net cage interaction.



## Chapter 4

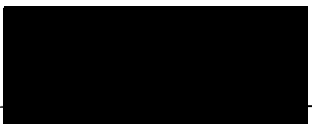
# Closed-Form Solutions to Interactions between Waves and Net Cages

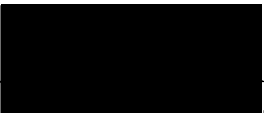
This chapter is originally published as


Ma, M., Zhang, H., Jeng, D.-S., and Wang, C. M. (2021). A semi-analytical model for studying hydroelastic behaviour of a cylindrical net cage under wave action. *Journal of Marine Science and Engineering*, 9:1445.

My contribution includes conceptualization, methodology, validation, formal analysis and writing-original draft preparation.

Signed:  Date: 02/02/2023  
Mingyuan Ma

Countersigned:  Date: 02/02/2023  
Prof. Hong Zhang (Principal Supervisor, School of Engineering and Built Environment, Griffith University)

Countersigned:  Date: 2/2/2023  
Prof. Dong-Sheng Jeng (Associate Supervisor, School of Engineering and Built Environment, Griffith University)

Countersigned:  Date: 02/02/2023  
Prof. Chien Ming Wang (Co-author, School of Civil Engineering, University of Queensland)

## **A semi-analytical model for studying hydroelastic behaviour of a cylindrical net cage under wave action**

**Abstract:** In the present study, a semi-analytical model based on the small-amplitude wave theory is developed to describe the wave fields around a single gravity-type cylindrical open fish net cage. The cage may be submerged to different depths below the free-water surface. The fish cage net is modelled as a flexible porous membrane, and the deflection of the net chamber is expressed by the transverse vibration equation of strings. The velocity potential is expanded in the form of the Fourier-Bessel series, and the unknown coefficients in these series are determined from matching the boundary conditions and the least squares method. The number of terms for the series solution to be used is determined from convergence studies. The model results exhibit significant hydroelastic characteristics of the net cages, including the distribution properties of wave surface, pressure drop at the net interface, structural deflection and wave loading along the cage height. In addition, the relationships between wave forces on the net cage with hydrodynamic and structural parameters are also revealed. The findings presented herein should be useful to engineers who are designing fish cage systems.

**Keywords:** Fish net cage; Hydroelastic analysis; Potential flow model; Wave scattering; Fourier-Bessel series; Porous medium theory.

## 4.1 Introduction

Fish farming not only provides an important protein supply for humans but also brings huge economic benefits. Average data from 2015 to 2017 indicates that fish products provide at least 20% of the animal protein intake of 3.3 billion people (FAO, 2020b), and aquatic products accounted for about 46.4% of the food and agriculture production in 2017 (Zhou, 2019). In addition, the aquaculture industry of Australia is in a stage of rapid development and reached an annual output value of AUD 3.3 billion in 2020 (Chen et al., 2021). In order to guarantee a stable output, the fishing cage system requires excellent reliability under environmental loads, such as waves and currents. Therefore, suitable modelling and studies on the dynamic response of the net cage to waves are crucial.

In many studies, the dynamic behaviour of fish cage nets is simulated by numerical models, for example, the bar element model (Tsukrov et al., 2003; Zhan et al., 2006) or the mass-spring model (Li et al., 2006; Zhao et al., 2008), in which the hydrodynamic force on each element is estimated by the Morison equation or the screen-type method proposed by Kristiansen and Faltinsen (2012). However, these models neglect the interferences of the structure and its motions on the flow field. For this reason, some researchers, exempli gratia, Bi et al. (2014) and Martin et al. (2021), introduced CFD techniques to achieve FSI, but this requires tremendous computational time. In the numerical experiment of Martin et al. (2021), it is reported that the simulation of a semi-submersible cage in irregular waves by FSI analysis takes around 185 h for 300 s of simulation time on 64 cores (Intel Sandy Bridge) with 2.6 Ghz and 2 GB memory per core. This is not feasible to model a full-scale fish net cage in detail in engineering practice. If some characteristics of the wave passing through the net can be simplified and solved analytically, then the computational time can be reduced significantly.

Usually, in theoretical analysis that allows for interaction between net cage and waves, the wave field is described by the linear potential flow theory, and the fish cage net is modelled as a porous medium membrane. The porous wavemaker theory is proposed by Chwang (1983) to analyse the water wave generated by the harmonic oscillation of a vertical porous barrier, where the porous flow is described by Darcy's law. With the eigenfunction expansion and matching the boundary conditions, the particular solution of the velocity potential can be derived for the scattering issue of small-amplitude waves passing through permeable barriers in Yu and Chwang (1994) and Lee and Chwang (2000). In terms of the interference effects among multiple rigid porous cylinders in waves, the scattering potential of each body in different local coordinates can be transformed by Graf's addition theorem in Sankarbabu et al. (2007) and Park et al. (2010). Furthermore, if waves interact with flexible structures, the motion of the structure can be approximately

described by the vibration equation of the continuum according to Abul-Azm and Williams (1987), Yip et al. (2002) and Behera and Sahoo (2015).

Recently, some studies have adopted the aforementioned theoretical approaches to analyse the interaction between waves and net cages. The transverse displacement of the circular cage is assumed to be governed by the vibration equation of the elastic beam in Mandal et al. (2013) and Su et al. (2015), and the deflection of the horizontal net plate can be described by the two-dimensional membrane vibration equation, which was introduced by Mandal and Sahoo (2016). Selvan et al. (2021) extended the theory of Mandal and Sahoo (2016) to the interference effect of multiple cages. Furthermore, Guo et al. (2020) present a detailed review about the mathematical modelling of wave interaction with flexible net-type structures.

Moreover, a few researchers employed numerical techniques based on the linear potential flow theory to investigate the wave-structure interaction problems. The scaled boundary finite element model is applied to investigate the interaction mechanism between waves and pile groups with arbitrary spatial layouts and cross-sections in Li et al. (2013b). A hybrid method is adopted to evaluate the wave force acting on a cube net cage in Ito et al. (2014), where the velocity potential of the far-field wave is expressed in the Fourier-Bessel series, and the ambient waves are solved by Green's theorem, i.e., the boundary element method (BEM). In Liu et al. (2020), the BEM and Morison equation are combined to investigate the hydrodynamic characteristics of a semi-submersible aquaculture facility. The numerical and experimental comparisons of Ito et al. (2014) and Liu et al. (2020) both show acceptable agreement.

Based on the above literature review, several research gaps are identified. Firstly, when evaluating hydrodynamic loads with empirical models (Morison equations or screen-type methods), the wave field distribution induced by diffraction and radiation effects around the net cage has to be determined. Secondly, fish net cages may be designed with submerged capabilities to avoid strong surface waves. However, the above analytical models from Su et al. (2015), Mandal and Sahoo (2016) and Selvan et al. (2021) do not consider this scenario. Thirdly, for the net cage exposed to a wave field, knowledge about its hydroelastic behaviours is scarce. Therefore, it is essential to establish an analytical model to predict some key factors that determine the wave responses of fish net cages.

In the present study, the interactions between waves and submersible cylindrical fish net cage are approximated by a semi-analytical solution based on linear hydroelastic theory. The characteristics of the cage response to wave (free water surface, pressure, hydrodynamic load, structural motion, etc.) are to be determined. This information is crucial for the design and application of fish cages. The linear model has advantages

## 4.2 Problem definition, assumption and theoretical formulation

---

in the derivation of analytical solutions even if the boundary value problem is relatively complicated. The potential flow theory is also convenient for dealing with the domain with an infinite boundary, which means that an extremely large wave field is feasible to be analysed. The paper is arranged as follows: Section 4.2 presents the assumptions, modelling, governing equation and boundary conditions for the wave-cage interaction problem. In Section 4.3, the method of solution for the governing equations and boundary value problems is elaborated. Section 4.4 presents the convergence studies and model validation. Section 4.5 presents the calculated results and explains the hydroelastic behaviour of the net cage under wave action, and parametric studies are established to reveal the relationship between the wave force on the net cage and various hydrodynamic and structural parameters. Finally, brief conclusions are given in Section 4.6.

## 4.2 Problem definition, assumption and theoretical formulation

In this study, a cylindrical net cage is considered as shown in Fig. 4.1, and it is convenient to describe the physical problem in a cylindrical coordinate system  $(r, \theta, z)$ . A small-amplitude wave propagates along the direction of  $\theta = 0$  with a circular frequency  $\omega$  and a wave height  $H$ . The mean water level is at  $z = 0$ , and the cage is submerged in a finite water depth of  $h$ . The central axis of the cage with a height of  $d_2$  is located at the position  $r = 0$ , and its top end can be submerged below the mean water level in  $d_1$ . In addition, the top end is constrained by mooring systems at  $z = -d_1$ , whilst the bottom end of  $z = -(d_1 + d_2)$  is free.

The flow domain may be divided into two zones: Region 1 ( $r > a, -h < z < 0$ ) is the external region outside the net cage, while Region 2 ( $r < a, -h < z < 0$ ) is the area within the circular net chamber. For the structural domain, the notations  $S_{net}$  and  $S_{gap}$  represent the net region of  $-(d_1 + d_2) \leq z \leq d_1$  and the gap portions of  $-d_1 < z \leq 0 \cup -h \leq z < -(d_1 + d_2)$ , respectively.

The problem at hand is to determine the hydroelastic behaviour of the submerged cylindrical net cage under wave action.

### 4.2.1 Governing equations

Assuming that the fluid is incompressible, irrotational and inviscid,  $\Phi_1$  and  $\Phi_2$  represent the velocity potentials in Regions 1 and 2, respectively, and the velocity potential  $\Phi_j(r, \theta, z, t)$

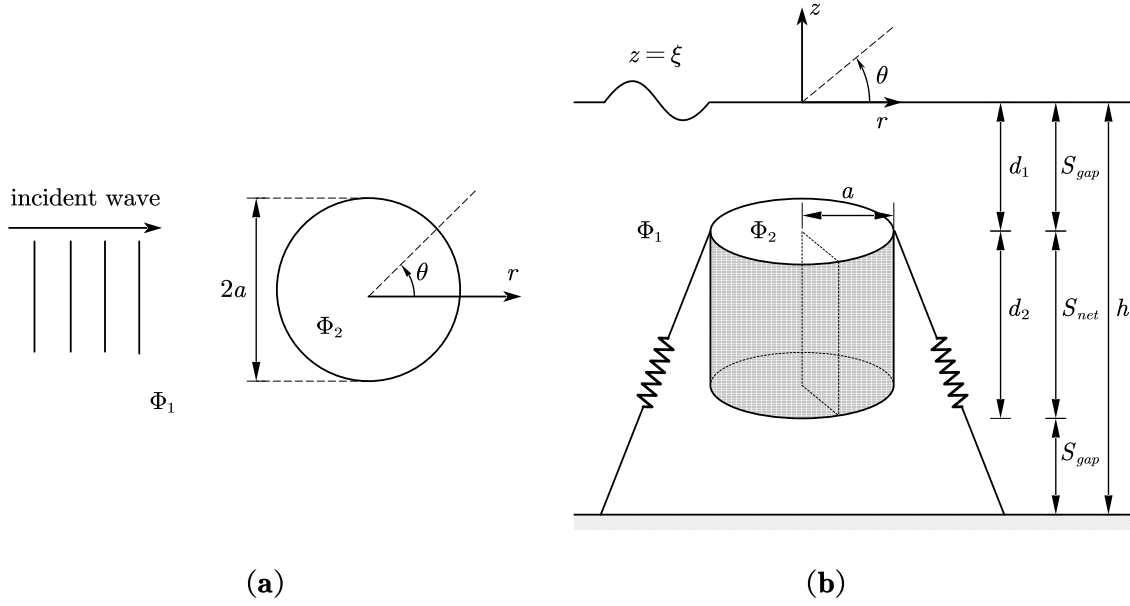


**Fig. 4.1** A sketch of a cylindrical net cage submerged in a finite water depth: (a) Plan view; (b) Isometric view.

( $j = 1, 2$ ) can be written as

$$\Phi_j = \text{Re} \left[ \varphi_j(r, \theta, z) e^{-i\omega t} \right], \quad (4.1)$$

where  $\varphi_j$  is the spatial component of the velocity potential, and it is governed by the Laplace equation in the cylindrical coordinate:

$$\frac{\partial^2 \varphi_j}{\partial r^2} + \frac{1}{r} \frac{\partial \varphi_j}{\partial r} + \frac{1}{r^2} \frac{\partial^2 \varphi_j}{\partial \theta^2} + \frac{\partial^2 \varphi_j}{\partial z^2} = 0. \quad (4.2)$$

In addition,  $\varphi_j$  can be represented as a superposition of the incident wave component  $\varphi^I$  and the scattered (diffraction and radiation) wave component  $\varphi_j^S$ , i.e.:

$$\varphi_j = \varphi^I + \varphi_j^S. \quad (4.3)$$

## 4.2.2 Boundary conditions

At the free water surface  $z = \xi$ , the linearised kinematic free surface (KFSBC) boundary condition satisfies

$$\frac{\partial \Phi_j}{\partial z} = \frac{\partial \xi}{\partial t} \quad \text{at } z = 0, \quad (4.4)$$

and the linearised dynamic free surface boundary condition (DFSBC) is

$$\xi = -\frac{1}{g} \frac{\partial \Phi_j}{\partial t} \quad \text{at } z = 0. \quad (4.5)$$



## 4.2 Problem definition, assumption and theoretical formulation

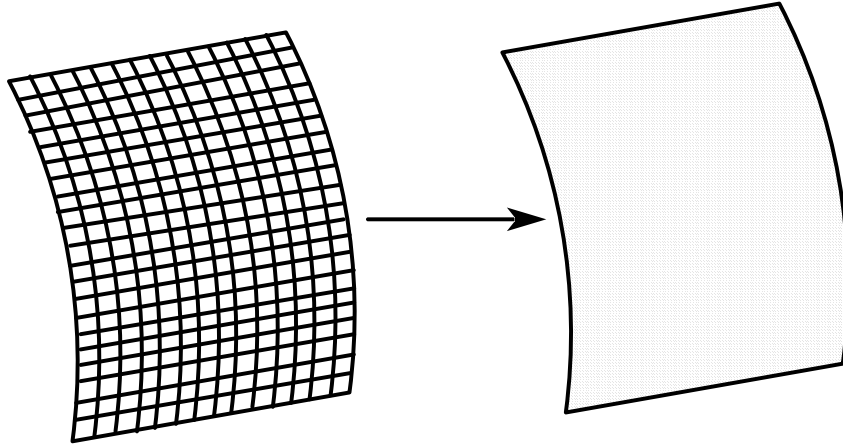


**Fig. 4.2** The fish cage net is modelled as a porous membrane.

By combining Eqs. (4.4) and (4.5), the boundary condition at the mean water level is

$$\frac{\partial \varphi_j}{\partial z} - \frac{\omega^2}{g} \varphi_j = 0 \quad \text{at } z = 0, \quad (4.6)$$

and the slippery boundary condition on the seabed is given by

$$\frac{\partial \varphi_j}{\partial z} = 0 \quad \text{at } z = -h. \quad (4.7)$$

Furthermore, the scattered potential component  $\varphi_j^S$  satisfies the Sommerfeld (1949) radiation condition when  $r$  approaches infinity, i.e.:

$$\lim_{r \rightarrow \infty} \sqrt{r} \left( \frac{\partial \varphi_1^S}{\partial r} - i\kappa_0 \varphi_1^S \right) = 0, \quad (4.8)$$

where  $\kappa_0$  is the incident wavenumber.

As shown in Fig. 4.2, the fish cage net is modelled as a porous membrane, so the penetration flow through the cage interface satisfies the linearised kinematic condition:

$$\frac{\partial \varphi_j}{\partial r} = i\tau(\varphi_2 - \varphi_1) - i\omega\eta \cos \theta \quad \text{at } r = a \text{ and } z \in S_{net}, \quad (4.9)$$

in which  $\eta$  is the spatial component of the transverse deflection of the cage along the incident direction of the wave, and  $\tau$  is the porous effect parameter of the net that is

expressed by an empirical formula given by Ito et al. (2014):

$$\tau = (1 + i\tau_i)\tau_r \text{ and } \tau_r = \frac{\kappa_0}{2\pi} \times \frac{(27.73\sqrt{\varepsilon + 469.0})\tau_0^2}{1 + (0.5510 - 0.01998\sqrt{\varepsilon})\tau_0}, \quad (4.10)$$

where  $\tau_0$  is the opening ratio of the net, i.e., the percentage of void space in the net,  $\varepsilon$  is the incident wave slope  $\kappa_0 H/2$ , and the imaginary part of  $\tau$  represents the fluid inertia effect. A high Keulegan–Carpenter number indicates a minor fluid inertia effect compared to the fluid drag effect. In Zhao et al. (2008), for the net twine with a diameter of a few millimetres, its  $K_C$  (Keulegan–Carpenter) number is 160 to 350 based on the laboratory tests, and the wave-induced inertia force is considered negligible compared to its drag force on the fish cage net. In the real sea condition, higher wave height and wave periods also mean a greater  $K_C$  number. Currently, there is no appropriate formula of  $\tau_i$  given for the cylindrical net cage; therefore, it is taken as 0 if there is no special explanation. Nevertheless, the influence of  $\tau_i$  is still discussed in Section 6. In addition, the continuity of the normal velocity and pressure of the flow at the interface between Regions 1 and 2 requires

$$\frac{\partial\varphi_1}{\partial r} = \frac{\partial\varphi_2}{\partial r} \quad \text{at } r = a \text{ and } -h < z < 0, \quad (4.11)$$

$$\varphi_1 = \varphi_2 \quad \text{at } r = a \text{ and } z \in S_{gap}. \quad (4.12)$$

On the other hand, it is assumed that the cross-section of the cage maintains its circular shape under wave action if the cage is imposed a great axial tension and has a small deformation relative to its overall size. Liu et al. (2021) showed a deformed net cage simulated by the finite element method (FEM) using truss elements, and it is observed that the cage approximately maintains a circular cross-section. Therefore, the transverse deflection of the cage is  $\zeta = \text{Re}[\eta(z)e^{-i\omega t}]$ , and the transverse vibration equation of the string to describe the complex amplitude  $\eta$  is given by Mandal and Sahoo (2016):

$$\frac{d^2\eta}{dz^2} + \frac{m_s\omega^2}{Q}\eta = -\frac{ai\omega\rho}{Q} \int_0^{2\pi} (\varphi_1 - \varphi_2)\cos(\pi - \theta)d\theta, \quad (4.13)$$

in which  $Q$  is the axial uniform tensile force in the net,  $m_s$  is the uniform mass of the net per unit length, and  $\rho$  is the water density. In Liu et al. (2021), a comparison between the analytical model based on Eq. (4.13) and the FEM simulation for the cylindrical net cage illustrates acceptable errors.

For the edge restraint condition of the net chamber, its top end is assumed to be constrained by the mooring systems according to Liu et al. (2021), and there is no transverse

traction at the bottom end, i.e.:

$$\begin{aligned}\frac{d\eta}{dz} &= 1/Qk_s\eta \quad \text{at } z = -d_1, \\ \frac{d\eta}{dz} &= 0 \quad \text{at } z = -(d_1 + d_2),\end{aligned}\tag{4.14}$$

where  $k_s$  is the spring constant of the mooring cables.

### 4.3 Derivation of the solutions

In view of the governing equation, Eq. (4.2), and the boundary conditions, Eqs. (4.6), (4.7) and (4.8), the solution of  $\varphi_1$  is sought in the form

$$\varphi_1 = \varphi^I + \varphi_1^S,\tag{4.15}$$

where

$$\varphi^I = \sum_{m=0}^{\infty} -\frac{igH \cosh[\kappa_0(z+h)]}{2\omega \cosh(\kappa_0h)} \mu_m J_m(\kappa_0 r) \cos(m\theta),\tag{4.16}$$

$$\mu_m = \begin{cases} 1, & m = 0 \\ 2i^m, & m > 0 \end{cases},\tag{4.17}$$

$$\varphi_1^S = \sum_{m=0}^{\infty} \sum_{n=0}^{\infty} A_{mn} R_m^1(\kappa_n r) f_n(z) \cos(m\theta),\tag{4.18}$$

$$R_m^1(\kappa_n r) = \begin{cases} \frac{H_m(\kappa_n r)}{H_m'(\kappa_n a)}, & n = 0 \\ \frac{K_m(\kappa_n r)}{K_m'(\kappa_n a)}, & n > 0 \end{cases},\tag{4.19}$$

$$f_n(z) = \begin{cases} \frac{\cosh[\kappa_n(z+h)]}{\cosh(\kappa_n h)}, & n = 0 \\ \frac{\cos[\kappa_n(z+h)]}{\cos(\kappa_n h)}, & n > 0 \end{cases}.\tag{4.20}$$

Similarly, according to the governing equation, Eq. (4.2), and the boundary conditions, Eqs. (4.6) and (4.7), the general solution of  $\varphi_2$  is

$$\varphi_2 = \varphi^I + \varphi_2^S,\tag{4.21}$$

where

$$\varphi_2^S = \sum_{m=0}^{\infty} \sum_{n=0}^{\infty} B_{mn} R_m^2(\kappa_n r) f_n(z) \cos(m\theta),\tag{4.22}$$

$$R_m^2(\kappa_n r) = \begin{cases} \frac{J_m(\kappa_n r)}{J_m(\kappa_n a)}, & n = 0 \\ \frac{I_m(\kappa_n r)}{I_m(\kappa_n a)}, & n > 0 \end{cases} . \quad (4.23)$$

In abovementioned equations,  $\kappa_n$ s are the real roots of the following dispersion relations:

$$\omega^2 = \begin{cases} g\kappa_n \tanh(\kappa_n h), & n = 0 \\ -g\kappa_n \tan(\kappa_n h), & n > 0 \end{cases} , \quad (4.24)$$

$A_{mn}$  and  $B_{mn}$  are the unknown constants,  $J_m$  is the first kind of Bessel function,  $H_m$  is the first kind of Hankel function,  $I_m$  is the first kind of modified Bessel function, and  $K_m$  is the second kind of modified Bessel function, where the subscript  $m$  is the order of the Bessel function.

By substituting Eqs. (4.16), (4.18) and (4.22) into the boundary condition Eq. (4.11) and applying the orthogonality operation of  $\cosh[\kappa_n(z+h)]$ ,  $\cos(\kappa_n h)$ ,  $n = 0, 1, 2 \dots$  over  $-h \leq z \leq 0$  and  $\cos(m\theta)$ ,  $m = 0, 1, 2 \dots$  over  $0 \leq \theta \leq 2\pi$ , the unknown constants in Eqs. (4.18) and (4.22) satisfy

$$A_{mn} = B_{mn}. \quad (4.25)$$

Therefore, one can write

$$\Delta\varphi = \varphi_1 - \varphi_2 = \sum_{m=0}^{\infty} \sum_{n=0}^{\infty} A_{mn} X_{mn} f_n(z) \cos(m\theta) \quad \text{at } r = a, \quad (4.26)$$

where

$$X_{mn} = R_m^1(\kappa_n a) - R_m^2(\kappa_n a). \quad (4.27)$$

By substituting Eq. (4.26) into Eq. (4.13) and noting the orthogonality of  $\cos(m\theta)$ ,  $m = 0, 1, 2 \dots$  over  $0 \leq \theta \leq 2\pi$ , Eq. (4.13) might be rewritten as

$$\frac{d^2\eta}{dz^2} + \alpha_1\eta = \alpha_2 \sum_{n=0}^{\infty} A_{1n} X_{1n} f_n(z), \quad (4.28)$$

where

$$\alpha_1 = m_s \omega^2 \Big|_Q \text{ and } \alpha_2 = \pi a i \omega \rho \Big|_Q. \quad (4.29)$$

Therefore, the general solution of  $\eta(z)$  is

$$\eta(z) = \sum_{b=1}^2 C_b e^{q_b z} + \sum_{n=0}^{\infty} A_{1n} F_n f_n(z), \quad (4.30)$$

### 4.3 Derivation of the solutions

in which

$$F_n = \begin{cases} \frac{\alpha_2 X_{1n}}{\alpha_1 + \kappa_n^2}, & n = 0 \\ \frac{\alpha_2 X_{1n}}{\alpha_1 - \kappa_n^2}, & n > 0 \end{cases}, \quad (4.31)$$

and  $q_b$ s are the roots of the characteristic equation of Eq. (4.28), where they are given by

$$q_1 = i\omega \sqrt{m_s Q} \text{ and } q_2 = -i\omega \sqrt{m_s Q}. \quad (4.32)$$

By substituting Eq. (4.30) into the boundary condition, Eq. (4.14), the constant  $C_b$ s are acquired through

$$\begin{cases} \sum_{b=1}^2 C_b (k_s - q_b Q) e^{-q_b d_1} + \sum_{n=0}^{\infty} A_{1n} [k_s F_n f_n(-d_1) - Q F_n f_n'(-d_1)] = 0 \\ \sum_{b=1}^2 C_b q_b e^{-q_b (d_1 + d_2)} + \sum_{n=0}^{\infty} A_{1n} F_n f_n'[-(d_1 + d_2)] = 0 \end{cases}. \quad (4.33)$$

For the net portion  $z \in S_{net}$ , substituting Eqs. (4.16), (4.18) and (4.26) into Eq. (4.9) and invoking the orthogonality of  $\cos(m\theta)$  again, one obtains, when  $m \neq 1$ ,

$$\sum_{n=0}^{\infty} A_{mn} \kappa_n f_n(z) + i\tau \sum_{n=0}^{\infty} A_{mn} X_{mn} f_n(z) - \frac{igH\kappa_0 \cosh[\kappa_0(z+h)]}{2\omega \cosh(\kappa_0 h)} \mu_m J_m'(\kappa_0 a) = 0, \quad (4.34)$$

when  $m = 1$ ,

$$\begin{aligned} & \sum_{n=0}^{\infty} A_{1n} \kappa_n f_n(z) + i\tau \sum_{n=0}^{\infty} A_{1n} X_{1n} f_n(z) + i\omega \sum_{n=0}^{\infty} A_{1n} F_n f_n(z) \\ & - \frac{igH\kappa_0 \cosh[\kappa_0(z+h)]}{2\omega \cosh(\kappa_0 h)} \mu_m J_m'(\kappa_0 a) + i\omega \sum_{j=1}^2 C_b e^{q_b z} = 0. \end{aligned} \quad (4.35)$$

For the gap portion  $z \in S_{gap}$ , substituting Eq. (4.26) into Eq. (4.12) and using the orthogonality of  $\cos(m\theta)$  yields

$$\sum_{n=0}^{\infty} A_{mn} X_{mn} f_n(z) = 0. \quad (4.36)$$

As a result, a system of equations can be obtained from Eqs. (4.34), (4.35) and (4.36):

$$S_m(z) = \sum_{n=0}^{\infty} A_{mn} \epsilon_{mn}(z) + \lambda_m(z) = 0, \quad (4.37)$$

where when  $m \neq 1$ ,

$$\epsilon_{mn}(z) = \begin{cases} (\kappa_n + i\tau X_{mn}) f_n(z), & z \in S_{net} \\ X_{mn} f_n(z), & z \in S_{gap} \end{cases}, \quad (4.38)$$

$$\lambda_m(z) = \begin{cases} -\frac{igH\kappa_0 \cosh[\kappa_0(z+h)]}{2\omega \cosh(\kappa_0 h)} \mu_m J'_m(\kappa_0 a), & z \in S_{net} \\ 0, & z \in S_{gap} \end{cases}, \quad (4.39)$$

and when  $m = 1$ ,

$$\epsilon_{mn}(z) = \begin{cases} (k_n + i\tau X_{mn} + i\omega F_n) f_n(z), & z \in S_{net} \\ X_{mn} f_n(z), & z \in S_{gap} \end{cases}, \quad (4.40)$$

$$\lambda_m(z) = \begin{cases} -\frac{igH\kappa_0 \cosh[\kappa_0(z+h)]}{2\omega \cosh(\kappa_0 h)} \mu_m J'_m(\kappa_0 a) + i\omega \sum_{j=1}^2 C_b e^{q_b z}, & z \in S_{net} \\ 0, & z \in S_{gap} \end{cases}. \quad (4.41)$$

Truncating the infinite series after  $N$ th terms in Eq. (4.37) yields

$$S_m(z) = \sum_{n=0}^N A_{mn} \epsilon_{mn}(z) + \lambda_m(z) = 0. \quad (4.42)$$

By manipulating the least-squares approximation for Eq. (4.42), one obtains

$$\int_{-h}^0 |S_m(z)|^2 dz = \min \Rightarrow \int_{-h}^0 S_m^* \frac{\partial S_m(z)}{\partial A_{mn}} dz = 0, \quad (4.43)$$

and a system of equations about  $A_{mn}$  is acquired by substituting Eq. (4.42) into Eq. (4.43):

$$\sum_{n=0}^N A_{mn}^* \Psi_{mn,l} = \Omega_{m,l}, \quad (4.44)$$

where

$$\Psi_{mn,l} = \int_{-h}^0 \epsilon_{mn}^* \epsilon_{m,l} dz \text{ and } \Omega_{m,l} = - \int_{-h}^0 \lambda_m^* \epsilon_{m,l} dz, \quad (4.45)$$

and  $m = 0, 1, 2, \dots, M$ ;  $l = 0, 1, 2, \dots, N$ .

Finally, in view of the linearised Bernoulli's equation, the complex dynamic pressure  $p$  is

$$p_j = -\rho \frac{\partial(\varphi_j e^{-i\omega t})}{\partial t}, \quad (4.46)$$

## 4.4 Convergence studies and model validation

and the complex pressure difference acting on the net interface is defined as

$$\Delta p = p_1 - p_2, \quad \text{at } r = a. \quad (4.47)$$

As a result, the complex function of the horizontal hydrodynamic force per unit length along the cage height is given by

$$f(z) = a \int_0^{2\pi} \Delta p \cos(\pi - \theta) d\theta = -\pi a i \omega \rho \sum_{n=0}^N A_{1n} X_{1n} f_n(z) e^{-i\omega t}, \quad (4.48)$$

and the wave force and the resulting overturning moment with respect to the top of the cage are

$$F = \int_{-(d_1+d_2)}^{-d_1} f(z) dz \quad \text{and} \quad M_o = \int_{-(d_1+d_2)}^{-d_1} f(z) \left( z + d_1 + \frac{d_2}{2} \right) dz. \quad (4.49)$$

Furthermore, according to the DFSBC, Eq. (4.5), the free water surface elevation  $\xi$  is given by

$$\xi_j = \text{Re} \left( \frac{i\omega \varphi_j e^{-i\omega t}}{g} \right). \quad (4.50)$$

## 4.4 Convergence studies and model validation

### 4.4.1 Convergence studies

In Section 4.3, the derived solution is written in the form of the Fourier-Bessel series, and the infinite terms have been truncated after  $N$ th and  $M$ th terms. Theoretically, the calculated result is only valid when the solution converges with the increasing number of the series term. Therefore, convergence studies are required to determine the truncated terms to use for accurate results. For the convergence studies, the following parameters are adopted:  $H = 7$  m,  $h = 200$  m,  $a = 50$  m,  $d_1 = 0$ ,  $d_2 = 50$  m and  $\tau_0 = 0.7$ . The nondimensional mooring spring constant  $\alpha = k_s/(m_s g)$  is 20, the nondimensional axial tensile force in the net  $\gamma = Q/(m_s g d_2)$  is taken as 1, and the nondimensional net mass per unit length  $\beta = m_s/(\rho d_2^2) = 0.001$ . The wave frequency  $\omega$  varies from 0.2 rad/s to 1.4 rad/s at an interval of 0.4 rad/s.

In Eq. (4.30), due to the orthogonality of  $\cos(m\theta)$ , the convergence of  $\eta$  is only determined by the series term generated by the wavenumbers from the dispersion relation

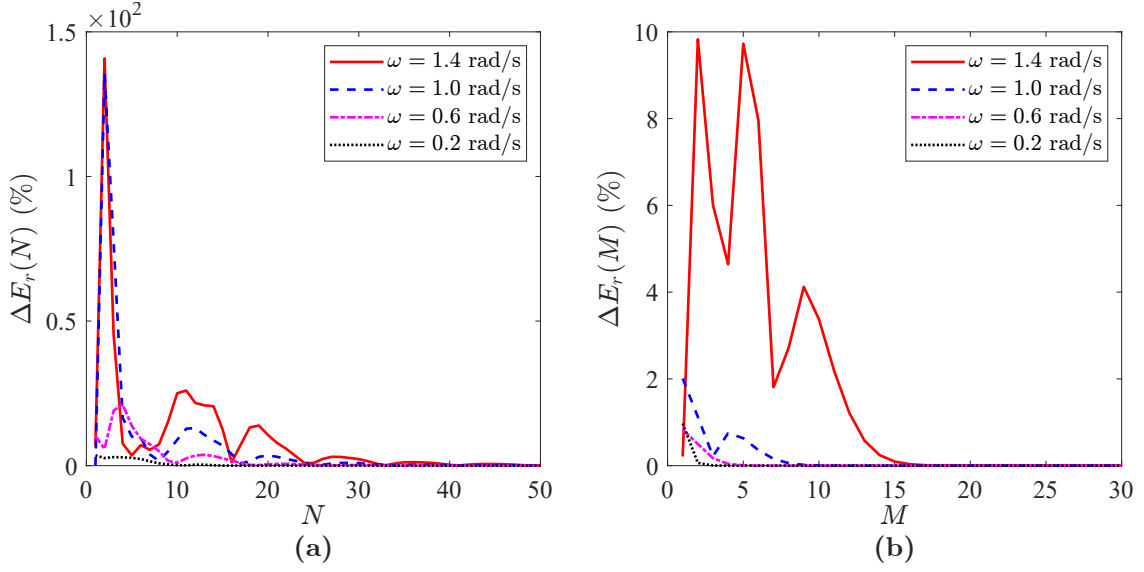


**Fig. 4.3** Convergence curves of control errors versus truncated terms for different wave frequencies: (a)  $\Delta E_r(N)$  versus  $N$ ; (b)  $\Delta E_r(M)$  versus  $M$ .

Eq. (4.24), so a control error  $\Delta E_r(N)$  versus the truncated term  $N$  is defined as

$$\Delta E_r(N) = \frac{\left| \eta\left(-d_1 - \frac{d_2}{2}\right)_{,N+1} - \eta\left(-d_1 - \frac{d_2}{2}\right)_{,N} \right|}{\left| \eta\left(-d_1 - \frac{d_2}{2}\right)_{,N} \right|}. \quad (4.51)$$

The variations of  $\Delta E_r(N)$  versus  $N$  from 1 to 50 are shown in Fig. 4.3a. The results exhibit different convergency speeds for different wave frequencies, and the values of  $\Delta E_r(N)$  converge more slowly when the wave frequency is larger. Notably, when  $N > 30$ , the maximum control error is less than 2.25% for all cases.

Alternatively, for the solution of the local wave field near the cage, the control error  $\Delta E_r(M)$  versus the truncated term  $M$  is defined as follows:

$$\Delta E_r(M) = \frac{\left| \sum_{z=-(d_1+d_2)}^{-d_1} \sum_{\theta=0}^{2\pi} \Delta\varphi(a, \theta, z)_{,M+1} - \sum_{z=-(d_1+d_2)}^{-d_1} \sum_{\theta=0}^{2\pi} \Delta\varphi(a, \theta, z)_{,M} \right|}{\left| \sum_{z=-(d_1+d_2)}^{-d_1} \sum_{\theta=0}^{2\pi} \Delta\varphi(a, \theta, z)_{,M} \right|}. \quad (4.52)$$

The curves of  $\Delta E_r(M)$  versus  $M$  from 1 to 50 are presented in Fig. 4.3b. Similarly, if the wave frequency is lower, the control error will show a more rapid decay, and the control errors of the whole cases are closed to 0 for when  $M > 18$ . Based on the convergence studies, it is sufficient to take  $N = 30$  and  $M = 20$  to guarantee the accuracy for the solution to the imposed wave action and cage displacement.



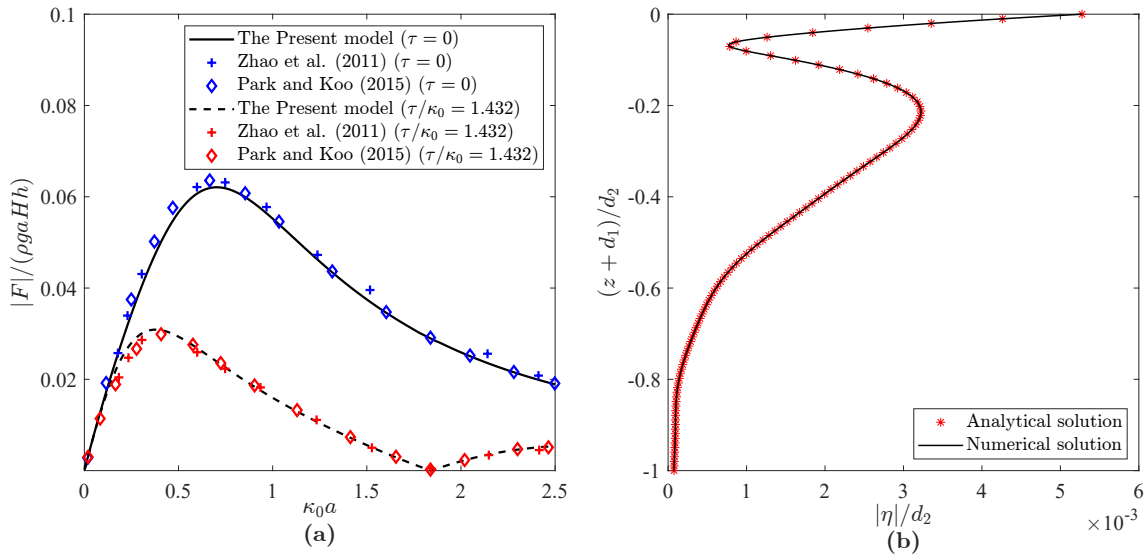


**Fig. 4.4** Model validations: (a) Horizontal wave force  $|F|$ ; (b) Cage deflection amplitude  $|\eta|$ .

#### 4.4.2 Model validation

In order to examine the correctness of the aforementioned formulations, consider a rigid impermeable or porous circular cage illustrated in Zhao et al. (2011) and Park and Koo (2015) with the parameters of  $h = 5$  m,  $a = 0.15$  m,  $d_1 = 0$  and  $d_2 = 0.3$  m. The structural parameters adopted  $\alpha = 1000$ ,  $\gamma = 1000$  and  $\beta = 1000$  to ensure the cage motion is negligible. The nondimensional horizontal wave force acting on the cage versus the normalized wavenumber  $\kappa_0 a$  is shown in Fig. 4.4a. There are no significant differences between the present model and the aforementioned studies. A small discrepancy observed is because a horizontal impermeable plate is considered at the bottom of the cage in Zhao et al. (2011) and Park and Koo (2015).

In addition, the current analytical solution of the cage deflection amplitude  $|\eta|$  is validated with the numerical solution generated by the Runge-Kutta method, where the parameters adopt those in the convergence studies and  $\omega = 1$  rad/s. Fig. 4.4b indicates that the derived analytical solution is completely consistent with the numerical results.

### 4.5 Results and discussions

This section discusses the hydroelastic spatial characteristics of the net cages by some numerical results. Five case groups were designed with various wave periods  $T$  (Cases A), net opening ratios  $\tau_0$  (Cases B), nondimensional mooring spring constants  $\alpha$  (Cases C), nondimensional axial tensile forces  $\gamma$  in the net (Cases D) and immersed depths  $d_1$  of the

cage (Cases E). The detailed parameter settings are shown in Table 4.1. In this analysis, a full-scale cage deployed in the marine aquaculture industry is considered, in which the cage radius  $a = 50$  m, the cage height  $d_2 = 50$  m, and the dimensionless net mass per unit length  $\beta = 0.001$ . Moreover, the wave height  $H = 7$  m and the water depth  $h = 200$  m are adopted.

### 4.5.1 Hydrodynamic behaviours

The present model can evaluate the distribution of the velocity potential  $\Phi$  of the fluid domain and then derive its corresponding dynamic pressure and free surface elevations at a series of discretised points. Here, Cartesian coordinates ( $x = r \cos \theta$  and  $y = r \sin \theta$ ) are established to facilitate the description of the results, where the central axis of the cage is located at the  $z$ -axis, and the incident wave propagates along the positive direction of the  $x$ -axis.

The free surface elevations  $\xi$  (m) around the cage with varied net opening ratios (Cases B1 to B4) are illustrated in Fig. 4.5, in which  $\xi$  is calculated from Eq. (4.50) in a domain of  $x/a = \pm 4$  and  $y/a = \pm 4$ . In this example,  $\xi$  adopted the values at time  $t/T = n$ ,  $n = 0, 1, 2, \dots, \infty$ , and the black circle is the demarcation between Regions 1 and 2. It can be observed that the presence of the cage causes perturbations to the wave surface, especially for the cage with an impermeable interface (i.e., net opening ratio  $\tau_0 = 0$ ). The transmitted wave passing through the cage will be attenuated, and its amplitude will gradually restore to its original state. This occurs because, when the scattered wave radiates away from the cage, the scattering potential gradually decays. Alternatively, the wave surface in the inner region of the cage also has different extents of attenuation, and the energy dissipation is the most severe, especially when  $\tau_0 = 0$ . It is worth noting that, due to the blocking effect of the porous net, the water surface elevation inside the cage is affected by a certain lag in propagation when compared with the waves outside the cage. Furthermore, when the opening ratio of the net is gradually increased, the disturbance of the cylindrical net cage to the wave surface will gradually become weak, and the observed wave scattering becomes relatively minor for the cases with  $\tau_0 > 0.3$ . In engineering practice, the adopted opening ratio of the fish cage net is usually greater than 0.6, so the influence of the net cage on the wave surface has become weak at this time.

Fig. 4.6 shows the amplitude distributions of the pressure differences  $\Delta p_a$  on the net chamber under different wave periods in Cases A1 to A4.  $\Delta p$  is defined in Eq. (4.47), and  $\Delta p_a$  is its modulus. The maximum values of  $\Delta p_a$  are mainly concentrated at the top of the cylindrical cage, in which the maximum values are greater when the wave periods

**Table 4.1** Case groups with different studied parameters (Study I).

Cases	$T$ (s)	$\tau$	$\alpha$	$\gamma$	$d_1$ (m)
A1	4	0.7	20	1	0
A2	6	0.7	20	1	0
A3	8	0.7	20	1	0
A4	10	0.7	20	1	0
B1	8	0.1	20	1	0
B2	8	0.2	20	1	0
B3	8	0.3	20	1	0
B4	8	0.4	20	1	0
B5	8	0.6	20	1	0
B6	8	0.7	20	1	0
B7	8	0.8	20	1	0
B8	8	0.9	20	1	0
C1	8	0.7	1	1	0
C2	8	0.7	10	1	0
C3	8	0.7	20	1	0
C4	8	0.7	Fixed end	1	0
D1	8	0.7	20	0.5	0
D2	8	0.7	20	1	0
D3	8	0.7	20	2	0
D4	8	0.7	20	4	0
E1	8	0.7	20	1	0
E2	8	0.7	20	1	10
E3	8	0.7	20	1	30
E4	8	0.7	20	1	50

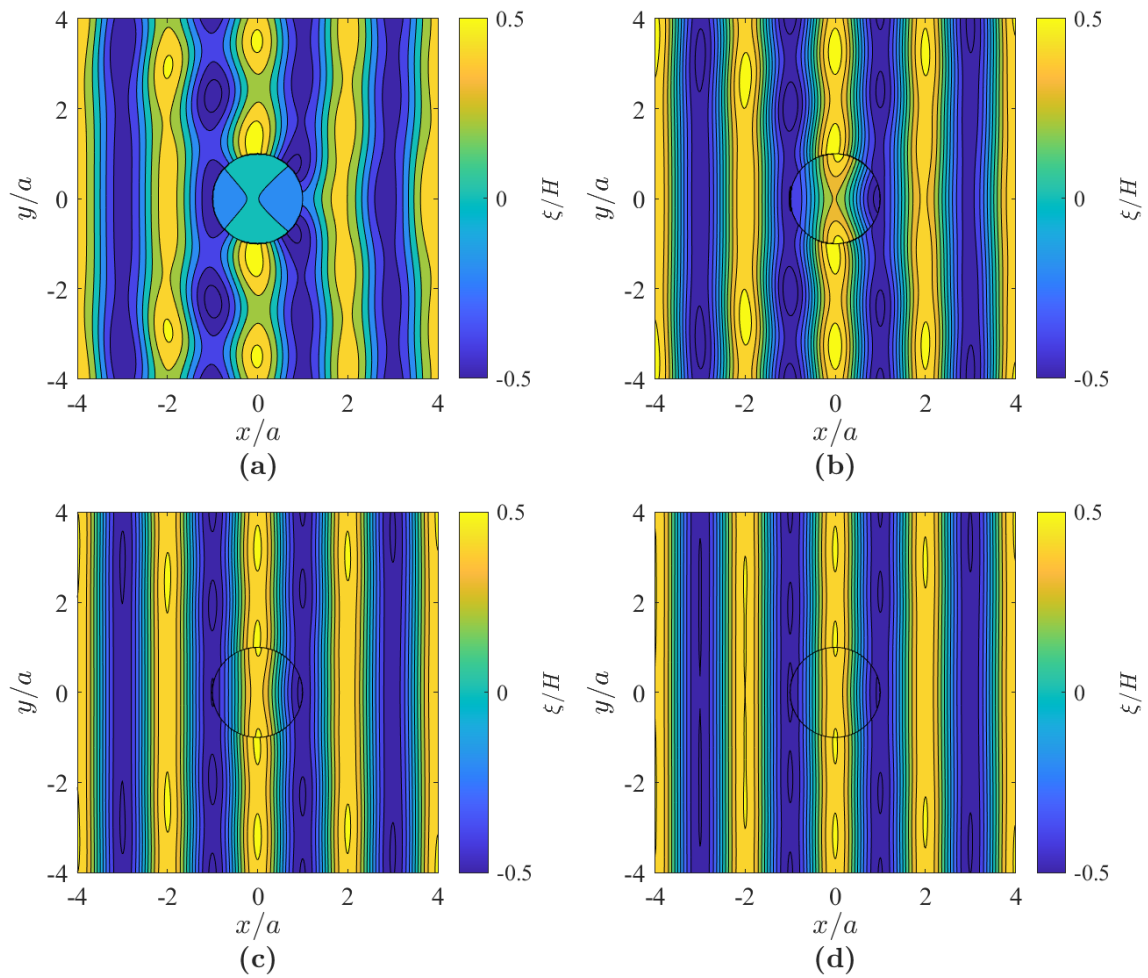


**Fig. 4.5** Free water surface elevations  $\xi$  around a cylindrical net cage with different opening ratios at  $t/T = n$ ,  $n = 0, 1, 2, \dots, \infty$ , Cases B1 to B4: (a)  $\tau_0 = 0$ ; (b)  $\tau_0 = 0.1$ ; (c)  $\tau_0 = 0.2$ ; (d)  $\tau_0 = 0.3$ .

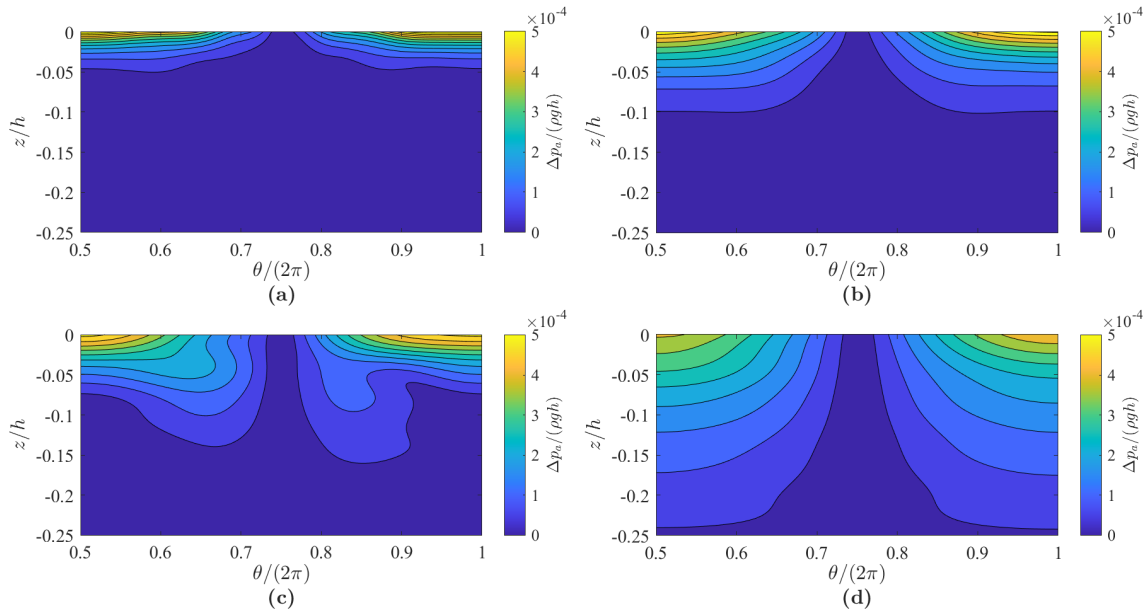


**Fig. 4.6** Amplitude distributions of pressure drop  $\Delta p_a$  on the net interface, Cases A1 to A4: (a)  $T = 4$  s; (b)  $T = 6$  s; (c)  $T = 8$  s; (d)  $T = 10$  s.

are smaller. Nevertheless, the values of  $\Delta p_a$  at the lower part of the cage are relatively minor, and the values at its bottom end are close to 0. These results demonstrate that the wave has a more significant impact on the top part of the cage. Notably, more areas on the cage surface will withstand the pressure drop with high amplitudes under the wave action with longer periods, because short waves mainly concentrate on the free-water surface. Moreover, due to the energy dissipation of the transmitted wave, the pressure drop amplitude  $\Delta p_a$  on the leeward side is also slightly higher.

### 4.5.2 Structural dynamic responses

In this section, the structural dynamic responses of the net cage are investigated. Two important indices are presented: the nondimensional amplitude of the structural transverse deflection  $|\eta|/d_2$ , and the nondimensional amplitude of the horizontal wave load per unit length  $K_f$  along the cage height. Following the work of Mandal and Sahoo (2016),  $K_f$  is defined as

$$K_f = \frac{|f(z)|}{\rho g a H}, \quad (4.53)$$

in which the horizontal wave load per unit length  $f(z)$  is found from Eq. (4.48). The curves of  $|\eta|/d_2$  and  $K_f$  versus the relative position defined as  $(z + d_1)/d_2$  are plotted in Figs. 4.7 to 4.11.

It can be observed that the greater transverse deflection of the net chamber occurs at the upper part of the cage, and the horizontal wave load per unit length is the largest at the top end of the cage. At the bottom of the structure, the values of  $|\eta|/d_2$  and  $K_f$  are the smallest. In addition, due to the assumption of structural edge constraints, the cage has obvious displacements at the top end (mooring constrained end), and the first-order derivatives to  $z$  are zero at the bottom end (lateral traction-free end) for the curves of  $|\eta|/d_2$ .

Fig. 4.7 presents the results of Cases A1 to A4 with  $T$  varying from 4 s to 10 s with an interval of 2 s. It can be seen that when  $T = 8$  s, the transverse deflection and wave load on the structure are much greater than the values of the other periods. That may indicate that the natural frequency of the net cage is close to the excited frequency of waves. In this case, the mode shape of the structure presents a first-order modal vibration.

In Fig. 4.8, Cases B5 to B8, when the porosity of the fish cage net increases, the transverse deflection amplitude at the upper part of the net chamber decreases but the value of the lower part slightly increases. With regard to the coefficient  $K_f$ , the values at the upper part of the cage have a greater difference, but when  $(z + d_1)/d_2$  is smaller than  $-0.3$ , these differences are relatively small. This is because these cases are set as floating conditions, and the porous effect of the fish cage net will have a more significant blocking impact on the flow close to the wave surface.

In Fig. 4.9, Cases C1 to C4 show the effect of the mooring cable stiffness, and there is also a fixed end case ( $\eta = 0$  at  $z = -d_1$ ) presented. When  $\alpha = 0.5$ , a weak spring stiffness results in the vanishing of peaks on the curves of  $|\eta|/d_2$  and a significant reduction of the normalised wave load  $K_f$ . Nevertheless, when  $\alpha > 10$ , its influence on wave action becomes relatively minor.

Referring to Fig. 4.10 (Cases D1 to D4), the distribution characteristics of  $|\eta|/d_2$  and  $K_f$  are similar when  $\gamma < 4$ . If the axial tension in the cage increases, the overall deformation of the cage can be suppressed, but the top displacement will increase. When  $\gamma = 4$ , there are no peaks along the curves of  $|\eta|/d_2$ . Moreover, the wave action is enhanced to a certain extent for a stiffer net cage.

In Fig. 4.11 (Cases D1 to D4), it can be seen that the wave effect will gradually become minimal as the diving depth of the cage increases. The corresponding structural deformation and wave load are also reduced significantly. This justifies the submergence of the cage into a deeper water level to avoid the strong surface waves. Moreover, the three-dimensional (3D) shapes of the net chamber with the maximum deformation are plotted at different submerged depths in Fig. 4.12, where the deflection values are magnified by an exaggerated scale of 5 times. Little wave response of the cage is observed when it is submerged at  $d_1/h = 0.25$ .

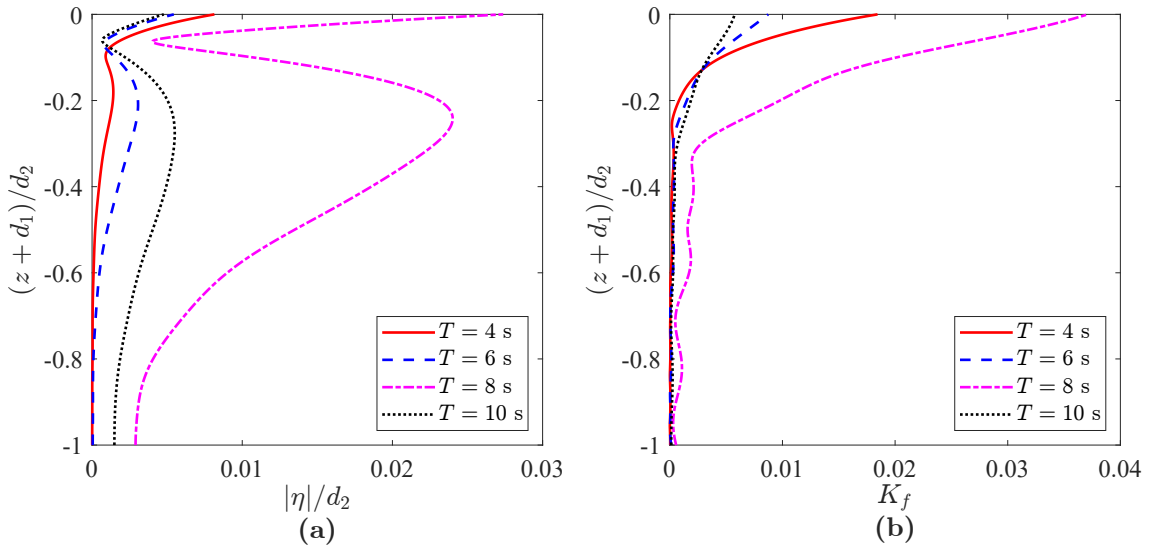


**Fig. 4.7** (a) Nondimensional transverse deflection amplitudes of cage  $|\eta|/d_2$ ; (b) Nondimensional horizontal wave load amplitudes per unit length  $K_f$  along cage height for various wave periods  $T$ , Cases A1 to A4.

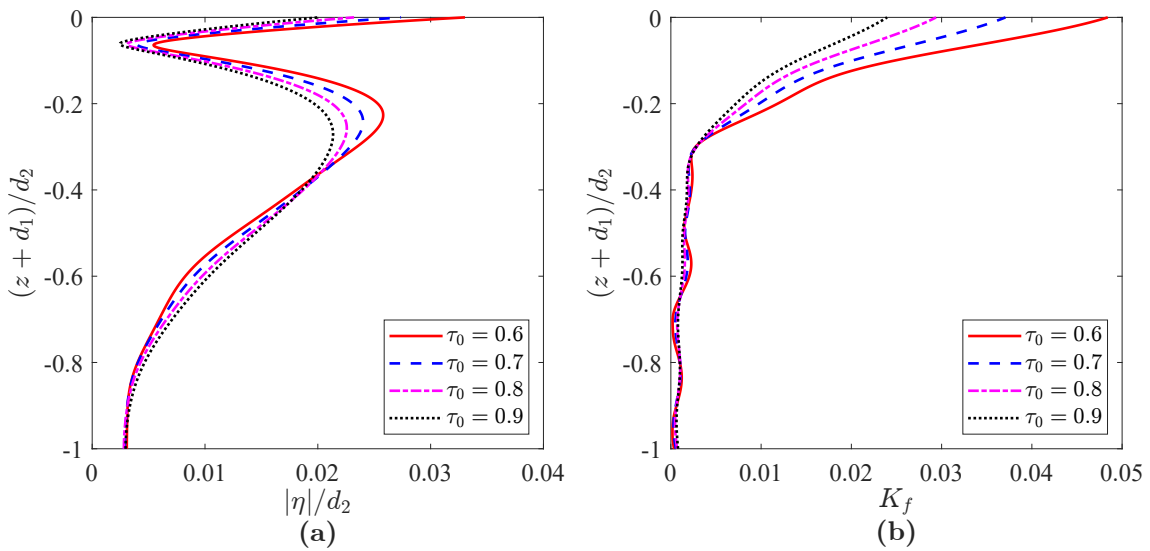


**Fig. 4.8** (a) Nondimensional transverse deflection amplitudes of cage  $|\eta|/d_2$ ; (b) Nondimensional horizontal wave load amplitudes per unit length  $K_f$  along cage height for various net opening ratios  $\tau_0$ , Cases B5 to B8.

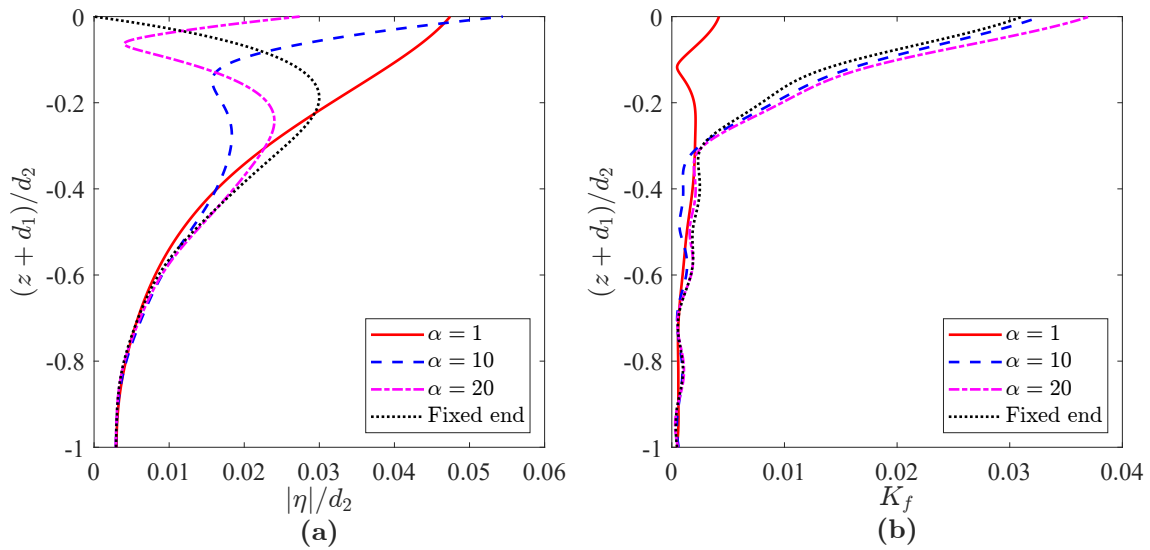


**Fig. 4.9** (a) Nondimensional transverse deflection amplitudes of cage  $|\eta|/d_2$ ; (b) Nondimensional horizontal wave load amplitudes per unit length  $K_f$  along cage height for various dimensionless mooring spring constants  $\alpha$ , Cases C1 to C4.

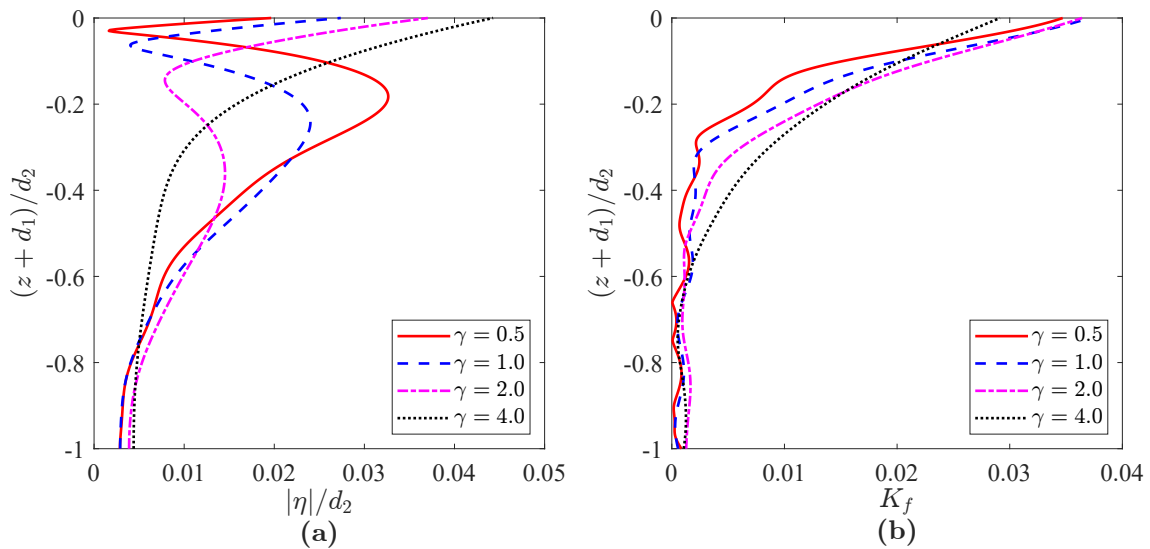


**Fig. 4.10** (a) Nondimensional transverse deflection amplitudes of cage  $|\eta|/d_2$ ; (b) Nondimensional horizontal wave load amplitudes per unit length  $K_f$  along cage height for various dimensionless axial tensile forces  $\gamma$  in the net, Cases D1 to D4.



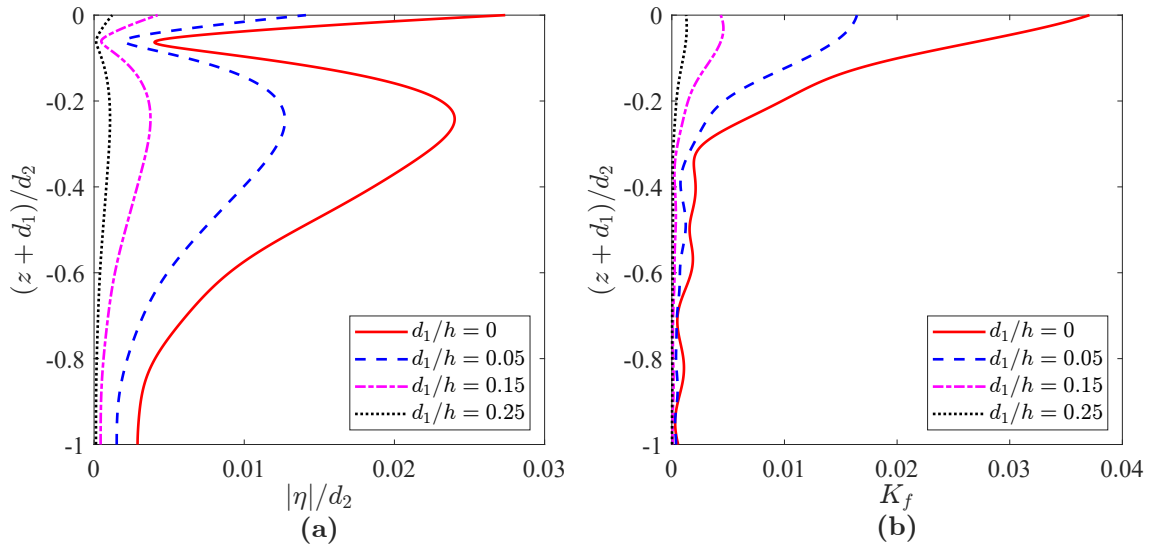


**Fig. 4.11** (a) Nondimensional transverse deflection amplitudes of cage  $|\eta|/d_2$ ; (b) Nondimensional horizontal wave load amplitudes per unit length  $K_f$  along cage height for various relative diving depths  $d_1/h$  of the cage, Cases E1 to E4.

### 4.5.3 Parametric studies

In order to investigate the effects of hydrodynamic and structural parameters on the wave loads, parametric studies are conducted in this section. The nondimensional amplitude of the hydrodynamic force  $K_F$  in the horizontal direction and the nondimensional amplitude of the overturning moment  $K_M$  with respect to the cage top are defined similarly to Mandal and Sahoo (2016):

$$K_F = \frac{|F|}{\rho g a H h} \text{ and } K_M = \frac{|M_o|}{\rho g a H h (d_1 + d_2)}, \quad (4.54)$$

in which the wave force  $F$  and the resulting overturning moment  $M_o$  are found from Eq. (4.49).

In the parametric studies, the following nondimensional hydrodynamic parameters are defined: the wave-effect parameter  $C_w = g/(\omega^2 h)$  defined by Chwang (1983), the incident wave steepness  $H/L$  and the relative water depth  $h/L$ , where  $L$  is the incident wavelength. The parameters related to the cage dimensions include the relative diameter of the cage  $2a/L$ , the relative dividing depths of the cage  $d_1/h$  and the relative height of the cage  $d_2/h$ . Furthermore, the structural parameters have the nondimensional mooring spring constant  $\alpha$ , the nondimensional axial tensile force in the net  $\gamma$ , the nondimensional net mass per unit length  $\beta$  and the net opening ratio  $\tau_0$ .

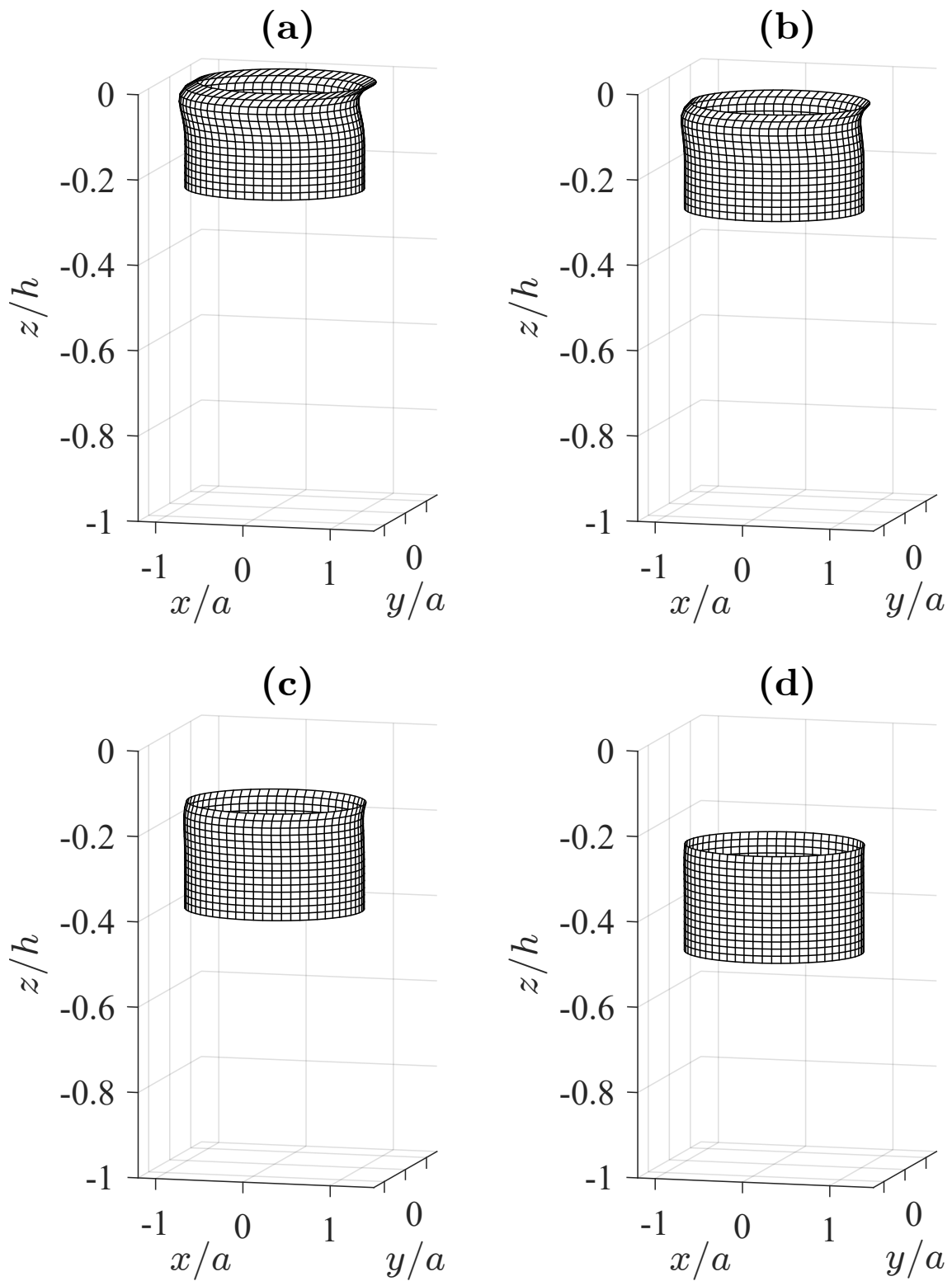


**Fig. 4.12** 3D shapes of a net cage at different submerged depths with the maximum deformation in an exaggerated scale of 5 times: (a)  $d_1/h = 0$ ; (b)  $d_1/h = 0.05$ ; (c)  $d_1/h = 0.15$ ; (d)  $d_1/h = 0.25$ .

### I. Hydrodynamic conditions

The relationship between the wave load on the cage and the wave frequency is given in Fig. 4.13. The curves of  $K_F$  and  $K_M$  versus  $C_w$  show multiple peak points and zero points. This may be because when the wavelength is at a specific value, the phase difference between the scattered waves in the outer region and the inner region near the circular cage is 180 degrees, resulting in wave attenuation. Conversely, if the phase difference is small, the wave action will be strengthened at this frequency. On the other hand, as in Section 4.3, the solution to the wave response is decomposed into an infinite superimposed modes associated with  $\kappa_n a$ , so the response peaks of the multiple modes manifest against varied exited wave frequencies.

As shown in Fig. 4.14, the coefficients  $K_F$  and  $K_M$  are firstly decreased to the minimum values with the relative wave height  $H/L$ , and then they start to increase. In the small-amplitude wave theory, the velocity of the water particle has a linear relationship with the wave height. However, Eq. (4.10) indicates that the real part  $\tau_r$  of the porous-effect parameter  $\tau$  is changed related to the varied incident wave slope  $\varepsilon = \kappa_0 H/2$ . As a result, the wave load acting on the fish cage net does not increase linearly with the wave height.

Referring to Fig. 4.15, when the water depth  $h$  increases from the values of the cage height to twice the wavelength, the values of  $K_F$  and  $K_M$  will decrease in opposition to the increase in the relative water depth  $h/L$ . It is worth noting that the water depth  $h$  is the denominator in the definition of the coefficients  $K_F$  and  $K_M$ , which may also contribute to the decrease in the values.

### II. Cage dimensions

As illustrated in Fig. 4.16, at a constant wavelength, by increasing the diameter of the cage, the curves of the coefficients  $K_F$  and  $K_M$  will experience multiple peak points and zeros points as well, where the hydrodynamic force will vanish when  $2a/L$  is around 0.59 and 1.70. The wave force on the cylindrical cage has a similar variation under various wave frequencies. Therefore, the ratio of the diameter of the circular cage to the wavelength is crucial in engineering design.

If the cage is submerged to a deeper location underwater, the effect of surface waves will be weakened, so the coefficients  $K_F$  and  $K_M$  will be reduced in Fig. 4.17. However, this decreasing trend will slow down as the wave action has been minimal at extremely deep water levels.

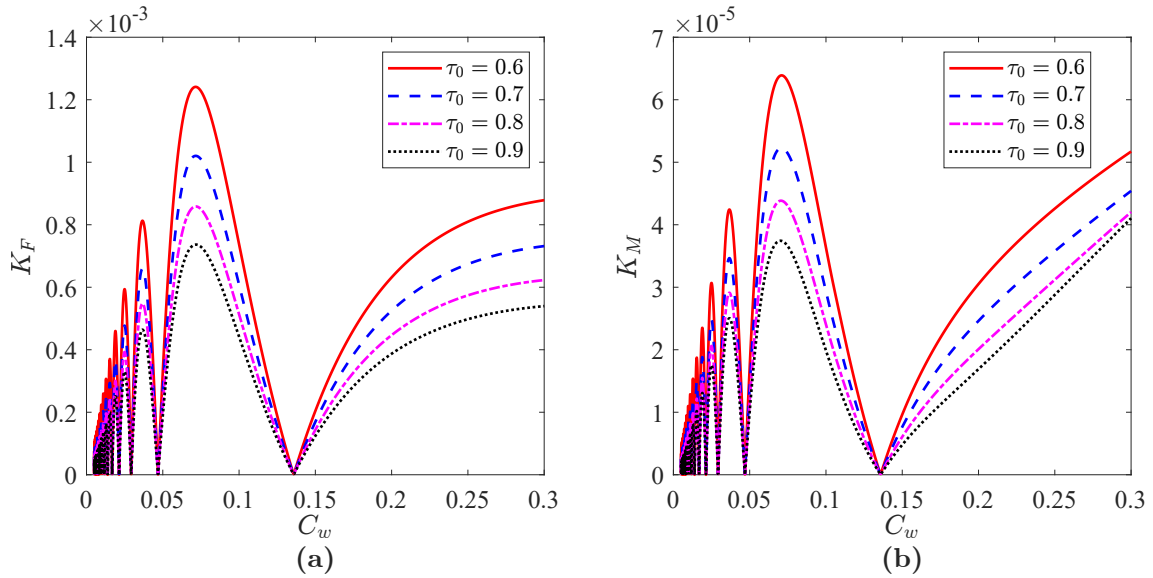


**Fig. 4.13** Effect of wave-effect parameter  $C_w$  on (a) Nondimensional amplitude of horizontal hydrodynamic force  $K_F$ ; (b) Nondimensional amplitude of horizontal overturning moment  $K_M$  for various net opening ratios  $\tau_0$ ,  $H = 7$  m,  $h = 200$  m,  $a = 50$  m,  $d_1 = 0$ ,  $d_2 = 50$  m,  $\alpha = 20$ ,  $\gamma = 1$  and  $\beta = 0.001$ .

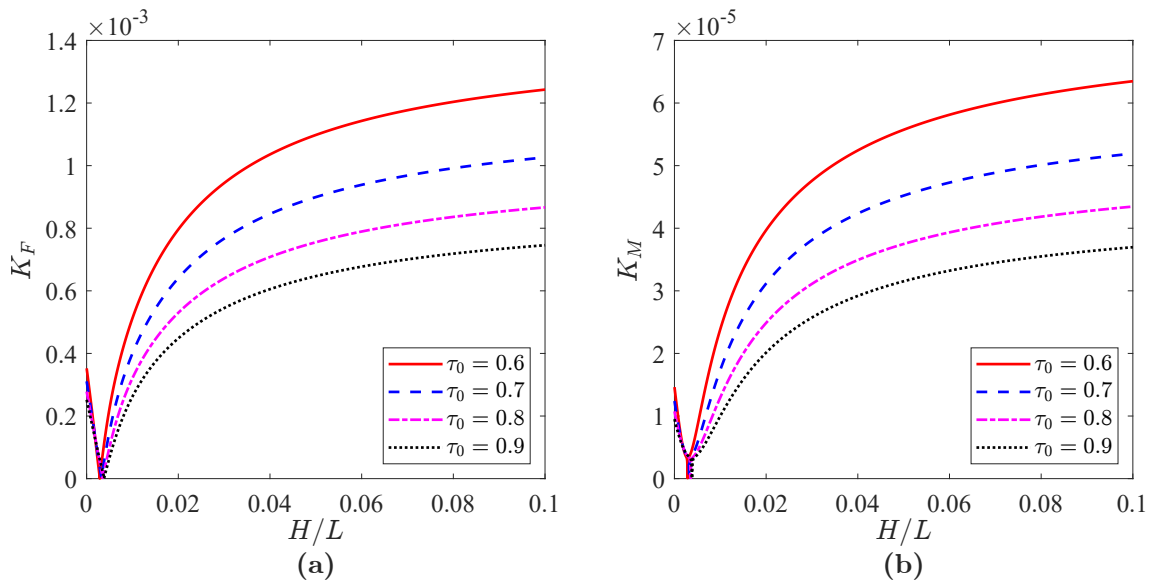


**Fig. 4.14** Effect of wave steepness  $H/L$  on (a) Nondimensional amplitude of horizontal hydrodynamic force  $K_F$ ; (b) Nondimensional amplitude of horizontal overturning moment  $K_M$  for various net opening ratios  $\tau_0$ ,  $T = 8$  s,  $h = 200$  m,  $a = 50$  m,  $d_1 = 0$ ,  $d_2 = 50$  m,  $\alpha = 20$ ,  $\gamma = 1$  and  $\beta = 0.001$ .

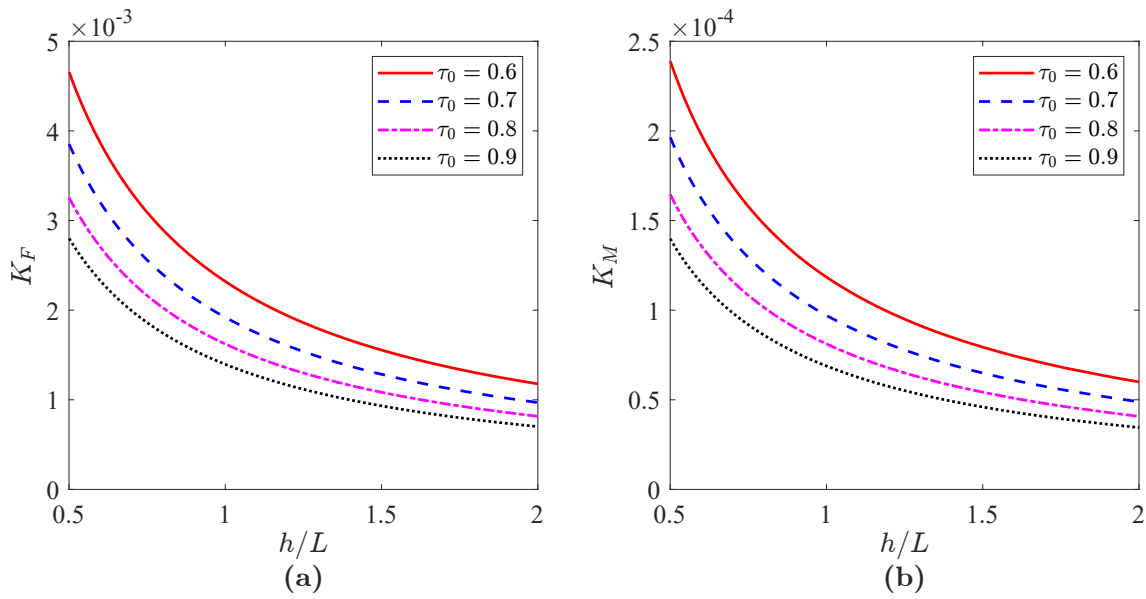


**Fig. 4.15** Effect of relative water depth  $h/L$  on (a) Nondimensional amplitude of horizontal hydrodynamic force  $K_F$ ; (b) Nondimensional amplitude of horizontal overturning moment  $K_M$  for various net opening ratios  $\tau_0$ ,  $T = 8$  s,  $H = 7$  m,  $a = 50$  m,  $d_1 = 0$ ,  $d_2 = 50$  m,  $\alpha = 20$ ,  $\gamma = 1$  and  $\beta = 0.001$ .

The effect of cage height on the wave load is shown in Fig. 4.18. Attentively, as the cage height  $d_2$  increases, the axial tensile force  $Q$  and the mass per unit length  $m_s$  of the net chamber will increase if the defined nondimensional parameters  $\gamma$  and  $\beta$  remain constant. This is unreasonable. Therefore, the relevant structural parameters are assumed to take the following values:  $Q/(m_s g a) = 1$  and  $m_s/(\rho a^2) = 0.001$ . Assuming that the top of the cage is at the mean water level, with the increase of the cage height, the values of  $K_F$  and  $K_M$  will rapidly rush to the peak point, and then begin to decrease. The magnitude of  $K_F$  will remain constant after  $d_2/h = 0.2$ . This is because the imposed wave pressure has been already negligible at the part of the cage close to the deep water level.

### III. Structural parameters

It can be observed from Fig. 4.19 that as the spring stiffness of the mooring rope increases, the wave action coefficients  $K_F$  and  $K_M$  increase to reach peak values, and then gradually decrease. When  $\alpha > 40$ , this trend is also slowed down.

The curves in Fig. 4.20 show that the coefficients  $K_F$  and  $K_M$  are greater with respect to increasing  $\gamma$ . This might be explained by the fact that more momentum of the fluid is dissipated when impacting on stiffer structures. However, the curves of  $K_F$  present a slowdown in the growth trend, but  $K_M$  increases approximately linearly when  $\gamma > 1$ .

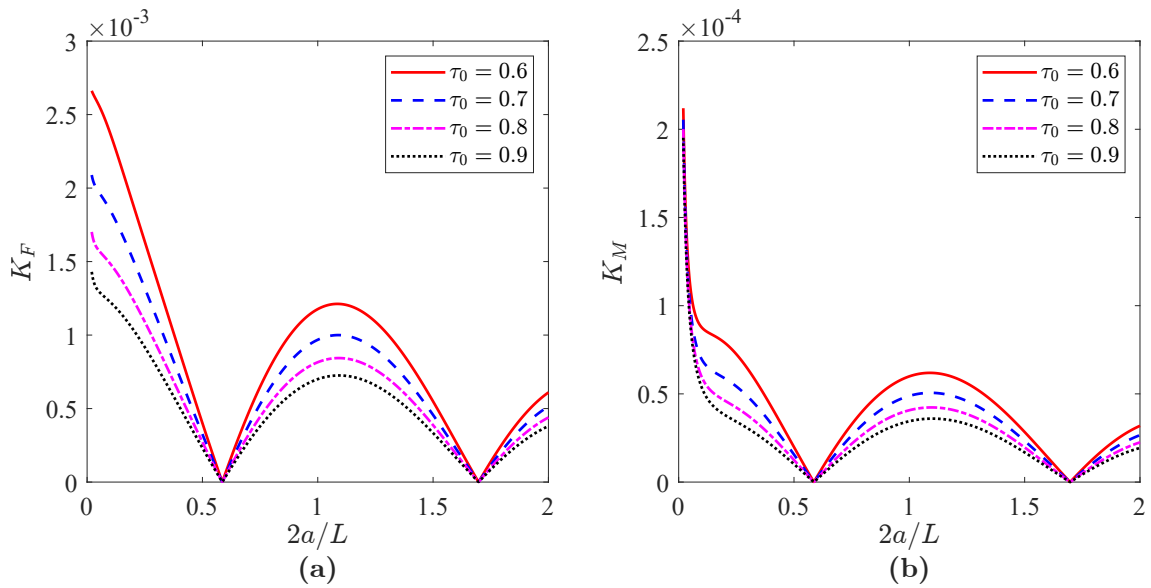


**Fig. 4.16** Effect of relative cage diameter  $2a/L$  on (a) Nondimensional amplitude of horizontal hydrodynamic force  $K_F$ ; (b) Nondimensional amplitude of horizontal overturning moment  $K_M$  for various net opening ratios  $\tau_0$ ,  $T = 8$  s,  $H = 7$  m,  $h = 200$  m,  $d_1 = 0$ ,  $d_2 = 50$  m,  $\alpha = 20$ ,  $\gamma = 1$  and  $\beta = 0.001$ .

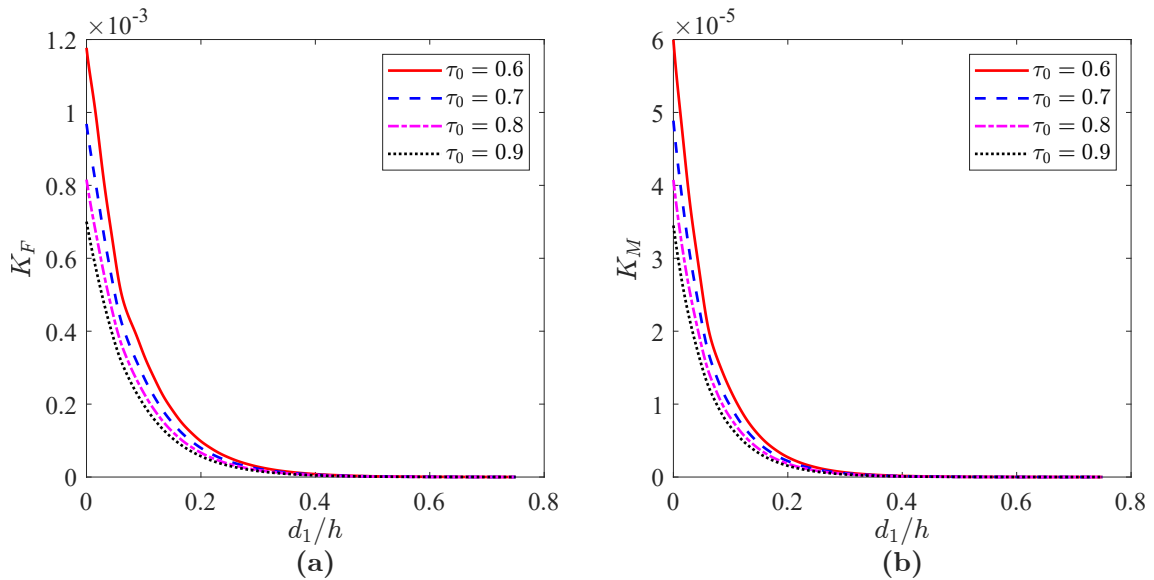


**Fig. 4.17** Effect of relative cage diving depth  $d_1/h$  on (a) Nondimensional amplitude of horizontal hydrodynamic force  $K_F$ ; (b) Nondimensional amplitude of horizontal overturning moment  $K_M$  for various net opening ratios  $\tau_0$ ,  $T = 8$  s,  $H = 7$  m,  $h = 200$  m,  $a = 50$  m,  $d_2 = 50$  m,  $\alpha = 20$ ,  $\gamma = 1$  and  $\beta = 0.001$ .

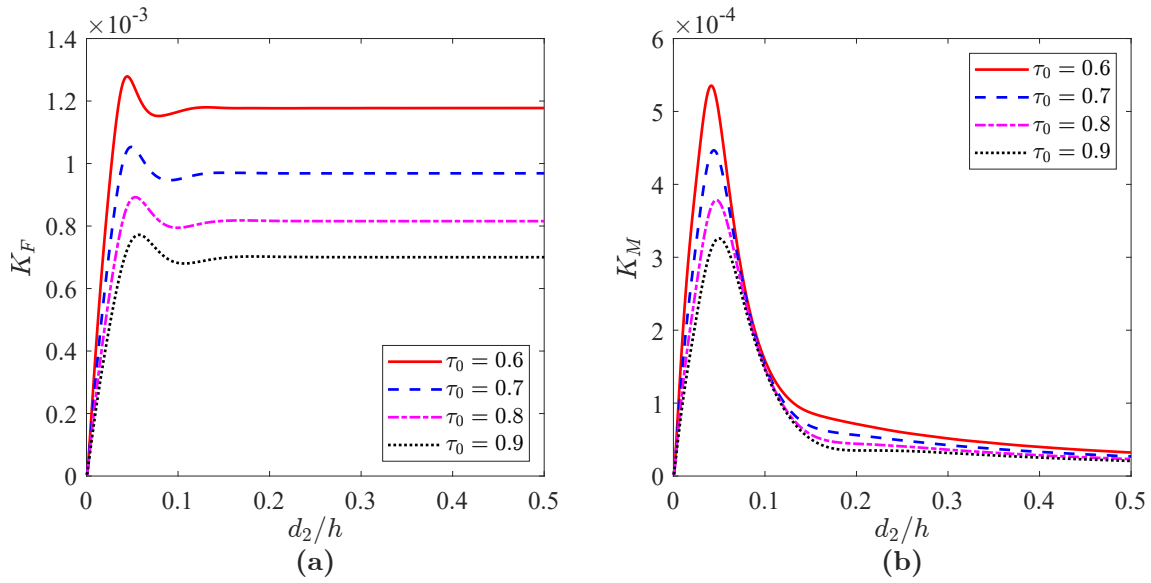


**Fig. 4.18** Effect of relative cage height  $d_2/h$  on (a) Nondimensional amplitude of horizontal hydrodynamic force  $K_F$ ; (b) Nondimensional amplitude of horizontal overturning moment  $K_M$  for various net opening ratios  $\tau_0$ ,  $T = 8$  s,  $H = 7$  m,  $h = 200$  m,  $a = 50$  m,  $d_1 = 0$ ,  $\alpha = 20$ ,  $Q/(m_s g a) = 1$  and  $m_s/(\rho a^2) = 0.001$ .

The mass of the fish cage net is generally determined by different net materials or biomass effects. In Fig. 4.21, in order to ensure a constant mooring stiffness and axial tension in the net, we have taken that  $k_s/(\rho g d_2^2) = 0.02$  and  $Q/(\rho g d_2^3) = 0.001$ . It can be observed that, with increasing  $\beta$  from 0 to 0.01, the wave force coefficient  $K_F$  initially decreases and then increases slowly, but the moment coefficient  $K_M$  decreases slightly first and then increases rapidly.

In Fig. 4.22, under different axial tensions in the net, the coefficients  $K_F$  and  $K_M$  show different varying trends when  $\tau_0 < 0.4$ . However, the increase in the porosity of the fish cage net is conducive for reducing the wave action when the opening ratio is over 0.4. Consequently, it is important that the porosity of the net is kept high, and it is essential to clean the net often to remove the biofouling organisms and hydroids to reduce the wave load on the fish cage. Notably, when the net opening ratio  $\tau_0 = 1$ , i.e., the net does not exist, the predicted wave forces are not zero. According to Ito et al. (2014), theoretically, the porous effect parameter  $\tau$  should go to infinity when the net interface becomes completely permeable, but Eq. (4.10) obviously does not obey this scenario. Therefore, a more suitable formula for the porous effect parameter is required in future studies.

On the other hand, although the assumption in Eq. (4.10) ignores the fluid inertia effect for the flow penetrating through the net interface, its influence still needs to be discussed. An empirical formula of  $\tau_i$  provided by Ito et al. (2014) indicates that most values are in a range of less than 1 for the cube net cage. Here, by assuming that the values of  $\tau_i$  for

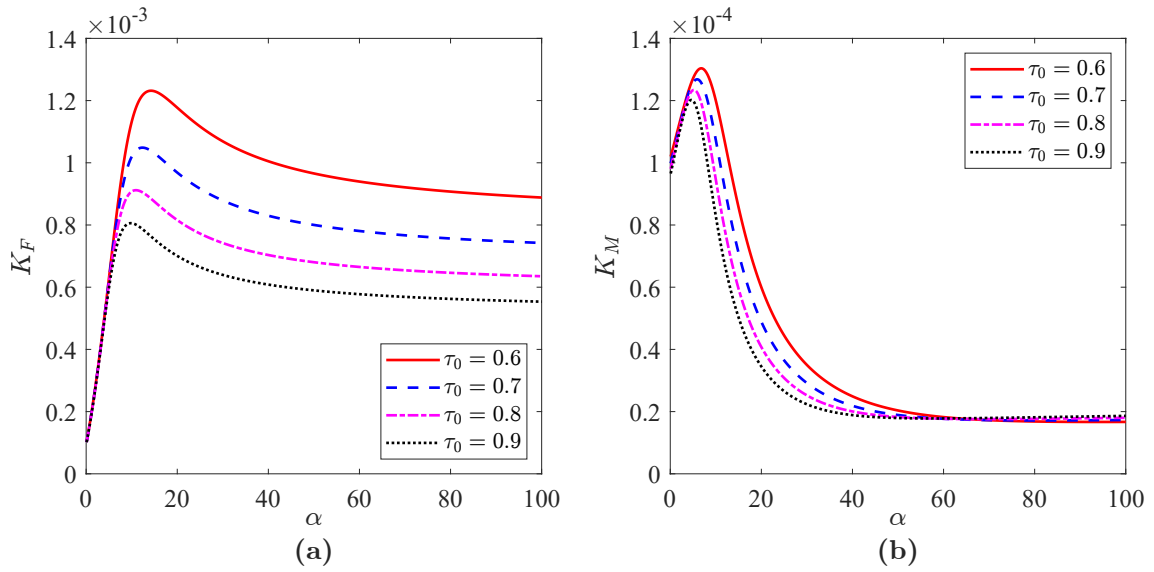


**Fig. 4.19** Effect of nondimensional mooring spring constant  $\alpha$  on (a) Nondimensional amplitude of horizontal hydrodynamic force  $K_F$ ; (b) Nondimensional amplitude of horizontal overturning moment  $K_M$  for various net opening ratios  $\tau_0$ ,  $T = 8$  s,  $H = 7$  m,  $h = 200$  m,  $a = 50$  m,  $d_1 = 0$ ,  $d_2 = 50$  m,  $\gamma = 1$  and  $\beta = 0.001$ .

most cylindrical net cages are less than 1, the variations of  $K_F$  and  $K_M$  with respect to  $\tau_i$  from 0 to 1 are shown in Fig. 4.23. These curves indicate a significant influence of  $\tau_i$  when the values of  $\gamma$  are high. A minor effect of  $\tau_i$  is seen when  $\gamma$  is smaller, especially for the coefficient  $K_M$ . As a result, the porous effect of the fish cage net will exhibit different properties with different axial tensions, and thus the fluid inertia effect parameter  $\tau_i$  still needs further investigation.

## 4.6 Conclusions

A semi-analytical model for wave-cage interaction is established based on the potential flow theory to investigate the hydroelastic behaviour of a cylindrical fish net cage under wave actions. The net cage is modelled as a flexible porous cylinder and its motions are governed by the string vibration equations. By separating variables, the general solution of this physics problem can be expressed by the Fourier-Bessel series. The unknown constants in these series are determined from matching the boundary conditions and the least squares method. Based on this study, the following conclusions may be drawn:

- i. The disturbance caused by the cage to the wave surface is weaker when the opening ratio of the net is greater than 0.3. The wave actions are stronger near the mean water level, as expected. Consequently, a submersible cage is recommended to avoid the high surface-wave energy.



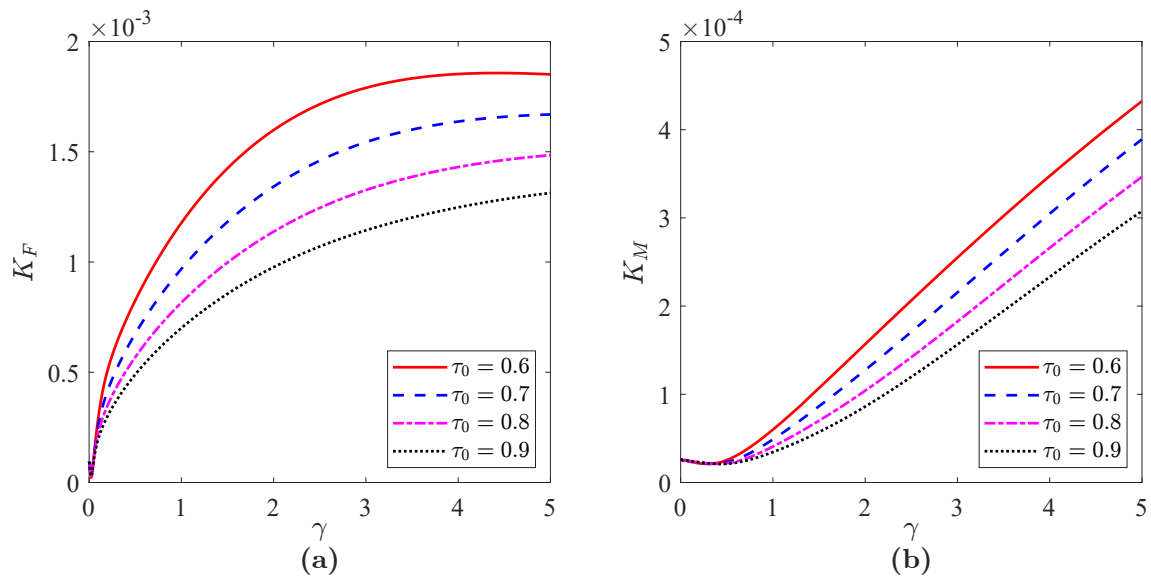


**Fig. 4.20** Effect of nondimensional axial tensile force  $\gamma$  in the net on (a) Nondimensional amplitude of horizontal hydrodynamic force  $K_F$ ; (b) Nondimensional amplitude of horizontal overturning moment  $K_M$  for various net opening ratios  $\tau_0$ ,  $T = 8$  s,  $H = 7$  m,  $h = 200$  m,  $a = 50$  m,  $d_1 = 0$ ,  $d_2 = 50$  m,  $\alpha = 20$  and  $\beta = 0.001$ .

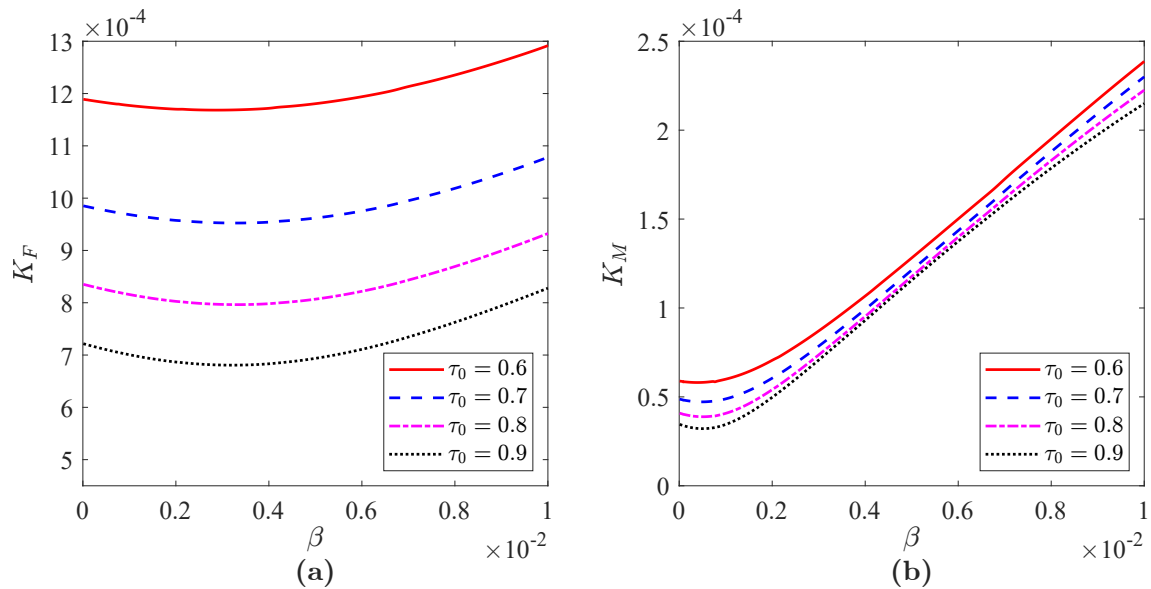


**Fig. 4.21** Effect of nondimensional net mass per unit length  $\beta$  on (a) Nondimensional amplitude of horizontal hydrodynamic force  $K_F$ ; (b) Nondimensional amplitude of horizontal overturning moment  $K_M$  for various net opening ratios  $\tau_0$ ,  $T = 8$  s,  $H = 7$  m,  $h = 200$  m,  $a = 50$  m,  $d_1 = 0$ ,  $d_2 = 50$  m,  $\alpha = 20$  and  $\gamma = 1$ .

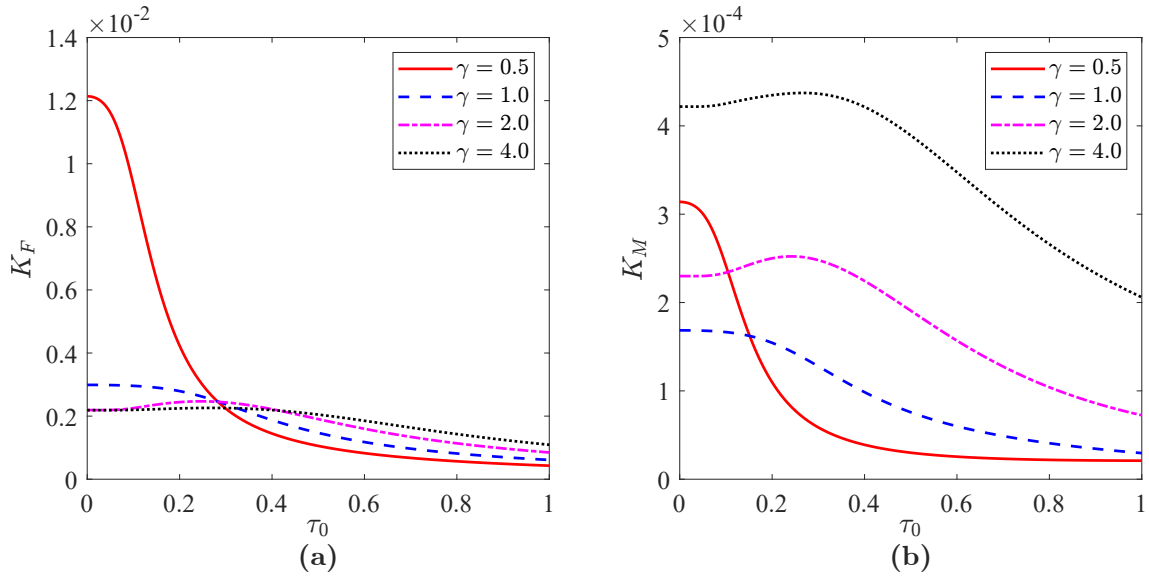


**Fig. 4.22** Effect of net opening ratio  $\tau_0$  on (a) Nondimensional amplitude of horizontal hydrodynamic force  $K_F$ ; (b) Nondimensional amplitude of horizontal overturning moment  $K_M$  for various nondimensional axial tensile forces  $\gamma$  in the net,  $T = 8$  s,  $H = 7$  m,  $h = 200$  m,  $a = 50$  m,  $d_1 = 0$ ,  $d_2 = 50$  m,  $\alpha = 20$  and  $\beta = 0.001$ .

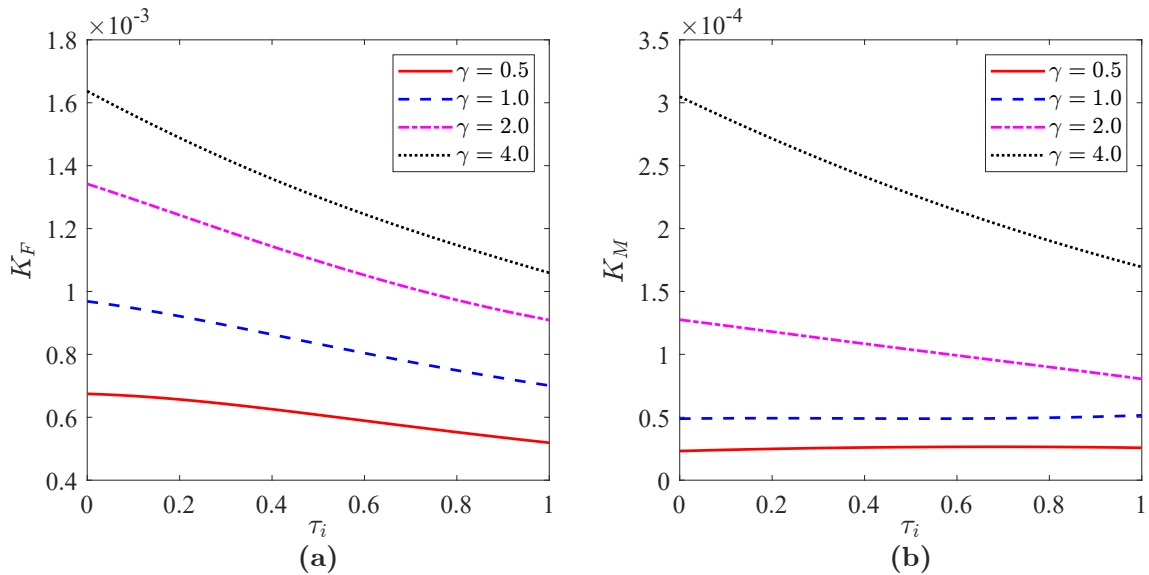


**Fig. 4.23** Effect of fluid inertia effect parameter  $\tau_i$  on (a) Nondimensional amplitude of horizontal hydrodynamic force  $K_F$ ; (b) Nondimensional amplitude of horizontal overturning moment  $K_M$  for various nondimensional axial tensile forces  $\gamma$  in the net,  $T = 8$  s,  $H = 7$  m,  $h = 200$  m,  $a = 50$  m,  $d_1 = 0$ ,  $d_2 = 50$  m,  $\tau_0 = 0.7$ ,  $\alpha = 20$  and  $\beta = 0.001$ .

- ii. Under different mooring stiffness and axial tension in the net, the deflection amplitude of the cage presents different distribution characteristics.
- iii. The net chamber will be subjected to critical wave responses at particular frequencies, but some specific ratios of the cage diameter to the wavelength might cause the vanishing of the wave force and the overturning moment on the cage.
- iv. Appropriately increasing the porosity and reducing the axial tension of the net chamber are beneficial in reducing the wave load.
- v. The porous effect of the fish cage net is significantly impacted by the axial tension in the cage.

The present study reveals some mechanical characteristics of the interaction between the wave and the net cage and provides a reference for the design and application of fish cage systems. However, the theories and formulas used in the present study are all based on linear models, so they cannot solve nonlinear problems in wider scenarios, such as nonlinear waves, quadratic porous flow models, etc., and the structural vibration equation may be oversimplified. Those problems will be considered and resolved in future studies.



# Chapter 5


## Analytical Schemes by Practicing the Shell-Membrane Theory


This chapter is originally published as

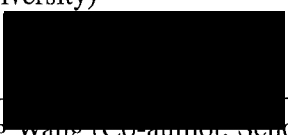
Ma, M., Zhang, H., Jeng, D.-S., and Wang, C.M. (2022). Analytical solutions of hydroelastic interactions between waves and submerged open-net fish cage modeled as a porous cylindrical thin shell. *Physics of Fluids*, 34:017104.

My contribution includes conceptualization, methodology, validation, formal analysis and writing-original draft preparation.

Signed:  Date: 02/02/2023  
Mingyuan Ma

Countersigned:  Date: 02/02/2023  
Prof. Hong Zhang (Principal Supervisor, School of Engineering and Built Environment, Griffith University)

Countersigned:  Date: 2/2/2023  
Prof. Dong-Sheng Jeng (Supervisor, School of Engineering and Built Environment, Griffith University)

Countersigned:  Date: 02/02/2023  
Prof. Chien Ming-wang (Co-author, School of Civil Engineering, University of Queensland)

## **Analytical solutions of hydroelastic interactions between waves and submerged open-net fish cage modelled as a porous cylindrical thin shell**

**Abstract:** In this paper, a new semi-analytical solution is proposed to describe the interactions between ocean waves and a flexible cylindrical net cage that is submerged at different depths below the mean water level. The flexible net is treated as a thin perforated shell, and its deformation is governed by the membrane vibration equation of cylindrical shells. The small-amplitude wave theory is adopted to simulate the wavefield, while the flow passing through the cage is described by the porous medium theory. The numerical results exhibit significant wave responses of the net cage, including the distribution properties of wave surfaces, dynamic pressure drops on the net interface and net structure displacements. Furthermore, the influences of several important design parameters on the hydrodynamic action imposed on the net cage are revealed by parametric studies. The present studies conclude that the significant wave impact is mainly concentrated on the free water surface, and increasing the porosity and flexibility of the net can alleviate the wave scattering and the hydrodynamic actions. In addition, at specific wave frequencies, the horizontal wave force acting on the cage will vanish. These findings should be useful to engineers who are designing offshore fish cage systems.

**Keywords:** Offshore fish net cage; Hydroelastic interaction; Small-amplitude wave theory; Membrane theory of cylindrical shells; Fourier-Bessel series; Porous medium theory.

## **5.1 Introduction**

Fish is one of the major sources of animal protein for mankind. With the ever-rising world's population and a declining wild fish capture due to overfishing, there is a clear demand for farmed fish to supplement wild capture fish. Data given from the State of World Fisheries and Aquaculture (FAO, 2018) show that from 1950 to 2016, the output of aquatic products increased to 170 tons per year with an 850% growth rate, of which marine aquatic products accounted for approximately 69%. In Australia, aquaculture industry has been in a fast-growing phase and provides high-quality, safe and sustainable seafood, with output values reaching 3.3 billion Australian dollars in 2020 (Chen et al., 2021). These developments in marine aquaculture have provided a strong motivation in carrying out research and development of larger fish cage systems. In general, fish farms are located in sheltered nearshore zones where the sea state condition is benign. With prolonged fish farming in these sheltered waters, the environmental system becomes highly stressed due to the accumulation of fish wastes and uneaten fish feed in the farm sites. In order to support sustainable fish farming, fishing industries are planning to move their nearshore farms to offshore sites where there is a larger water depth that helps in dispersing wastes around the fish cages and provides the fish with more space to swim in taller cages (Chu et al., 2020). Nonetheless, moving fish cage systems to offshore sites still face several challenges that include a higher energy environment (with stronger waves, currents and winds) and deeper waters. This would mean that fish cages and mooring systems have to be more robust, larger and durable to withstand the harsher environmental conditions or be submerged to move away from strong surface waves, and be operated remotely or unmanned in order to keep workers from harm's way.

To understand the hydroelastic behaviours related to the design of fish net cage systems, numerical modelling and simulations have been commonly used. The mesh line/bar model (Tsukrov et al., 2003; Zhan et al., 2006) or mass-spring model (Li et al., 2006; Zhao et al., 2008) is often utilised for numerical modelling of fish cage nets, where the hydrodynamic force can be evaluated by the Morison equation (Li et al., 2006; Tsukrov et al., 2003; Zhao et al., 2008) or screen type method (Kristiansen and Faltinsen, 2012). However, the influence of the net structure and its deformation on the flow field cannot be ignored. Therefore, some researchers, exempli gratia, Bi et al. (2014) and Yao et al. (2016), take into consideration the fluid-structure coupling by developing CFD models, but this requires a large amount of computational time. In addition, detailed numerical modelling is inefficient and uneconomical for a large full-scale fish net cage in existing computing power for engineering. Therefore, if a part of the computations can be done analytically, then a semi-analytical method will reduce the computational time significantly.

Theoretically, in hydrodynamic analysis, it is feasible to model the fish cage net as a porous medium allowing for water to flow through the cage. Chwang (1983) proposed a porous wavemaker theory based on the potential flow theory, where the porous flow is governed by Darcy's law, and the solution of velocity potential is written in the form of Fourier-Bessel series for the studies on wave diffraction caused by rigid porous barriers (Lee and Chwang, 2000; Yu and Chwang, 1994). Later, Sankarbabu et al. (2007) and Park et al. (2010) studied the wave interference among an array of rigid porous cylinders, where several local cylindrical coordinates were established for each cylinder, and the total diffraction potential was regarded as the superposition of the diffraction potential generated by each cylinder through Graf's addition theorem. Furthermore, Liang et al. (2021) constructed a hypersingular integral equation to simulate the interaction between water waves and horizontal thin plates. Recently, some optimised numerical methods have also received attention in the field of wave-structure interaction. Ito et al. (2014) developed a hybrid method to calculate the wave force acting on a cube net cage restrained by mooring cables, in which the Fourier-Bessel expansion was utilised for the far-field waves, and the boundary element method (BEM) was applied for the ambient waves. Li et al. (2013b) introduced a scaled boundary finite element model (SBFEM) to investigate the wave-group pile interaction for any number of piles with different cross-sections and spatial layouts. These two numerical methods (BEM and SBFEM) greatly improve the computational efficiency through dimensionality reduction, but high numerical accuracy is guaranteed at the same time.

On the other hand, the structural dynamic issues can be solved by combining the kinematic boundary conditions on the net interface and the vibration equation of continua. Abul-Azm and Williams (1987) investigated the vibrations of flexible impermeable cylinders excited by horizontal wave actions, in which the displacements of these cylinders are governed by the transverse vibration equation of a one-dimensional elastic beam. According to the analytical solution of Behera and Sahoo (2015), if the wave propagates through a horizontal flexible structure, special dispersion relations need to be determined through the kinematic boundary conditions on the solid interface. Then, Zheng et al. (2020a) expanded this topic into the problem of multiple horizontal porous disks in a three-dimensional wave field, where the vertical displacements of these disks are governed by the two-dimensional membrane vibration equation without shear and bending stiffness. However, Kar et al. (2020) considered the shear and bending effects in the flexible structures in the investigation of long-wave Bragg scattering induced by multiple floating horizontal plates above the undulating seabed. Based on the foregoing discussion, some researchers attempted to adopt this approach to analyse the flexible net cage approximately. The 1-D transverse vibration equation of elastic beams or strings are utilised to express



the horizontal deformation of the cylindrical net cage (Mandal et al., 2013; Mandal and Sahoo, 2016; Su et al., 2015). Mandal and Sahoo (2016) considered the horizontal net plate at the bottom of the cage as well, whose deflection is described by the 2-D membrane vibration equation. Lately, Selvan et al. (2021) extended the work of Mandal and Sahoo (2016) to the interference effects of multiple moored net cages in waves. Nevertheless, if the cross-sectional size of the net chamber is too large relative to its vertical dimension, it may represent an over-simplification of the horizontal motion of the cage modelled as the 1-D problem. A net cage typically deforms in the front and behind differently in the wave propagating direction. Moreover, the structural motion is simply expressed by the 1-D or 2-D vibration equation of the continua, where the variations in stress terms due to the elastic deformations are neglected. This assumption is also considered unrealistic.

As a result, it may be more appropriate to approximate the net chamber as a porous thin cylindrical shell rather than a beam or string. Vibration analysis of cylindrical shells is widely discussed in acoustic research. Flügge (1973) has done tremendous work on the theory of stresses in shells, including membrane theories and bending theories of the shell, where the former assumes that the shell cannot provide bending stiffness. Lee et al. (1993) used Donnell's equation to describe the free and forced vibration of the shell and the corresponding solution method in the study of wave propagation on the shell. Chen et al. (2015) discussed the motion equations and boundary value problems of a composite structure assembled by conical shells, cylindrical shells and circular plates. Guo et al. (2017) studied the vibration and acoustic radiation of a finite cylindrical shell submerged underwater based on the potential flow theory and Flügge's shell equations (Flügge, 1973), but the corresponding boundary value problems were not discussed. In addition, the application of membrane theories to the free vibration issue of a cylindrical shell is well summarised and presented by Belubekyan et al. (2017).

Based on the aforementioned literature review, some research gaps are identified. Firstly, the evaluation of hydrodynamic loads based on empirical formulas (Morison equations or screen type methods) cannot reveal the wave scattering effects (diffraction and radiation effects) caused by the flexible net structure. Secondly, in the existing hydroelastic solutions, it is considered to be oversimplified and unreasonable that the vertical net chamber is modelled based on the transverse vibration equation of the 1-D elastic beams of strings, because the real motion of the cage should be a 3-D problem. Lastly, when the fish net cage moves from the nearshore to an offshore site, knowledge about its hydroelastic response is lacking. Therefore, it is urgent to develop a more precise and efficient model to explore the key factors affecting the dynamic responses of fish net cages that are exposed to high-energy environments.

In the present study, a semi-analytical solution is derived based on the linear potential flow theory and the membrane vibration equation of cylindrical shells to ascertain the hydroelastic behaviours of submersible cylindrical open-net fish cages under wave actions. This method will allow the analyst to rapidly determine the particular solution of the net chamber displacements and the wave field. The layout of this paper is as follows: in Section 5.2, the problem at hand is articulated, and the assumptions and theoretical formulation are presented. The specific solution of this physical problem is outlined in Section 5.3. In Section 5.4, the convergence and validation of the proposed semi-analytical solution are presented. Section 5.5 exhibits the numerical results and explains the significant hydroelastic characteristics of the net cages, and a parametric study is presented to understand the relationships between some pertinent design parameters and the wave actions on the cage, which is beneficial to the application of offshore fish farming. Finally, some key conclusions are given in Section 5.6.

## 5.2 Problem definition, assumption and theoretical formulation

A cylindrical net cage is shown in Fig. 5.1, where the  $z$ -axis of a cylindrical coordinate system  $(r, \theta, z)$  is placed at the central axis of the cage. The water depth is denoted by  $h$ , and the mean water level is at  $z = 0$ . The wave propagates in a direction of  $\theta = 0$ , and the free water surface elevation is  $z = \xi$ . The cage is submerged to a depth  $d_1$  below the mean water level, with a radius of  $a$  and a height of  $d_2$ .

The flow field is divided into two zones: Zone 1 ( $r > a, -h \leq z \leq 0$ ) is in the external region outside the net cage, while Zone 2 ( $r \leq a, -h \leq z \leq 0$ ) is in the inner region of the net cage. For the structural region,  $S_{net}$  is the net portion  $-(d_1 + d_2) \leq z \leq -d_1$ , and  $S_{gap}$  is the gap portion  $-d_1 < z \leq 0 \cup -h \leq z < -(d_1 + d_2)$ . Moreover, the upper edge of the net is clamped at  $z = -d_1$ , and its lower end is assumed to be traction-free at  $z = -(d_1 + d_2)$ .

The aim of the present study is to determine the hydroelastic behaviour (free water surface elevation, dynamic pressure, structural displacement, wave load, etc.) of a flexible, submerged and cylindrical fish net cage under wave action.

### 5.2.1 Governing equations

The fluid is assumed to be incompressible and inviscid, and the flow is irrotational. Considering a small-amplitude wave with a circular frequency  $\omega$  and a wave height  $H$ , the

## 5.2 Problem definition, assumption and theoretical formulation

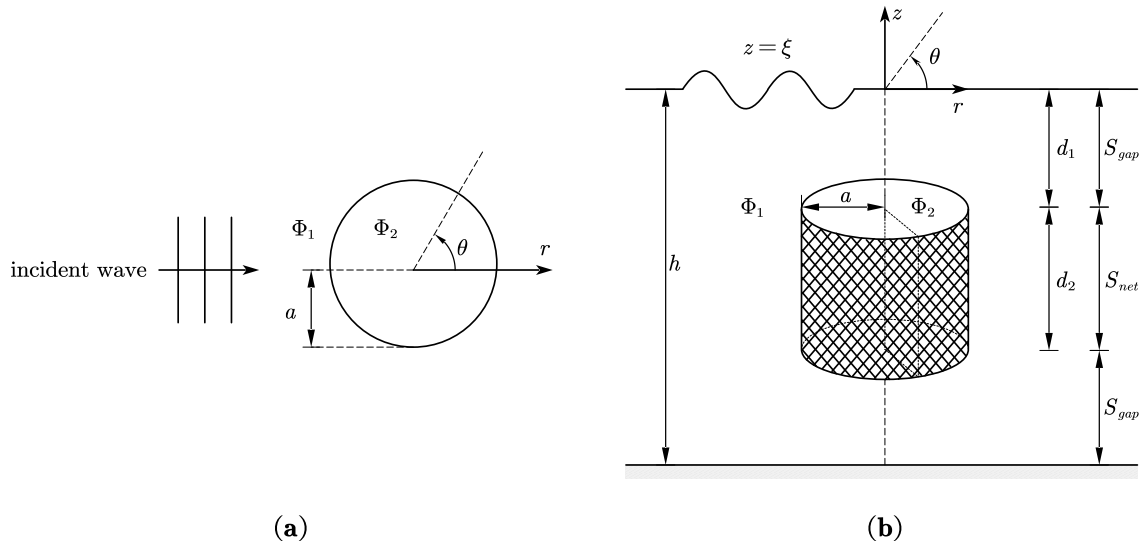


**Fig. 5.1** Submerged cylindrical fish net cage in a constant water depth and under wave action: (a) Plan view; (b) Isometric view.

velocity potential  $\Phi_j(r, \theta, z, t)$  ( $j = 1, 2$  denotes Zones 1 and 2, respectively) of the flow field may be expressed as:

$$\Phi_j = \text{Re} \left[ \varphi_j(r, \theta, z) e^{-i\omega t} \right], \quad (5.1)$$

where  $\varphi_j$  is the complex amplitude of the velocity potential and satisfies the Laplace equation in the cylindrical coordinate system:

$$\frac{\partial^2 \varphi_j}{\partial r^2} + \frac{1}{r} \frac{\partial \varphi_j}{\partial r} + \frac{1}{r^2} \frac{\partial^2 \varphi_j}{\partial \theta^2} + \frac{\partial^2 \varphi_j}{\partial z^2} = 0. \quad (5.2)$$

The complex amplitude of the velocity potential  $\varphi_j$  can be represented as a sum of the incident wave velocity potential  $\varphi^I$  and the scattered wave velocity potential  $\varphi_j^S$  due to diffraction and radiation, i.e.:

$$\varphi_j = \varphi^I + \varphi_j^S. \quad (5.3)$$

On the other hand, the net chamber is equivalent to a perforated cylindrical shell as shown in Fig. 5.2a. According to the Flügge (1973) membrane theory, the equations of motion and constitutive elastic law for the shell element illustrated in Fig. 5.2b are given by

$$\begin{cases} \frac{\partial N_z}{\partial z} + \frac{1}{a} \frac{\partial N_{z\theta}}{\partial \theta} = \rho_s t_s \frac{\partial^2 U}{\partial t^2} \\ \frac{1}{a} \frac{\partial N_\theta}{\partial \theta} + \frac{\partial N_{z\theta}}{\partial z} = \rho_s t_s \frac{\partial^2 V}{\partial t^2} \\ \frac{N_\theta}{a} + \Delta p = -\rho_s t_s \frac{\partial^2 W}{\partial t^2} \end{cases}, \quad (5.4)$$

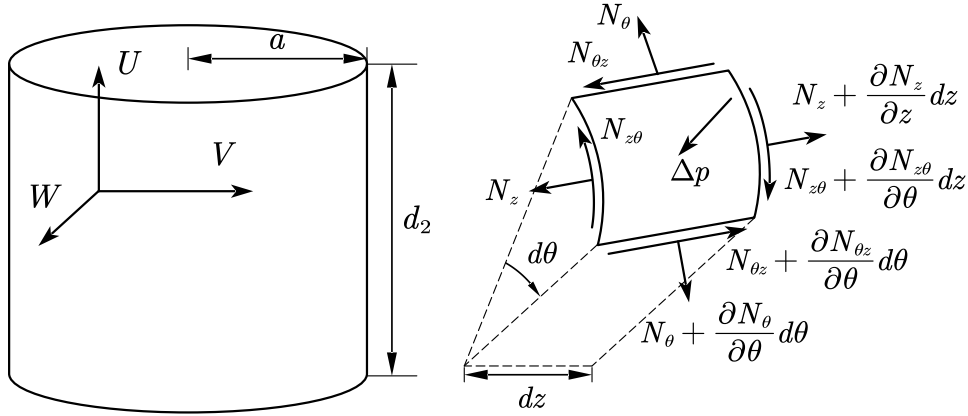


**Fig. 5.2** Sketch of a cylindrical shell: (a) Displacement components; (b) Membrane stress resultants in a shell element.

$$\begin{cases} N_z = C \left( \frac{\partial U}{\partial z} + \frac{\nu}{a} \frac{\partial V}{\partial \theta} + \frac{\nu}{a} W \right) \\ N_\theta = C \left( \frac{1}{a} \frac{\partial V}{\partial \theta} + \frac{W}{a} + \nu \frac{\partial U}{\partial z} \right) \\ N_{z\theta} = \frac{C(1-\nu)}{2} \left( \frac{1}{a} \frac{\partial U}{\partial \theta} + \frac{\partial V}{\partial z} \right) \end{cases} \quad (5.5)$$

$U$  is the axial displacements (positive along the upward direction of  $z$ ),  $V$  is the circumferential displacement (positive in the anti-clockwise direction of increasing  $\theta$ ), and  $W$  is the radial displacement (positive when outward).  $N_z$ ,  $N_\theta$  and  $N_{z\theta}$  are the membrane stress resultants lying in the tangential planes of the shell element, respectively, which means the shell cannot provide a bending stiffness.  $E$  is the elastic modulus of the shell,  $G$  is the shear modulus of the shell,  $\nu$  is the Poisson's ratio of the shell,  $\rho_s$  is the shell bulk density,  $t_s$  is the shell thickness and the coefficient  $C = Et_s(1 - \nu^2)^{-1}$ .  $\Delta p$  is the pressure drop acting normal to the net surface.

Substituting Eq. (5.5) into Eq. (5.4) yields:

$$\begin{cases} \nabla^2 U + \frac{1+\nu}{1-\nu} \frac{\partial}{\partial z} \left( \frac{\partial U}{\partial z} + \frac{1}{a} \frac{\partial V}{\partial \theta} \right) + \frac{2\nu}{(1-\nu)a} \frac{\partial W}{\partial z} = \frac{1}{c_s} \frac{\partial^2 U}{\partial t^2} \\ \nabla^2 V + \frac{1}{a} \frac{1+\nu}{1-\nu} \frac{\partial}{\partial \theta} \left( \frac{\partial U}{\partial z} + \frac{1}{a} \frac{\partial V}{\partial \theta} \right) + \frac{2}{(1-\nu)a^2} \frac{\partial W}{\partial \theta} = \frac{1}{c_s} \frac{\partial^2 V}{\partial t^2} \\ \frac{1}{a} \frac{\partial V}{\partial \theta} + \frac{W}{a} + \nu \frac{\partial U}{\partial z} + \frac{a}{C} \Delta p = -\frac{\rho_s a t_s}{C} \frac{\partial^2 W}{\partial t^2} \end{cases} \quad (5.6)$$

where

$$\nabla^2 = \frac{\partial^2}{\partial z^2} + \frac{1}{a^2} \frac{\partial^2}{\partial \theta^2} \quad \text{and} \quad c_s = \frac{G}{\rho_s} \quad (5.7)$$

### 5.2.2 Boundary conditions

At the free water surface at  $z = \xi$ , the linearised kinematic free surface (KFSBC) boundary condition is

$$\frac{\partial \Phi_j}{\partial z} = \frac{\partial \xi}{\partial t} \quad \text{at } z = 0, \quad (5.8)$$

and dynamic free surface boundary condition (DFSBC) satisfies that

$$\xi = -\frac{1}{g} \frac{\partial \Phi_j}{\partial t} \quad \text{at } z = 0. \quad (5.9)$$

In view of Eqs. (5.8) and (5.9), the boundary condition on the mean water level is given by

$$\frac{\partial \varphi_j}{\partial z} - \frac{\omega^2}{g} \varphi_j = 0 \quad \text{at } z = 0, \quad (5.10)$$

and the slippery boundary condition applied on the seabed is given by

$$\frac{\partial \varphi_j}{\partial z} = 0 \quad \text{at } z = -h. \quad (5.11)$$

When  $r$  approaches infinity, the scattered wave potential  $\varphi_j^S$  satisfies the Sommerfeld (1949) radiation condition:

$$\lim_{r \rightarrow \infty} \sqrt{r} \left( \frac{\partial \varphi_1^S}{\partial r} - i\kappa_0 \varphi_1^S \right) = 0, \quad (5.12)$$

where  $\kappa_0$  is the wavenumber of the incident wave.

For the hydrodynamic analysis of net cages from some scholars, for example, Bi et al. (2014) and Ito et al. (2014), the net can be treated as a porous medium as shown in Fig. 5.3, so the flow passing through the net surface is governed by the kinematic condition:

$$\frac{\partial \Phi_j}{\partial r} = i\kappa_0 \tau (\Phi_2 - \Phi_1) + \frac{\partial W}{\partial t} \quad \text{at } r = a \text{ and } z \in S_{net}, \quad (5.13)$$

in which  $\tau$  is the porous-effect parameter of the porous medium (Yu and Chwang, 1994):

$$\tau = \tau_r + i\tau_i = \frac{\tau_0}{\kappa_0 t_s} \frac{f_r + if_i}{f_r^2 + f_i^2}, \quad (5.14)$$

where  $\tau_0$ ,  $f_r$  and  $f_i$  are the net porosity (the percentage of void space in the net), linearised porous resistance coefficient and fluid inertia coefficient, respectively. The real part  $\tau_r$  represents the porous resistance effect, and the imaginary part  $\tau_i$  means the fluid inertia effect. Mandal and Sahoo (2016) indicated that the coefficients  $f_r$  and  $f_i$  depend on fluid

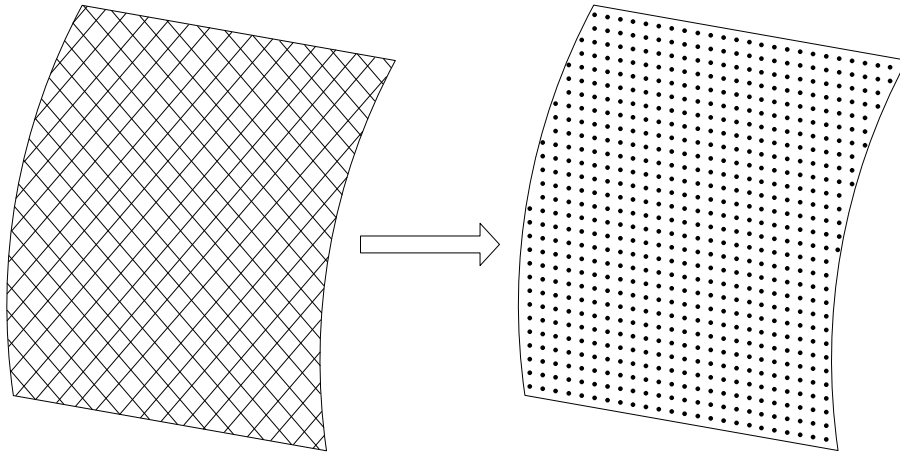


**Fig. 5.3** The fish cage net is modelled as a porous membrane.

viscosity, medium porosity, geometric shape and surface properties of the porous medium, which need to be calibrated by experimental data. From Eq. (5.14), it can be found that  $\tau$  is related to the wave frequency and water depth. Ito et al. (2014) also revealed that  $\tau$  can be influenced by the wave height. Moreover, the diameter of the net twine determines the net opening ratio. Consequently,  $\tau$  is a parameter dependent on Keulegan–Carpenter number ( $K_C$ ). According to Hamelin et al. (2013), when the  $K_C$  number is higher, the amplitude of the wave-induced drag effect is gradually close to the values of steady flow. The experimental investigations of Zhao et al. (2008) illustrated that the  $K_C$  number of the net structure ranges from 150 to 350, and the fluid inertia force is far smaller than the wave drag force simultaneously. As a result, this might enable  $\tau_r$  to be predicted by the fluid mechanics at the steady flow. Additionally, if the ratio of the permeability coefficient in the macroscopic porous medium model to that obtained in the micro-fluid simulation is within a certain range, there will be a reasonable consistency between the two models (Tang et al., 2020). Notably, in the studies of the cube net cage, Ito et al. (2014) found that the added mass effect caused by net acceleration is very important, especially when the overall size of the cage is large relative to the incident wavelength. The added mass will trigger an additional flow inertia effect. The continuity of normal velocity and pressure at the interface between Zones 1 and 2 requires

$$\frac{\partial \varphi_1}{\partial r} = \frac{\partial \varphi_2}{\partial r} \quad \text{at } r = a \text{ and } -h < z < 0, \quad (5.15)$$

$$\varphi_1 = \varphi_2 \quad \text{at } r = a \text{ and } z \in S_{gap}. \quad (5.16)$$

Moreover, according to Belubekyan et al. (2017), for the edge value problems of the net chamber, a traction-free condition on the bottom end yields

$$N_z = 0 \text{ and } N_{z\theta} = 0 \quad \text{at } z = -(d_1 + d_2), \quad (5.17)$$

and if the top end is clamped, it satisfies that

$$U = 0 \text{ and } V = 0 \quad \text{at } z = -d_1. \quad (5.18)$$

It can be found that the radial displacement  $W = 0$  cannot be satisfied for the clamped constraint condition. The specific reason will be discussed later.

## 5.3 Derivation of the solutions

### 5.3.1 Fluid domain

Subjected to the governing equation Eq. (5.2) and the boundary conditions of Eqs. (5.10) to (5.12),  $\varphi_1(r, \theta, z)$  may be expressed in the suitable form:

$$\varphi_1 = \varphi^I + \varphi_1^S, \quad (5.19)$$

where

$$\varphi^I = \sum_{m=-\infty}^{+\infty} -\frac{igH \cosh[\kappa_0(z+h)]}{2\omega \cosh(\kappa_0 h)} i^m J_m(\kappa_0 r) e^{im\theta}, \quad (5.20)$$

$$\varphi_1^S = \sum_{m=-\infty}^{+\infty} \sum_{n=1}^{+\infty} A_{mn} \frac{K_m(\kappa_n r)}{K_m'(\kappa_n a)} \frac{\cos[\kappa_n(z+h)]}{\cos(\kappa_n h)} e^{im\theta}. \quad (5.21)$$

Similarly, for Zone 2, the velocity potential satisfies the governing equation Eq. (5.2) and the boundary conditions of Eqs. (5.10) and (5.11). Therefore, the general solution of  $\varphi_2(r, \theta, z)$  is

$$\varphi_2 = \varphi^I + \varphi_2^S, \quad (5.22)$$

where

$$\varphi_2^S = \sum_{m=-\infty}^{+\infty} \sum_{n=1}^{+\infty} B_{mn} \frac{I_m(\kappa_n r)}{I_m'(\kappa_n a)} \frac{\cos[\kappa_n(z+h)]}{\cos(\kappa_n h)} e^{im\theta}, \quad (5.23)$$

and  $\kappa_n$ s is the positive real roots of the following dispersion relations:

$$\begin{cases} \omega^2 = g\kappa_n \tanh(\kappa_n h), & n = 0 \\ \kappa_n = -i\kappa_0, & n = 1 \\ \omega^2 = -g\kappa_n \tan(\kappa_n h), & n > 1 \end{cases} . \quad (5.24)$$

$A_{mn}$  and  $B_{mn}$  are the unknown constants,  $J_m$  is the first kind of Bessel functions of the  $m$ th orders,  $I_m$  is the first kind of modified Bessel functions of the  $m$ th orders, and  $K_m$  is the second kind of modified Bessel functions of the  $m$ th orders.

In view of the velocity continuity, by substituting Eqs. (5.19) to (5.23) into the boundary condition Eq. (5.15), a relationship is obtained by the orthogonality of  $[\cos \kappa_n(z+h)]$  over  $-h \leq z \leq 0$  and  $e^{im\theta}$  over  $0 \leq \theta \leq 2\pi$ :

$$A_{mn} = B_{mn}. \quad (5.25)$$

According to the linearised Bernoulli's equation, the dynamic pressure  $p$  is given by:

$$p_j = \text{Re} \left[ -\rho \frac{\partial(\varphi_j e^{-i\omega t})}{\partial t} \right], \quad (5.26)$$

where  $\rho$  is the water density, and the pressure drop acting on the net surface is defined as

$$\Delta p = p_1 - p_2 = \text{Re} [i\omega\rho(\varphi_1 - \varphi_2) e^{-i\omega t}] \quad \text{at } r = a. \quad (5.27)$$

Therefore, the complex functions of the wave force and the corresponding overturning moment to the top of the cage in the horizontal direction are

$$F = ai\omega\rho \int_{-(d_1+d_2)}^{-d_1} \int_0^{2\pi} (\varphi_1 - \varphi_2) \cos(\pi - \theta) d\theta dz e^{-i\omega t}, \quad (5.28)$$

$$M_o = ai\omega\rho \int_{-(d_1+d_2)}^{-d_1} \int_0^{2\pi} (\varphi_1 - \varphi_2) \cos(\pi - \theta) (z + d_1) d\theta dz e^{-i\omega t}. \quad (5.29)$$

Moreover, because of the linearised dynamic boundary condition Eq. (5.9), the free surface elevations  $\xi$  are given by

$$\xi_j = \text{Re} \left( \frac{i\omega\varphi_j e^{-i\omega t}}{g} \right). \quad (5.30)$$



### 5.3.2 Structural domain

For the structural governing equation Eq. (5.6), the solutions are sought in the form:

$$\begin{aligned} U &= \text{Re} \left[ \sum_{m=-\infty}^{+\infty} U_m(z) e^{im\theta} e^{-i\omega t} \right] \\ V &= \text{Re} \left[ \sum_{m=-\infty}^{+\infty} V_m(z) e^{im\theta} e^{-i\omega t} \right] . \\ W &= \text{Re} \left[ \sum_{m=-\infty}^{+\infty} W_m(z) e^{im\theta} e^{-i\omega t} \right] \end{aligned} \quad (5.31)$$

By substituting Eq. (5.31) and Eq. (5.27) into Eq. (5.6) and using the orthogonal operation, the following equations are obtained:

$$\begin{bmatrix} L_1 & L_2 & L_3 \\ L_2 & L_4 & L_5 \\ L_3 & L_5 & L_6 \end{bmatrix} \begin{bmatrix} U_m \\ V_m \\ W_m \end{bmatrix} = \begin{bmatrix} 0 \\ 0 \\ f_m^p \end{bmatrix}, \quad (5.32)$$

and the differential operators are as follows:

$$\begin{aligned} L_1 &= \frac{d^2}{dz^2} + \frac{\omega^2}{\epsilon c_s} - \frac{m^2}{\epsilon a^2} \\ L_2 &= \frac{im}{a} \left( 1 - \frac{1}{\epsilon} \right) \frac{d}{dz} \\ L_3 &= \frac{\nu}{a} \frac{d}{dz} \\ L_4 &= \frac{1}{\epsilon} \frac{d^2}{dz^2} + \frac{\omega^2}{\epsilon c_s} - \frac{m^2}{a^2} \\ L_5 &= \frac{im}{a^2} \\ L_6 &= \frac{1}{a^2} - \frac{\rho_{st_s} \omega^2}{C} \end{aligned} \quad (5.33)$$

where,

$$\epsilon = \frac{2}{1-\nu}, \quad f_m^p = -\frac{i\omega\rho}{C} \sum_{n=1}^{+\infty} A_{mn} X_{mn} \frac{\cos[k_n(z+h)]}{\cos(k_n h)} \quad \text{and} \quad X_{mn} = \frac{K_m(k_n r)}{K_m'(k_n a)} - \frac{I_m(k_n r)}{I_m'(k_n a)}. \quad (5.34)$$

By invoking the operators  $L_2$  and  $L_1$  to the first and second equation in Eq. (5.33) respectively,  $U_m$  is eliminated. Thus

$$(L_2L_2 - L_1L_4)V_m = -(L_2L_3 - L_1L_5)W_m. \quad (5.35)$$

By conducting the same manipulation to  $V_m$ , we obtain

$$(L_2L_2 - L_1L_4)U_m = -(L_2L_5 - L_3L_4)W_m. \quad (5.36)$$

Finally, by applying the operator  $(L_2L_2 - L_1L_4)$  to the third equation in Eq. (5.32), we have

$$\begin{aligned} & [-L_3(L_2L_5 - L_3L_4) - L_5(L_2L_3 - L_1L_5) + L_6(L_2L_2 - L_1L_4)]W_m \\ & = (L_2L_2 - L_1L_4)f_m^P. \end{aligned} \quad (5.37)$$

Therefore,  $U_m$ ,  $V_m$  and  $W_m$  can be expressed as

$$U_m(z) = \sum_{b=1}^4 \alpha_{mb} C_{mb} e^{q_{mb}z} + \sum_{n=1}^{+\infty} A_{mn} \gamma_{mn} F_{mn} \frac{\sin[\kappa_n(z+h)]}{\cos(\kappa_n h)}, \quad (5.38)$$

$$V_m(z) = \sum_{b=1}^4 \beta_{mb} C_{mb} e^{q_{mb}z} + \sum_{n=1}^{+\infty} A_{mn} \delta_{mn} F_{mn} \frac{\cos[\kappa_n(z+h)]}{\cos(\kappa_n h)}, \quad (5.39)$$

$$W_m(z) = \sum_{b=1}^4 C_{mb} e^{q_{mb}z} + \sum_{n=1}^{+\infty} A_{mn} F_{mn} \frac{\cos[\kappa_n(z+h)]}{\cos(\kappa_n h)}, \quad (5.40)$$

where  $q_{mb}$  represents the four roots of the characteristic equation of Eq. (5.37),  $C_{mb}$  is the unknown constant determined by the edge conditions Eqs. (5.17) and (5.18), and the second term of Eq. (5.40) is a particular solution of Eq. (5.37). Furthermore, the unknown constants  $\alpha_{mb}$ ,  $\gamma_{mb}$ ,  $\beta_{mb}$  and  $\delta_{mb}$  can be obtained from Eqs. (5.35) and (5.36).

There are four unknown  $C_{mb}$  in Eqs. (5.38) to (5.40), that is, only four edge constraints can be satisfied. Nevertheless, there are five boundary value conditions for the cage, i.e.,  $N_z = 0$  and  $N_{z\theta} = 0$  at the traction free end, and  $U = 0$ ,  $V = 0$  and  $W = 0$  at the fixed end. Therefore, some choices must be made from them. Flügge (1973) gave a justification that there are the internal forces  $N_z$  and  $N_{z\theta}$  at the shell edge to enforce the displacements  $U$  and  $V$ , but there is no internal force in the direction of  $W$  at the shell edge. It therefore seems most reasonable to determine  $U = 0$ ,  $V = 0$  for the fixed end. By substituting Eqs. (5.38) to (5.40) into Eqs. (5.17) and (5.18), respectively, and utilising the orthogonal operation, a group of equations are derived as follows:

for the traction-free end at  $z = -(d_1 + d_2)$ ,

$$\begin{aligned} & \sum_{n=1}^{+\infty} A_{mn} (ak_n \gamma_{mn} F_{mn} + imv \delta_{mn} F_{mn} + v F_{mn}) \frac{\cos[\kappa_n(z+h)]}{\cos(\kappa_n h)} \\ & + \sum_{b=1}^4 C_b^K (a\alpha_{mb} q_{mb} + imv \beta_{mb} + v) e^{q_{mb} z} = 0, \end{aligned} \quad (5.41)$$

$$\begin{aligned} & \sum_{n=1}^{+\infty} A_{mn} (im\gamma_{mn} F_{mn} - ak_n \delta_{mn} F_{mn}) \frac{\sin[\kappa_n(z+h)]}{\cos(\kappa_n h)} \\ & + \sum_{b=1}^4 C_m^b (im\alpha_{mb} + a\beta_{mb} q_{mb}) e^{q_{mb} z} = 0, \end{aligned} \quad (5.42)$$

and for the clamped end at  $z = -d_1$ ,

$$\sum_{n=1}^{+\infty} A_{mn} \gamma_{mn} F_{mn} \frac{\sin[\kappa_n(z+h)]}{\cos(\kappa_n h)} + \sum_{b=1}^4 C_m^b \alpha_{mb} e^{q_{mb} z} = 0, \quad (5.43)$$

$$\sum_{n=1}^{+\infty} A_{mn} \delta_{mn} F_{mn} \frac{\cos[\kappa_n(z+h)]}{\cos(\kappa_n h)} + \sum_{b=1}^4 C_m^b \beta_{mb} e^{q_{mb} z} = 0. \quad (5.44)$$

### 5.3.3 Fluid-structure interaction

For the net region  $z \in S_{net}$ , by substituting Eqs. (5.1), (5.19) to (5.23), (5.31) and (5.40) into Eq. (5.13) as well as noting the orthogonality of  $e^{im\theta}$  on  $0 \leq \theta \leq 2\pi$ , the following equations can be obtained:

$$\begin{aligned} & \sum_{n=1}^{+\infty} A_{mn} (\kappa_n + i\kappa_0 \tau X_{mn} + i\omega F_{mn}) \frac{\cos[\kappa_n(z+h)]}{\cos(\kappa_n h)} + \sum_{b=1}^4 C_{mb} i\omega e^{q_{mb} z} \\ & - \frac{igH\kappa_0 \cosh[\kappa_0(z+h)]}{2\omega \cosh(\kappa_0 h)} {}_1^m J_m'(\kappa_0 a) = 0. \end{aligned} \quad (5.45)$$

For the gap region  $z \in S_{gap}$ , by substituting Eqs. (5.19) to (5.23) into Eq. (5.16) and due to the orthogonal operation, one obtains

$$\sum_{n=1}^{+\infty} A_{mn} X_{mn} \frac{\cos[\kappa_n(z+h)]}{\cos(\kappa_n h)} = 0. \quad (5.46)$$

Therefore, a system of equations can be derived from Eqs. (5.45) and (5.46):

$$S_m(z) = \sum_{n=1}^{+\infty} A_{mn} \zeta_{mn}(z) + \sum_{\kappa=1}^4 C_{m\kappa} \chi_{m\kappa}(z) + \lambda_m(z) = 0, \quad (5.47)$$

where

$$\zeta_{mn}(z) = \begin{cases} (\kappa_n + i\kappa_0 \tau X_{mn} + i\omega F_{mn}) \frac{\cos[\kappa_n(z+h)]}{\cos(\kappa_n h)}, & z \in S_{net} \\ X_{mn} \frac{\cos[\kappa_n(z+h)]}{\cos(\kappa_n h)}, & z \in S_{gap} \end{cases}, \quad (5.48)$$

$$\chi_{m\kappa}(z) = \begin{cases} i\omega e^{q_{m\kappa} z}, & z \in S_{net} \\ 0, & z \in S_{gap} \end{cases}, \quad (5.49)$$

$$\lambda_m(z) = \begin{cases} -\frac{igH\kappa_0}{2\omega} \frac{\cosh[\kappa_0(z+h)]}{\cosh(\kappa_0 h)} i^m J_m'(\kappa_0 a), & z \in S_{net} \\ 0, & z \in S_{gap} \end{cases}. \quad (5.50)$$

In Eq. (5.47), truncating the infinite series after  $N$ th terms yields

$$S_m(z) = \sum_{n=1}^N A_{mn} \zeta_{mn}(z) + \sum_{\kappa=1}^4 C_{m\kappa} \chi_{m\kappa}(z) + \lambda_m(z) = 0. \quad (5.51)$$

For Eq. (5.51), by employing the least squares approximation, there is

$$\int_{-h}^0 |S_m(z)|^2 dz = \min \Rightarrow \int_{-h}^0 S_m^* \frac{\partial S(z)}{\partial A_{mn}} dz = 0. \quad (5.52)$$

Therefore, by substituting Eq. (5.51) into Eq. (5.52), a system of equations is obtained:

$$\begin{bmatrix} P_{m1,1}^1 & \cdots & P_{mn,1}^1 & P_{m1,1}^2 & \cdots & P_{m\kappa,1}^2 \\ \vdots & \ddots & \vdots & \vdots & \ddots & \vdots \\ P_{m1,l}^1 & \cdots & P_{mn,l}^1 & P_{m1,l}^2 & \cdots & P_{m\kappa,l}^2 \\ P_{m1,1}^3 & \cdots & P_{mn,1}^3 & P_{m1,1}^4 & \cdots & P_{m\kappa,1}^4 \\ \vdots & \ddots & \vdots & \vdots & \ddots & \vdots \\ P_{m1,4}^3 & \cdots & P_{mn,4}^3 & P_{m1,4}^4 & \cdots & P_{m\kappa,4}^4 \end{bmatrix} \begin{bmatrix} A_{m1} \\ \vdots \\ A_{mn} \\ C_{m1} \\ \vdots \\ C_{m\kappa} \end{bmatrix}^* = \begin{bmatrix} Q_{m1} \\ \vdots \\ Q_{ml} \\ 0 \\ \vdots \\ 0 \end{bmatrix}, \quad (5.53)$$

where

$$P_{mn,l}^1 = \int_{-h}^0 \zeta_{mn}^* \zeta_{ml} dz, \quad P_{m\kappa,l}^2 = \int_{-h}^0 \chi_{m\kappa}^* \zeta_{ml} dz \quad \text{and} \quad Q_{m,l} = - \int_{-h}^0 \lambda_m^* \zeta_{ml} dz. \quad (5.54)$$

The coefficient matrixes  $\mathbf{P}^3$  and  $\mathbf{P}^4$  are determined from the chosen edge conditions in Eqs. (5.41) to (5.44), and  $m = -M, \dots, -1, 0, 1, \dots, M$ ;  $l = 1, 2, \dots, N$ .

As a result, the unknown constants  $A_{mn}$  and  $C_{mb}$  can be calculated out by solving Eq. (5.53), and the corresponding velocity potentials  $\Phi_j$  and structural displacements  $U$ ,  $V$  and  $W$  are obtained.

## 5.4 Convergence studies and model validation

### 5.4.1 Convergence studies

In order to verify the validity of the proposed analytical solutions, convergence and comparative studies were carried out. In the eigenfunction expansion method, the solution is theoretically correct and valid when the sum of the infinite series converges with respect to increasing the number of series terms. In numerical processes, it is necessary to truncate the terms up to a certain value with acceptable accuracy for the solution. Therefore, a convergence analysis is essential for numerical simulations. Herein, we adopt the following values for the parameters:  $H = 7$  m,  $h = 200$  m,  $a = 50$  m,  $t_s/a = 10^{-4}$ ,  $d_1/h = 0$ ,  $d_2/(2a) = 0.5$ ,  $\nu = 0.3$  and  $\tau = 1+1i$ . The shell bulk density has  $\rho_s/\rho = 1.2$ , and the nondimensional elastic modulus of the shell  $\eta = E/(\rho_s t_s h)$  is taken as  $10^3$ . In addition, a wave-effect parameter  $C_w = g/(\omega^2 h)$  is defined by Chwang (1983).

Concerning the truncated term  $N$  in Eq. (5.28), the wave force  $F$  is only determined by the root numbers of the dispersion relationship Eq. (5.24) due to the orthogonality of  $e^{im\theta}$ . These roots correspond to the non-propagating evanescent mode (Zhu and Mitchell, 2009). Therefore, a control error  $\Delta E_r(N)$  with respect to  $N$  is defined as

$$\Delta E_r(N) = \frac{|F_{N+1} - F_N|}{|F_N|}. \quad (5.55)$$

As shown in Fig. 5.4a, it can be observed that the variations of  $\Delta E_r(N)$  differ for different wave frequencies, and the convergence speed is slower when the wave effect number is larger. It is found that when  $N > 30$ , the maximum control error is less than 0.133% for all cases. Numerically, the term generated by the wavenumber of the dispersion relationship Eq. (5.24) is relatively small and is only associated with local waves near the cylinder (Zhu and Mitchell, 2009).

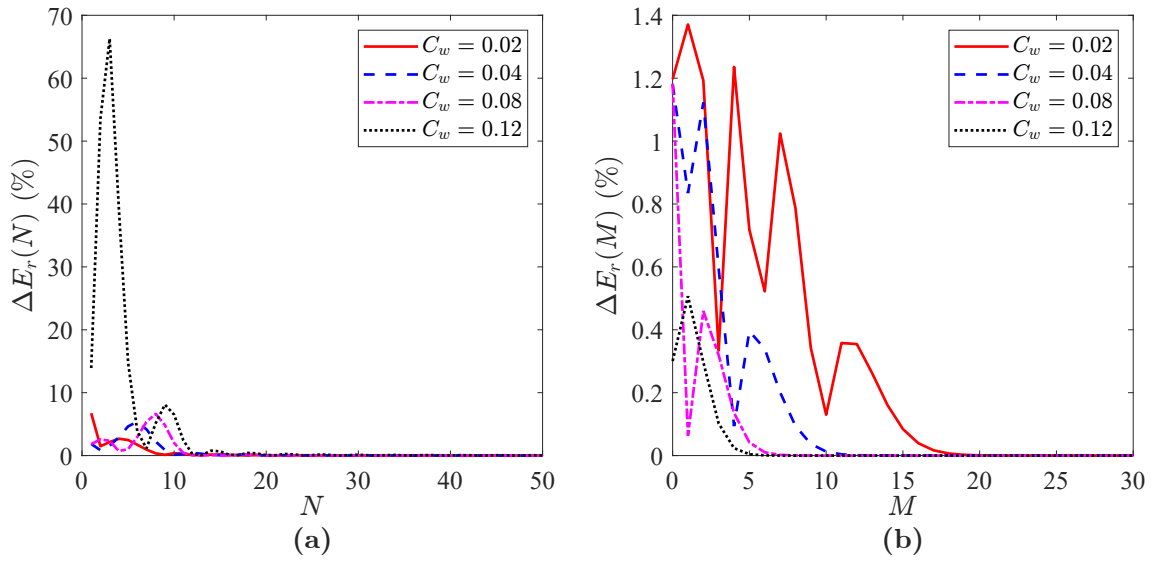


**Fig. 5.4** Convergence analysis for truncated terms of  $N$  and  $M$ : (a) Variations of  $\Delta E_r(N)$  versus  $N$ ; (b) Variations of  $\Delta E_r(M)$  versus  $M$ .

Alternatively, in terms of the local waves near the cylinder, a control error  $\Delta E_r(M)$  versus  $M$  is defined as

$$\Delta E_r(M) = \frac{\left| \sum_{z=-(d_1+d_2)}^{-d_1} \sum_{\theta=0}^{2\pi} (\varphi_1 - \varphi_2)_{M+1} - \sum_{z=-(d_1+d_2)}^{-d_1} \sum_{\theta=0}^{2\pi} (\varphi_1 - \varphi_2)_M \right|}{\left| \sum_{z=-(d_1+d_2)}^{-d_1} \sum_{\theta=0}^{2\pi} (\varphi_1 - \varphi_2)_M \right|}, \quad (5.56)$$

and the values of  $\Delta E_r(M)$  are presented in Fig. 5.4b. However, it can be observed that if the wave effect number is smaller, the convergence speed of the term  $M$  is slower, but when  $M > 20$ , the relative errors are near 0 for the whole cases. As a result, in this study, it is sufficient to take  $N = 31$  and  $M = 20$  to determine the imposed wave action on the net cage.

## 5.4.2 Model validation

The present solutions were compared with the results obtained by Zhu and Mitchell (2009) and Su et al. (2015) for the free water surface elevation around a rigid hollow cylindrical shell. In Fig. 5.5a, the free surface elevation is plotted along  $\theta = 0$  for the case:  $\omega = 1.2$  rad/s,  $H = 2$  m,  $h = 6$  m,  $a = 10$  m,  $d_1/h = 0$  and  $d_2/(2a) = 0.1$ . The other parameters are set as  $\tau = 0$  and  $\eta = 10^8$  to guarantee that the structure is impermeable and extremely rigid. In Fig. 5.5a, when the wave surface propagates from the inside of the cylinder ( $r < a$ ) to the outer region ( $r > a$ ), there is a phase difference at  $r/a = 1$  due to the obstruction of the

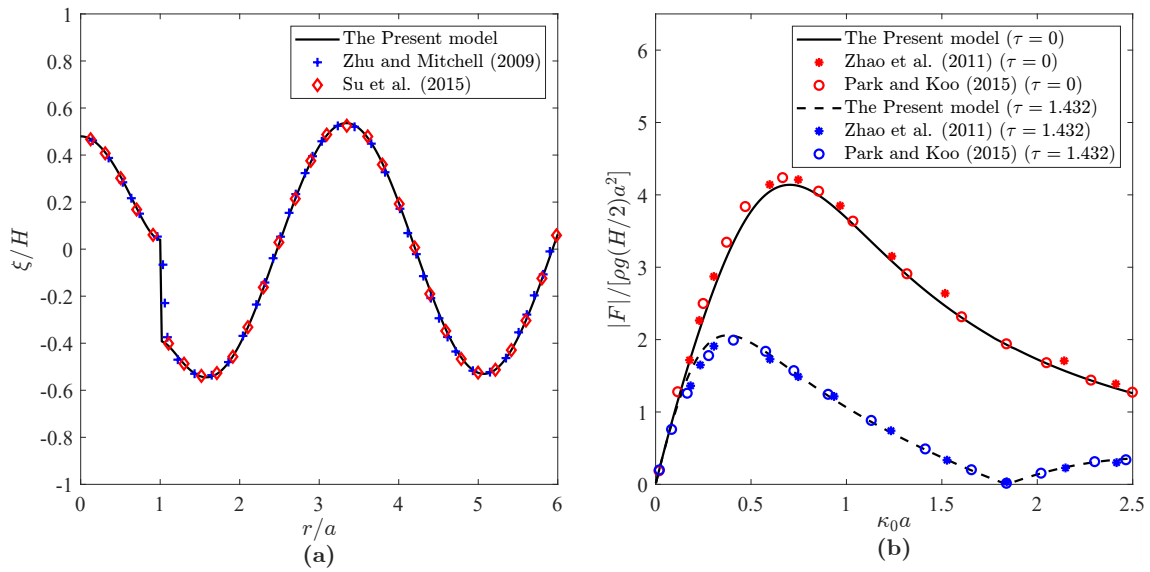


**Fig. 5.5** Model validations: (a) Normalised free water surface elevation variations  $\xi/H$ ; (b) Normalised horizontal wave force  $|F|/[\rho g(H/2)a^2]$ .

circular wall, and there is a minor difference between the results of the present model and aforementioned researchers.

In addition, comparisons about the horizontal wave force on a rigid floating porous cage with the results of Zhao et al. (2011) and Park and Koo (2015) are illustrated in Fig 5.5b. The parameters adopted that  $a = 0.15$  m,  $d_1 = 0$ ,  $d_2 = 0.3$  m and  $h = 5$  m. The modulus of the horizontal wave force  $|F|$  is normalised by  $\rho g(H/2)a^2$ , and its tendency with the nondimensional wave number  $\kappa_0 a$  is consistent with the data from the abovementioned researchers. A minor discrepancy observed is because Zhao et al. (2011) and Park and Koo (2015) introduced a thin and impermeable horizontal plate at the bottom of the cage.

## 5.5 Results and discussions

This section will identify some critical hydroelastic characteristics of net cages from the simulated results of the current model. The discussions focus on the variation of wave surface profile, the distribution of wave load and the corresponding structural deformation. In this analysis, four case groups were designed with various wave effect parameters  $C_w$  (Cases A), net porous effect parameters  $\tau$  (Cases B), nondimensional net elastic modulus  $\eta$  (Cases C) and relative cage diving depths  $d_1/h$  (Cases D). The detailed parameter settings are shown in Table 5.1. A sample metocean data presented by El-Reedy (2019) shows that the maximum wave height is 7.2 m associated with the wave period 8 s for an annual recurrence interval of 100 years for a particular offshore platform location, and the water

**Table 5.1** Case groups with different studied parameters (Study II).

Cases	$C_w$	$\tau$	$\eta/10^3$	$d_1/h$
A1	0.04	1+1i	1	0
A2	0.06	1+1i	1	0
A3	0.08	1+1i	1	0
A4	0.12	1+1i	1	0
B1	0.08	1+1i	1	0
B2	0.08	2+2i	1	0
B3	0.08	3+3i	1	0
B4	0.08	4+4i	1	0
C1	0.08	1+1i	0.5	0
C2	0.08	1+1i	1	0
C3	0.08	1+1i	2	0
C4	0.08	1+1i	4	0
D1	0.08	1+1i	1	0
D2	0.08	1+1i	1	0.05
D3	0.08	1+1i	1	0.10
D4	0.08	1+1i	1	0.15

depth should be over 50 m or three times the cage height for the offshore fish cage (Chu et al., 2020). As a result, we have taken  $H = 7$  m and  $h = 200$  m as the offshore condition here. Furthermore, the adopted cage dimensions and structural parameters are taken from the cases deployed in practice, that is,  $a = 50$  m,  $t_s/a = 10^{-4}$ ,  $d_2/(2a) = 0.5$  and  $\rho_s/\rho = 1.2$ . Here, to facilitate the description of the results, a cartesian coordinate ( $x = r \cos \theta$  and  $y = r \sin \theta$ ) is also used, i.e., the wave propagates in the positive direction of the  $x$ -axis, and the central axis of the cage is still located at the  $z$ -axis of the coordinate.

### 5.5.1 Wave surface profiles

The contour maps of the free surface elevations around the cage during a wave period  $T$  are presented in Fig. 5.6. The non-dimensional free surface elevation  $\xi/H$  is plotted in a range of  $x/a = \pm 4$  and  $y/a = \pm 4$  using Eq. (5.30), and the area inside the black circle is the Zone 2 ( $r/a < 1$ ). It can be observed that the presence of the cage causes perturbations to the wave surface. Fig. 5.7 shows the free surface elevations with time series of some positions in Zones 1 and 2. Owing to the blocking effects and motions of the porous net, the waves passing through the net interface will be affected by a certain lag in propagation



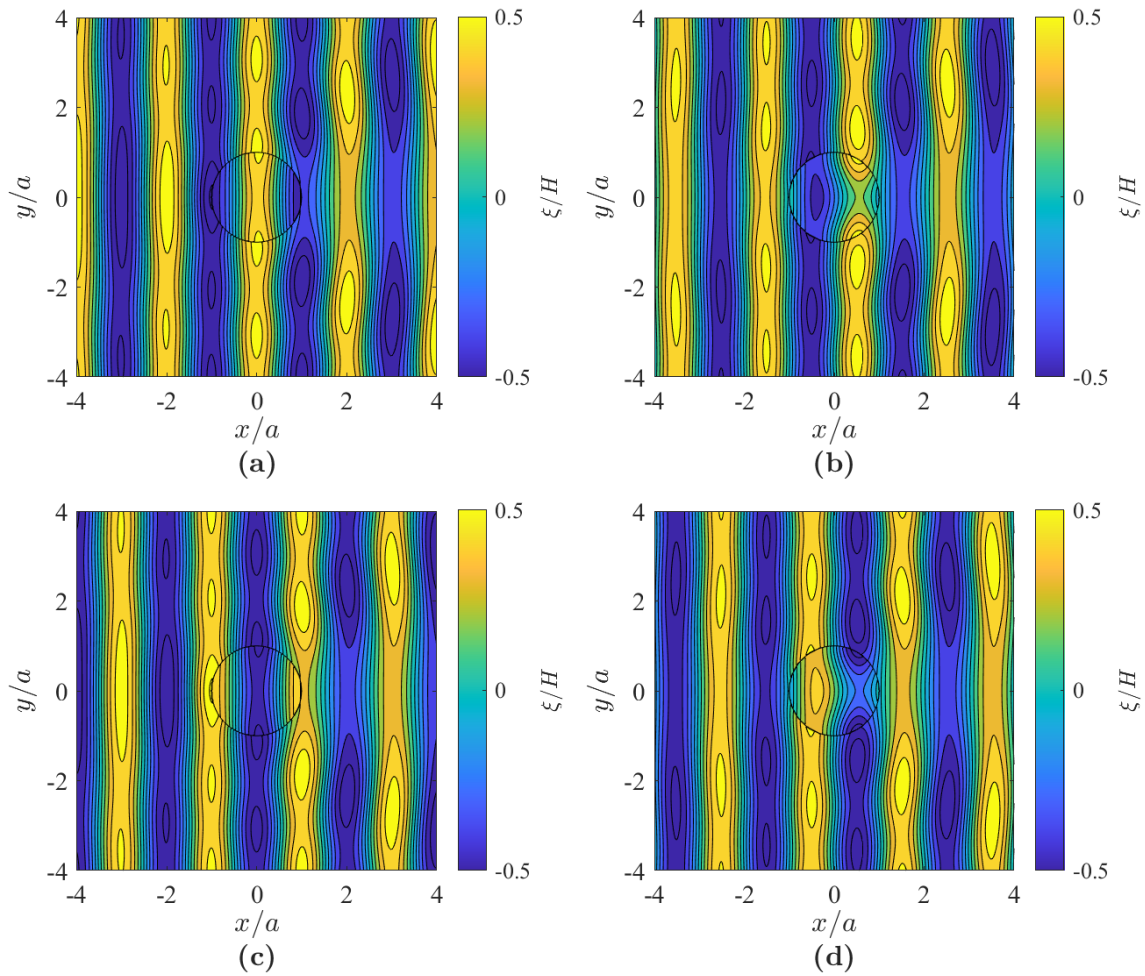


**Fig. 5.6** Variations of free water surface elevations  $\xi$  around a cylindrical net cage over time: (a)  $t/T = 0$ ; (b)  $t/T = 1/4$ ; (c)  $t/T = 1/2$ ; (d)  $t/T = 3/4$ , Case A3.

as compared to the waves outside the cage, and the amplitude of the transmitted wave passing through the cage also has a significant attenuation.

On the other hand, the amplitude of the wavefield is contoured in Figs. 5.8 to 5.10. Due to the superposition of the incident waves and scattered wave, the wave amplitude is distributed in the form of an arc-shaped band. There are some leaf-like areas where the water surface oscillations are enhanced or weakened significantly in front of the windward side of the cage. Inside the cage and near its leeward side, the wave energy is dissipated to the greatest extent, and a long "wake area" is generated behind the cage, in which the wave amplitude is severely attenuated. Under different wave frequencies (referring to Fig. 5.8), these arc-shaped bands are widened as  $C_w$  increases, and the distribution of those leaf-like areas is also different. However, if the porosity increases (seen in Fig. 5.9) and the stiffness decreases (seen in Fig. 5.10) for the net cage, its disturbance to the wave field will be weakened.

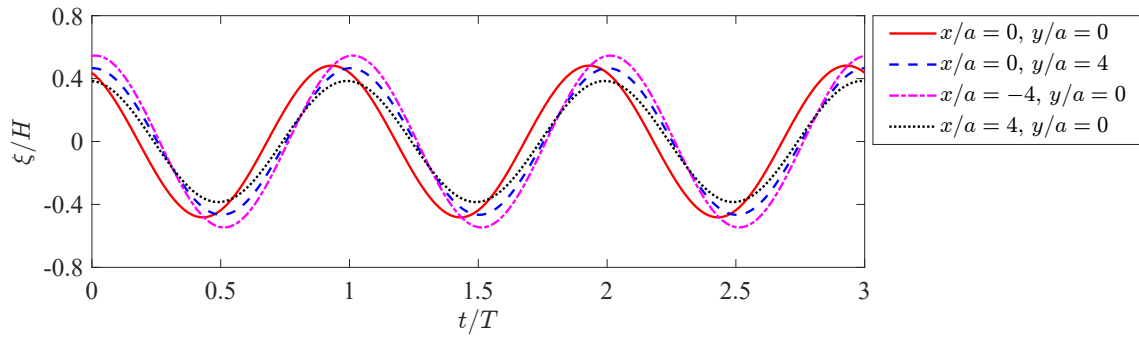


**Fig. 5.7** Variations of normalized free water surface elevations  $\xi/H$  with time series for different positions in zones 1 and 2, Case A3.

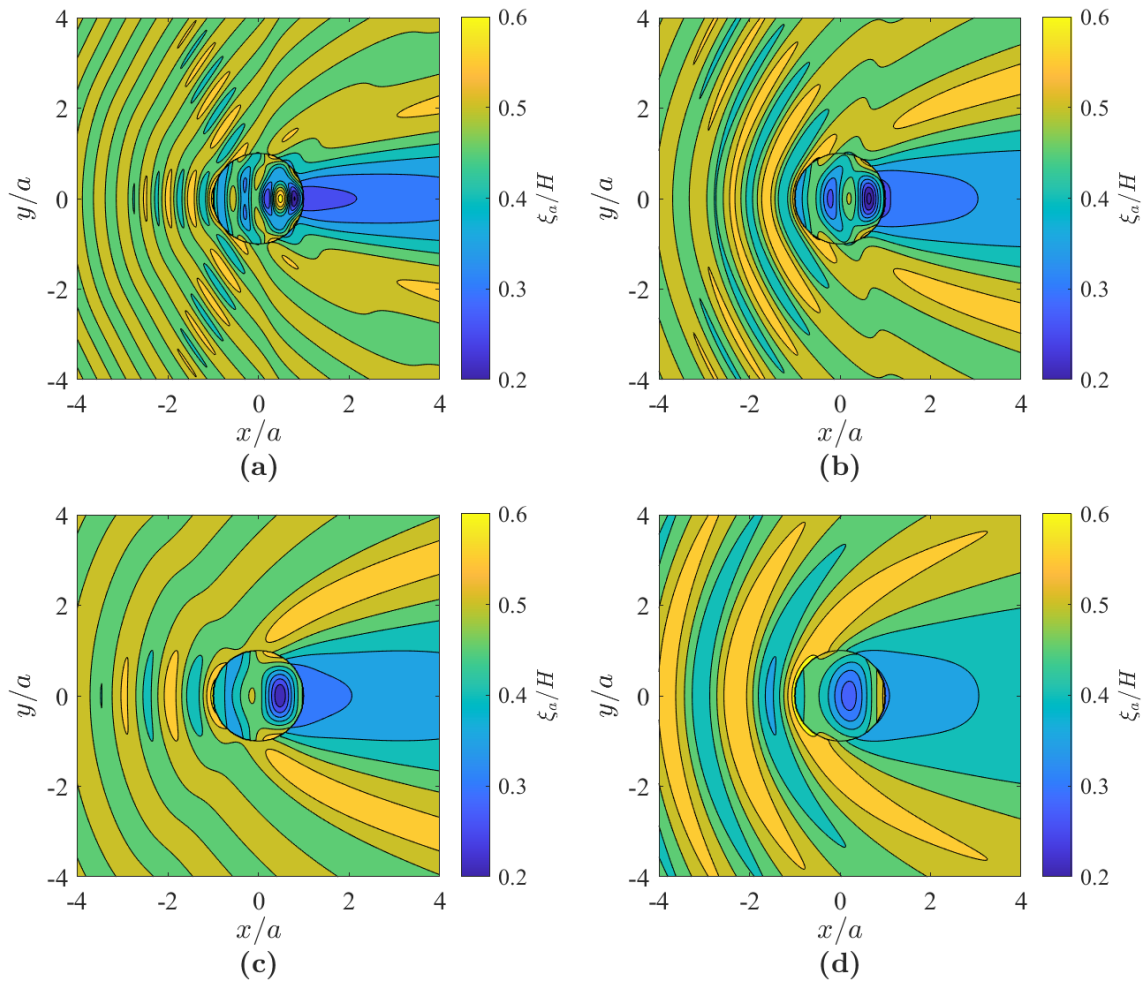


**Fig. 5.8** Amplitudes of free surface elevations  $\xi_a$  around a cylindrical net cage with various wave-effect parameters  $C_w$ : (a)  $C_w = 0.04$ ; (b)  $C_w = 0.06$ ; (c)  $C_w = 0.08$ ; (d)  $C_w = 0.12$ , Cases A1–A4.

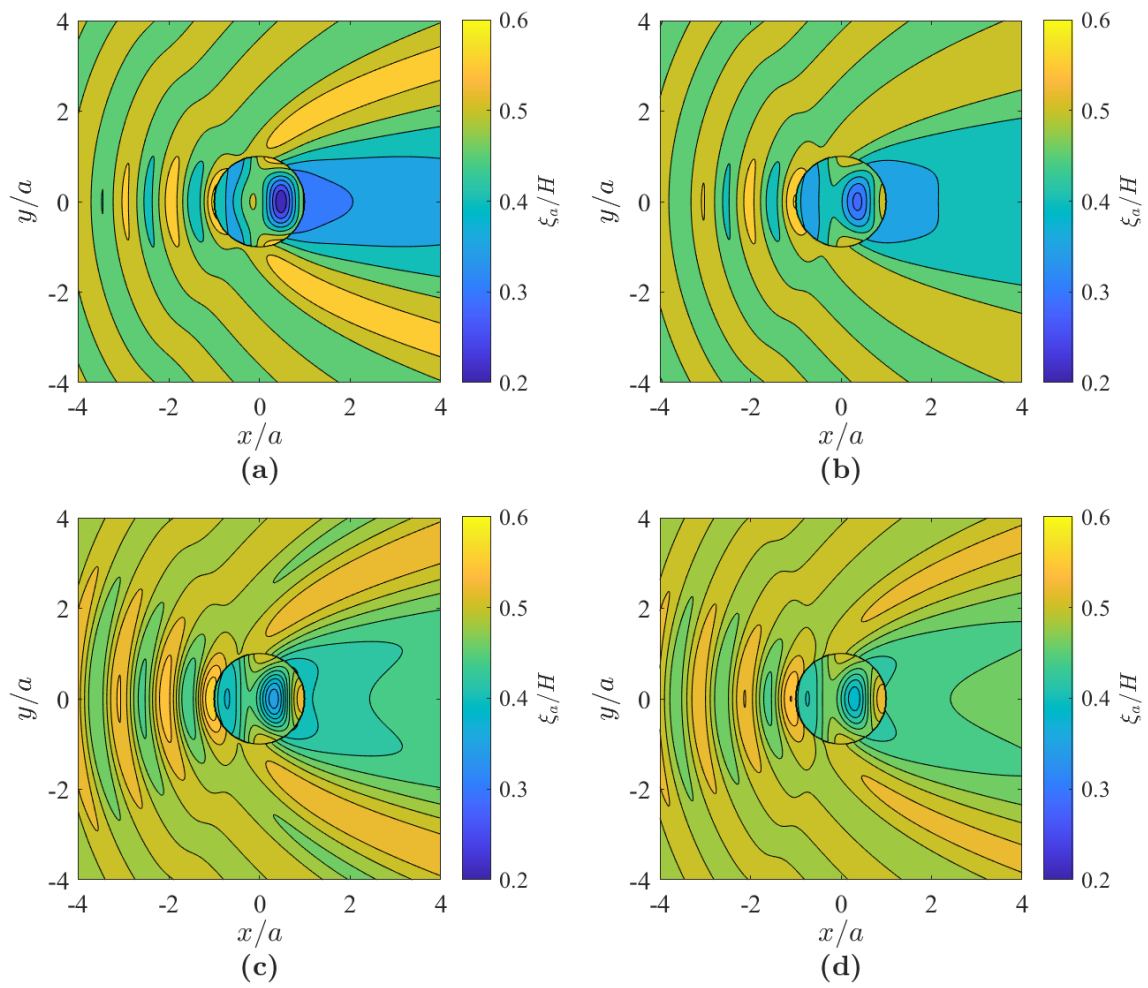


**Fig. 5.9** Amplitudes of free surface elevations  $\xi_a$  around a cylindrical net cage with various porous effect parameters  $\tau$ : (a)  $\tau = 1 + 1i$ ; (b)  $\tau = 2 + 2i$ ; (c)  $\tau = 3 + 3i$ ; (d)  $\tau = 4 + 4i$ , Cases B1–B4.

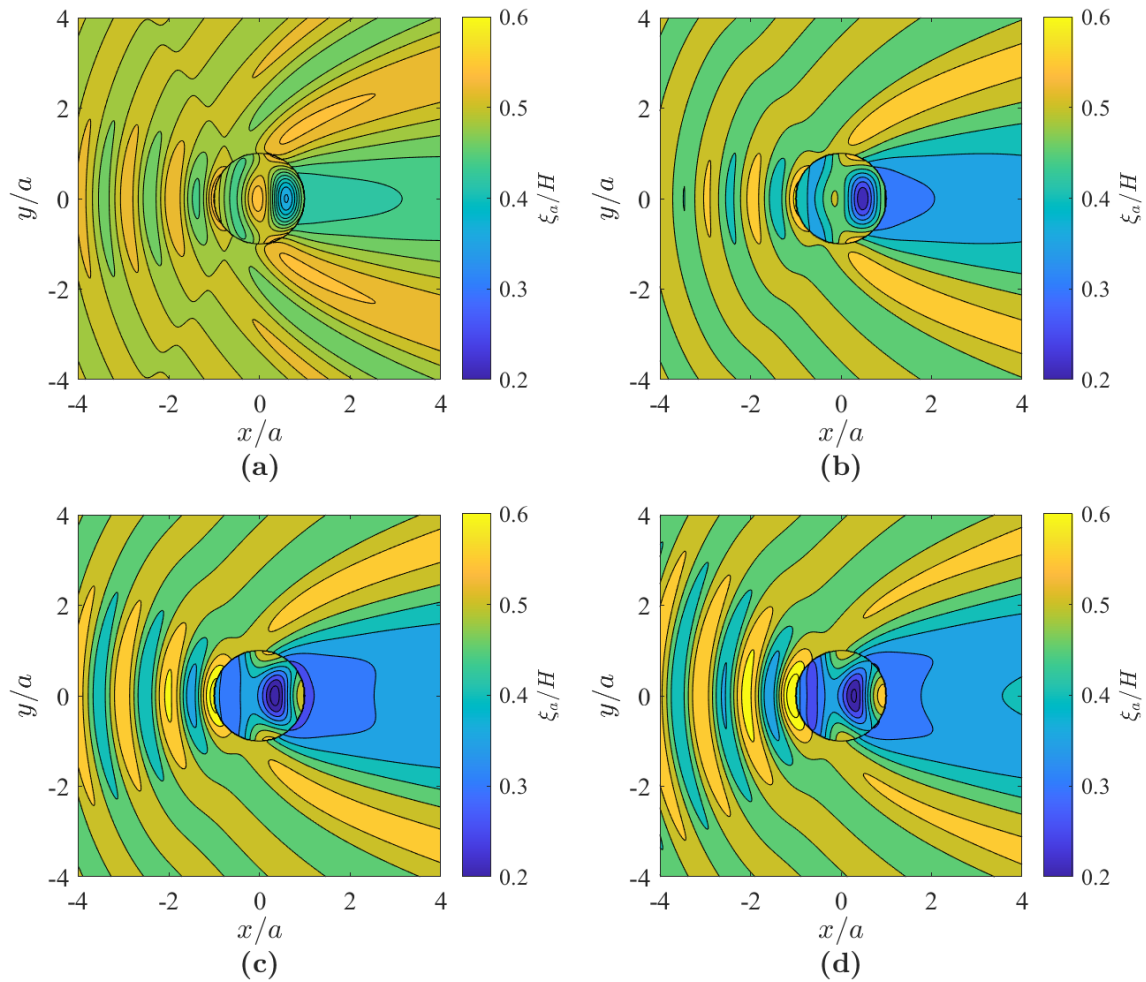


**Fig. 5.10** Amplitudes of free surface elevations  $\xi_a$  around a cylindrical net cage with various nondimensional elastic modulus  $\eta$ : (a)  $\eta = 0.5 \times 10^3$ ; (b)  $\eta = 1 \times 10^3$ ; (c)  $\eta = 2 \times 10^3$ ; (d)  $\eta = 4 \times 10^3$ , Cases C1–C4.

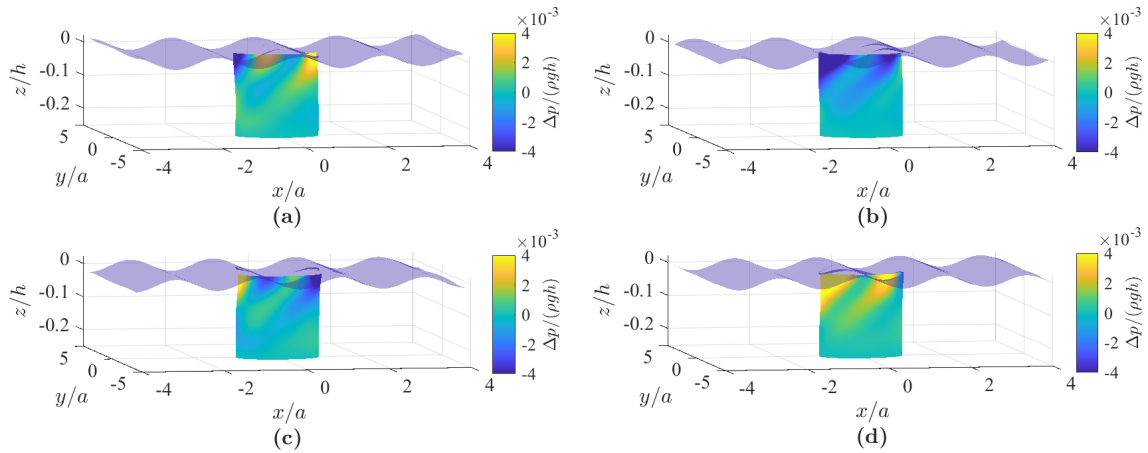


**Fig. 5.11** Free surfaces and dynamic responses of a cylindrical net cage over time: (a)  $t/T = 0$ ; (b)  $t/T = 1/4$ ; (c)  $t/T = 1/2$ ; (d)  $t/T = 3/4$ , Case A3.

### 5.5.2 Structural dynamic responses

Fig. 5.11 shows the dynamic response of the net cage over time. The colour on the cylinder represents the values of the nondimensional pressure drop  $\Delta p/(\rho gh)$  on the net interface (positive when inward and negative when outward) as calculated from Eq. (5.27). The windward side of the cylinder obviously has higher pressure differences at the time of one-quarter or three-quarter period. When compared to the bottom part, the wave load near the upper part of the cage is also greater. This means that the wave has a more significant effect when it is near the free water surface. It is noted that because the small-amplitude wave theory simplifies the free water surface to the mean water level as the boundary, it is seen that the part of the cylinder exposed above the wave surface is still imposed the pressure action.

In order to investigate the spatial distribution of structural displacements and hydrodynamic loads, the amplitudes of these variables are contoured in Fig. 5.12, where half of the circumferential scale of the cage ( $\pi \leq \theta \leq 2\pi$ ) is plotted due to symmetry. Owing to the edge constraint condition, the axial and circumferential displacements of the cage vanish at  $z/h = 0$ , but the radial displacement and pressure differences are maximum due to strong surface waves. For the axial displacements, radial displacements and pressure drops, their peak values are all at  $\theta/(2\pi) = 0.5$  and 1 (windward and leeward sides). Nevertheless, two peak values of the tangential displacements occur near the positions of  $\theta/(2\pi) = 0.608$  and 0.78.

Finally, the structural deformations are illustrated in Figs. 5.13 to 5.16. From Fig. 5.13, it can be observed that the short wave is more predominant near the free surface, but the wave action is stronger in deeper water for the long wave. In addition, the structural

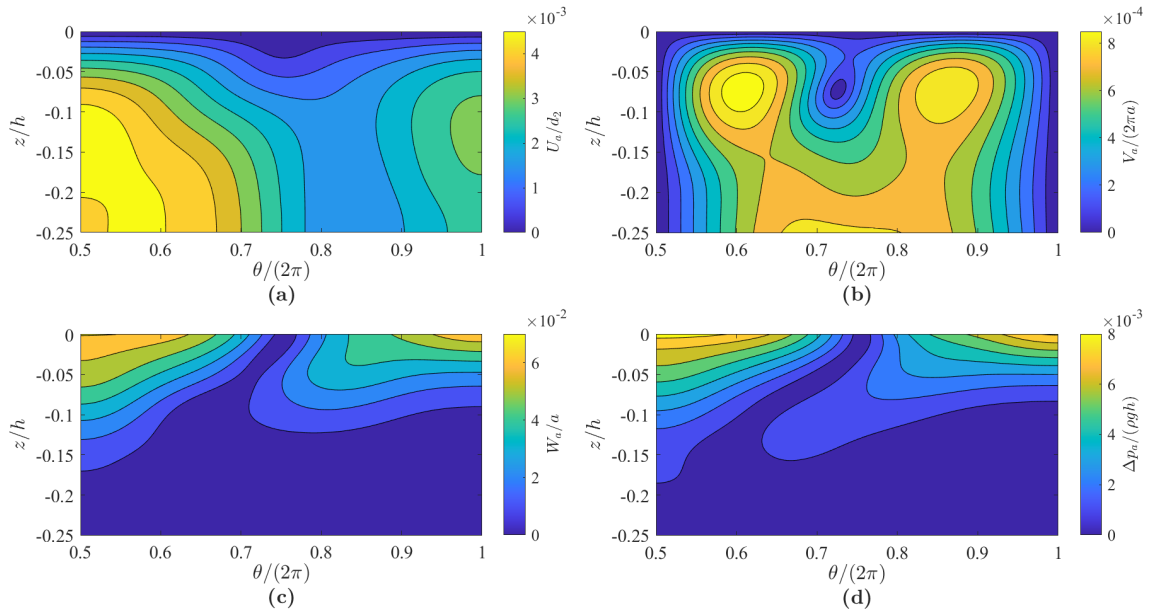


**Fig. 5.12** Spatial contours of (a) Axial displacement amplitude  $U_a$ ; (b) Circumferential displacement amplitude  $V_a$ ; (c) Radial displacement amplitude  $W_a$ ; (d) Pressure drop amplitude  $\Delta p_a$ , Case A3.

motion exhibits different frequency responses. With a higher opening ratio of the net, the wave scattering will be weakened, as shown in Fig. 5.9. According to Eq. (5.27), this results in the reduction of wave loads acting on the cage, and thus the cage deformations are reduced (Fig. 5.14). However, the area where the pressure difference points outward (positive values) become larger on the windward side. Similarly, a stiffer cage can enhance wave scattering (Fig. 5.10), and the loss of fluid momentum will increase as interacting with it. Therefore, in Fig. 5.15, although a low magnitude of  $\eta$  will increase the flexibility of the net, the corresponding wave action is decreased. In Fig. 5.16, when the cage is submerged to a deeper depth, the wave effect will gradually become minimal, resulting in the wave actions and structural deformations been suppressed significantly. This justifies that the submergence of the cage into a deeper water depth is beneficial to avoid the strong impact due to surface waves.

### 5.5.3 Parametric studies

In this section, the effects of variable wave and structural parameters on the hydrodynamic forces are investigated. Similar to Mandal and Sahoo (2016), two nondimensional amplitudes about the horizontal wave force ( $K_F$ ) and the corresponding overturning moment to the top of the cage ( $K_M$ ) are defined as here:

$$K_F = \frac{|F|}{\rho g a H h} \text{ and } K_M = \frac{|M_o|}{\rho g a H h (d_1 + d_2)}, \quad (5.57)$$

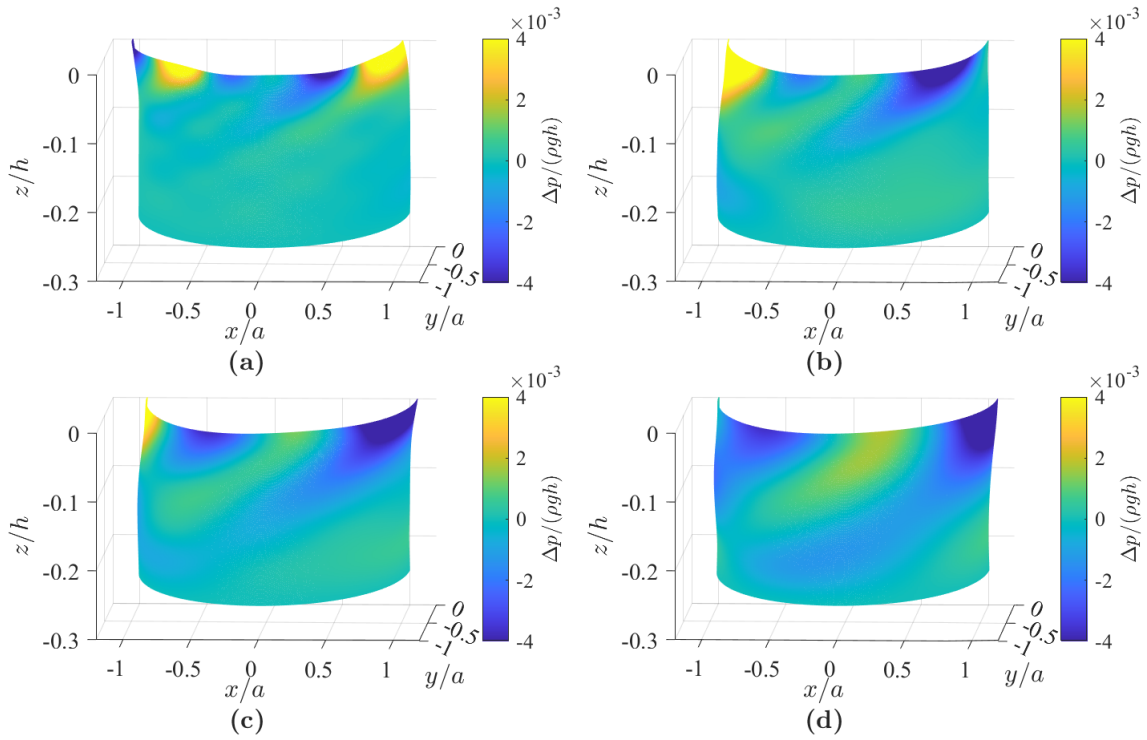


**Fig. 5.13** Pressure drops  $\Delta p$  on a cylindrical net cage and corresponding deformations with various wave-effect parameters  $C_w$  at  $t = T/2$ : (a)  $C_w = 0.04$ ; (b)  $C_w = 0.06$ ; (c)  $C_w = 0.08$ ; (d)  $C_w = 0.12$ , Cases A1–A4.

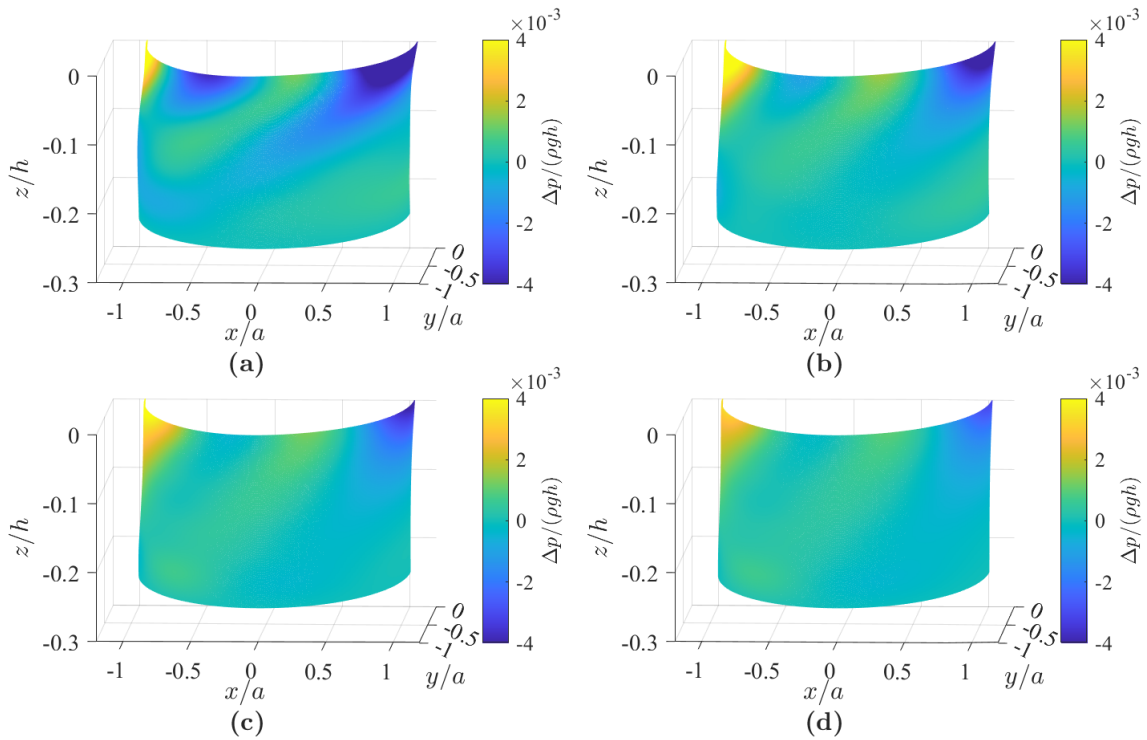


**Fig. 5.14** Pressure drops  $\Delta p$  on a cylindrical net cage and corresponding deformations with various porous effect parameters  $\tau$  at  $t = T/2$ : (a)  $\tau = 1 + 1i$ ; (b)  $\tau = 2 + 2i$ ; (c)  $\tau = 3 + 3i$ ; (d)  $\tau = 4 + 4i$ , Cases B1–B4.

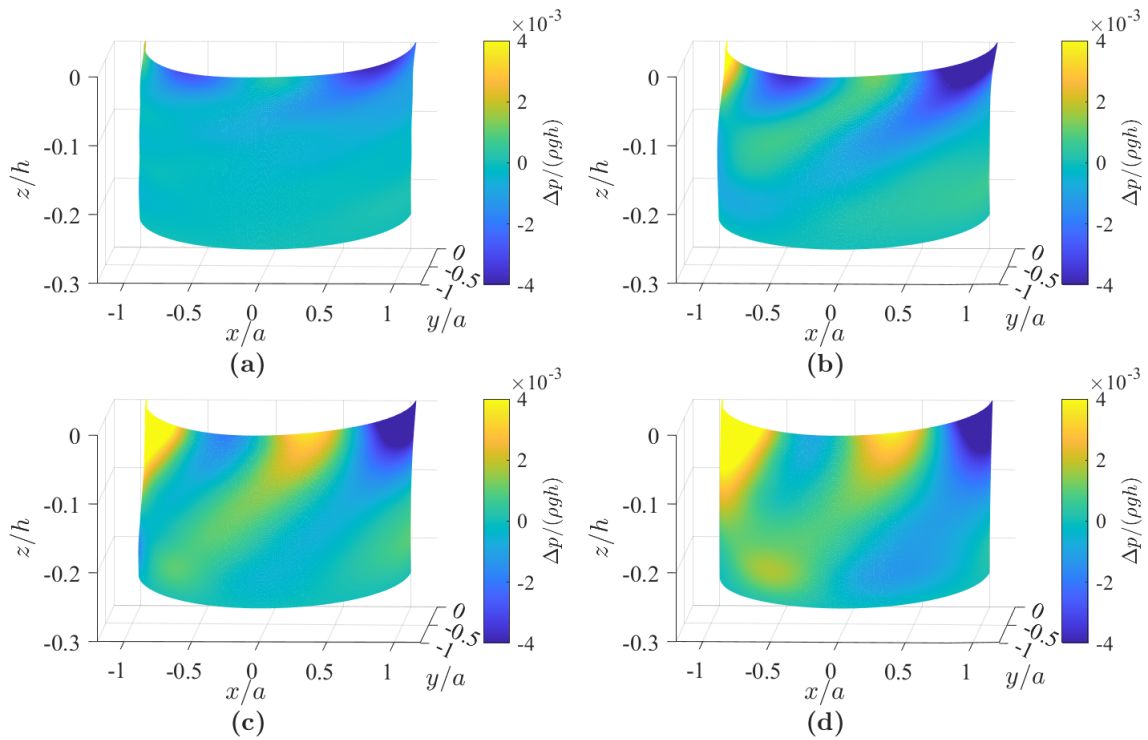


**Fig. 5.15** Pressure drops  $\Delta p$  on a cylindrical net cage and corresponding deformations with various nondimensional elastic modulus  $\eta$  at  $t = T/2$ : (a)  $\eta = 0.5 \times 10^3$ ; (b)  $\eta = 1 \times 10^3$ ; (c)  $\eta = 2 \times 10^3$ ; (d)  $\eta = 4 \times 10^3$ , Cases C1–C4.

where the wave force  $F$  and the overturning moment  $M_o$  are defined in Eqs. (5.28) and (5.29). In the current analysis, the considered design parameters include the wave-effect parameter  $C_w$  and the cage's parameters about the relative diameter  $2a/L$  ( $L$  is the wavelength), the relative diving depth  $d_1/h$ , the slenderness ratio  $d_2/(2a)$ , the nondimensional elastic modulus  $\eta$  and the porous effect parameter  $\tau$ . The following parameters are kept constant:  $H = 7$  m,  $h = 200$  m,  $t_s = 0.005$  m and  $\rho_s/\rho = 1.2$ .

### I. Wave frequency effects

With the variations of wave frequency, the curves of  $K_F$  and  $K_M$  present several zero points and peak points in Fig. 5.17. The magnification or vanishing of the force is due to the destructive interference of the incident and scattered waves (Mandal et al., 2013). Furthermore, increasing the porosity can reduce  $K_F$ , but  $K_M$  does not obey this situation. From Fig. 5.14, when  $\tau$  increases, the area on the windward side that bears a positive pressure drop also increases, which may lead to the increase of the overturning moment.



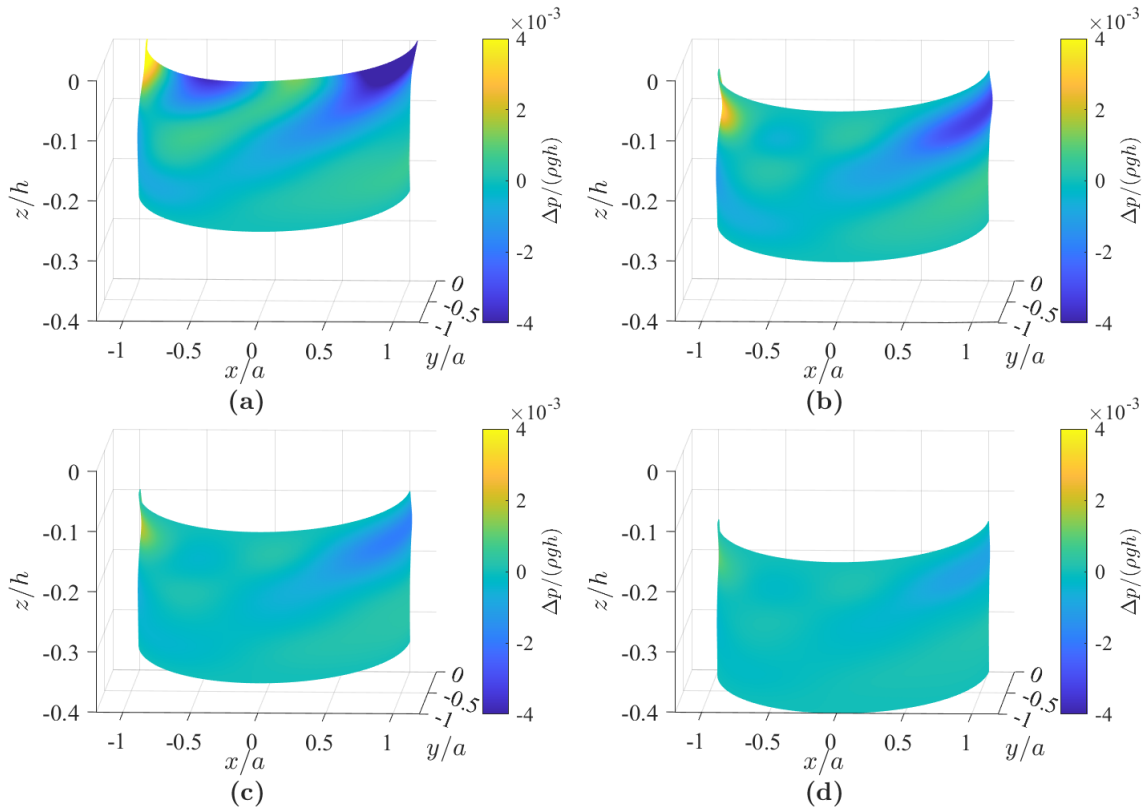


**Fig. 5.16** Pressure drops  $\Delta p$  on a cylindrical net cage and corresponding deformations with various relative diving depths  $d_1/h$  at  $t = T/2$ : (a)  $d_1/h = 0$ ; (b)  $d_1/h = 0.05$ ; (c)  $d_1/h = 0.10$ ; (d)  $d_1/h = 0.15$ , Cases D1–D4.

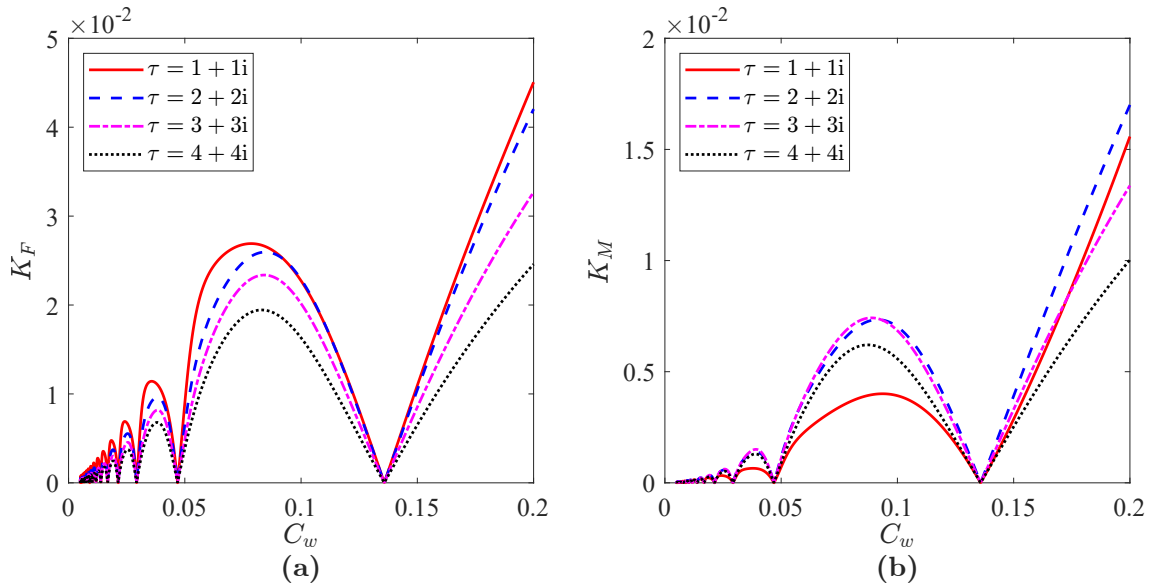


**Fig. 5.17** Influences of wave effect parameters  $C_w$  on nondimensional amplitudes of (a) Horizontal wave forces  $K_F$ ; (b) Overturning moments  $K_M$  under various porous effect parameters  $\tau$ ,  $t_s/a = 10^{-4}$ ,  $d_1/h = 0$ ,  $d_2/(2a) = 0.5$  and  $\eta = 10^3$ .

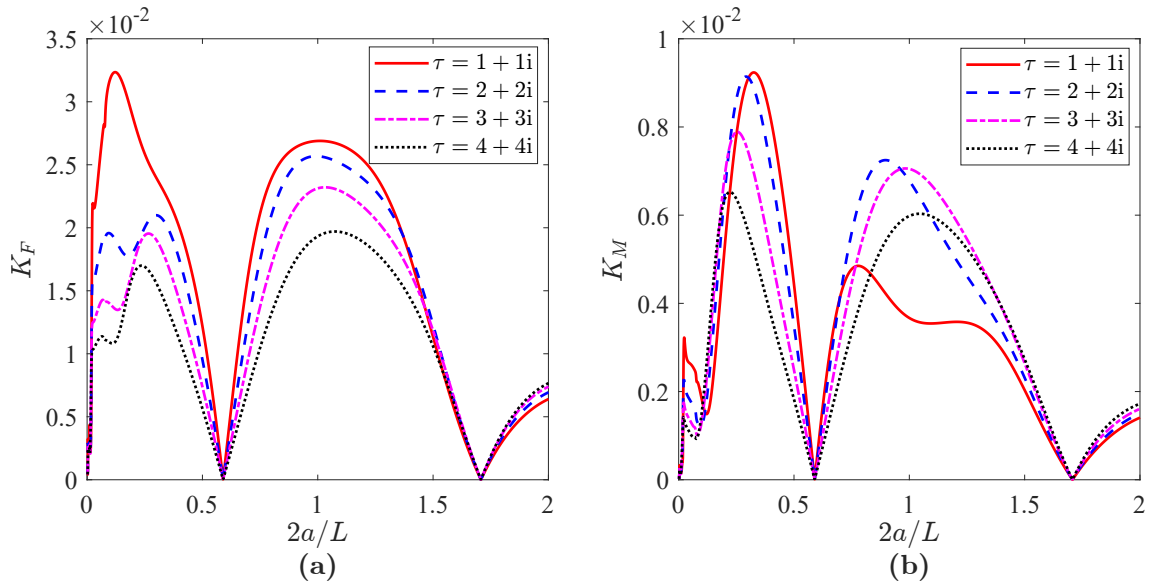


**Fig. 5.18** Influences of relative diameters  $2a/L$  of the cage on nondimensional amplitudes of (a) Horizontal wave forces  $K_F$ ; (b) Overturning moments  $K_M$  under various porous effect parameters  $\tau$ ,  $C_w = 0.08$ ,  $d_1/h = 0$ ,  $d_2/(2a) = 0.5$  and  $\eta = 10^3$ .

## II. Dimensions and locations of the cage

With respect to the influence of the cage diameter, these curves also show several similar zero points and peak points in Fig. 5.18. It is observed that the magnitudes of  $K_F$  and  $K_M$  reach zero as  $2a/L$  is approximately 0.59 or 1.70, where the wave effect parameter  $C_w$  keeps 0.08. As a result, from Figs. 5.17 and 5.18, it can be concluded that the ratio between the cage diameter and the wavelength can determine the enhancement or vanish of the wave force.

When the cage is submerged to a deeper depth, the structure will be subjected to a weaker dynamic pressure due to surface waves. This is the main reason that contributed to the decrease of the coefficients  $K_F$  and  $K_M$  versus the relative diving depth  $d_1/h$  in Fig. 5.19. However, as the relative diving depth  $d_1/h$  increases, the varying tendency of  $K_F$  and  $K_M$  will also gradually slow down.

Fig. 5.20 shows the variations of the wave actions when the cage height increases from zero to the water depth in a floating condition. These curves indicate that the values of  $K_F$  and  $K_M$  will sharply increase to the peak values, then decrease gradually and approach a constant value. This is because, although higher cage height can increase more forced areas on the structure, the wave pressure in deeper water has already become relatively minor.

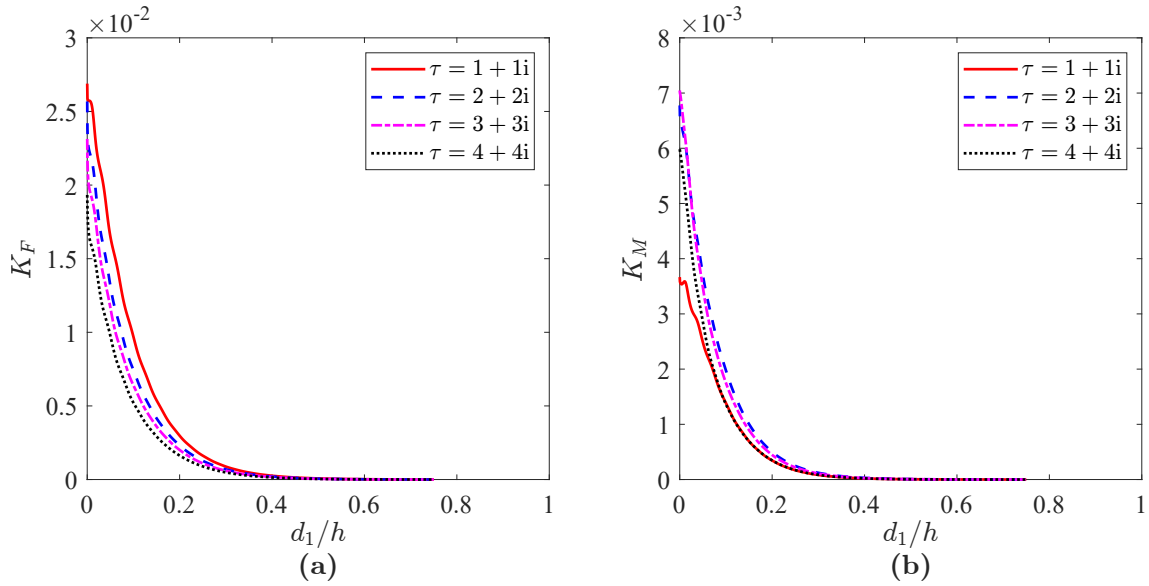


**Fig. 5.19** Influences of relative diving depths  $d_1/h$  of the cage on nondimensional amplitudes of (a) Horizontal wave forces  $K_F$ ; (b) Overturning moments  $K_M$  under various porous effect parameters  $\tau$ ,  $C_w = 0.08$ ,  $t_s/a = 10^{-4}$ ,  $d_2/(2a) = 0.5$  and  $\eta = 10^3$ .

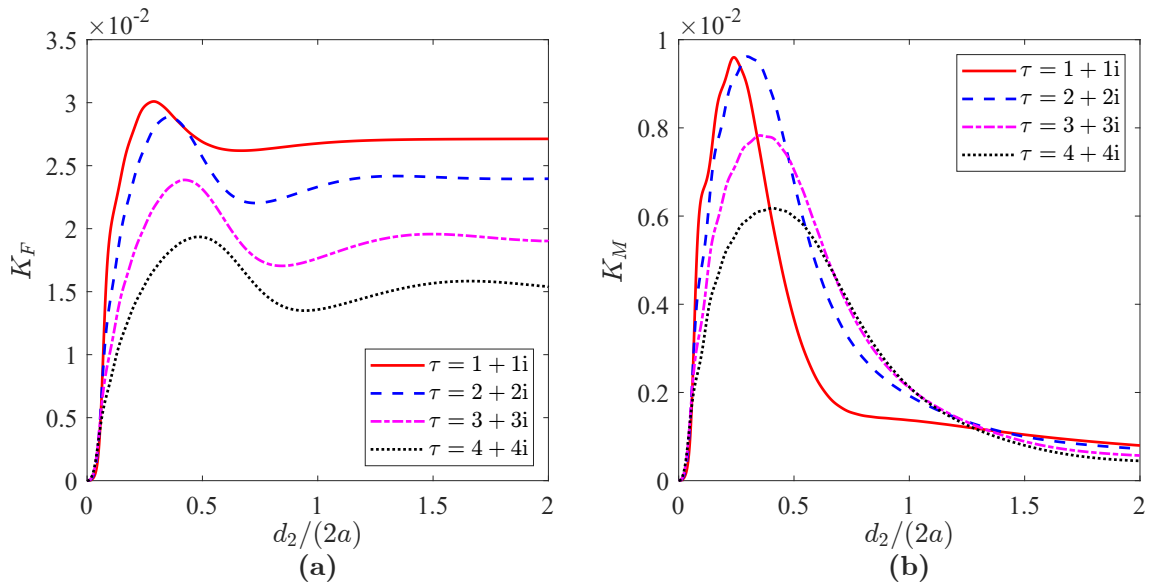


**Fig. 5.20** Influences of slenderness ratios  $d_2/(2a)$  of the cage on nondimensional amplitudes of (a) Horizontal wave forces  $K_F$ ; (b) Overturning moments  $K_M$  under various porous effect parameters  $\tau$ ,  $C_w = 0.08$ ,  $t_s/a = 10^{-4}$ ,  $d_1/h = 0$  and  $\eta = 10^3$ .

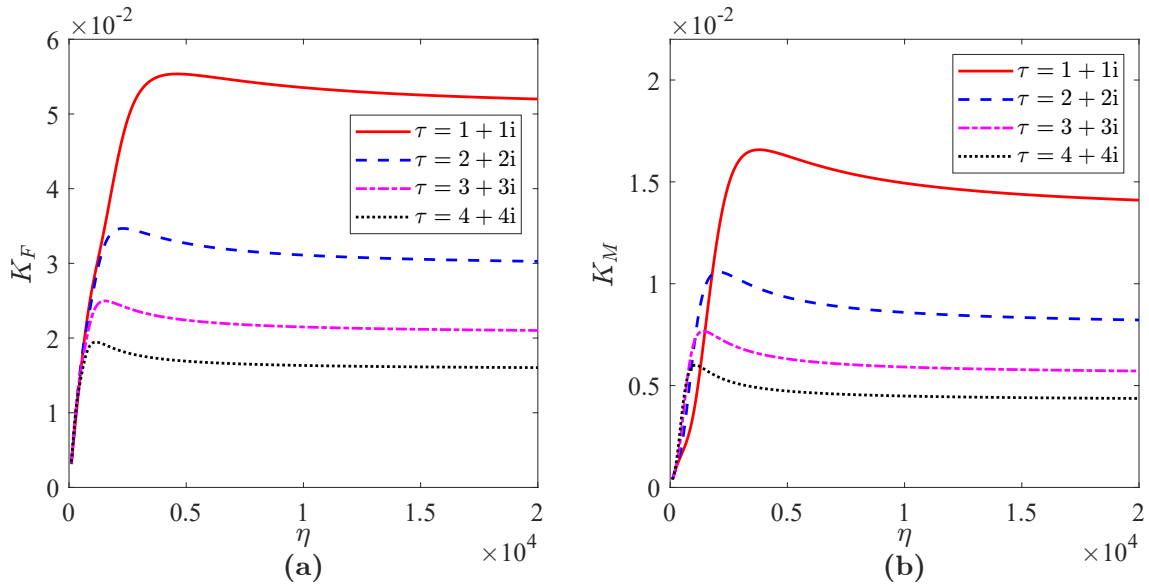


**Fig. 5.21** Influences of nondimensional elastic modulus  $\eta$  of the cage on nondimensional amplitudes of (a) Horizontal wave forces  $K_F$ ; (b) Overturning moments  $K_M$  under various porous effect parameters  $\tau$ ,  $C_w = 0.08$ ,  $t_s/a = 10^{-4}$ ,  $d_1/h = 0$  and  $d_2/(2a) = 0.5$ .

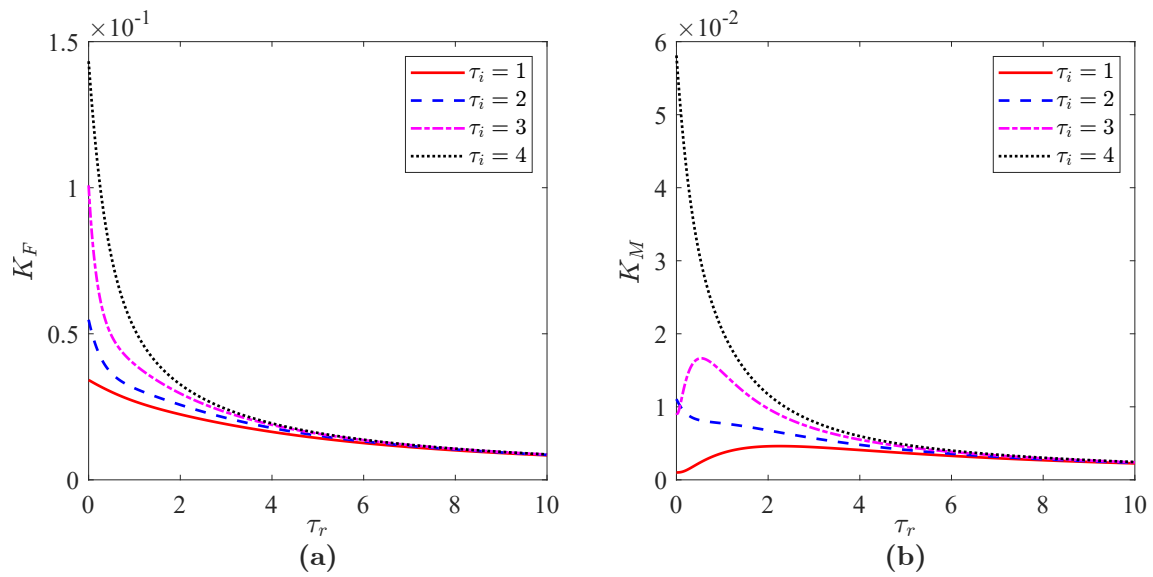
### III. Structural stiffness and porous effects

Fig. 5.21 illustrates that the flexibility of the net has a significant influence on the wave load when  $\eta$  is less than  $5 \times 10^3$ . The tendency of  $K_F$  and  $K_M$  will increase to the peak and decrease slowly until it remains stable. This scenario is explained in the aforementioned section. The magnitude of the pressure drop  $\Delta p$  on the cage will be greater with the increased structural stiffness, and the interference of the displacement of the net on the wavefield has been relatively minor when it is extremely rigid.

In Figs. 5.22 and 5.23, the influence of the real part  $\tau_r$  (porous resistance) and the imaginary part  $\tau_i$  (fluid inertia) of the porous effect parameter  $\tau$  is discussed. An increase in  $\tau_r$  will decrease  $K_F$ , but  $K_M$  will not always decrease under different values of  $\tau_i$ . However, for different  $\tau_r$ , both coefficients will increase to peaks as  $\tau_i$  increases, and then begin to decrease. Therefore, different properties are revealed for the horizontal wave force and the overturning moment with respect to the porous resistance effect.

## 5.6 Conclusions

The hydroelastic behaviour of the submersible cylindrical fish net cage interacting with waves in offshore deep water site was investigated in detail through the semi-analytical solutions. The fish cage net was treated as a porous medium membrane and the motion



**Fig. 5.22** Influences of porous resistance parameters  $\tau_r$  of the cage on nondimensional amplitudes of (a) Horizontal wave forces  $K_F$ ; (b) Overturning moments  $K_M$  under various fluid inertia parameters  $\tau_i$ ,  $C_w = 0.08$ ,  $t_s/a = 10^{-4}$ ,  $d_1/h = 0$ ,  $d_2/(2a) = 0.5$  and  $\eta = 10^3$ .

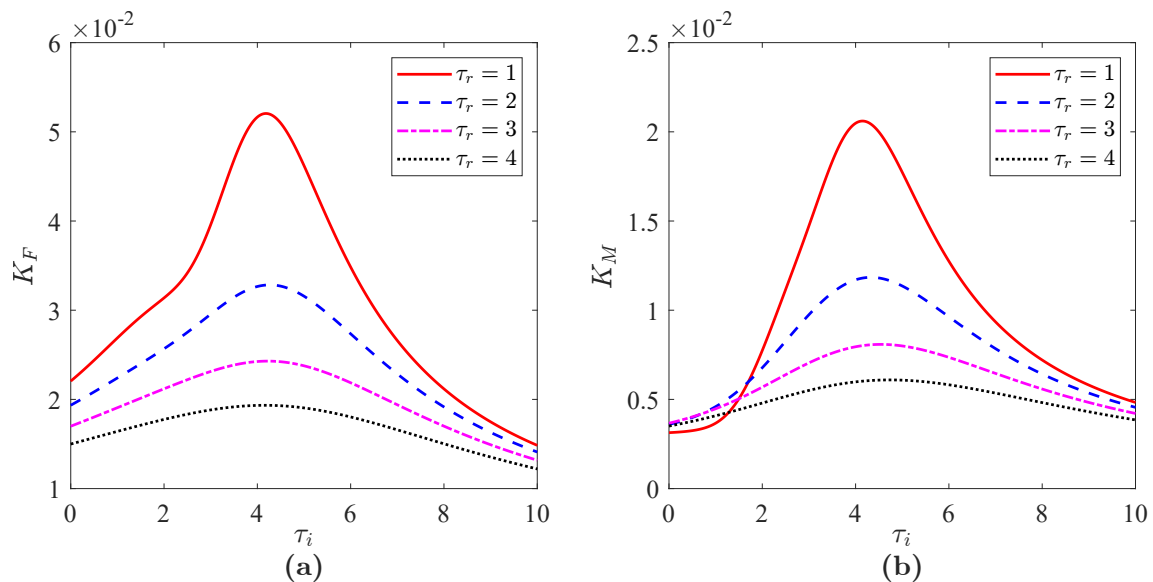


**Fig. 5.23** Influences of fluid inertia parameters  $\tau_i$  of the cage on nondimensional amplitudes of (a) Horizontal wave forces  $K_F$ ; (b) Overturning moments  $K_M$  under various porous resistance parameters  $\tau_r$ ,  $C_w = 0.08$ ,  $t_s/a = 10^{-4}$ ,  $d_1/h = 0$ ,  $d_2/(2a) = 0.5$  and  $\eta = 10^3$ .

of the cage is governed by the membrane vibration equation of the cylindrical shell. The hydrodynamic model is expressed by the potential flow theory, and the solution of the flow field is expanded into a Fourier-Bessel series. Finally, the particular solution of the wave-cage interaction is obtained by matching the boundary conditions and the least squares method.

Based on numerical examples, the following conclusions can be drawn:

- i. The fish net cage causes a certain perturbation to the wave surface. On the windward side of the cage, the wave amplitudes are distributed in arc-shaped band regions due to the superposition of incident waves and scattered waves, and there are some leaf-like regions within enhanced perturbations to waves. Besides, a wake-like area will appear behind the leeward side of the cage to attenuate the wave energy significantly.
- ii. Increasing the porosity and flexibility of the net can suppress wave scattering and the hydrodynamic action.
- iii. The wave impact and the corresponding structural dynamic responses are more significant near the mean water level, so submersible cages are recommended to avoid strong wave surface loads and excessive structural deformations.
- iv. The cylindrical net chamber will produce critical dynamic responses at specific wave frequencies, and the horizontal wave forces and overturning moment that the net cage bears vanish under the specific ratios of the cage diameter to the wavelength.

The findings from this study provide a better understanding of the hydroelastic characteristics of fish net cages and the feasibility of offshore aquaculture. Nevertheless, the hydrodynamic model and theoretical formulation presented herein cannot handle the non-linear effects of waves and the quadratic porous flow theory. Furthermore, the membrane theory of cylindrical shells also has limitations when dealing with complex constraint conditions. In future studies, these problems will be tackled. Moreover, the interaction among multiple fish net cages in waves will be studied.

# Chapter 6

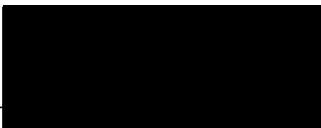
## Theoretical extension to wave interference effects in multi-cage systems

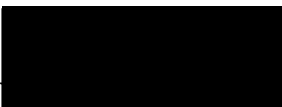

This chapter is originally published as

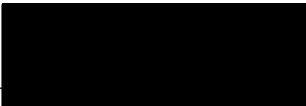
Ma, M., Zhang, H., Jeng, D.-S., and Wang, C.M. (2022). Hydroelastic interactions between waves and an array of submersible flexible fish cages. *Ocean Engineering*, 266:113035.

My contribution includes conceptualization, methodology, validation, formal analysis and writing-original draft preparation.

Signed:  Date: 02/02/2023  
Mingyuan Ma

Countersigned:  Date: 02/02/2023  
Prof. Hong Zhang (Principal Supervisor, School of Engineering and Built Environment, Griffith University)

Countersigned:  Date: 2/2/2023  
Prof. Dong-Sheng  (Co-supervisor, School of Engineering and Built Environment, Griffith University)

Countersigned:  Date: 02/02/2023  
Prof. Chien Ming wang (Co-author, School of Civil Engineering, University of Queensland)

## Hydroelastic interactions between waves and an array of submersible flexible fish cages

**Abstract:** In this study, a semi-analytical solution is developed to investigate the wave interference and corresponding dynamic responses of an array of submersible flexible fish cages. The net chamber is modelled as a perforated cylindrical shell, and the penetration flow through the cage interface is described by a porous medium model. Based on the potential flow theory, the solution to this physical problem is expanded as a series of eigenfunctions in the local coordinate system of each cage, and the scattered wave potentials generated by all cages are superimposed wherein Graf's addition theorem is employed for the coordinate transformation. The mean wave drift effect is also explored, which is a nonlinear phenomenon derivable from the first-order solution. The results indicate that the interference of waves is determined by wavenumbers, cage spacings or net porosities, and significant wave responses are manifested near the top part of the cage. Additionally, the first-order wave force vanishes at a ratio of cage diameter to wavelength = 0.59, and, along the direction of wave incidence, the rear cages experience opposite mean wave drift loads relative to those on the front cages. These studies provide benchmark results for understanding the hydroelastic characteristics of multi-cage systems.

**Keywords:** Fish cage array; Hydroelastic interaction; Wave interference; Porous medium model; Shell-membrane theory; Eigenfunction expansion



## 6.1 Introduction

Marine aquaculture has become an essential contributor to the world's fish supply chain and creates enormous economic value. According to DNV (2021), global marine aquaculture production is predicted to increase by 155% from 2020 to 2050. However, accompanied by this growth trend, nearshore fish farms have almost reached their production capacities, and further expansion is difficult due to competing users and environmental pressures. Thus, aquaculture operators are considering moving their farms to offshore sites where there are abundant space, more pristine water and deeper water columns for better waste disposal (Gentry et al., 2017). Data from FAO (2020a) also indicate that the proportion of the finfish production capacity offshore will increase relative to the sheltered one from 2020. Against this backdrop, relevant offshore fish farming techniques are gaining traction in research. An offshore fish farm comprising multiple circular or rectangular cages is an ideal approach, but how to decide the optimal fluid-structure parameters and array layout is a topic worthy of attention. For example, flow conditions or different spacings among the cages may cause interactions among the wakes from individual cages, leading to stronger combined water blockage and more intensive velocity reduction within the cage array (Klebert et al., 2013). Similarly, wave interference due to the superposition of scattered waves induced by individual cages also results in changes in the wave energy around the array. Therefore, proper modelling is required to simulate the hydroelastic behaviour of such systems.

Abundant and advanced theories underpin the development of numerical techniques for predicting the hydroelastic behaviour of net cages. Generally, a fish cage net is assumed not to provide bending stiffness, so it is usually modelled as a massed node-spring model (Chen et al., 2021; Zhao et al., 2008) or a finite element model with truss elements (Li et al., 2013a) where the hydrodynamic loads are evaluated by the Morison equation or the screen-type method. These numerical techniques are also employed in cases with multiple cages (Liu et al., 2022; Xu et al., 2013b; Zhang et al., 2021). Nonetheless, the flow pattern around the cages cannot be captured, especially the water blockage effect that may be enhanced in the cage array. Accordingly, fluid-structure coupling algorithms using CFD models have been also established in some works of literature (Cheng et al., 2022; Martin et al., 2021; Yao et al., 2016), but this is accompanied by tremendous computational time for some full-scale cases. In view of this, hybrid analytical-numerical approaches may be a more practicable and promising solution.

A net-type structure may be considered a porous medium macroscopically, and the potential flow theory has been widely applied to determine wave-porous structure interactions. Chwang (1983) proposed a theoretical model of the wavefield generated by a

porous wavemaker in which Darcy's law was introduced to dampen the wave. Yu and Chwang (1994) investigated wave diffraction due to a circular porous barrier using the eigenfunction-expansion method. Following these studies, Su et al. (2015) and Mandal and Sahoo (2016) derived solutions for interactions between waves and a single flexible net cage in which the net chamber was simplified as a one-dimensional beam or string to describe its transverse deflection, but the latter also considered the deformation of the bottom net plate modelled as a two-dimensional membrane. Ma et al. (2021) extended their work to a submersible cage with mooring systems. Furthermore, Ito et al. (2014) developed a hybrid method to calculate the wave force on a cube net cage wherein the far-field wave was expressed in a Fourier-Bessel series, and the boundary element method (BEM) was utilised for the ambient waves. The net of the cube cage was modelled as a perforated membrane governed by the Helmholtz equation.

Nevertheless, in the above analysis, it may be oversimplified for the modelling of net chambers because the motion of the net should be a three-dimensional problem, and stress variations caused by structural deformations were ignored. Strand and Faltinsen (2020) derived a solution for the dynamic structural stress induced by waves for a closed fish cage, but the analysis was limited to a 2-D case modelled as a flexible beam. Flügge (1973) demonstrated the constitutive relation in three-dimensional shell structures analytically based on the membrane theory and the bending theory, respectively, and the former assumed that the thin shell structure cannot provide bending stiffness. Lee et al. (1993) and Belubekyan et al. (2017) elaborated on particular solutions for the free vibration of a cylindrical shell by employing the two theories. Ji et al. (2019) proposed the first-order solution of a vibrating cylindrical shell filled with fluid, and Guo et al. (2017) simulated the vibration and acoustic radiation of a cylindrical shell submerged in water by combining the eigenfunction expansion method and BEM. Based on the aforementioned theoretical studies, Ma et al. (2022) introduced the membrane theory of shells to describe the dynamic response of net cages under ocean wave excitation. However, only a single cage was considered in their study, although multi-cage systems have been commonly used in the aquacultural industry.

In terms of multiple structures in waves, the Kagemoto and Yue (1986) interaction theory provides an exact solution to the wavefield around multiple impermeable cylinders by using the eigenfunction expansion and Graf's addition theorem. This theory was applied in the interactions between waves and a group of floating rigid porous cages (Park and Koo, 2015; Park et al., 2010). For flexible structures, Zheng et al. (2020b) investigated the wave response of an array of floating porous elastic plates, and Selvan et al. (2021) extended the work of Mandal and Sahoo (2016) to a system of multiple flexible fish cages. Recently, the application of other numerical methods in this field has also received much attention. Wang

and Wu (2007) proposed a time domain analysis method for second-order wave diffraction around an array of cylinders based on the finite element method. Li et al. (2011) employed the scaled boundary finite element method (SBFEM) to solve the dynamic response of a single pile when interacting with waves, and Li et al. (2013b) extended the work to multiple piles with arbitrary cross-sections and layouts. Gharechae and Ketabdari (2022) developed a BEM-based solution for an array of aquaculture cages. Both the SBFEM and BEM can reduce the spatial dimension of the studied problem by one (Li et al., 2015). In addition, Chen et al. (2011) proposed the null-field boundary integral equation method (BIEM) for wave diffraction among multiple porous cylinders.

The abovementioned literature and methodologies suggest that the porous medium theory and continuum vibration equations provide a theoretical basis for developing hydroelastic solutions to wave-cage interaction, and the interference of waves among multiple cages can be realised by the Kagimoto and Yue (1986) interaction theory or solved numerically. However, there are several research gaps. First, the pivotal factors determining the effects of wave interference in fish cage arrays have not been systematically investigated and understood. Second, the model assumption of oversimplifying the net chamber as a single string or beam may be unreasonable in some of the aforementioned analytical solutions (Mandal and Sahoo, 2016; Su et al., 2015). Moreover, only limited research studies on the mean drift loads of waves acting on fish net cages are available, and they are less well understood.

In this paper, a semi-analytical solution is derived based on the potential flow theory and membrane theory of shells to ascertain the hydroelastic characteristics of an array of submersible flexible cylindrical open-net cages. It extends the work of Ma et al. (2022) from the case of a single cage to multiple cages with arbitrary dimensions, layouts and incident wave directions, and the mean wave drift loads are introduced as well. The overall layout of this paper is as follows: Section 6.2 elaborates on the problem configuration, and the corresponding method of solutions is outlined in Section 6.3. The convergence analysis and model validation to support the proposed semi-analytical solution are established in Section 6.4. Section 6.5 presents the numerical results, including the wavefield distribution, the dynamic responses of the cages and some parametric studies. Finally, key findings and subsequent research directions are summarised in Section 6.6.

## 6.2 Problem definition, assumption and theoretical formulation

A series of submersible cylindrical cages with the numbers  $j = 1, 2, \dots, NC$  are considered as shown in Fig. 6.1a. A global Cartesian coordinate system  $(x - y - z)$  is established, in which the mean water level is at  $z = 0$ , and the incident wave propagates in the direction with an angle  $\beta$  with respect to the positive  $x$ -axis. Several local coordinate systems  $(r^j - \theta^j - z)$  are established in the cages' centres. In the local coordinate system of the  $k$ th ( $j = k$ ) cylinder, the cylindrical coordinates of any point are  $(r^k, \theta^k, z)$ , and  $(R^{jk}, \alpha^{jk})$  is the polar coordinate of the centre for the  $k$ th cylinder in the local coordinate systems of other cylinders ( $j = 1, 2, \dots, NC, j \neq k$ ). As illustrated in Fig. 6.1b, in a finite water depth  $h$ , each cage has a radius  $a^j$ , an immersed depth  $d_1^j$  and a cage height  $d_2^j$ .

The fluid in the wavefield is assumed to be irrotational and inviscid. Therefore, as shown in Fig. 6.1b, the velocity potential in the external region of all cylinders is denoted as  $\Phi_e$ , and the velocity potential in the internal region ( $r^j < a^j$  and  $0 < z < h$ ) of each cylinder is  $\Phi_i^j$ . As this paper focuses on the hydroelastic behaviour of an array of suspended cylindrical porous nets in interaction with waves, the edges of these suspended net chambers are assumed to be clamped on their top ends  $z = -d_1^j$ , and the bottom ends at  $z = -(d_1^j + d_2^j)$  are free traction.

The objective of the present study is to determine the hydroelastic behaviours (free water surface elevations, hydrodynamic loads, structural dynamic responses, wave load, etc.) of multiple flexible, submerged and cylindrical fish net cages under wave action, including wave interference.

### 6.2.1 Governing equations

The wave is assumed to satisfy the small-amplitude wave theory with a circular frequency  $\omega$  and a wave height  $H$ . Therefore, the velocity potential at any point in the flow field can be written as:

$$\Phi(x, y, z, t) = \text{Re} \left[ \varphi(x, y, z) e^{-i\omega t} \right], \quad (6.1)$$

and the complex amplitude  $\varphi$  of the velocity potential satisfies the Laplace equation:

$$\frac{\partial^2 \varphi}{\partial x^2} + \frac{\partial^2 \varphi}{\partial y^2} + \frac{\partial^2 \varphi}{\partial z^2} = \frac{\partial^2 \varphi^j}{\partial (r^j)^2} + \frac{1}{r^j} \frac{\partial \varphi^j}{\partial r^j} + \frac{1}{(r^j)^2} \frac{\partial^2 \varphi^j}{\partial (\theta^j)^2} + \frac{\partial^2 \varphi^j}{\partial z^2} = 0, \quad (6.2)$$

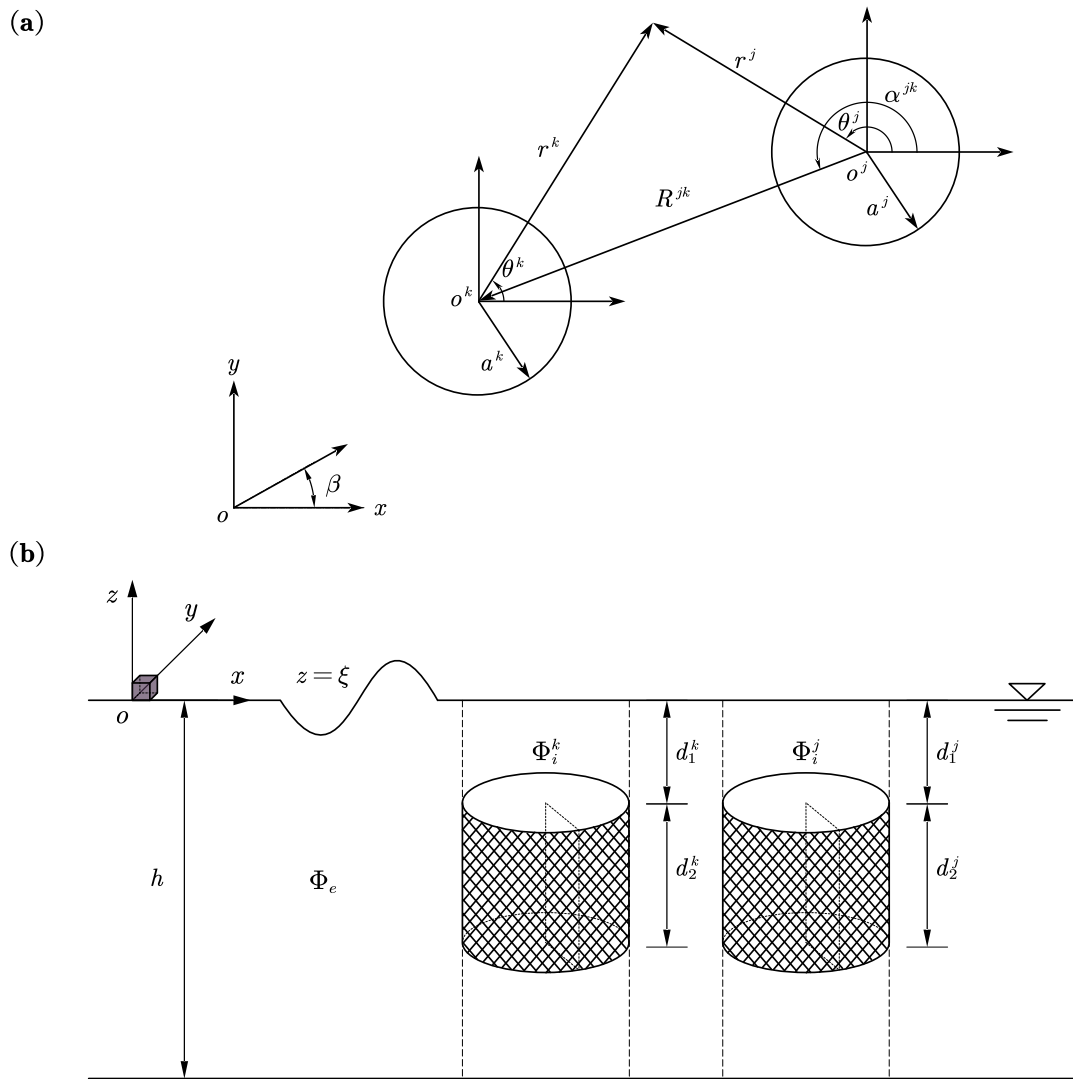


**Fig. 6.1** Sketches and parameter definitions of multiple cylindrical net cages: (a) Plan view; (b) Isometric view.

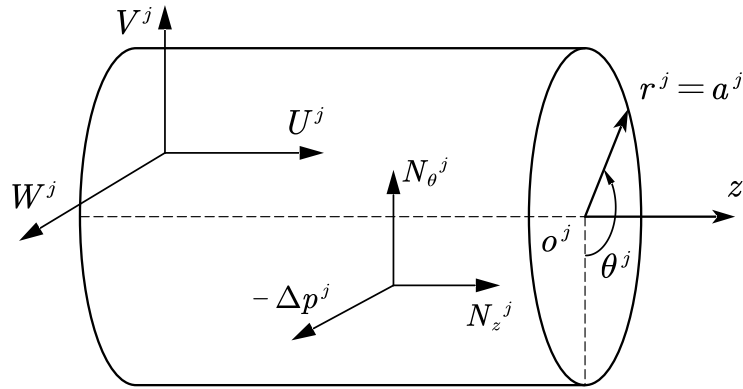


Fig. 6.2 A sketch and parameter definitions of a cylindrical shell.

where  $\varphi$  can be decomposed into the component  $\varphi^I$  caused by the incident wave and the component  $\varphi^S$  caused by the scattered wave. The scattering potential is caused by wave diffraction and wave radiation due to structural oscillations.

On the other hand, a novel method is proposed for modelling the fish cage. The net chamber is equivalent to a perforated cylindrical thin shell, as shown in Fig. 6.2. According to the Flügge (1973) membrane theory, the equations of motions for the shell element are given by

$$\begin{cases} \nabla^2 U^j + \frac{1+\nu^j}{1-\nu^j} \frac{\partial}{\partial z} \left( \frac{\partial U^j}{\partial z} + \frac{1}{a^j} \frac{\partial V^j}{\partial \theta^j} \right) + \frac{2\nu^j}{(1-\nu^j)a^j} \frac{\partial W^j}{\partial z} = \frac{1}{c_s^j} \frac{\partial^2 U^j}{\partial t^2} \\ \nabla^2 V^j + \frac{1}{a^j} \frac{1+\nu^j}{1-\nu^j} \frac{\partial}{\partial \theta^j} \left( \frac{\partial U^j}{\partial z} + \frac{1}{a^j} \frac{\partial V^j}{\partial \theta^j} \right) + \frac{2}{(1-\nu^j)(a^j)^2} \frac{\partial W^j}{\partial \theta^j} = \frac{1}{c_s^j} \frac{\partial^2 V^j}{\partial t^2} \\ \frac{1}{a^j} \frac{\partial V^j}{\partial \theta^j} + \frac{W^j}{a^j} + \nu^j \frac{\partial U^j}{\partial z} + \frac{a^j}{C^j} \Delta p^j = -\frac{\rho_s^j a^j t_s^j}{C^j} \frac{\partial^2 W^j}{\partial t^2} \end{cases}, \quad (6.3)$$

where

$$\nabla^2 = \frac{1}{(a^j)^2} \frac{\partial^2}{\partial (\theta^j)^2} + \frac{\partial^2}{\partial z^2} \text{ and } c_s^j = \frac{G^j}{\rho_s^j}. \quad (6.4)$$

For each cage from  $j = 1, 2, \dots, NC$ ,  $U^j$  is the axial displacement (positive along the upward direction of  $z$ ),  $V^j$  is the circumferential displacement (positive in the direction of increasing  $\theta^j$ ), and  $W^j$  is the radial displacement (positive when outward). The coefficient  $C^j = E^j t_s^j [1 - (\nu^j)^2]^{-1}$ , where  $E^j$  is the elastic modulus of the shell,  $G^j$  is the shear modulus of the shell,  $\nu^j$  is the Poisson's ratio of the shell,  $\rho_s^j$  is the shell bulk density, and  $t_s^j$  is the shell thickness.  $\Delta p^j$  is the first-order pressure drop acting normal to the shell surface.

### 6.2.2 Boundary conditions

According to Dean and Dalrymple (1991), the kinematic boundary condition and the dynamic boundary condition at the free water surface  $z = \xi$  are respectively linearised as

$$\frac{\partial \Phi}{\partial z} = \frac{\partial \xi}{\partial t} \quad \text{at } z = 0, \quad (6.5)$$

$$\xi = -\frac{1}{g} \frac{\partial \Phi}{\partial t} \quad \text{at } z = 0. \quad (6.6)$$

By combining Eqs. (6.5) and (6.6), the boundary at the mean water level has

$$\frac{\partial^2 \Phi}{\partial t^2} + g \frac{\partial \Phi}{\partial z} = 0 \quad \text{at } z = 0. \quad (6.7)$$

On the seabed, the slippery boundary condition is applied:

$$\frac{\partial \Phi}{\partial z} = 0 \quad \text{at } z = -h, \quad (6.8)$$

and the scattering potential satisfies the radiation condition at infinity from Sommerfeld (1949):

$$\lim_{r^j \rightarrow \infty} \sqrt{r_j} \left( \frac{\partial \Phi_e^{S,j}}{\partial r_j} \pm i \kappa_0 \varphi_e^{S,j} \right) = 0. \quad (6.9)$$

In the above equations,  $g$  is the gravity acceleration and  $\kappa_0$  is the incident wavenumber.

The fish cage net is treated as a porous structure, so the penetration flow on the net interface is governed by the kinematic condition:

$$\frac{\partial \Phi_e^j}{\partial r^j} = i \kappa_0 \tau^j (\Phi_i^j - \Phi_e^j) + \frac{\partial W^j}{\partial t} \quad \text{at } r^j = a^j \text{ and } -(d_1^j + d_2^j) \leq z \leq -d_1^j. \quad (6.10)$$

The dimensionless porous-effect parameter  $\tau^j$  of the porous medium is given by Yu and Chwang (1994):

$$\tau^j = \frac{\tau_0^j}{\kappa_0 t_s^j} \frac{f_r^j + i f_i^j}{(f_r^j)^2 + (f_i^j)^2} = \tau_r^j + i \tau_i^j. \quad (6.11)$$

in which  $\tau_0^j$  is the net porosity, and  $f_r^j$  and  $f_i^j$  denote the linearised porous resistance coefficient and fluid inertia coefficient, respectively. The real part  $\tau_r^j$  represents the porous resistance effect, and the imaginary part  $\tau_i^j$  is due to the fluid inertial effect. Moreover, the continuity of velocity and pressure yields:

$$\frac{\partial \Phi_e^j}{\partial r^j} = \frac{\partial \Phi_i^j}{\partial r^j} \quad \text{at } r^j = a^j \text{ and } -h \leq z \leq 0, \quad (6.12)$$

$$\Phi_e^j = \Phi_i^j \quad \text{at } r^j = a^j \text{ and } -h \leq z \leq -(d_1^j + d_2^1) \cup -d_1^j \leq z \leq 0. \quad (6.13)$$

For the edge constraints of the net chambers, the traction-free condition at the bottom ends is given by Belubekyan et al. (2017):

$$\frac{\partial U^j}{\partial z} + \frac{\nu^j}{a^j} \frac{\partial V^j}{\partial \theta^j} + \frac{\nu^j}{a^j} W^j = 0 \text{ and } \frac{1}{a^j} \frac{\partial U^j}{\partial \theta^j} + \frac{\partial V^j}{\partial z} = 0 \quad \text{at } z = -(d_1^j + d_2^1), \quad (6.14)$$

and the clamped condition at the top ends satisfies

$$U^j = 0 \text{ and } V^j = 0 \quad \text{at } z = -d_1^j. \quad (6.15)$$

## 6.3 Derivation of the solutions

### 6.3.1 Fluid domain

Here, an innovative analytical approach to describing wave interference among multiple cages is presented. The wavefield can be regarded as the superposition of scattered waves from all cages and incident waves, and the scattered wave potentials due to each cage are transformed in different local coordinate systems by Graf's addition theorem, which greatly facilitates the derivation of particular solutions.

In view of the governing equation Eq. (6.2) and the boundary conditions of Eqs. (6.7) to (6.9), the velocity potential complex amplitude  $\varphi_e$  in the external region of the cages can be sought in the following form:

$$\varphi_e = \varphi^{I,j} + \varphi_e^S, \quad (6.16)$$

in which

$$\varphi^{I,j} = -\frac{igH \cosh[\kappa_0(z+h)]}{2\omega \cosh(\kappa_0 h)} e^{i\kappa_0 R^j \cos(\theta^j - \beta)} \sum_{m=-\infty}^{+\infty} i^m J_m(\kappa_0 r^j) e^{im(\theta^j - \beta)}, \quad (6.17)$$

$$\varphi_e^S = \sum_{j=1}^{NC} \sum_{m=-\infty}^{+\infty} \sum_{n=0}^{+\infty} A_{mn}^j R_{1m}^j(\kappa_n r^j) f_n(z) e^{im\theta^j}, \quad (6.18)$$

and the velocity potential complex amplitude  $\varphi_i^j$  in the internal region of each cage is

$$\varphi_i^j = \varphi^{I,j} + \varphi_i^{S,j}, \quad (6.19)$$



in which

$$\varphi_i^{S,j} = \sum_{m=-\infty}^{+\infty} \sum_{n=0}^{+\infty} B_{mn}^j R_{2m}^j(\kappa_n r^j) f_n(z) e^{im\theta^j}. \quad (6.20)$$

In the abovementioned equations, we have

$$R_{1m}^j(\kappa_n r^j) = \frac{H_m(\kappa_n r^j)}{H_m'(\kappa_n a^j)}, \quad R_{2m}^j(\kappa_n r^j) = \frac{J_m(\kappa_n r^j)}{J_m'(\kappa_n a^j)} \quad \text{and} \quad f_n(z) = \frac{\cosh[\kappa_n(z+h)]}{\cosh(\kappa_n h)}. \quad (6.21)$$

Furthermore, in Eq. (6.17),  $R_j$  and  $\Theta_j$  are the polar coordinates of each cylinder's centre in the global coordinate systems, and  $\kappa_n$ s are obtained by following the dispersion relation:

$$\omega^2 = g\kappa_n \tanh(\kappa_n h), \quad (6.22)$$

in which  $\kappa_0$  is the positive real root of Eq. (6.22) when  $n = 0$ , and  $\kappa_n$ s are the infinite positive imaginary roots of Eq. (6.22) when  $n > 0$ .  $A_{mn}^j$  and  $B_{mn}^j$  are the unknown constants.  $J_m$  is the first kind of Bessel function of the  $m$ th order, and  $H_m$  is the first kind of Hankel function of the  $m$ th order.

In the local coordinate system of the  $k$ th cylinder, Graf's addition theorem is invoked according to Abramowitz and Stegun (1965):

$$H_m(\kappa_n r^j) \times e^{im\theta^j} = \sum_{l=-\infty}^{+\infty} H_{m-l}(\kappa_n R^{jk}) \times J_{-l}(\kappa_n r^k) \times (-1)^{-l} \times e^{il\theta^k} \times e^{i(m-l)\alpha^{jk}}. \quad (6.23)$$

Notably, Eq. (6.23) is only valid when  $r^k < R^{jk}$ . Therefore, in the local coordinate system of the  $k$ th cylinder, Eq. (6.18) can be rewritten as

$$\varphi_e^{S,k} = \sum_{m=-\infty}^{+\infty} \sum_{n=0}^{+\infty} A_{mn}^k R_{1m}^k(\kappa_n r^k) f_n(z) e^{im\theta^k} + \sum_{j=1, j \neq k}^{NC} \sum_{m=-\infty}^{+\infty} \sum_{n=0}^{+\infty} \sum_{l=-\infty}^{+\infty} A_{ln}^j Y_{mnl}^{jk}(\kappa_n r^k) f_n(z) e^{im\theta^k}, \quad (6.24)$$

in which

$$Y_{mnl}^{jk}(\kappa_n r^k) = \frac{H_{l-m}(\kappa_n R^{jk})}{H_l'(\kappa_n a^j)} J_m(\kappa_n r^k) e^{i(l-m)\alpha^{jk}}. \quad (6.25)$$

Owing to the velocity continuity in Eq. (6.12) and the orthogonality of  $\cosh[\kappa_n(z+h)]$  over  $-h \leq z \leq 0$  and  $e^{im\theta}$  over  $0 \leq \theta \leq 2\pi$ , the following relationship is obtained:

$$B_{mn}^k - A_{mn}^k = \sum_{j=1, j \neq k}^{NC} \sum_{l=-\infty}^{+\infty} A_{ln}^j S_{mnl}^{jk}, \quad (6.26)$$

where

$$S_{mnl}^{jk} = \frac{H_{l-m}(\kappa_n R^{jk})}{H_l'(\kappa_n a^j)} J_m(\kappa_n a^k) e^{i(l-m)\alpha^{jk}}. \quad (6.27)$$

As a result, in the local coordinate system of the  $k$ th cylinder, Eq. (6.20) can also be rewritten as

$$\varphi_i^{S,k} = \sum_{m=-\infty}^{+\infty} \sum_{n=0}^{+\infty} A_{mn}^k R_{2m}^k(\kappa_n r^k) f_n(z) e^{im\theta^k} + \sum_{j=1, j \neq k}^{NC} \sum_{m=-\infty}^{+\infty} \sum_{n=0}^{+\infty} \sum_{l=-\infty}^{+\infty} A_{ln}^j Y_{mnl}^{jk}(\kappa_n r^k) f_n(z) e^{im\theta^k}, \quad (6.28)$$

and

$$\varphi_e^k - \varphi_i^k = \sum_{m=-\infty}^{+\infty} \sum_{n=0}^{+\infty} A_{mn}^k X_{mn}^k f_n(z) e^{im\theta^k} \quad \text{at } r^j = a^j, \quad (6.29)$$

where

$$X_{mn}^k = R_{1m}^k(\kappa_n a^k) - R_{2m}^k(\kappa_n a^k). \quad (6.30)$$

According to Bernoulli's equation, the dynamic pressure  $p$  is given by:

$$p = -\rho \frac{\partial \Phi}{\partial t} - \frac{\rho}{2} (\nabla \Phi \cdot \nabla \Phi), \quad (6.31)$$

where  $\rho$  is the water density, and the linearised form of the dynamic pressure  $p$  is

$$p = -\rho \frac{\partial \Phi}{\partial t} = \text{Re} \left[ -\rho \frac{\partial(\varphi e^{-i\omega t})}{\partial t} \right], \quad (6.32)$$

so the first-order pressure drop on each cage is defined as

$$\Delta p^j = p_e^j - p_i^j = \text{Re} \left[ i\omega \rho (\varphi_e^j - \varphi_i^j) e^{-i\omega t} \right] \quad \text{at } r^j = a^j. \quad (6.33)$$

As a result, the complex functions of the first-order wave force components in  $x$ -direction and  $y$ -direction acting on each cage are respectively

$$F_x^j = i\omega \rho a^j \int_{-(d_1^j+d_2^j)}^{-d_1^j} \int_0^{2\pi} (\varphi_e^j - \varphi_i^j) \cos(\pi - \theta^j) d\theta^j dz e^{-i\omega t}, \quad (6.34)$$

$$F_y^j = i\omega \rho a^j \int_{-(d_1^j+d_2^j)}^{-d_1^j} \int_0^{2\pi} (\varphi_e^j - \varphi_i^j) \sin(\pi - \theta^j) d\theta^j dz e^{-i\omega t}. \quad (6.35)$$

At present, there is limited literature on mean wave drift forces acting on fish cages, so the current study proposes a novel method to determine the mean wave drift forces. Although

### 6.3 Derivation of the solutions

the developed model is based on the linear wave theory, the mean wave drift forces can still be derived through the first-order solution. This is because the second-order potential has no contribution to the time-averaged value as the second-order term (Faltinsen, 1993). Therefore, the components of mean wave drift forces in  $x$ -direction and  $y$ -direction acting on each cage are

$$\begin{aligned}\overline{F_x^j} &= a^j \int_{-(d_1^j+d_2^j)}^{-d_1^j} \int_0^{2\pi} (p_e^j - p_i^j) \cos(\pi - \theta^j) d\theta^j dz e^{-i\omega t} \\ &= a^j \int_{-(d_1^j+d_2^j)}^{-d_1^j} \int_0^{2\pi} (\overline{p_e^j} - \overline{p_i^j}) \cos(\pi - \theta^j) d\theta^j dz e^{-i\omega t},\end{aligned}\quad (6.36)$$

$$\begin{aligned}\overline{F_y^j} &= a^j \int_{-(d_1^j+d_2^j)}^{-d_1^j} \int_0^{2\pi} (p_e^j - p_i^j) \sin(\pi - \theta^j) d\theta^j dz e^{-i\omega t} \\ &= a^j \int_{-(d_1^j+d_2^j)}^{-d_1^j} \int_0^{2\pi} (\overline{p_e^j} - \overline{p_i^j}) \sin(\pi - \theta^j) d\theta^j dz e^{-i\omega t},\end{aligned}\quad (6.37)$$

where the overline is the time-averaged operator. According to Eq. (6.31), the time-averaged dynamic pressure on each cage is

$$\begin{aligned}\overline{p^j} &= -\rho \frac{\partial \Phi^j}{\partial t} - \frac{\rho}{2} (\nabla \Phi^j \cdot \nabla \Phi^j) \\ &= -\frac{\rho}{2} \left\{ \left[ \text{Re} \left( \frac{\partial \varphi^j}{\partial r^j} e^{-i\omega t} \right) \right]^2 + \left[ \text{Re} \left( \frac{1}{a^j} \frac{\partial \varphi^j}{\partial \theta^j} e^{-i\omega t} \right) \right]^2 + \left[ \text{Re} \left( \frac{\partial \varphi^j}{\partial z} e^{-i\omega t} \right) \right]^2 \right\} \\ &= -\frac{\rho}{4} \left\{ \text{Re} \left[ \frac{\partial \varphi^j}{\partial r^j} \left( \frac{\partial \varphi^j}{\partial r^j} \right)^* \right] + \text{Re} \left[ \frac{1}{(a^j)^2} \frac{\partial \varphi^j}{\partial \theta^j} \left( \frac{\partial \varphi^j}{\partial \theta^j} \right)^* \right] + \text{Re} \left[ \frac{\partial \varphi^j}{\partial z} \left( \frac{\partial \varphi^j}{\partial z} \right)^* \right] \right\} \\ &= -\frac{\rho}{4} \left( \left| \frac{\partial \varphi^j}{\partial r^j} \right|^2 + \frac{1}{(a^j)^2} \left| \frac{\partial \varphi^j}{\partial \theta^j} \right|^2 + \left| \frac{\partial \varphi^j}{\partial z} \right|^2 \right) \quad \text{at } r^j = a^j.\end{aligned}\quad (6.38)$$

In order to facilitate the subsequent discussion of the results, the above wave forces are normalised as

$$K_{F_x^j} = \frac{|F_x^j|}{\rho g a^j h H}, \quad K_{F_y^j} = \frac{|F_y^j|}{\rho g a^j h H}, \quad \overline{K_{F_x^j}} = \frac{|\overline{F_x^j}|}{\rho g a^j h H} \quad \text{and} \quad \overline{K_{F_y^j}} = \frac{|\overline{F_y^j}|}{\rho g a^j h H}. \quad (6.39)$$

Moreover, because of the boundary condition Eq. (6.6), the free surface elevations  $\xi$  are given by

$$\xi = \text{Re} \left( \frac{i\omega\varphi e^{-i\omega t}}{g} \right). \quad (6.40)$$

### 6.3.2 Structural domain

For the governing equation Eq. (6.3) of the structural domain, the displacement components can be written as

$$\begin{aligned} U^j &= \text{Re} \left[ \sum_{m=-\infty}^{+\infty} U_m^j(z) e^{im\theta^j} e^{-i\omega t} \right] \\ V^j &= \text{Re} \left[ \sum_{m=-\infty}^{+\infty} V_m^j(z) e^{im\theta^j} e^{-i\omega t} \right] . \\ W^j &= \text{Re} \left[ \sum_{m=-\infty}^{+\infty} W_m^j(z) e^{im\theta^j} e^{-i\omega t} \right] \end{aligned} \quad (6.41)$$

in which the general solutions of  $U_m^j$ ,  $V_m^j$  and  $W_m^j$  can be expressed in the form:

$$\begin{aligned} U_m^j(z) &= \sum_{b=1}^4 \alpha_{mb}^j C_{mb}^j e^{q_{mb}^j z} + \sum_{n=0}^{+\infty} A_{mn}^j \gamma_{mn}^j F_{mn}^j f_n^1(z) \\ V_m^j(z) &= \sum_{b=1}^4 \beta_{mb}^j C_{mb}^j e^{q_{mb}^j z} + \sum_{n=0}^{+\infty} A_{mn}^j \delta_{mn}^j F_{mn}^j f_n(z) , \\ W_m^j(z) &= \sum_{b=1}^4 C_{mb}^j e^{q_{mb}^j z} + \sum_{n=0}^{+\infty} A_{mn}^j F_{mn}^j f_n(z) \end{aligned} \quad (6.42)$$

where

$$f_n^1(z) = \frac{\sinh[\kappa_n(z+h)]}{\cosh(\kappa_n h)}. \quad (6.43)$$

$C_{mb}^j$  is the unknown constant determined by the boundary value conditions in Eqs. (6.14) and (6.15). Furthermore, the determination of the unknown constants  $q_{mb}^j$ ,  $\alpha_{mb}^j$ ,  $\beta_{mb}^j$  and  $\gamma_{mb}^j$  has been elaborated on by Ma et al. (2022).

By substituting Eq. (6.42) into Eqs. (6.42) and (6.15) and applying the orthogonal operation, one obtains the following four equations:

$$\begin{cases} \sum_{n=0}^{+\infty} A_{mn}^j E_{mn1}^j + \sum_{b=1}^4 C_{mb}^j E_{mb1}^j = 0 \\ \sum_{n=0}^{+\infty} A_{mn}^j E_{mn2}^j + \sum_{b=1}^4 C_{mb}^j E_{mb2}^j = 0 \\ \sum_{n=0}^{+\infty} A_{mn}^j E_{mn3}^j + \sum_{b=1}^4 C_{mb}^j E_{mb3}^j = 0 \\ \sum_{n=0}^{+\infty} A_{mn}^j E_{mn4}^j + \sum_{b=1}^4 C_{mb}^j E_{mb4}^j = 0 \end{cases}, \quad (6.44)$$

in which

$$\begin{aligned} E_{mn1}^j &= \gamma_{mn}^j F_{mn}^j f_n^1(-d_1^k) \\ E_{mn2}^j &= \delta_{mn}^j F_{mn}^j f_n(-d_1^k) \\ E_{mn3}^j &= (a^j \kappa_n \gamma_{mn}^j F_{mn}^j + i m \nu^j \delta_{mn}^j F_{mn}^j + \nu^j F_{mn}^j) f_n[-(d_1^k + d_1^k)] \\ E_{mn4}^j &= (i m \gamma_{mn}^j F_{mn}^j + a^j \kappa_n \delta_{mn}^j F_{mn}^j) f_n^1[-(d_1^k + d_1^k)] \\ E_{mb1}^j &= \alpha_{mb}^j e^{-q_{mb}^j d_1^k} \\ E_{mb2}^j &= \beta_{mb}^j e^{-q_{mb}^j d_1^k} \\ E_{mb3}^j &= (a^j \alpha_{mb}^j q_{mb}^j + i m \nu^j \beta_{mb}^j + \nu^j) e^{-q_{mb}^j (d_1^k + d_1^k)} \\ E_{mb4}^j &= (i m \alpha_{mb}^j + a^j \beta_{mb}^j q_{mb}^j) e^{-q_{mb}^j (d_1^k + d_1^k)} \end{aligned} \quad (6.45)$$

### 6.3.3 Fluid-structure interactions

After obtaining the general solutions of the fluid domain and structural domain, the unknown constants  $A_{mn}^j$  can be determined only by the aforementioned boundary condition Eqs. (6.10) and (6.13) to obtain the particular solution to this physical problem.

At the boundary  $r^k = a^k$  for the  $k$ th cage, by substituting Eqs. (6.1), (6.16), (6.17), (6.24), (6.29), (6.41) and (6.42) into Eq. (6.10) and invoking the orthogonality manipulation along the net region  $-(d_1^j + d_2^j) \leq z \leq -d_1^j$ , one obtains

$$\begin{aligned} & \sum_{n=0}^{+\infty} A_{mn}^k (\kappa_n + i \kappa_0 \tau^k X_{mn}^k + i \omega F_{mn}^k) f_n(z) + \sum_{b=1}^4 C_{mb}^k i \omega e^{q_{mb}^k z} + \sum_{j=1, j \neq k}^{NC} \sum_{n=0}^{+\infty} \sum_{l=-\infty}^{+\infty} A_{ln}^j \kappa_n S_{mnl}^{jk} f_n(z) \\ & - \frac{i g H \kappa_0 \cosh[\kappa_0 (z+h)]}{2 \omega \cosh(\kappa_0 h)} e^{i \kappa_0 R^k \cos(\Theta^k - \beta)} \frac{i^m}{e^{i m \beta}} J_m'(\kappa_0 a^j) = 0. \end{aligned} \quad (6.46)$$

## Theoretical extension to wave interference effects in multi-cage systems

Similarly, by substituting Eqs. (6.1) and (6.29) into Eq. (6.13) and utilising the orthogonality operation along the gap region  $-h \leq z \leq -(d_1^j + d_2^j) \cup -d_1^j \leq z \leq 0$ , one obtains

$$\sum_{n=0}^{+\infty} A_{mn}^k X_{mn}^k f_n(z) = 0. \quad (6.47)$$

Therefore, Eqs. (6.46) and (6.47) can be described in a general form:

$$Z_m^k(z) = \sum_{n=0}^{+\infty} A_{mn}^k \zeta_{mn}^k(z) + \sum_{b=1}^4 C_{mb}^k \chi_{mb}^k(z) + \sum_{j=1, j \neq k}^{NC} \sum_{n=0}^{+\infty} \sum_{l=-\infty}^{+\infty} A_{ln}^j \eta_{mnl}^{jk}(z) + \lambda_m^k(z) = 0. \quad (6.48)$$

in which

$$\begin{aligned} \zeta_{mn}^k(z) &= \begin{cases} (\kappa_n + i\kappa_0 \tau^k X_{mn}^k + i\omega F_{mn}^k) f_n(z), & -(d_1^k + d_2^k) \leq z \leq -d_1^k \\ X_{mn}^k f_n(z), & -h \leq z \leq (d_1^k + d_2^k) \cup -d_1^k \leq z \leq 0 \end{cases} \\ \chi_{mb}^k(z) &= \begin{cases} i\omega e^{d_{mb}^k z}, & -(d_1^k + d_2^k) \leq z \leq -d_1^k \\ 0, & -h \leq z \leq (d_1^k + d_2^k) \cup -d_1^k \leq z \leq 0 \end{cases} \\ \eta_{mnl}^{jk}(z) &= \begin{cases} \kappa_n S_{mnl}^{jk} f_n(z), & -(d_1^k + d_2^k) \leq z \leq -d_1^k \\ 0, & -h \leq z \leq (d_1^k + d_2^k) \cup -d_1^k \leq z \leq 0 \end{cases} \\ \lambda_m^k(z) &= \begin{cases} -\frac{igH\kappa_0 \cosh[\kappa_0(z+h)]}{2\omega \cosh(\kappa_0 h)} e^{i\kappa_0 R^k \cos(\Theta^k - \beta)} \frac{i^m}{e^{im\beta}} J_m'(\kappa_0 a^j), & -(d_1^k + d_2^k) \leq z \leq -d_1^k \\ 0, & -h \leq z \leq (d_1^k + d_2^k) \cup -d_1^k \leq z \leq 0 \end{cases} \end{aligned} \quad (6.49)$$

By applying the least squares approximation, one gets

$$\int_{-h}^0 |Z_m^k(z)|^2 dz = \min \Rightarrow \int_{-h}^0 Z_m^k(z) \frac{\partial Z_m^k(z)}{\partial A_{mn}^k} dz = 0. \quad (6.50)$$

By truncating the infinite series terms outside the range of  $n = 1$  to  $N$ ,  $m = -M$  to  $M$  and  $l = -M$  to  $M$  in Eq. (6.48) and substituting it into Eq. (6.50), one obtains a system of

equations for  $m = -M$  to  $M$ :

$$\begin{aligned}
 & \sum_{n=0}^N A_{mn}^k \int_{-h}^0 \zeta_{mn}^k \zeta_{m0}^k dz + \sum_{b=1}^4 C_{mb}^k \int_{-h}^0 \chi_{mb}^k \zeta_{m0}^k dz \\
 & + \sum_{j=1, j \neq k}^{NC} \sum_{l=-M}^M \sum_{n=0}^N A_{ln}^j \int_{-h}^0 \eta_{mnl}^{jk} \zeta_{m0}^k dz = - \int_{-h}^0 \lambda_m^k \zeta_{m0}^k dz \\
 & \vdots \\
 & \sum_{n=0}^N A_{mn}^k \int_{-h}^0 \zeta_{mn}^k \zeta_{mN}^k dz + \sum_{b=1}^4 C_{mb}^k \int_{-h}^0 \chi_{mb}^k \zeta_{mN}^k dz \\
 & + \sum_{j=1, j \neq k}^{NC} \sum_{l=-M}^M \sum_{n=0}^N A_{ln}^j \int_{-h}^0 \eta_{mnl}^{jk} \zeta_{mN}^k dz = - \int_{-h}^0 \lambda_m^k \zeta_{mN}^k dz
 \end{aligned} \tag{6.51}$$

It can be found that each cage from  $j = 1$  to  $NC$  must satisfy Eq. (6.44) and Eq. (6.51), so the unknown constants  $A_{mn}^j$  and  $C_{mb}^j$  can have closed-form solutions.

Consequently, an overall matrix equation with respect to the constants  $A_{mn}^j$  and  $C_{mb}^j$  can be expressed as

$$\begin{bmatrix} \mathbf{O}^1 & \mathbf{P}^2 & \dots & \mathbf{P}^{NC-1} & \mathbf{P}^{NC} \\ \mathbf{P}^1 & \mathbf{O}^2 & \dots & \mathbf{P}^{NC-1} & \mathbf{P}^{NC} \\ \vdots & \vdots & \ddots & \vdots & \vdots \\ \mathbf{P}^1 & \mathbf{P}^2 & \dots & \mathbf{O}^{NC-1} & \mathbf{P}^{NC} \\ \mathbf{P}^1 & \mathbf{P}^2 & \dots & \mathbf{P}^{NC-1} & \mathbf{O}^{NC} \end{bmatrix} \begin{bmatrix} \mathbf{A}^1 \\ \mathbf{A}^2 \\ \vdots \\ \mathbf{A}^{NC-1} \\ \mathbf{A}^{NC} \end{bmatrix} = \begin{bmatrix} \mathbf{Q}^1 \\ \mathbf{Q}^2 \\ \vdots \\ \mathbf{Q}^{NC-1} \\ \mathbf{Q}^{NC} \end{bmatrix}, \tag{6.52}$$

where the submatrix in Eq. (6.52) is

$$\begin{aligned}
 \mathbf{O}^k &= \begin{bmatrix} \mathbf{O}_{-M}^k & & \\ & \ddots & \\ & & \mathbf{O}_M^k \end{bmatrix}, \quad \mathbf{P}^j = \begin{bmatrix} \mathbf{P}_{-M,-M}^j & \dots & \mathbf{P}_{-M,M}^j \\ \vdots & \ddots & \vdots \\ \mathbf{P}_{M,-M}^j & \dots & \mathbf{P}_{M,M}^j \end{bmatrix}, \\
 \mathbf{A}^j &= [\mathbf{A}_{-M}^j \quad \dots \quad \mathbf{A}_M^j]^{\mathbf{H}}, \quad \mathbf{Q}^j = [\mathbf{Q}_{-M}^j \quad \dots \quad \mathbf{Q}_M^j]^{\mathbf{T}},
 \end{aligned} \tag{6.53}$$

and

$$\begin{aligned}
 \mathbf{O}_m^k &= \begin{bmatrix} \int_{-h}^0 \zeta_{m0}^k * \zeta_{m0}^k & \cdots & \int_{-h}^0 \zeta_{mN}^k * \zeta_{m0}^k & \int_{-h}^0 \chi_{m1}^k * \zeta_{m0}^k & \cdots & \int_{-h}^0 \chi_{m4}^k * \zeta_{m0}^k \\ \vdots & \ddots & \vdots & \vdots & \ddots & \vdots \\ \int_{-h}^0 \zeta_{m0}^k * \zeta_{mN}^k & \cdots & \int_{-h}^0 \zeta_{mN}^k * \zeta_{mN}^k & \int_{-h}^0 \chi_{m1}^k * \zeta_{mN}^k & \cdots & \int_{-h}^0 \chi_{m4}^k * \zeta_{mN}^k \\ E_{m01}^j * & \cdots & E_{mN1}^j * & E_{m11}^j * & \cdots & E_{m41}^j * \\ \vdots & \ddots & \vdots & \vdots & \ddots & \vdots \\ E_{m04}^j * & \cdots & E_{mN4}^j * & E_{m14}^j * & \cdots & E_{m44}^j * \end{bmatrix}, \\
 \mathbf{P}_{ml}^j &= \begin{bmatrix} \int_{-h}^0 \eta_{m0l}^{jk} * \zeta_{m0}^k & \cdots & \int_{-h}^0 \eta_{mNl}^{jk} * \zeta_{m0}^k & 0 & \cdots & 0 \\ \vdots & \ddots & \vdots & \vdots & \ddots & \vdots \\ \int_{-h}^0 \eta_{m0l}^{jk} * \zeta_{mN}^k & \cdots & \int_{-h}^0 \eta_{mNl}^{jk} * \zeta_{mN}^k & 0 & \cdots & 0 \\ & & 0 & \cdots & 0 & 0 \\ & & \vdots & \ddots & \vdots & \vdots \\ & & 0 & \cdots & 0 & 0 \end{bmatrix}, \\
 \mathbf{A}_m^j &= [A_{m0}^j \quad \cdots \quad A_{mN}^j \quad C_{m1}^j \quad \cdots \quad C_{m4}^j], \\
 \mathbf{Q}_m^j &= \left[ -\int_{-h}^0 \lambda_m^k * \zeta_{m0}^k dz \quad \cdots \quad -\int_{-h}^0 \lambda_m^k * \zeta_{mN}^k dz \quad 0 \quad \cdots \quad 0 \right].
 \end{aligned} \tag{6.54}$$

Based on the above mathematical derivations, the distribution of the wavefield around the net cage array and the corresponding dynamic responses of the cages can be obtained. In this paper, we choose an array of cages with two rows by three columns for the discussion, and the layout is illustrated in Fig. 6.3. A numerical code based on MATLAB language has been developed for the simulated results.

## 6.4 Convergence studies and model validation

### 6.4.1 Convergence studies

For the eigenfunction-expansion method, the accuracy of the solution is acceptable only when the series converges. Therefore, convergence studies had to be carried out to establish the appropriate truncation terms  $N$  and  $M$  for use in the analysis. The convergence studies adopted the constant parameters:  $H = 7$  m,  $\beta = \pi/4$ ,  $h = 200$  m,  $a^j = 50$  m,  $t_s^j/a^j = 10^{-4}$ ,



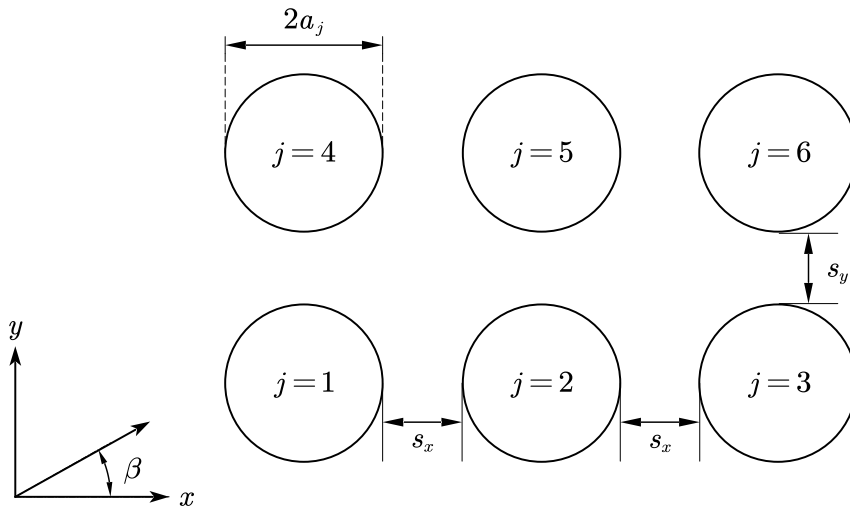


**Fig. 6.3** Layout of an array of cylindrical net cages with two rows by three columns.

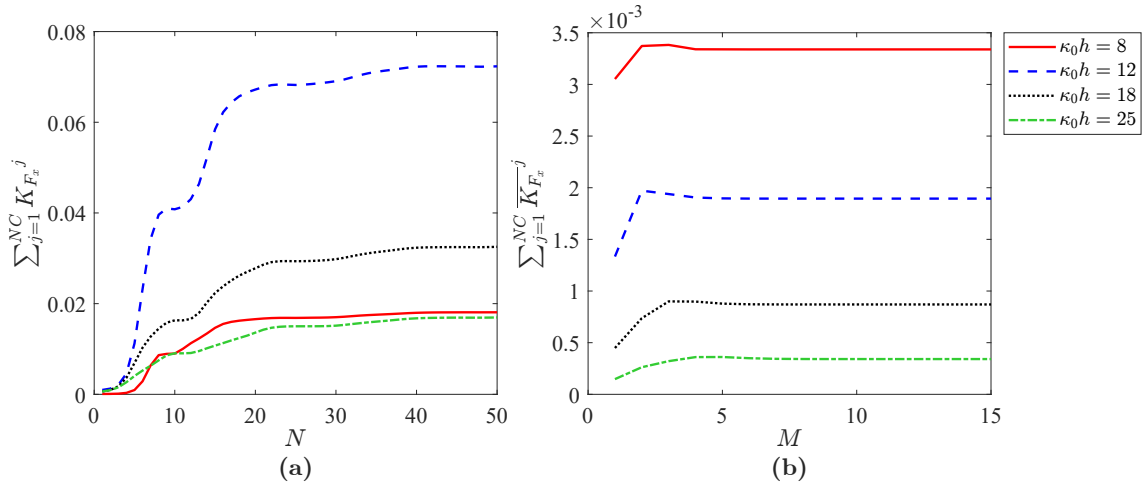
$d_1^j/h = 0.05$ ,  $d_2^j/h = 0.25$ ,  $\tau^j = 1 + 1i$ ,  $\nu^j = 0.3$ ,  $\rho_s^j/\rho = 1.2$ ,  $E^j/(\rho_s^j gh) = 10^3$  and  $s_x/h = s_y/h = 0.1$ .

Fig. 6.4a shows the sum of the coefficients  $K_{F_x}^j$  from Eq. (6.39) for all cages versus the truncated term  $N$ , in which the first-order wave force  $F_x^j$  in Eq. (6.34) is only determined by the root number  $n$  of the dispersion relationship Eq. (6.34) due to the orthogonality of  $e^{im\theta}$ . It can be seen that the solution is converged when  $N \leq 40$ .

Alternatively, the mean wave drift force  $\overline{F_x}^j$  in Eq. (6.36) is dependent on both the numbers of series terms  $n$  and  $m$  because of the existence of the nonlinear term. In the convergence study of the truncated term  $M$  (Fig. 6.4b), where  $N$  is taken as 40 (referring to Fig. 6.4a), the sum of the coefficients  $\overline{K_{F_x}^j}$  from Eq. (6.39) of all cages starts being gradually stabilised when  $M$  is greater than 5. As a result, in the current study, it is essential to take  $N = 40$  and  $M = 10$  to guarantee adequate accuracy and a reasonable computational amount when determining the wave action on the net cage.

## 6.4.2 Model validation

For the model verification, we first compared our results with those obtained by Chen et al. (2011) who employed the BIEM for the free water surface elevation amplitude  $\xi_a$  around four rigid permeable cylinders, as shown in Fig. 6.5.  $\xi_a$  is the modulus of the complex function in Eq. (6.40). The other constant parameters are  $H = 1$ ,  $\beta = \pi/4$ ,  $a^j = 0.2$ ,  $\kappa_0 a^j = \pi/2$ ,  $h/a^j = 5$ ,  $d_1^j/h = 0$ ,  $d_2^j/h = 1$ ,  $\tau^j = 1$ ,  $\nu^j = 0.3$ ,  $\rho_s^j/\rho = 1.2$ ,  $E^j/(\rho_s^j gh) = 10^9$  and  $s_x/h = s_y/h = 0.4$ . It can be seen that the results agree very well. Note that  $E^j/(\rho_s^j gh) = 10^9$  is assumed in order to guarantee that the deformation of the cylinder can be neglected.



**Fig. 6.4** Convergence studies for the truncated terms  $N$  and  $M$ : (a)  $\sum_{j=1}^{NC} K_{F_x}^j$  versus  $N$ ; (b)  $\sum_{j=1}^{NC} \overline{K_{F_x}^j}$  versus  $M$ ,  $N = 40$ . The other constant parameters are  $H = 7$  m,  $\beta = \pi/4$ ,  $h = 200$  m,  $a^j = 50$  m,  $t_s^j/a^j = 10^{-4}$ ,  $d_1^j/h = 0.05$ ,  $d_2^j/h = 0.25$ ,  $\tau^j = 1+1i$ ,  $\nu^j = 0.3$ ,  $\rho_s^j/\rho = 1.2$ ,  $E^j/(\rho_s^j gh) = 10^3$  and  $s_x/h = s_y/h = 0.1$ .

The close agreement of results demonstrates that the developed analytical solution can accurately describe the wavefield distribution around multiple porous cylindrical structures.

Second, the present solution can also predict results in reasonably good agreement with the solutions obtained by Park and Koo (2015) for the total wave force along the  $x$ -axis direction on four rigid floating porous cages wherein the constant parameters are  $H = 1$ ,  $a^j = 8.44$  m,  $h = 200$  m,  $d_1^j/h = 0$ ,  $d_2^j/h = 0.175$ ,  $\nu^j = 0.3$ ,  $\rho_s^j/\rho = 1.2$ ,  $E^j/(\rho_s^j gh) = 10^9$  and  $s_x/h = s_y/h = 0.347$ , and the first-order wave force  $F_x^j$  is from Eq. (6.34). Some slight discrepancies are observed due to the presence of an impermeable bottom horizontal thin plate in the work of Park and Koo (2015), especially for the condition with short waves (seen in Fig. 6.6).

In addition, in order to validate the solution for the hydroelastic interactions between waves and net cages, the present model is compared with the solutions of Ma et al. (2022) for the wave force on a single flexible net cage. The constant parameters are taken as  $H = 7$  m,  $\beta = 0$ ,  $h = 200$  m,  $a^j = 50$  m,  $t_s^j/a^j = 10^{-4}$ ,  $d_1^j/h = 0$ ,  $d_2^j/h = 0.25$ ,  $\nu^j = 0.3$ ,  $\rho_s^j/\rho = 1.2$  and  $E^j/(\rho_s^j gh) = 10^3$ . For the cage layout in Fig. 6.3, the interaction among the cages due to the wave interference effect is insignificant when considering a limiting scenario where  $s_x/h = s_y/h = 10^5$ . At this time, the wave forces on each cage will be close to those on the single cage. In Fig. 6.7, the coefficient  $K_{F_x}^j$  is calculated from Eq. (6.39). There are no apparent differences between the current results and the results of Ma et al. (2022), thus validating the present solution that describes FSI.

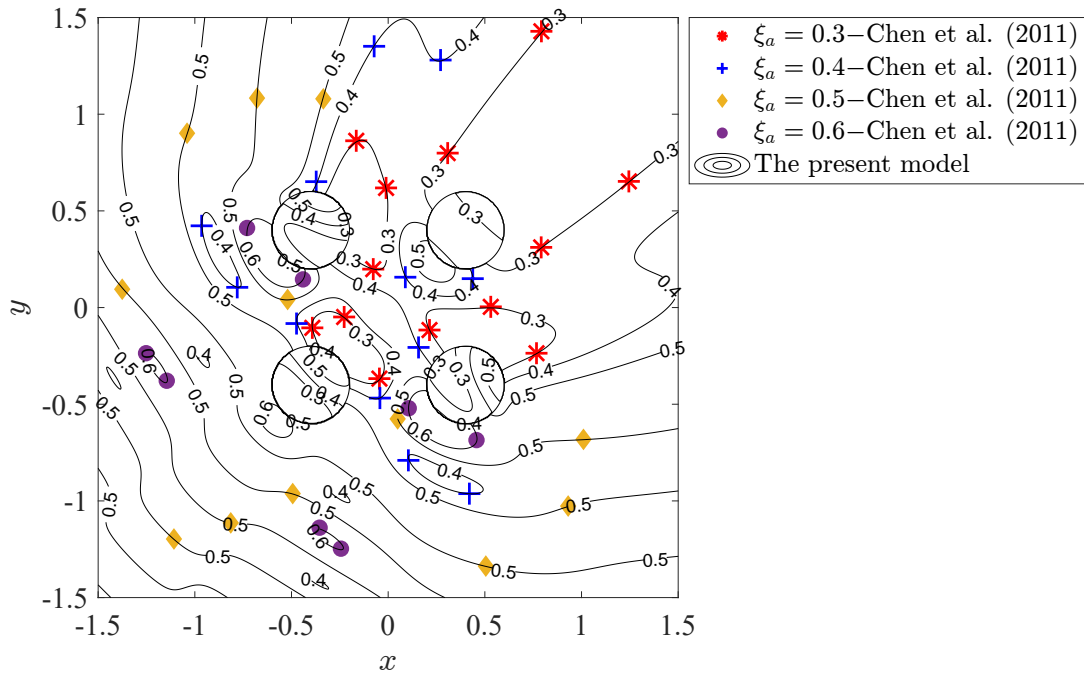


**Fig. 6.5** Comparison of the free water surface elevation amplitude  $\xi_a$  around four porous cylinders. The other constant parameters are  $H = 1$ ,  $\beta = \pi/4$ ,  $a^j = 0.2$ ,  $\kappa_0 a^j = \pi/2$ ,  $h/a^j = 5$ ,  $d_1^j/h = 0$ ,  $d_2^j/h = 1$ ,  $\tau^j = 1$ ,  $\nu^j = 0.3$ ,  $\rho_s^j/\rho = 1.2$ ,  $E^j/(\rho_s^j gh) = 10^9$  and  $s_x/h = s_y/h = 0.4$ .

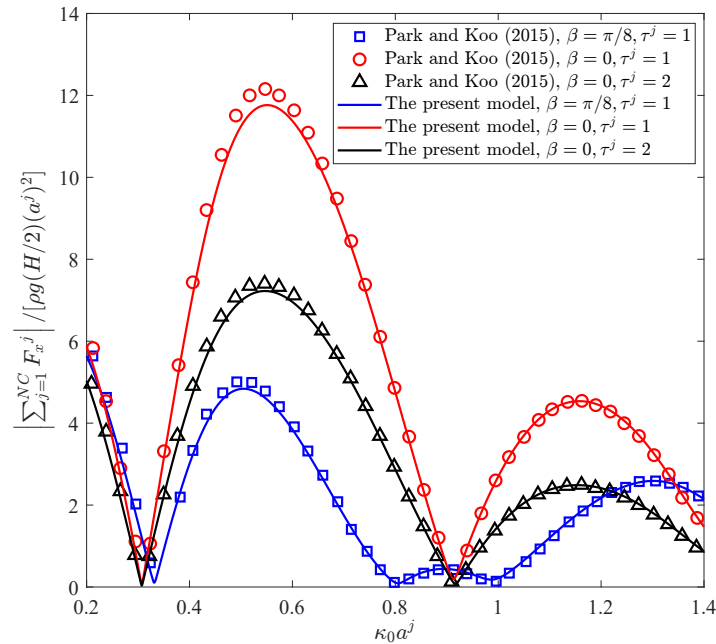


**Fig. 6.6** Comparison of the total wave force on four floating porous cages. The other constant parameters are  $H = 1$ ,  $a^j = 8.44$  m,  $h = 200$  m,  $d_1^j/h = 0$ ,  $d_2^j/h = 0.175$ ,  $\nu^j = 0.3$ ,  $\rho_s^j/\rho = 1.2$ ,  $E^j/(\rho_s^j gh) = 10^9$  and  $s_x/h = s_y/h = 0.347$ .

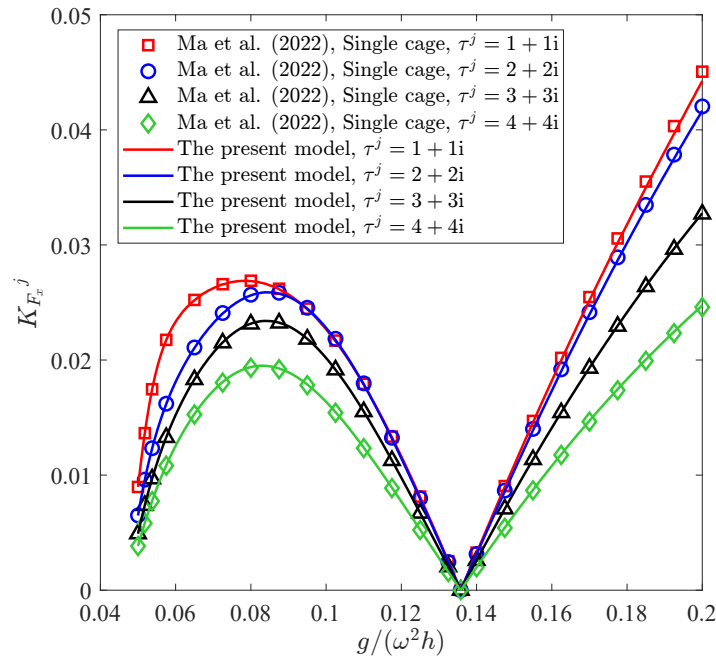


**Fig. 6.7** Comparison of the normalised wave forces  $K_{F_x}^j$  on an array of flexible porous cages and a single flexible porous cage. The other constant parameters are  $H = 7$  m,  $\beta = 0$ ,  $h = 200$  m,  $a^j = 50$  m,  $t_s^j/a^j = 10^{-4}$ ,  $d_1^j/h = 0$ ,  $d_2^j/h = 0.25$ ,  $\nu^j = 0.3$ ,  $\rho_s^j/\rho = 1.2$ ,  $E^j/(\rho_s^j gh) = 10^3$  and  $s_x/h = s_y/h = 10^5$ .

## 6.5 Results and discussions

In this section, some important hydroelastic characteristics of a fish cage array in waves are discussed from the analytical solutions developed. In the sea trial examples, the cage array is designed with a real scale practised in engineering. For the return period from 50 to 100 years, the sample metocean data in El-Reedy (2019) illustrate that the maximum wave height is from 6.6 to 7.2 m associated with the wave period from 7.7 to 8.0 s. It is also recommended that the fish cages be located at a site where the water depth is greater than three times the cages' height (Cardia and Lovatelli, 2015). To facilitate consecutive discussions, several case groups with varied studied parameters are defined in Table 6.1, and the constant parameters are adopted as  $H = 7$  m,  $h = 200$  m,  $a^j = 50$  m,  $t_s^j/a^j = 10^{-4}$ ,  $d_1^j/h = 0.05$ ,  $d_2^j/h = 0.25$ ,  $\nu^j = 0.3$ ,  $\rho_s^j/\rho = 1.2$  and  $E^j/(\rho_s^j gh) = 10^3$ .

### 6.5.1 Wave interference effects

Wave interference is caused by the overlapping and superposition of incident waves and scattered waves generated by multiple cages in space, resulting in enhanced or weakened fluid oscillations in some areas. By plotting the contour maps of the wave amplitude  $\xi_a$ ,

**Table 6.1** Case groups with different studied parameters (Study III).

Cases	$\beta$	$\kappa_0 h$	$\tau^j$	$s_x/h = s_y/h$
A1	0	12	1+1i	0.1
A2	$\pi/6$	12	1+1i	0.1
A3	$\pi/3$	12	1+1i	0.1
A4	$\pi/2$	12	1+1i	0.1
B1	$\pi/4$	8	1+1i	0.1
B2	$\pi/4$	12	1+1i	0.1
B3	$\pi/4$	18	1+1i	0.1
B4	$\pi/4$	25	1+1i	0.1
C1	$\pi/4$	12	1+1i	0.1
C2	$\pi/4$	12	1+1i	0.2
C3	$\pi/4$	12	1+1i	0.3
C4	$\pi/4$	12	1+1i	0.4
D1	$\pi/4$	12	0	0.1
D2	$\pi/4$	12	1+1i	0.1
D3	$\pi/4$	12	2+2i	0.1
D4	$\pi/4$	12	3+3i	0.1

one can have a better understanding of the feature of this phenomenon.  $\xi_a$  is the modulus of the complex function in Eq. (6.40).

Fig. 6.8 shows the amplitude distribution of the free water elevation around the net cage array when incident waves propagate in different directions. It can be observed that there are some "wake areas" on the leeward sides of the cages along the direction of wave incidence where the wave amplitude is severely attenuated, especially for the rear cages. In the inner regions of these cages, the wave amplitude also has different extents of reductions.

As shown in Fig. 6.9, if the incident wavelength is gradually reduced while the array layout is maintained, the distribution of the wave surface exhibits a weaker perturbation. This is because the diffraction effect of the wave becomes minor as the incident wavelength becomes smaller relative to the interval among the cages. Conversely, if the spacing among the cages is increased while maintaining a constant incident wavelength, the perturbation is also weakened to an extent, as seen in Fig. 6.10. As a result, increasing the ratio of wavelength to cage spacing can intensify the wave interference effects.

With regard to the porous effect of cages, an impermeable case reveals different properties from permeable cases. In Fig. 6.11a, an apparent increase of the wave amplitude occurs inside the impermeable cages, but the permeable cages are beneficial to dissipate

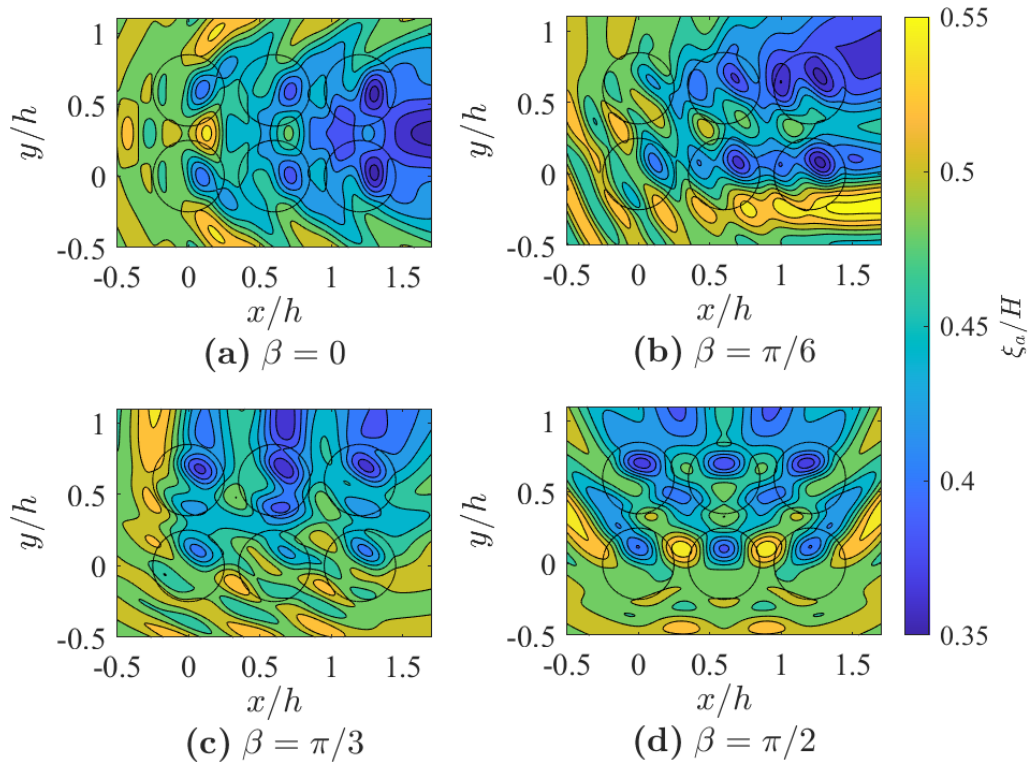


**Fig. 6.8** Contour plots of the free water surface elevation amplitude  $\xi_a$  around a  $2 \times 3$  array of net cages under different incident wave angles, (a) to (d): Cases A1 to A4.

the wave energy, as seen in Figs. 6.11b to 6.11d. As a result, porous fish cages are more appropriate choices in industrial practice. Additionally, as the opening ratio of the fish cage net increases, its disturbance to the wave surface will be minor as well.

From the above contour plots of the wave amplitude, it can be found that when the wave interference effect is significant, the oscillation amplitude of the liquid inside the cage is weakened to a certain extent, which is beneficial for fish to thrive. In low-energy environments, more feed energy is available for fish growth rather than being wasted compensating for swimming behaviour (Wiegerink et al., 2022).

### 6.5.2 Structural dynamic responses

For the structural dynamic response, the first-order pressure and mean pressure acting on the cage can be calculated from Eqs. (6.32) and (6.38), and the displacements of the cages are obtained from Eqs. (6.41) and (6.42). The amplitudes of these physical quantities are the moduli of the corresponding complex functions.

Case B2 ( $\beta = \pi/4$ ) is selected to discuss the dynamic behaviours of the net cages. The deformed net cages and corresponding first-order pressure drop on the interface of each

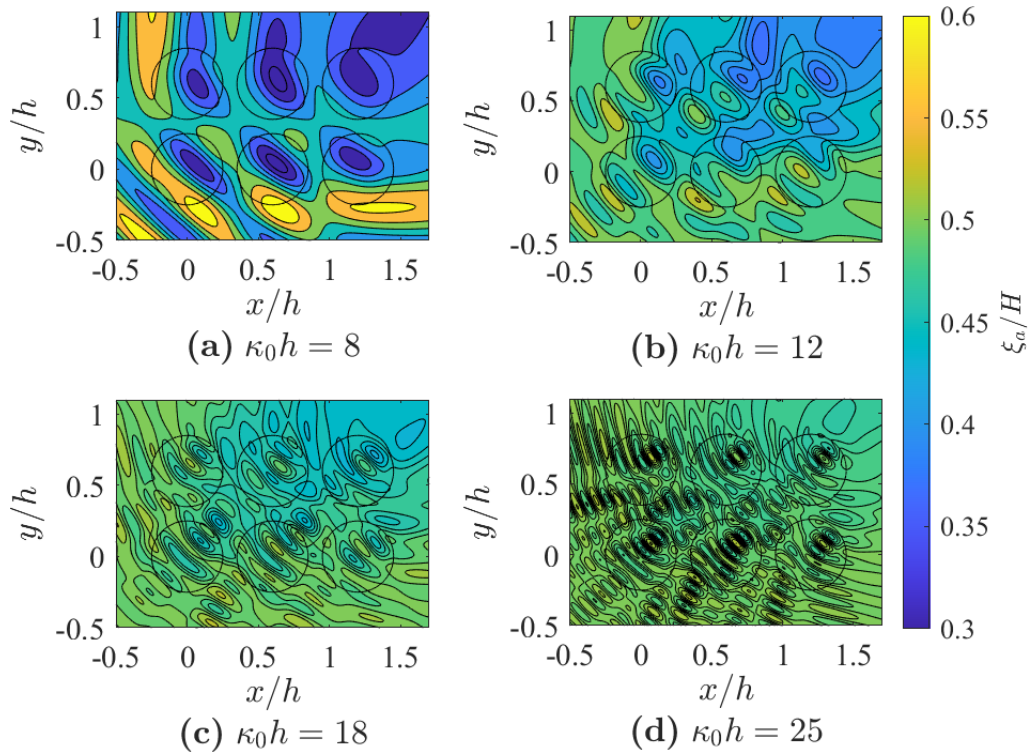


**Fig. 6.9** Contour plots of the free water surface elevation amplitude  $\xi_a$  around a  $2 \times 3$  array of net cages under different incident wavelengths, (a) to (d): Cases B1 to B4.

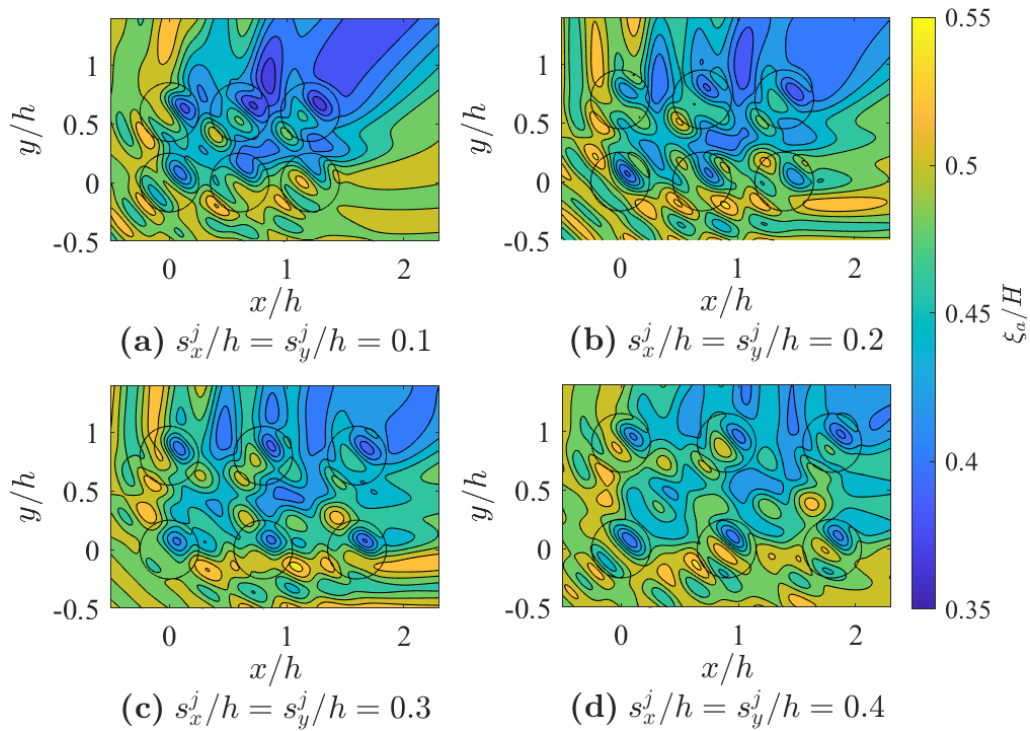


**Fig. 6.10** Contour plots of the free water surface elevation amplitude  $\xi_a$  around a  $2 \times 3$  array of net cages under different cage spacings, (a) to (d): Cases C1 to C4.

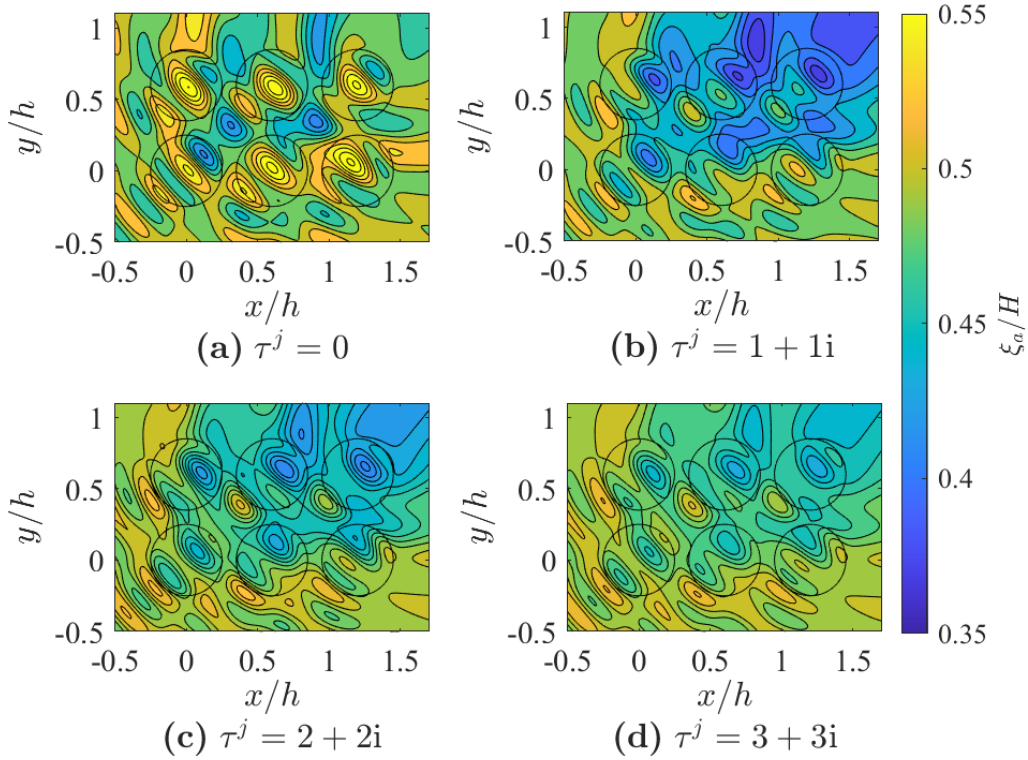


**Fig. 6.11** Contour plots of the free water surface elevation amplitude  $\xi_a$  around a  $2 \times 3$  array of net cages under different net porous effect parameters, (a) to (d): Cases D1 to D4.

cage are illustrated in Fig. 6.12 when time  $t$  is equal to half of the wave period, and the overall displacements of the cages have been exaggerated to twice the scale. Critical wave actions and dynamic responses mainly occur at the top part of the cages near the free water surface, and the dynamic response of each cage has unequal phase differences.

The amplitude distribution of the first-order pressure drop on each cage is shown in Fig. 6.13. For all cages, their foremost peak values of  $\Delta p_a^j$  are located around  $\theta^j/(2\pi) = 0.625$  (windward side) and  $z/h = -0.1$ , and the minor peaks are near the position of  $\theta^j/(2\pi) = 0.125$  (leeward side) and  $z/h = -0.925$ . However, for the time-averaged values of the pressure drop  $\overline{\Delta p_a^j}$  on these cages (Fig. 6.14), the peaks appear closer to the top of the cages, and their circumferential positions are also slightly different. Notably, the mean wave drift loads acting on cages  $j = 4$  and  $5$  are in the opposite direction to those imposed on cages  $j = 1, 2, 3$  and  $4$  (positive values indicate that the loads are pointed towards the cages' centres, while negative values mean that the loads are pointed away from the cages' centres). In other words, the mean drift effect of the waves drives the front and rear cages closer to each other in the direction of incidence. This phenomenon may be because the rear cages are affected by the transmitted waves passing through the cages in the front. Therefore, the mooring pre-tension should be provided to suppress the corresponding displacements in the design.



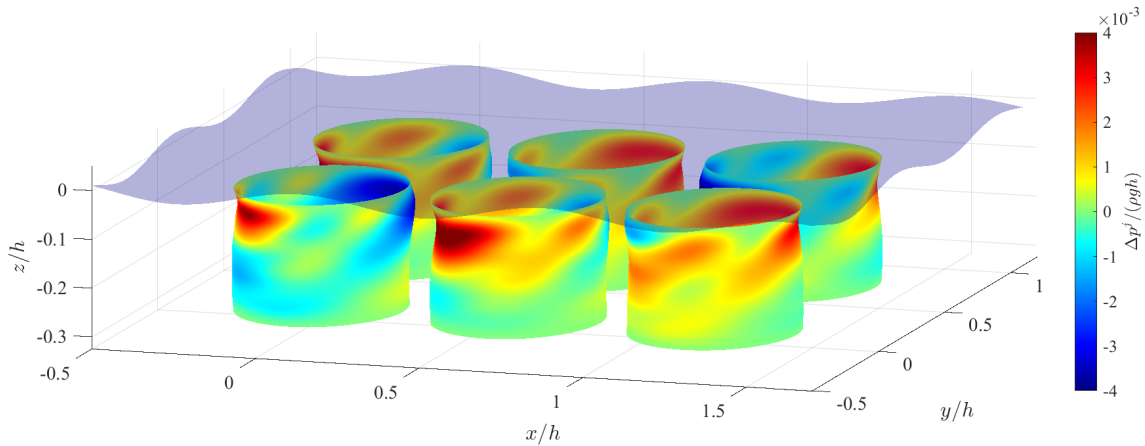


**Fig. 6.12** First-order pressure drop  $\Delta p^j$  on a  $2 \times 3$  array of net cages with an exaggerated deformation of twice the scale and the nearby free water surface (purple shaded), Case B2.

Finally, the amplitudes of the displacement components for all cages are contoured in Figs. 6.15 to 6.17. At the top end of these cages, their axial displacement amplitudes  $U_a^j$  and circumferential displacement amplitudes  $V_a^j$  are both zero due to the edge constraint Eq. (6.15). The major and minor peaks of  $U_a^j$  are around  $\theta^j/(2\pi) = 0.625$  and  $0.125$ , respectively. However, the magnitudes of  $V_a^j$  present peaks around  $\theta^j/(2\pi) = 0.27, 0.5, 0.75$  and  $0.97$ . As for the radial displacement amplitude  $W_a^j$ , its distribution is similar to the amplitude contour plots of the first-order pressure drop  $\Delta p_a^j$  because the pressure drop is the dominant action driving the radial deformation of the cage in Eq. (6.3).

### 6.5.3 Parametric studies

Parametric studies on the wave forces acting on the array of net cages are performed, which are compared with the results from the case with a single cage as well. The parameters that may significantly impact wave interference in the fish cage array are considered, including the incident wave angle  $\beta$ , the incident wavenumber  $\kappa_0$ , the porous resistance and fluid inertial parameters of the net  $\tau_r^j$  and  $\tau_i^j$ , the cage radius  $a^j$  and the spacings  $s_x$  and  $s_y$  among these cages. The normalised wave force coefficients are calculated according to Eqs. (6.34) to (6.37) and (6.39). The other parameters are controlled as  $H = 7$  m,  $h = 200$  m,  $t_s^j = 0.005$  m,  $d_1^j/h = 0.05$ ,  $d_2^j/h = 0.25$ ,  $\nu^j = 0.3$ ,  $\rho_s^j/\rho = 1.2$  and  $E^j/(\rho_s^j g h) = 10^3$  if there are no specific explanations.

Regarding the overall tendency, when the incident wave angle changes from  $0$  to  $\pi/2$ , it is reasonable that the wave force components in the  $x$ -axis direction on the cages gradually decrease and that the components in the  $y$ -axis direction manifest an increase, as indicated in Fig. 6.18. For cage  $j = 3$ , its nondimensional wave force components  $K_{F_x^j}$  and  $\overline{K}_{F_x^j}$

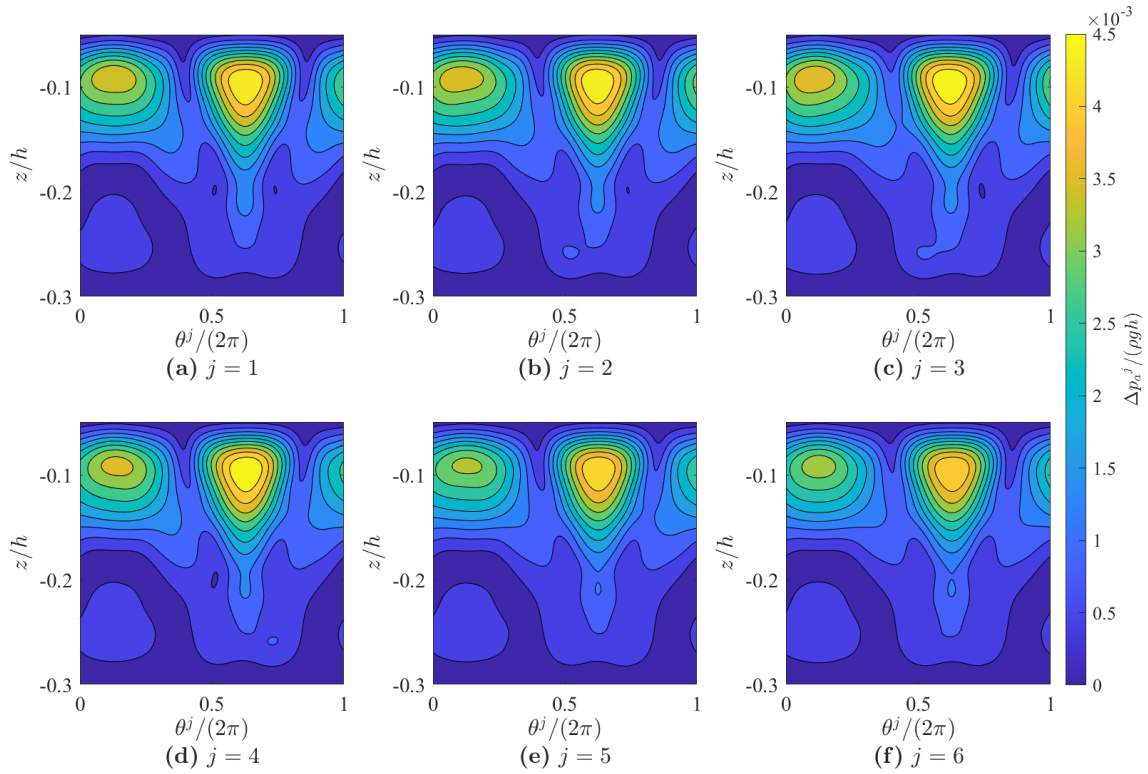


**Fig. 6.13** Spatial contour plots of the amplitude of first-order pressure drop  $\Delta p_a^j$  on the interface of each cage, Case B2.

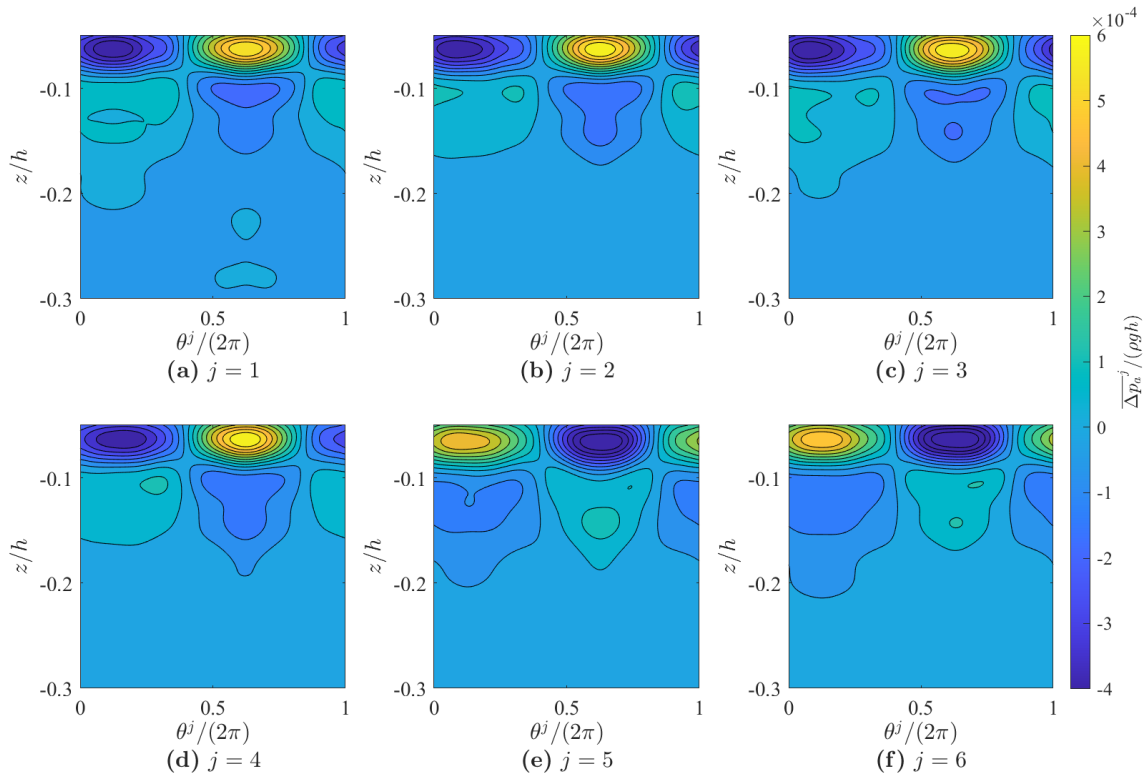


**Fig. 6.14** Spatial contour plots of the amplitude of time-averaged pressure drop  $\overline{\Delta p_a^j}$  on the interface of each cage, Case B2.

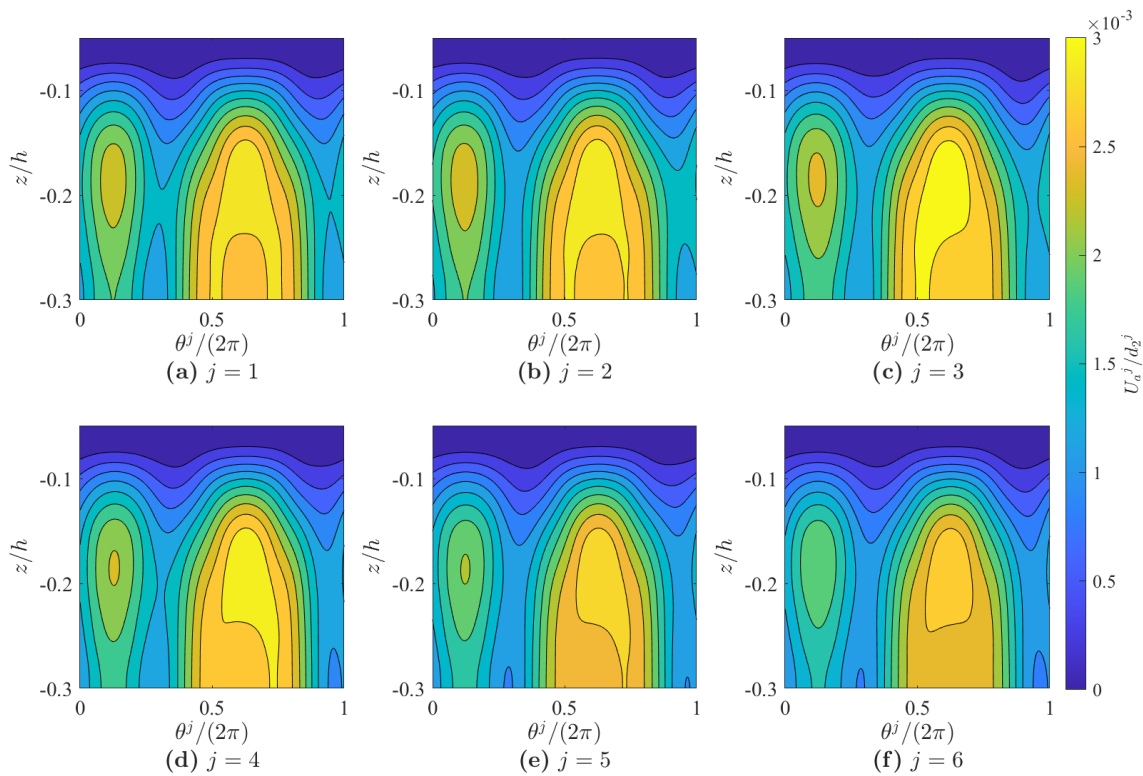


**Fig. 6.15** Spatial contour plots of the amplitude of axial displacement  $U_a^j$  of each cage, Case B2.

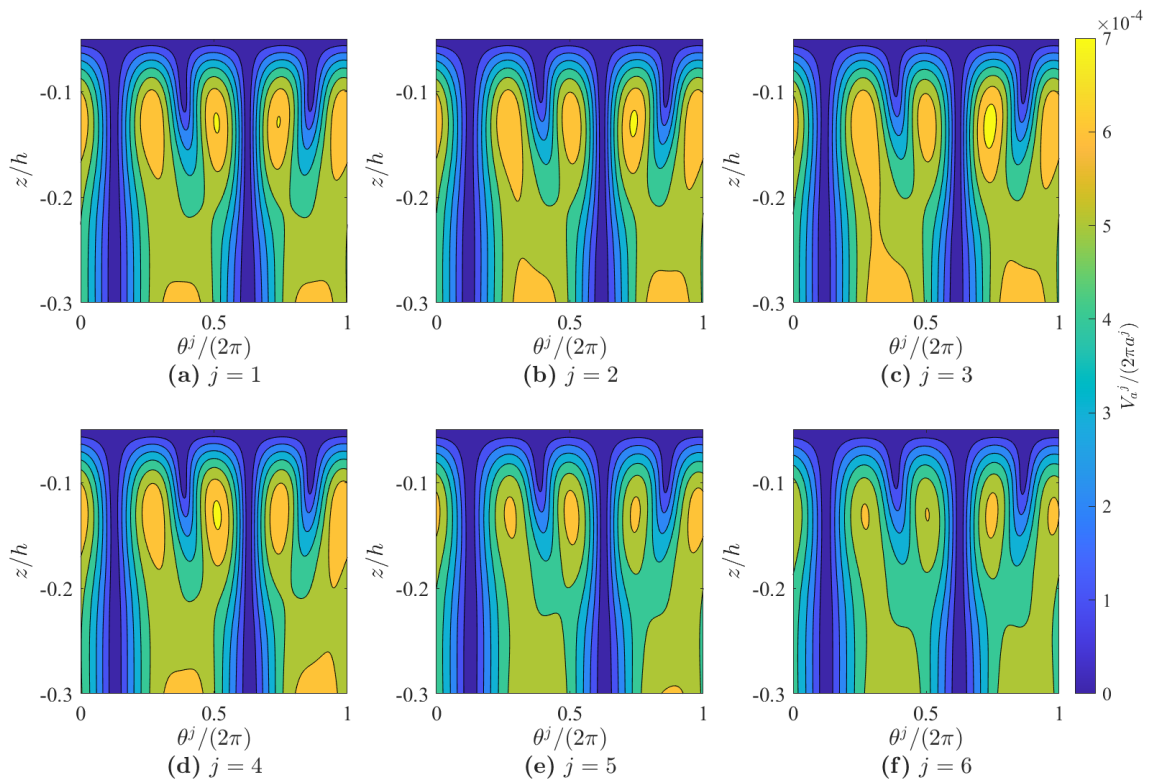


**Fig. 6.16** Spatial contour plots of the amplitude of circumferential displacement  $V_a^j$  of each cage, Case B2.

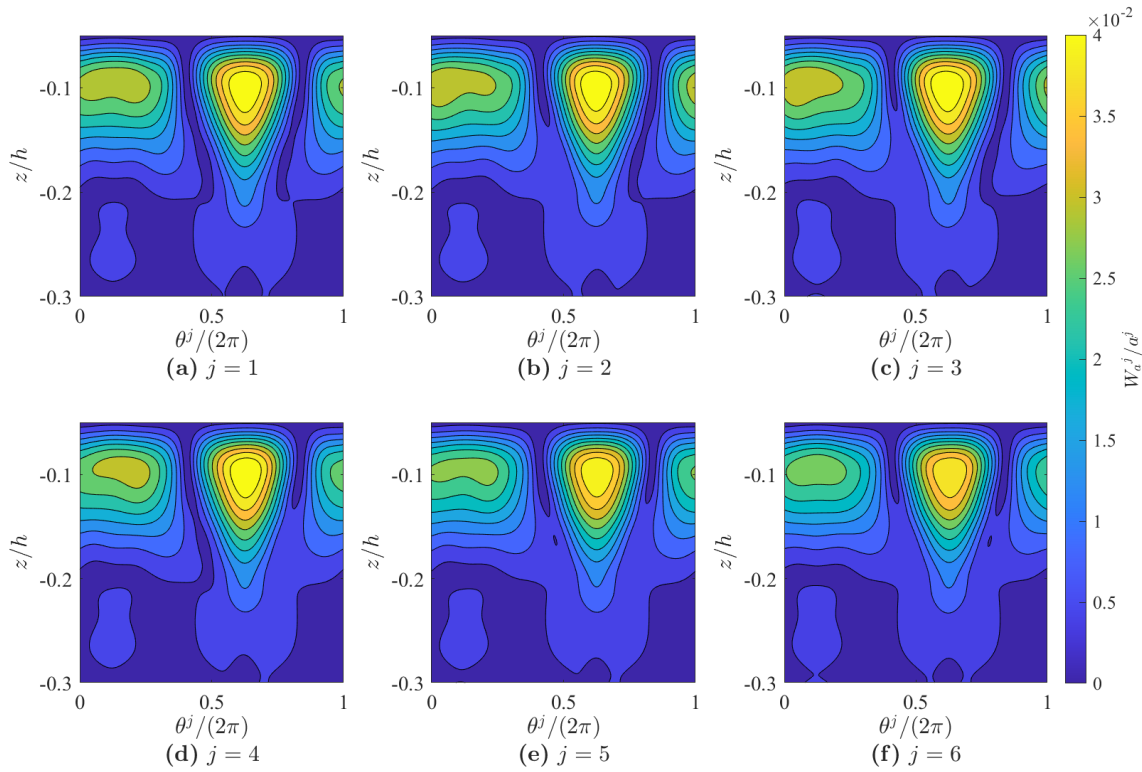


**Fig. 6.17** Spatial contour plots of the amplitude of axial displacement  $W_a^j$  of each cage, Case B2.

reach peak points when  $\beta/(2\pi)$  is 0.0205 and 0.106, and the nondimensional wave force components  $K_{F_y}^j$  and  $\overline{K_{F_y}}^j$  of cage  $j = 4$  present a peak point at  $\beta/(2\pi) = 0.241$ . In addition, the peak points of the mean wave drift force coefficients  $\overline{K_{F_x}}^j$  and  $\overline{K_{F_y}}^j$  appear when  $\beta/(2\pi) = 0.01025$  and 0.189, respectively, for cage  $j = 6$ . Nevertheless, under varied incident wave angles, the wave force coefficients of cage  $j = 1$  are approximately consistent with those of the single cage where no peak point is presented. This means that the other cages are influenced significantly by the interaction among the multiple cages.

For all cages, the wave forces reach the maximum values in the range when  $\kappa_0 h$  is less than 2 as shown in Fig. 6.19. Notably, the imposed first-order wave forces are all zero at  $\kappa_0 h = 7.45$ . According to Mandal et al. (2013), the vanishing of the force is due to the destructive interference of the incident and scattered waves, and this also corresponds to the slosh modes inside the cylinder (Mackay, 2020). In this scenario, the mean wave drift force is the dominant action. As  $\kappa_0 h$  increases, the wave interference effect is not significant in the array because of a shorter wavelength relative to the spacing among the cages, so there are no distinct differences in the wave forces acting on these cages in the array and the single cage.

In Fig. 6.20, if the diameters of these cages in the array gradually increase at a constant wavelength  $L$ , the interference effect of the waves is enhanced, resulting in significant

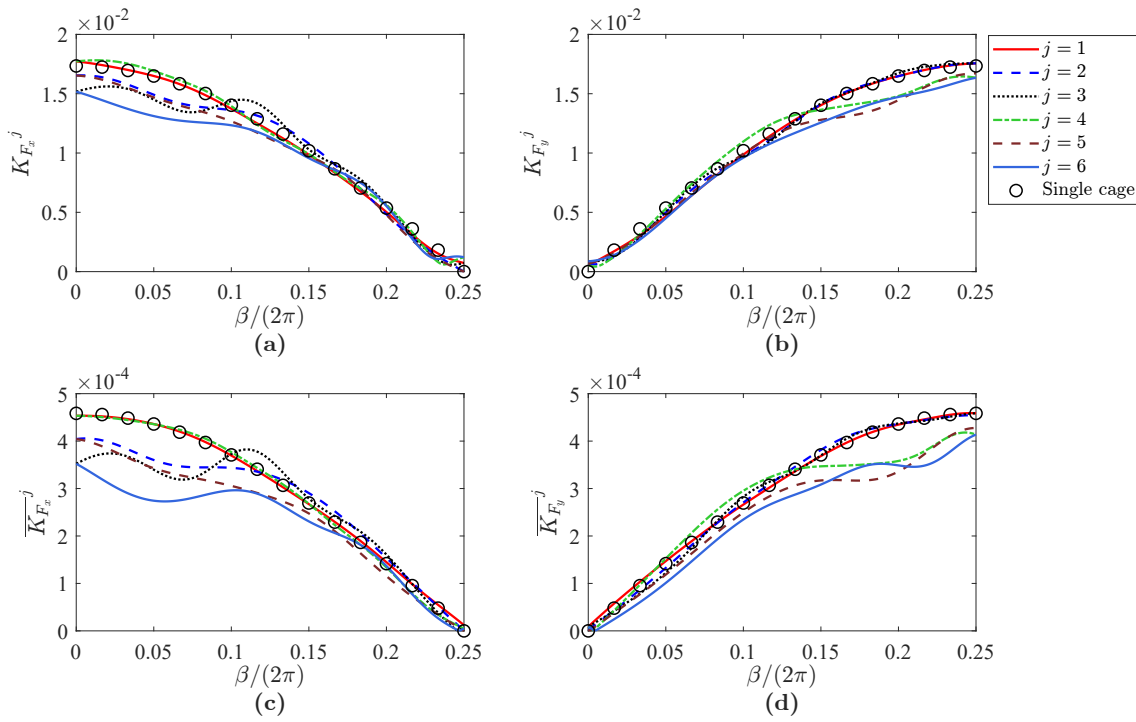


**Fig. 6.18** Normalised first-order wave forces: (a) Component  $K_{F_x}^j$ ; (b) Component  $K_{F_y}^j$  and normalised mean wave drift forces: (c) Component  $\overline{K_{F_x}^j}$ ; (d) Component  $\overline{K_{F_y}^j}$  on each cage versus varied nondimensional incident wave angles  $\beta/(2\pi)$ . The other constant parameters are  $\kappa_0 h = 12$ ,  $t_s^j/a^j = 10^{-4}$ ,  $\tau^j = 1+1i$  and  $s_x/h = s_y/h = 0.1$ .

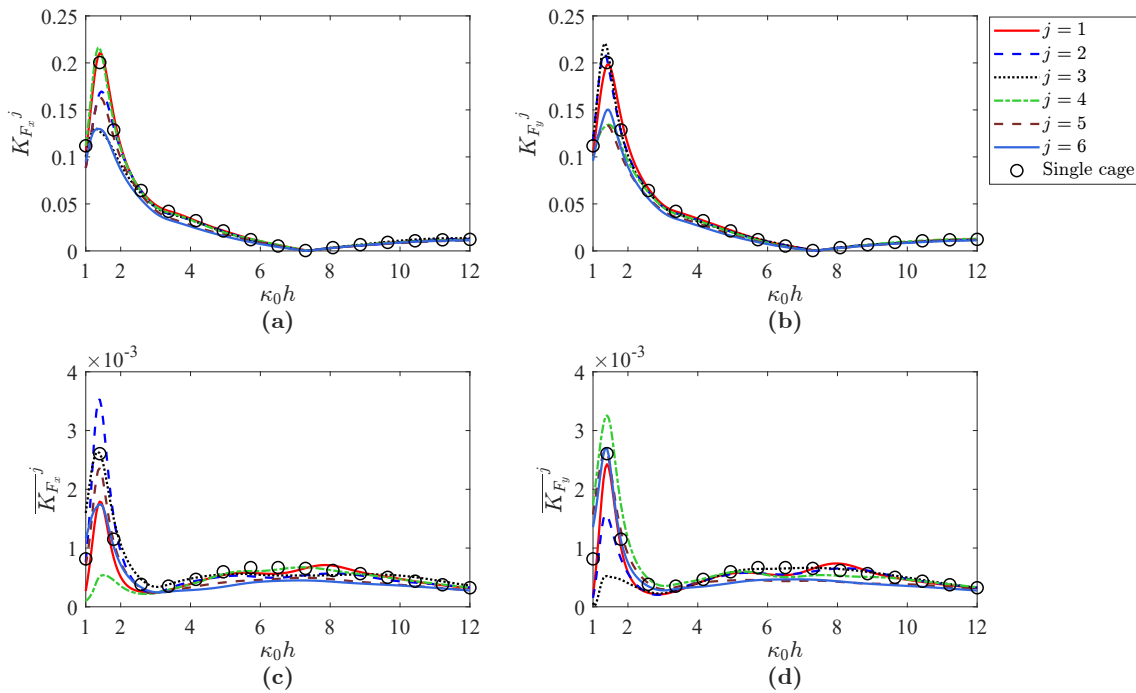


**Fig. 6.19** Normalised first-order wave forces: (a) Component  $K_{F_x}^j$ ; (b) Component  $K_{F_y}^j$  and normalised mean wave drift forces: (c) Component  $\overline{K_{F_x}^j}$ ; (d) Component  $\overline{K_{F_y}^j}$  on each cage versus varied nondimensional incident wavelengths  $\kappa_0 h$ ,  $\beta = \pi/4$ ,  $t_s^j/a^j = 10^{-4}$ ,  $\tau^j = 1+1i$  and  $s_x/h = s_y/h = 0.1$ .

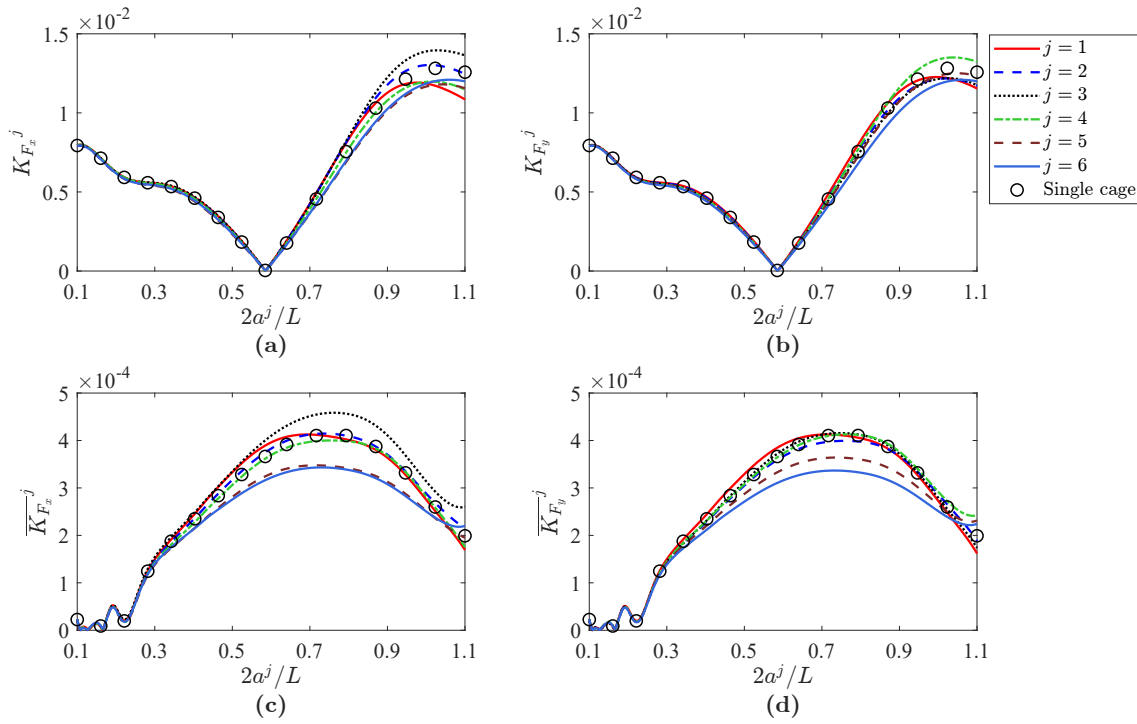


**Fig. 6.20** Normalised first-order wave forces: (a) Component  $K_{F_x}^j$ ; (b) Component  $K_{F_y}^j$  and normalised mean wave drift forces: (c) Component  $\overline{K_{F_x}^j}$ ; (d) Component  $\overline{K_{F_y}^j}$  on each cage versus varied relative diameters of the cages  $2a^j/L$ ,  $\beta = \pi/4$ ,  $\kappa_0 h = 12$ ,  $\tau^j = 1+1i$  and  $s_x/h = s_y/h = 0.1$ .

differences in the wave force coefficients, especially for the mean wave drift forces. At this time, the results of cage  $j = 2$  are relatively closer to those of the single cage. For all cages, the peaks of the first-order wave forces manifest in the range of relative diameters  $2a^j/L = 0.9$  to  $1.1$ , but the peaks of the mean wave drift forces fall within the scope of  $2a^j/L = 0.6$  to  $0.8$ . Notably, the phenomenon of the first-order wave force vanishing still occurs at a specific ratio of  $2a^j/L = 0.59$ .

As observed from Figs. 6.21a and 6.21b, with respect to increasing the porous resistance effect parameters  $\tau_r^j$ , the coefficients  $K_{F_x}^j$  and  $K_{F_y}^j$  always maintain a decreasing tendency. The coefficients  $\overline{K_{F_x}^j}$  and  $\overline{K_{F_y}^j}$  rise to the maximum values and then start to decrease thereafter in Figs. 6.21c and 6.21d. Furthermore, higher values of  $\tau_r^j$  can diminish the perturbation effect caused by the cage array on the waves so that the wave actions on all cages are closer. Alternatively, the first-order wave force shows an overall growth trend versus the increased fluid inertial parameters  $\tau_i^j$  in Figs. 6.22a and 6.22b where two peak points exist on the curves, but the mean wave drift forces are still predicted to reach the maximum values and then gradually decline, as seen from Figs. 6.22c and 6.22d. It is noteworthy that most cages in the array can withstand minor wave forces compared with the single cage for greater  $\tau_i^j$ .

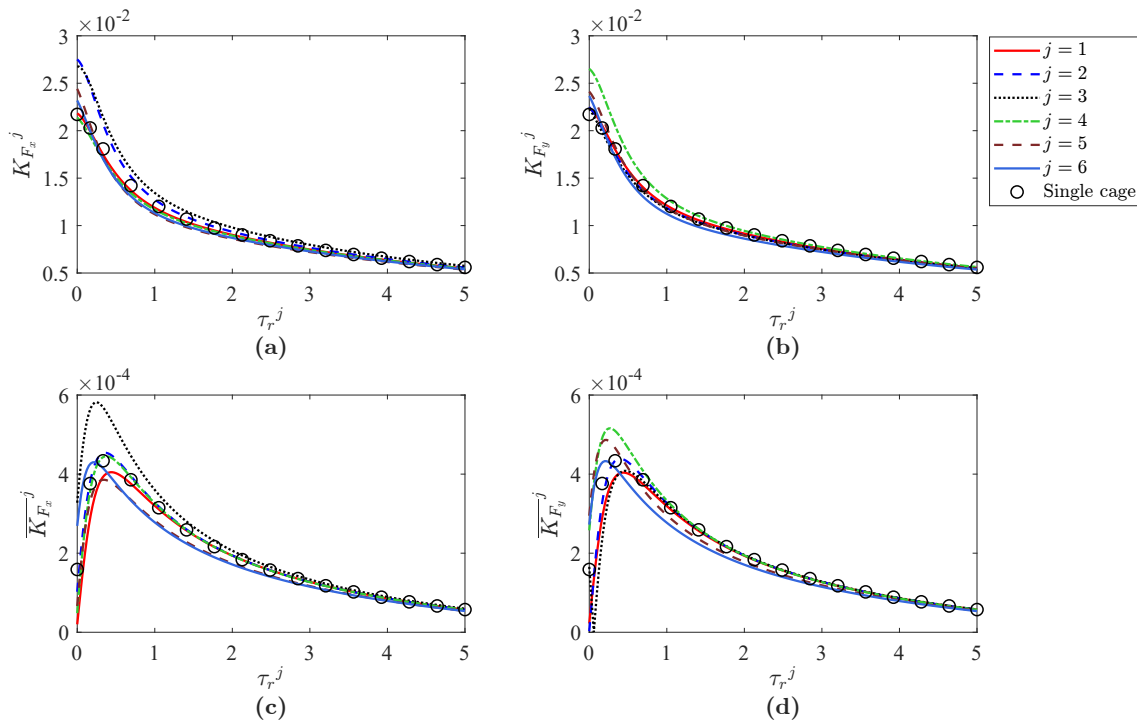


**Fig. 6.21** Normalised first-order wave forces: (a) Component  $K_{F_x}^j$ ; (b) Component  $K_{F_y}^j$  and normalised mean wave drift forces: (c) Component  $\overline{K_{F_x}^j}$ ; (d) Component  $\overline{K_{F_y}^j}$  on each cage versus varied porous resistance effect parameters of the net  $\tau_r^j$ ,  $\beta = \pi/4$ ,  $\kappa_0 h = 12$ ,  $t_s^j/a^j = 10^{-4}$ ,  $\tau_i^j = 1$  and  $s_x/h = s_y/h = 0.1$ .

The above parameter studies indicate that the wave forces are increased for some cages and decreased for others in the array compared with those for the single-cage case due to the interference effect of the waves. However, this manifestation is quite complex, so a higher structural strength for the cages in an array is recommended to guarantee safety performance and facilitate engineering design.

As illustrated in Figs. 6.23 to 6.26, to determine the optimal layout of the fish net cage array, more extensive calculations are carried out to contour the functions of  $K_{F_x}^j$ ,  $K_{F_y}^j$ ,  $\overline{K_{F_x}^j}$  and  $\overline{K_{F_y}^j}$  for each cage versus the cage spacings  $s_x$  and  $s_y$ , both of which are in the range from  $0.01L$  to  $L$ . It can be seen from Figs. 6.23 and 6.25 that cages  $j = 2$  and  $3$  have to withstand greater critical wave force components along the  $x$ -axis, but the magnitude of cage  $j = 6$  is relatively minor in most instances. Alternatively, for the wave actions along the  $y$ -axis, the magnitude of cage  $j = 4$  is more significant in most ranges, and the impact on cage  $j = 6$  is also weaker in Figs. 6.24 and 6.26.

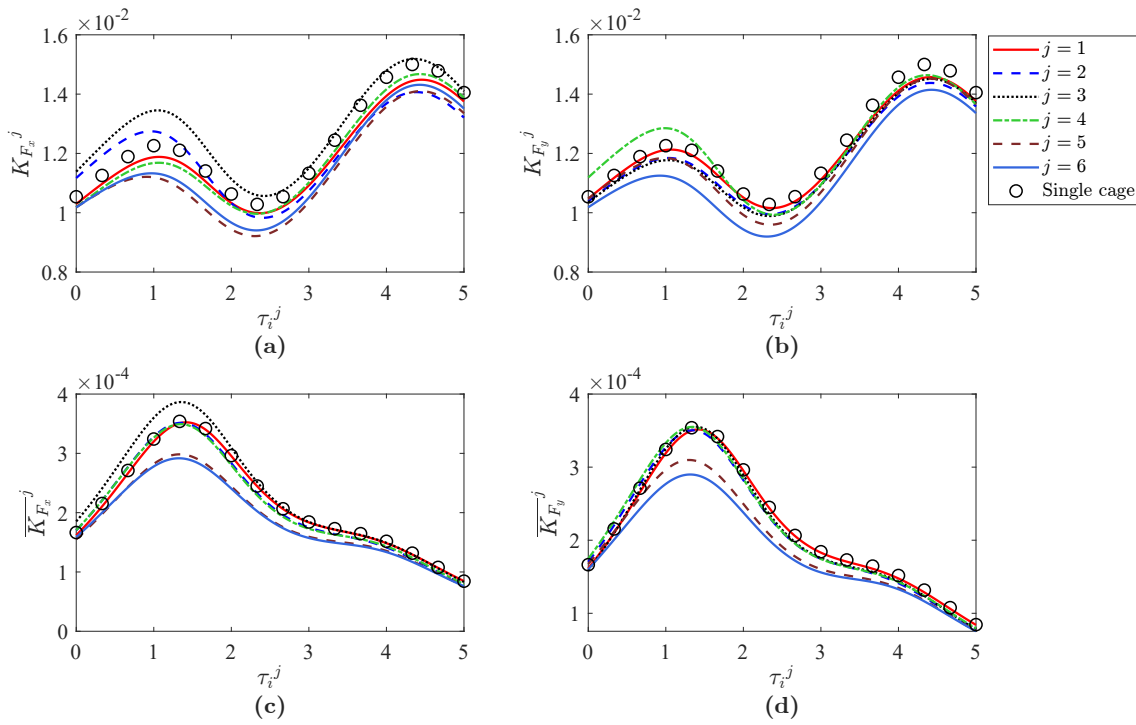


**Fig. 6.22** Normalised first-order wave forces: (a) Component  $K_{F_x}^j$ ; (b) Component  $K_{F_y}^j$  and normalised mean wave drift forces: (c) Component  $\overline{K_{F_x}^j}$ ; (d) Component  $\overline{K_{F_y}^j}$  on each cage versus varied fluid inertial effect parameters of the net  $\tau_i^j$ ,  $\beta = \pi/4$ ,  $\kappa_0 h = 12$ ,  $t_s^j/a^j = 10^{-4}$ ,  $\tau_r^j = 1$  and  $s_x/h = s_y/h = 0.1$ .

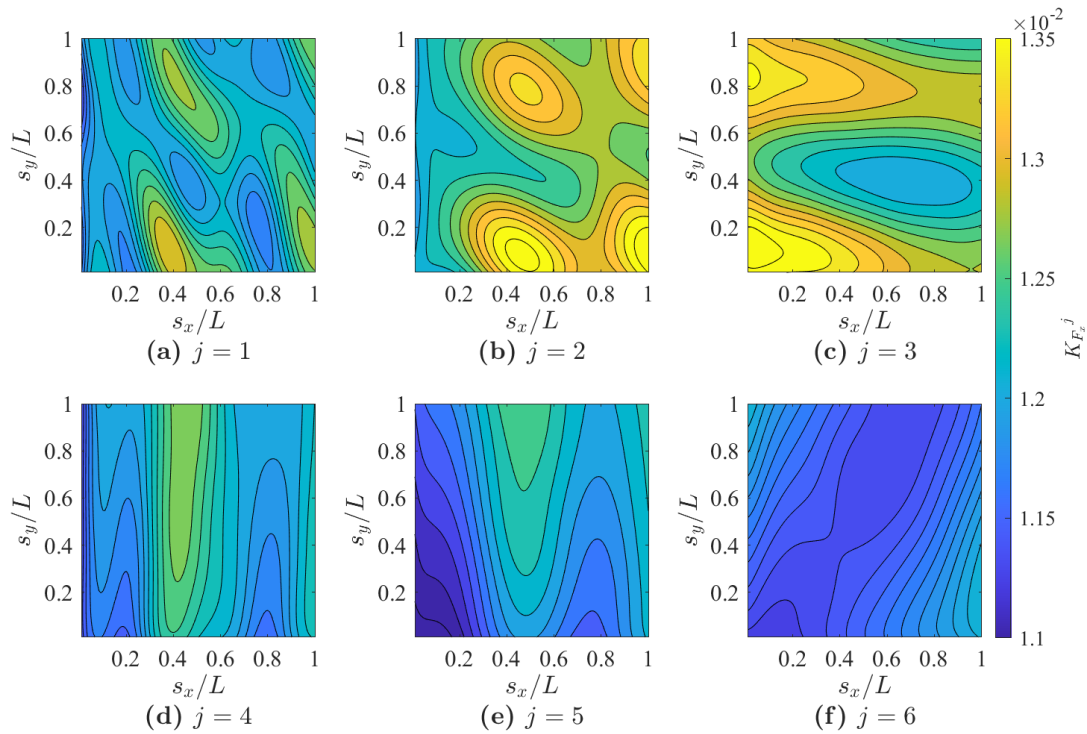


**Fig. 6.23** Contour plots of the normalised first-order wave force component  $K_{F_x}^j$  on each cage as a function versus relative cage spacings  $s_x/L$  and  $s_y/L$ ,  $\beta = \pi/4$ ,  $\kappa_0 h = 12$ ,  $t_s^j/a^j = 10^{-4}$  and  $\tau^j = 1+1i$ .



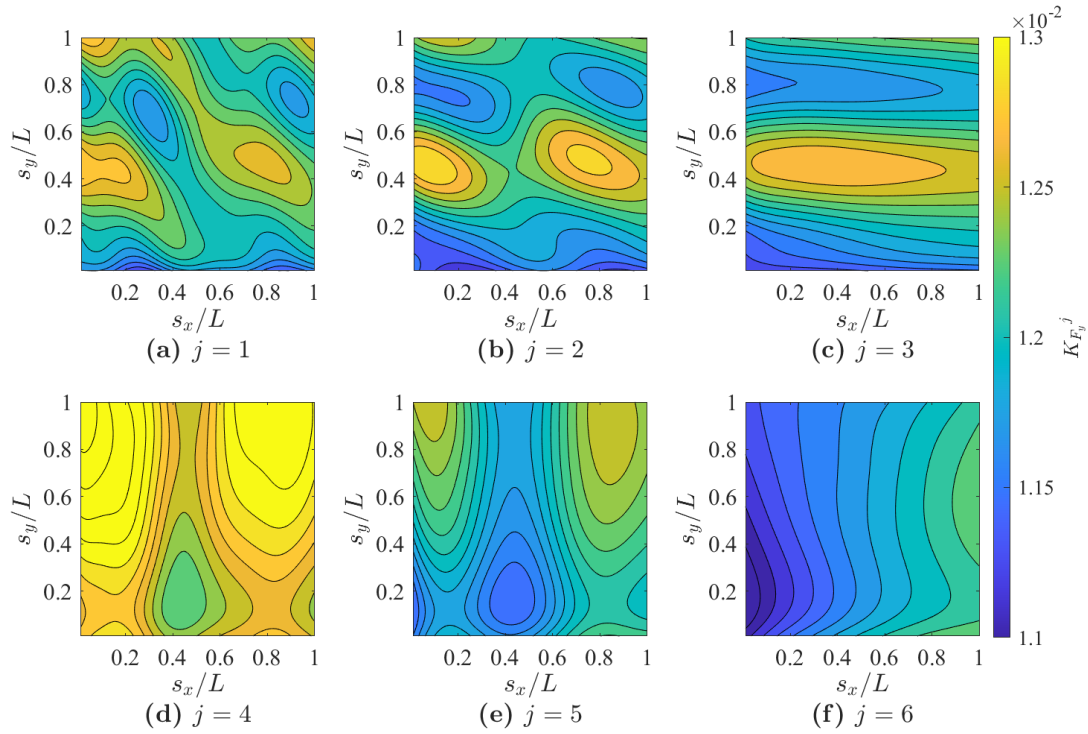


**Fig. 6.24** Contour plots of the normalised first-order wave force component  $K_{F_y}^j$  on each cage as a function versus relative cage spacings  $s_x/L$  and  $s_y/L$ ,  $\beta = \pi/4$ ,  $\kappa_0 h = 12$ ,  $t_s^j/a^j = 10^{-4}$  and  $\tau^j = 1+i$ .

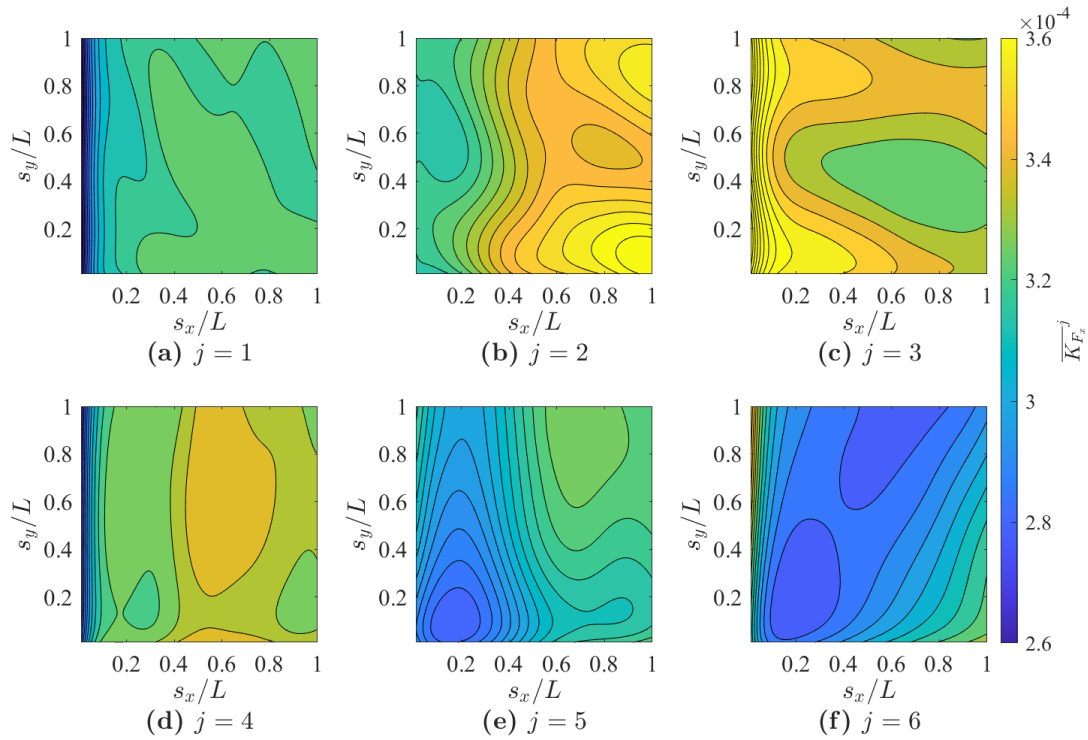


**Fig. 6.25** Contour plots of the normalised mean wave drift force component  $\overline{K_{F_x}^j}$  on each cage as a function versus relative cage spacings  $s_x/L$  and  $s_y/L$ ,  $\beta = \pi/4$ ,  $\kappa_0 h = 12$ ,  $t_s^j/a^j = 10^{-4}$  and  $\tau^j = 1+i$ .

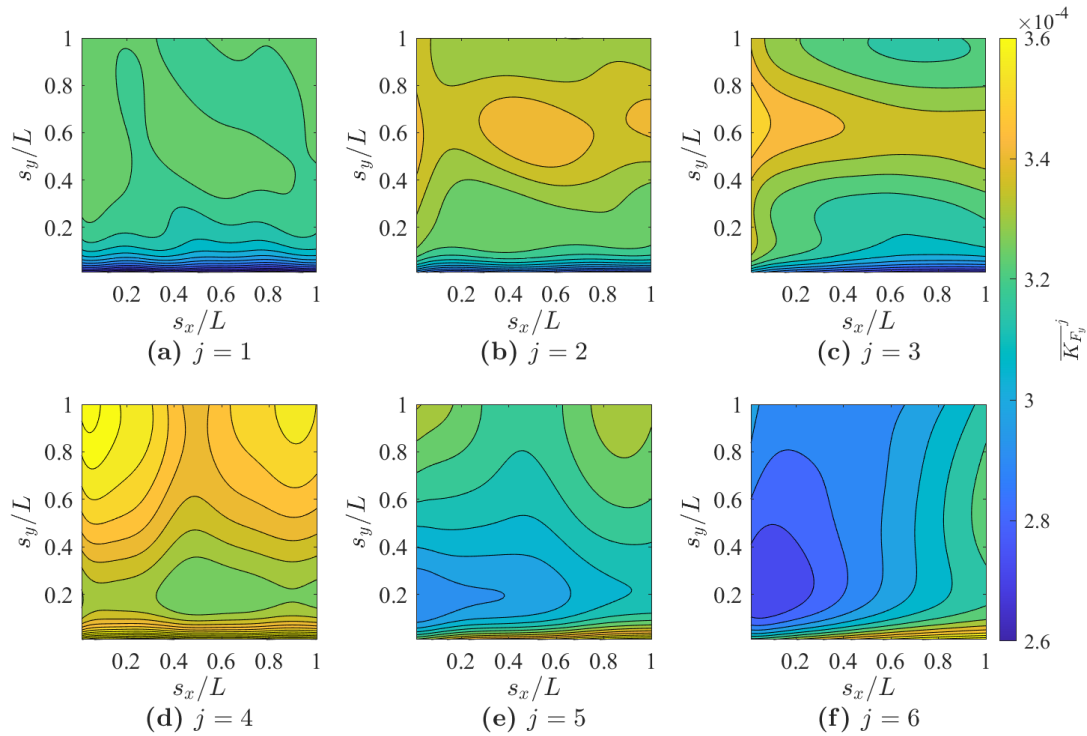


**Fig. 6.26** Contour plots of the normalised mean wave drift force component  $\overline{K_{F_y}^j}$  on each cage as a function versus relative cage spacings  $s_x/L$  and  $s_y/L$ ,  $\beta = \pi/4$ ,  $\kappa_0 h = 12$ ,  $t_s^j/a^j = 10^{-4}$  and  $\tau^j = 1 + i$ .

## 6.6 Conclusions

The interference effects and hydroelastic behaviours of an array of submerged flexible fish net cages in waves were effectively investigated through semi-analytical solutions. The wave-net cage interactions were determined based on the potential flow theory and porous medium model, and the net chambers were modelled as cylindrical shells whose motions were governed by the shell-membrane theory. The general solution to the wavefield and structural portion was expressed in the form of a Fourier-Bessel series by an eigenfunction expansion. The scattered wave potentials generated by each cage in the local coordinate system were superimposed, and Graf's addition theorem was employed for the coordinate transformation. Finally, a closed-form solution to the present physical problem was obtained by matching the corresponding boundary conditions and the least squares method.

In the study, the results, such as free water surface elevations, hydrodynamic loads and structural deformations, were discussed for a  $2 \times 3$  array of net cages under different hydrodynamic and structural parameters. Moreover, the mean wave drift effect, a nonlinear property derived from the first-order solution, was initially discussed. The key conclusions are summarised as follows:

- i. On the leeward side of a porous cage array, there are wake-like regions along the incident wave direction where the wave energy is severely dissipated.
- ii. Increasing the wavenumbers, cage spacings and net porosities is beneficial to weaken the interference effect of the waves in a net cage array.
- iii. It is recommended to increase the strength of the top part of the cage where significant hydrodynamic effects and corresponding dynamic responses manifest under wave action.
- iv. Along the direction of wave incidence, the rear cages will withstand opposite mean wave drift loads compared to those imposed on the front cages. Therefore, the mooring pre-tension can be considered to suppress the corresponding displacements.
- v. The wave forces acting on net cages will have maximum peaks in the low-frequency range of the waves.
- vi. It is useful for practical engineering design that the first-order wave forces acting on all cages in an array can be neglected at the specific ratio of cage diameter to wavelength  $2a^j/L = 0.59$ .

The present study extended the theory of hydroelastic interaction between waves and fish cages to the interference phenomenon of waves among multiple cages and the mean drift effect of waves. Benefitting from most numerical computations being replaced analytically, the semi-analytical solutions could quickly determine the physical field information at any spatial and temporal positions and were not limited by the scale of the studied case. The introduction of the shell-membrane theory efficiently addressed oversimplification in modelling fish cages, and Graf's addition theorem facilitated the coordinate transformation of the scattered wave potential generated by each cage in different local coordinate systems. As for the practical implications, the developed hydroelastic model may be an efficient analysis tool for engineers designing offshore fish cage systems. By predicting the distribution characteristics of the wave amplitude around cages, it facilitates identifying a low-energy environment suitable for fish growth. The structural dynamic response analysis and parametric studies of wave forces can be helpful to avoid the safety risks associated with the strength failure of the cage. In addition, some benchmark results provided in the present study can be applied for validating other numerical models. It is worth noting that the current works still have certain limitations in engineering practice. For fish cages designed in real sea conditions, more complex hydrodynamic phenomena need to be considered, such as higher-order Stokes waves, wave-current interactions, turbulence effects, et cetera, and the cages are usually designed with arbitrary shapes to satisfy functionality. These will be focused on and explored in future research studies.



# Chapter 7

## Conclusions

This chapter revisits the research background, motivation and objectives of this Ph.D. thesis. A general discussion addresses the main research outcomes of the three study elements. Finally, some research limitations of the existing studies and future lines of work are explored.

### 7.1 Research restatement

Due to the increasing global demand for aquatic products and the environmental pollution and resource conflicts caused by nearshore aquaculture, the development of offshore fish farming has inevitably become popular. Related emerging industries are consequently the subject of much research. A review of the relevant literature reveals research gaps in the field of hydroelastic interaction between waves and fish cages. An understanding of the theoretical mechanism of this physical phenomenon and a summary of key natural features will help engineers explore practical methods related to fish cage systems in offshore areas. Therefore, the following research question is explored in this Ph.D. thesis: “what are the hydroelastic behaviours of open-net fish cages under wave action?”.

The main objectives achieved by this research are as follows:

1. Analysis and understanding of the theoretical mechanism of the hydroelastic interaction between waves and open-net fish cages;
2. Conceptualisation and development of an efficient hydroelastic analysis tool to predict the wave response of fish cages;
3. Identifying the dynamic response characteristics of a fish cage under wave excitation and the cage’s influence on the wavefield through numerical experiments.

## Conclusions

---

To achieve these objectives, a series of original studies have been completed to explore the mechanism of wave-net cage interaction in this thesis. Semi-analytical approaches were adopted to directly couple the governing equations of the fluid and structural domains, and the closed-form solutions to the research problem were derived through the eigenfunction expansion method. A complete numerical execution framework was developed and compared to traditional numerical models. A part of the discretisation schemes was replaced by the analytical form, which reduced computational requirements. The simulation results also revealed some prime hydroelastic properties of the net cage.

## 7.2 General discussions and key findings

This Ph.D. study proposes a semi-analytical method to investigate the hydroelastic interaction between waves and open-net fish cages. The research program has been divided into several distinct activities. Initially, a theoretical framework of modelling and corresponding methodology were developed to understand the interaction phenomena between waves and fish cages (Chapter 4). However, the governing equations of the net chamber were over-simplified. Therefore, the shell-membrane theory was introduced to overcome this deficiency (Chapter 5). Finally, the model was extended to the case with multiple cages, including the wave interference effects (Chapter 6). Convergence and comparative studies validated the rationality of the developed model, and some key FSI features for fish cages were identified through the simulation results.

### 7.2.1 An establishment for the semi-analytical solution

The first study element of the project was to determine the governing equations for the fluid and structural domains, as well as the corresponding boundary value conditions (Chapter 4). The central technique was expressing the blocking effect of the fish cage net and the influence of its motion on the flow conditions. It was necessary to incorporate the porous medium model into the kinematic boundary conditions on the cage interface. Through the eigenfunction expansion method, the general solution of the governing equation was written as a Fourier Bessel series, and the closed-form solutions could be achieved by matching the boundary conditions and applying the least squared method.

The simulation results in Study I indicated that an individual fish cage causes a certain disturbance to the wave surface, but this effect becomes minor as the opening ratio of the net increases. Moreover, the significant wave effect is observed near the top part of the

cage, as indicated in the contour plots of the pressure drop distribution. The effect of short waves is mainly concentrated at the mean water level.

Plots of the amplitude distributions of hydrodynamic loads and transverse deflections along the cage height indicate that the cage manifests severe wave responses at specific wave frequencies and that the mooring stiffness and axial tension of the cage affect these distribution characteristics significantly. In addition, the dynamic response of the cage gradually diminishes as the diving depth increases.

Parametric studies verified the effects of different hydrodynamic and structural parameters on the wave forces and overturning moments acting on the cage. Firstly, the wave forces and overturning moments vanish at some specific ratios of cage diameter to wavelength. As the cage draft and mooring stiffness increase, these values increase to a peak and then diminish to a stable level. Increasing the axial tension and net opening ratio of the cage also suppresses the wave action. Finally, the inertial effect of the fluid in the porous medium model is nonnegligible.

### 7.2.2 Model updating by introducing the shell-membrane theory

A review of the literature on hydroelastic modelling of flexible fish cages revealed that some of the proposed analytical solutions have simplified the motion of the net chamber to a one-dimensional problem and neglected the stress variation in the net caused by structural deformation. Therefore, in the second study element of the project (Chapter 5), shell-membrane theory was introduced to overcome this deficiency. The axial and circumferential motion of the cage can be considered free vibration due to the inviscid assumption of the fluid, but the radial displacement is mainly driven by the wave load. To solve the governing equation of shell structures, one must determine the characteristic root equations and the particular solution due to the inhomogeneous term.

In Study II, contour plots of the wave amplitude distribution around the cage indicated that a distinct “wake region” appears near the leeward side of the cage, where wave energy is significantly dissipated. Reducing the net opening ratio and flexibility of the cage enhances the perturbation of the wavefield. There are also phase differences between the propagating waves outside and inside the cage.

The updated FSI model can also predict the displacement distribution on the cage surface in addition to the distribution of pressure drop. The cage exhibits different dynamic response characteristics at different wave frequencies, and increasing the porosity and flexibility of the fish cage net suppresses its deformation. Furthermore, consistent with the findings in Study I, a submersible fish cage was suggested to avoid strong surface waves.

## Conclusions

---

The parametric studies in Study II yielded some similar conclusions to those in Study I, but the porous effect parameters of the fish cage net were discussed further. The wave force and overturning moment present different variations with the increased porous resistance effect parameter under different fluid inertia effects, and peak points are predicted on the curves of both wave force and overturning moment versus the fluid inertia parameter.

### 7.2.3 Wave interference effects in an array of fish cages

In practice, a fish farm usually consists of multiple fish cages to increase production, so it is necessary to predict the hydroelastic interactions between waves and a fish cage array as in Chapter 6. The wave interference effect can be described as the overlap and superposition of the scattered waves generated by each individual cage in space. In the modelling process, the scattered waves generated by each cage were described by a local coordinate system located in the cage's centre, and the coordinate transformation was performed using Graf's addition theorem. The kinematic boundary condition on the interface of the cage requires information from the other cages, so the matrix equation coupling all cages can be established directly. In addition, the present model directly provides the mean wave drift force because the second-order solution has no contribution to the time-averaged values.

The wave amplitude distribution around the fish cage array also indicated that there is a "wake-like" wave energy dissipation region on the cages' leeward side. Increasing the wave frequency, cage spacing and porosity of the net can effectively suppress the wave interference effect, but such changes are not conducive to creating a low-energy environment for fish to thrive. In addition, relative to permeable cages, impermeable cages exhibit different wave amplitude distribution properties. Specifically, wave amplitude increases significantly inside impermeable cages. The contour plots of the wave load on the cage surfaces reveal that the mean wave drift loads acting on the rear cages are opposite to those acting on the front cages along the incident wave direction.

Parametric studies indicated that the wave forces acting on the cages in the array have maximum peaks in the low-frequency range of waves, and the wave forces are predicted to be zero at a specific ratio of cage diameter to wavelength as discussed in Studies I and II. Notably, the difference in wave force acting on an array of cages and a single cage mainly depends on the ratio of cage layout spacing or cage dimension to wavelength and the net porosity. Moreover, extensive calculations were performed to characterise wave forces as a function of cage spacing, which contribute to determining the optimal layout of fish cage arrays.



## **7.3 Scientific contributions**

It is nontrivial to analyse and understand the interaction between waves and fish cages. The difficulty arises because the fish cage net is a permeable and flexible structure, and it is very difficult to establish a realistic microscopic model due to computational limits. The hydroelastic models developed in the previous literature currently have some limitations in applications, and there is a large knowledge gap in the mechanistic studies related to FSI in this field. The current Ph.D. thesis has not only provided innovations regarding the fundamental theory and perspectives in relevant modelling techniques but also introduced hydroelastic models that are suitable for offshore fish farming applications.

### **7.3.1 Implications in theoretical developments**

One of the research focuses of this Ph.D. thesis is to expand the fundamental theory in the field of wave-porous cage interaction. In Study I, extensive work was performed to analyse the fish cages in arbitrary submerged positions, which improved the generalisability of the model. Study II introduced the membrane theory of shells and relevant methods of solutions, which addresses knowledge gaps in modelling the cage structure when deriving the closed-form solution to wave-porous cage interactions. Study III systematically investigated the mechanism of wave interference effects in fish cage arrays and proposed an approach to calculate the mean wave drift force acting on the fish cage. These studies offer significant contributions to the fundamental theory and serve as a basis for future work in this field.

Analytical methods can be used to reveal and understand the nature of wave-cage interactions. The three previously discussed studies indicate that fluctuation solutions all consist of infinite superpositions of harmonic function modes, and convergence analysis can effectively address the influence of these decoupled modes on the results. In addition, the boundary conditions directly determine the uniqueness of the solution for the studied object in the mathematical derivation. However, the number of unknowns is more than the number of algebraic equations in Eqs. (4.30), (5.35) and (6.32). Therefore, there is no ideal closed-form solution to the existing research question, and the least squared method gives only an optimal approximation.

### 7.3.2 Implications in engineering practice

The present Ph.D. thesis directly delivers a closed-form solution to the research problem rather than an approximate solution derived by interpolation-based numerical methods. Compared to numerical solutions, analytical solutions, consisting of a series of functions and mathematical operators, can more efficiently predict the field distribution at any location and time with better accuracy. This precision is not limited by a discrete scale. Because the existing model is based on linear theory, it does not require excessive numerical computations to solve large coupling matrix equations directly instead of utilising iterative methods, and computational instability can also be avoided when performing the simulation.

Traditional numerical models do have better generalisability in engineering problems. However, in applications, model validations are often required due to the issue of numerical precision, while analytical solutions can directly give the most accurate results using the same control equations and boundary conditions. Therefore, the semi-analytic model proposed in this thesis may provide benchmark results for validating other numerical models.

Feasibility studies of offshore fish farming are still being explored. This thesis provides an effective analytical tool for engineers designing fish cage systems. From the simulation results, some crucial hydroelastic mechanisms and characteristics of the fish cage under offshore wave conditions are summarised. This work provides information that can be applied to the future development of offshore fish cage systems.

Finally, due to the introduction of porous medium models, the developed semi-analytical solution can not only predict the hydroelastic behaviour of fish cages but also be applied to other porous structures interacting with waves. For example, arranging floating breakwaters or porous barriers around fish cages or other offshore structures is beneficial for mitigating wave action. Mandal et al. (2013) have proposed an analytical solution for the wave response of a porous concentric circle structure and used similar modelling techniques to those in the current thesis.

## 7.4 Research limitations and future work

At present, the Ph.D. thesis has developed an essential theoretical framework and techniques underlying the development of hydroelastic models for fish cages. Some simulation results are also discussed that may serve as reference for the design of future offshore fish cage systems. Nevertheless, the limitations of these studies should also be consid-

ered, including the modelling assumptions, studied objects, functionality et cetera. These limitations indicate the scope of the existing studies and provide avenues for future work.

### 7.4.1 Research limitations

In the modelling process, several linear approximations are assumed. Firstly, the small amplitude wave theory neglects the nonlinear term in the free water surface boundary conditions, and only the zero-order terms in the Taylor expansions of the relevant physical quantities are retained when the wave steepness is assumed to be a small quantity. Similarly, the kinematic boundary conditions of the cage interface cannot be satisfied at the interface's instantaneous location due to the negligence of the higher-order terms in the Taylor expansion when the displacement amplitude is small compared to the cross-section dimension of the cage. Thirdly, Darcy's law is adopted in the porous medium model, which implies that the condition of the flow penetrating through the net surface is laminar. In addition, the governing equations of the cage structure cannot handle the nonlinear constitutive relation and large deformations of the material.

The applicable functions of the model still has limitations. Currently, the coupling between the floating collar and net chamber is not considered, and the motions of mooring cables have a significant impact on the whole cage systems, such as, stress concentration. On the other hand, in realistic offshore environments, wave conditions are naturally nonlinear and irregular, especially when the wave steepness is greater, the nonlinear effects on the free water surface become more significant. For submersible fish cages, there is a high likelihood of encountering current loads, and they are significantly influenced as well. In the case of array configuration, the wake generated by upstream cages can cause shielding effects, which can affect the oxygen concentration inside the downstream cages (the oxygen content is extremely vital for the welfare of fish). Moreover, wave-current interactions are also a common phenomenon in the marine environment, wherein significant changes can manifest for the flow pattern and wave field.

### 7.4.2 Future work lines

Combining the literature review and research limitations, some feasible future research directions can be identified.

The solution to some important nonlinear problems is one future research direction. The small amplitude wave theory is only applicable to some specific wave conditions, so the introduction of high-order Stokes waves is necessary. Malenica et al. (1999) have proposed

## Conclusions

---

an analytical solution to the diffraction of second-order waves around multiple cylinders, which provides some ideas for model updating. In addition, in the aforementioned literature review, the hydrodynamic force acting on the net is quadratically related to the flow velocity for the flow conditions with a high Reynolds number, so the quadratic porous medium model presented in Molin (2011) may have to replace Darcy's law. Compared to linear porous flow models, quadratic porous flow models assume that turbulent effects are much greater than viscous effects (Chen, 2016), making them suitable for flow separation near fishing cage nets caused by sharp openings or high Reynolds numbers conditions.

To improve the generalisability of the model, the hydroelastic model of a completed fish cage system coupling floating collars, net chambers and mooring systems will be developed. Such a model would be applicable to the cage with arbitrary cross-sectional shapes. Gharechae et al. (2020) and Park and Wang (2022) have proposed relevant solutions to the floating rings interacting with waves, which may be embedded in the model developed in this thesis. Additionally, the impact of currents on fish cages is not negligible, especially, the effect of flow patterns on the distribution of oxygen inside the cage. At present, there are two ways to introduce current effects into existing models. The first method is to directly modify the boundary conditions of the potential flow model to couple the velocity potential induced by the currents with the velocity potential of the waves. The second method can be borrowed from Zhao et al. (2007) and Xu et al. (2013a,b) to equivalently transform the incident wave and incoming current into a modified incident wave through wave-current interaction theory. Then, the distribution of oxygen concentration around the fish farm can be simulated by a CFD model based on the obtained flow pattern.

## **Acknowledgement of funding supports**

The author is very grateful to Griffith University to provide GU International Postgraduate Research Scholarship and Australian Government RTP Stipend Scholarship to support the Ph. D. research.

The author acknowledges the financial support of the Blue Economy Cooperative Research Centre, established and supported under the Australian Government's Cooperative Research Centres Program, grant number CRC20180101.

Many thanks to Griffith Cities Research Institute for providing HDR Journal Publishing and Editorial Assistance Scheme (JPEAS).



# References

- Abramowitz, M. and Stegun, I. (1965). *Handbook of Mathematical Functions with Formulas, Graphs, and Mathematical Tables*. Dover Publications.
- Abul-Azm, A. and Williams, A. (1987). Interference effects between flexible cylinders in waves. *Ocean Engineering*, 14:19–38.
- Aquastructures (2022). *The AquaSim Package Theory User Manual*. Aquastructures.
- Bai, X., Zhao, Y., Dong, G., and Bi, C. (2018). Probabilistic analysis and fatigue life assessment of floating collar of fish cage due to random wave loads. *Applied Ocean Research*, 81:93–105.
- Behera, H. and Sahoo, T. (2015). Hydroelastic analysis of gravity wave interaction with submerged horizontal flexible porous plate. *Journal of Fluids and Structures*, 54:643–660.
- Belubekyan, M., Ghazaryan, K., and Marzocca, P. (2017). Localised membrane vibration of cylindrical shells. *The Journal of the Acoustical Society of America*, 141:1947–1952.
- Berstad, A. J., Walaunet, J., and Heimstad, L. F. (2012). Loads from currents and waves on net structures. In *Proceedings of the ASME 2012 31st International Conference on Ocean, Offshore and Arctic Engineering OMAE2012 July*, volume 7, pages 95–104.
- Bi, C.-W., Zhao, Y.-P., Dong, G.-H., Xu, T.-J., and Gui, F.-K. (2014). Numerical simulation of the interaction between flow and flexible nets. *Journal of Fluids and Structures*, 45:180–201.
- Bouhoubeiny, E., Germain, G., and Druault, P. (2011). Time-resolved piv investigations of the flow field around cod-end net structures. *Fisheries Research*, 108:344–355.
- Boussinesq, J. (1903). *Theorie Analytique de la Chaleur*, volume 2. Gauthier-Villars.
- Brebbia, C. and Walker, S. (1979). *Dynamic Analysis of Offshore Structures*. Butterworth & Co. (Publishers) Ltd.
- Bris, F. L. and Marichal, D. (1998). Numerical and experimental study of submerged supple nets: Applications to fish farms. *Journal of Marine Science and Technology*, 3:161–170.
- Cardia, F. and Lovatelli, A. (2015). *Aquaculture Operations in Floating HDPE Cages: a Field Handbook*. FAO & Ministry of Agriculture of the Kingdom of Saudi Arabi.

## References

---

- Chaplin, J., Bearman, P., Cheng, Y., Fontaine, E., Graham, J., Herfjord, K., Huarte, F. H., Isherwood, M., Lambrakos, K., Larsen, C., Meneghini, J., Moe, G., Pattenden, R., Triantafyllou, M., and Willden, R. (2005). Blind predictions of laboratory measurements of vortex-induced vibrations of a tension riser. *Journal of Fluids and Structures*, 21:25–40.
- Chen, D., Wang, C., and Zhang, H. (2021). Examination of net volume reduction of gravity-type open-net fish cages under sea currents. *Aquacultural Engineering*, 92:102128.
- Chen, H. (2016). *Modelling of Floating Fish Cage Dynamics with Computational Fluid Dynamics (Ph. D. thesis)*. Technical University of Denmark.
- Chen, J., Lin, Y., Lee, Y., and Wu, C. (2011). Water wave interaction with surface-piercing porous cylinders using the null-field integral equations. *Ocean Engineering*, 38:409–418.
- Chen, M., Xie, K., Jia, W., and Xu, K. (2015). Free and forced vibration of ring-stiffened conical–cylindrical shells with arbitrary boundary conditions. *Ocean Engineering*, 108:241–256.
- Cheng, H., Li, L., Aarsæther, K. G., and Ong, M. C. (2020). Typical hydrodynamic models for aquaculture nets: A comparative study under pure current conditions. *Aquacultural Engineering*, 90:102070.
- Cheng, H., Ong, M. C., Li, L., and Chen, H. (2022). Development of a coupling algorithm for fluid-structure interaction analysis of submerged aquaculture nets. *Ocean Engineering*, 243:110208.
- Choc, Y. and Casarell, M. (1971). Hydrodynamic resistance of towed cables. *Journal of Hydronautics*, 5:126–131.
- Chu, Y., Wang, C., Park, J., and Lader, P. (2020). Review of cage and containment tank designs for offshore fish farming. *Aquaculture*, 519:734928.
- Chwang, A. T. (1983). A porous-wavemaker theory. *Journal of Fluid Mechanics*, 132:395–406.
- Conte, F. (2004). Stress and the welfare of cultured fish. *Applied Animal Behaviour Science*, 86:205–223.
- Dai, J., Wang, C. M., Utsunomiya, T., and Duan, W. (2018). Review of recent research and developments on floating breakwaters. *Ocean Engineering*, 158:132–151.
- Davidson, J. and Ringwood, J. (2017). Mathematical modelling of mooring systems for wave energy converters—a review. *Energies*, 10:666.
- Dean, R. G. and Dalrymple, R. A. (1991). *Water wave mechanics for engineers and scientists*, volume 2. world scientific publishing company.
- Devilliers, M., Vincent, B., and Mnassri, I. (2016). A new adaptive mesh refinement to model water flow around fishing nets. *Ocean Engineering*, 113:34–43.



- DNV (2021). *Marine Aquaculture Forecast to 2050*. Det Norske Veritas Group.
- Dong, G.-H., Hao, S.-H., Zhao, Y.-P., Zong, Z., and Gui, F.-K. (2010). Elastic responses of a flotation ring in water waves. *Journal of Fluids and Structures*, 26:176–192.
- Dong, G.-H., Tang, M.-F., Xu, T.-J., Bi, C.-W., and Guo, W.-J. (2019). Experimental analysis of the hydrodynamic force on the net panel in wave. *Applied Ocean Research*, 87:233–246.
- El-Reedy, M. (2019). *Offshore Structures: Design, Construction and Maintenance*. Elsevier Science & Technology, 2nd edition.
- Faltinsen, O. (1993). *Sea Loads on Ships and Offshore Structures*. Cambridge University Press.
- Faltinsen, O. and Timokha, A. (2009). *Sloshing*. Cambridge University Press.
- Faltinsen, O. M. (2014). Hydrodynamics of marine and offshore structures. *Journal of Hydrodynamics*, 26:835–847.
- Faltinsen, O. M. and Shen, Y. (2018). Wave and current effects on floating fish farms. *Journal of Marine Science and Application*, 17:284–296.
- FAO (2018). *The State of World Fisheries and Aquaculture 2018-Meeting the Sustainable Development Goals*. United Nations.
- FAO (2020a). Fao fisheries statistics. <https://www.fao.org/fishery/statistics/en>.
- FAO (2020b). *The State of World Fisheries and Aquaculture 2020*. Food and Agriculture Organization of the United Nations.
- Flügge, W. (1973). *Stresses in Shells*. Springer Berlin Heidelberg.
- Fredheim, A. (2003). Hydroelastic analysis of a fishing net in steady inflow conditions. In *Proceedings of the 3rd International Conference on Hydroelasticity in Marine Technology, Oxford, United Kingdom, Edited by Eatock Taylor, ISBN: 0-952-62081-2, Paper: P2003-3 Proceedings*.
- Fredheim, A. (2005). *Current Forces on Net Structures (Ph. D. thesis)*. Technical University of Denmark.
- Fredheim, A. and Langan, R. (2009). Advances in technology for off-shore and open ocean finfish aquaculture. In *New Technologies in Aquaculture*, pages 914–944. Elsevier.
- Fu, S. and Moan, T. (2012). Dynamic analyses of floating fish cage collars in waves. *Aquacultural Engineering*, 47:7–15.
- Gansel, L., McClimans, T. A., and Myrhaug, D. (2010). Average flow inside and around fish cages with and without fouling in a uniform flow. In *International Conference on Offshore Mechanics and Arctic Engineering*, volume 49125, pages 275–283.

## References

---

- Gentry, R. R., Froehlich, H. E., Grimm, D., Kareiva, P., Parke, M., Rust, M., Gaines, S. D., and Halpern, B. S. (2017). Mapping the global potential for marine aquaculture. *Nature Ecology & Evolution*, 1:1317–1324.
- Gharechae, A. and Ketabdari, M. J. (2022). Analytical solution based on bem to oblique waves scattering by thin arc-shaped permeable barrier applied for array of aquaculture cages. *Engineering Analysis with Boundary Elements*, 134:241–258.
- Gharechae, A., Ketabdari, M. J., Kitazawa, D., and Li, Q. (2020). Semi-analytical and experimental study on array of elastic circular floaters vertical motions in regular sea waves. *Ocean Engineering*, 217:107851.
- Gjørsund, S. H. and Enerhaug, B. (2010). Flow through nets and trawls of low porosity. *Ocean Engineering*, 37:345–354.
- Guo, W., Li, T., Zhu, X., Miao, Y., and Zhang, G. (2017). Vibration and acoustic radiation of a finite cylindrical shell submerged at finite depth from the free surface. *Journal of Sound and Vibration*, 393:338–352.
- Guo, Y., Mohapatra, S., and Soares, C. G. (2020). Review of developments in porous membranes and net-type structures for breakwaters and fish cages. *Ocean Engineering*, 200:107027.
- Hamelin, J., Love, J., Tait, M., and Wilson, J. (2013). Tuned liquid dampers with a keulegan–carpenter number-dependent screen drag coefficient. *Journal of Fluids and Structures*, 43:271–286.
- Haritos, N. and He, D. (1992). Modelling the response of cable elements in an ocean environment. *Finite Elements in Analysis and Design*, 11:19–32.
- Hedges, T. and Lee, B. (1992). The equivalent uniform current in wave-current computations. *Coastal Engineering*, 16:301–311.
- Helsley, C. and Kim, J. (2005). Mixing downstream of a submerged fish cage: A numerical study. *IEEE Journal of Oceanic Engineering*, 30:12–19.
- Higuera, P. (2015). *Application of computational fluid dynamics to wave action on structures (Ph. D. thesis)*. Universidade de Cantabria.
- Hoerner, S. (1965). *Fluid-Dynamic Drag: Practical Information on Aerodynamic Drag and Hydrodynamic Resistance*. NJ: Hoerner Fluid Dynamics.
- Holmer, M. (2010). Environmental issues of fish farming in offshore waters: perspectives, concerns and research needs. *Aquaculture Environment Interactions*, 1:57–70.
- Hou, H.-M., Dong, G.-H., Xu, T.-J., and Zhao, Y.-P. (2019). System reliability evaluation of mooring system for fish cage under ultimate limit state. *Ocean Engineering*, 172:422–433.
- Hou, H.-M., Dong, G.-H., Xu, T.-J., Zhao, Y.-P., and Bi, C.-W. (2018a). Dynamic analysis of embedded chains in mooring line for fish cage system. *Polish Maritime Research*, 25:83–97.

- Hou, H.-M., Dong, G.-H., Xu, T.-J., Zhao, Y.-P., Bi, C.-W., and Gui, F.-K. (2018b). Fatigue reliability analysis of mooring system for fish cage. *Applied Ocean Research*, 71:77–89.
- Huang, X.-H., Guo, G.-X., Tao, Q.-Y., Hu, Y., Liu, H.-Y., Wang, S.-M., and Hao, S.-H. (2016). Numerical simulation of deformations and forces of a floating fish cage collar in waves. *Aquacultural Engineering*, 74:111–119.
- Ito, S., Kinoshia, T., and Bao, W. (2014). Hydrodynamic behaviors of an elastic net structure. *Ocean Engineering*, 92:188–197.
- Ji, M., Inaba, K., and Triawan, F. (2019). Vibration characteristics of cylindrical shells filled with fluid based on first-order shell theory. *Journal of Fluids and Structures*, 85:275–291.
- Kagemoto, H. and Yue, D. K. P. (1986). Interactions among multiple three-dimensional bodies in water waves: an exact algebraic method. *Journal of Fluid Mechanics*, 166:189.
- Kar, P., Sahoo, T., and Meylan, M. H. (2020). Bragg scattering of long waves by an array of floating flexible plates in the presence of multiple submerged trenches. *Physics of Fluids*, 32:096603.
- Kim, B. W., Sung, H. G., Kim, J. H., and Hong, S. Y. (2013). Comparison of linear spring and nonlinear fem methods in dynamic coupled analysis of floating structure and mooring system. *Journal of Fluids and Structures*, 42:205–227.
- Kim, Y.-H. (2012). Analysis of turbulence and tilt by in-situ measurements inside the codend of a shrimp beam trawl. *Ocean Engineering*, 53:6–15.
- Klebert, P., Lader, P., Gansel, L., and Oppedal, F. (2013). Hydrodynamic interactions on net panel and aquaculture fish cages: A review. *Ocean Engineering*, 58:260–274.
- Kristiansen, T. and Faltinsen, O. M. (2012). Modelling of current loads on aquaculture net cages. *Journal of Fluids and Structures*, 34:218–235.
- Kristiansen, T. and Faltinsen, O. M. (2015). Experimental and numerical study of an aquaculture net cage with floater in waves and current. *Journal of Fluids and Structures*, 54:1–26.
- Lader, P., Dempster, T., Fredheim, A., and Østen Jensen (2008). Current induced net deformations in full-scale sea-cages for atlantic salmon (*salmo salar*). *Aquacultural Engineering*, 38:52–65.
- Lader, P. and Enerhaug, B. (2005). Experimental investigation of forces and geometry of a net cage in uniform flow. *IEEE Journal of Oceanic Engineering*, 30:79–84.
- Lader, P. and Fredheim, A. (2006). Dynamic properties of a flexible net sheet in waves and current—a numerical approach. *Aquacultural Engineering*, 35:228–238.
- Lader, P., Jensen, A., Sveen, J. K., Fredheim, A., Enerhaug, B., and Fredriksson, D. (2007a). Experimental investigation of wave forces on net structures. *Applied Ocean Research*, 29:112–127.

## References

---

- Lader, P. F., Olsen, A., Jensen, A., Sveen, J. K., Fredheim, A., and Enerhaug, B. (2007b). Experimental investigation of the interaction between waves and net structures—damping mechanism. *Aquacultural Engineering*, 37:100–114.
- Langan, R. (2009). Opportunities and challenges for off-shore farming. *New technologies in aquaculture: Improving production efficiency, quality and environmental management. Part, 6*:896–913.
- Lee, D., Jarzynski, J., and Berthelot, Y. H. (1993). A study of wave propagation on a cylindrical shell using fiber optic laser doppler velocimetry. *The Journal of the Acoustical Society of America*, 94:196–212.
- Lee, M. M. and Chwang, A. T. (2000). Scattering and radiation of water waves by permeable barriers. *Physics of Fluids*, 12:54–65.
- Li, L., Fu, S., Xu, Y., Wang, J., and Yang, J. (2013a). Dynamic responses of floating fish cage in waves and current. *Ocean Engineering*, 72:297–303.
- Li, M., Zhang, H., and Guan, H. (2011). Study of offshore monopile behaviour due to ocean waves. *Ocean Engineering*, 38:1946–1956.
- Li, M., Zhang, H., Guan, H., and Lin, G. (2013b). Three-dimensional investigation of wave–pile group interaction using the scaled boundary finite element method. part i: Theoretical developments. *Ocean Engineering*, 64:174–184.
- Li, M., Zhang, Y., Zhang, H., and Guan, H. (2015). Numerical stability and accuracy of the scaled boundary finite element method in engineering applications. *The ANZIAM Journal*, 57:114–137.
- Li, P., Faltinsen, O. M., and Lugni, C. (2016). Nonlinear vertical accelerations of a floating torus in regular waves. *Journal of Fluids and Structures*, 66:589–608.
- Li, Y.-C., Zhao, Y.-P., Gui, F.-K., and Teng, B. (2006). Numerical simulation of the hydrodynamic behaviour of submerged plane nets in current. *Ocean Engineering*, 33:2352–2368.
- Liang, H., Zheng, S., Shao, Y., Chua, K. H., Choo, Y. S., and Greaves, D. (2021). Water wave scattering by impermeable and perforated plates. *Physics of Fluids*, 33:077111.
- Liu, H.-F., Bi, C.-W., and Zhao, Y.-P. (2020). Experimental and numerical study of the hydrodynamic characteristics of a semisubmersible aquaculture facility in waves. *Ocean Engineering*, 214:107714.
- Liu, J. and Lin, G. (2013). Scaled boundary fem solution of short-crested wave interaction with a concentric structure with double-layer arc-shaped perforated cylinders. *Computers & Fluids*, 79:82–104.
- Liu, S., Bi, C., Yang, H., Huang, L., Liang, Z., and Zhao, Y. (2019). Experimental study on the hydrodynamic characteristics of a submersible fish cage at various depths in waves. *Journal of Ocean University of China*, 18:701–709.

- Liu, Z., Mohapatra, S. C., and Soares, C. G. (2021). Finite element analysis of the effect of currents on the dynamics of a moored flexible cylindrical net cage. *Journal of Marine Science and Engineering*, 9:159.
- Liu, Z., Wang, S., and Soares, C. G. (2022). Numerical study on the mooring force in an offshore fish cage array. *Journal of Marine Science and Engineering*, 10:331.
- Løland, G. (1991). *Current forces on and flow through fish farms (Ph. D. thesis)*. University of Trondheim.
- Ma, M., Zhang, H., Jeng, D.-S., and Wang, C. M. (2021). A semi-analytical model for studying hydroelastic behaviour of a cylindrical net cage under wave action. *Journal of Marine Science and Engineering*, 9:1445.
- Ma, M., Zhang, H., Jeng, D.-S., and Wang, C. M. (2022). Analytical solutions of hydroelastic interactions between waves and submerged open-net fish cage modeled as a porous cylindrical thin shell. *Physics of Fluids*, 34:017104.
- Mackay, E. (2020). Differences in wave forces on thin porous structures using linear and quadratic dissipation.
- Malenica, S., Taylor, R. E., and Huang, J. B. (1999). Second-order water wave diffraction by an array of vertical cylinders. *Journal of Fluid Mechanics*, 390:349–373.
- Mandal, S., Datta, N., and Sahoo, T. (2013). Hydroelastic analysis of surface wave interaction with concentric porous and flexible cylinder systems. *Journal of Fluids and Structures*, 42:437–455.
- Mandal, S. and Sahoo, T. (2016). Gravity wave interaction with a flexible circular cage system. *Applied Ocean Research*, 58:37–48.
- Martin, T., Kamath, A., and Bihs, H. (2020). A lagrangian approach for the coupled simulation of fixed net structures in a eulerian fluid model. *Journal of Fluids and Structures*, 94:102962.
- Martin, T., Tsarau, A., and Bihs, H. (2021). A numerical framework for modelling the dynamics of open ocean aquaculture structures in viscous fluids. *Applied Ocean Research*, 106:102410.
- Meng, X.-N. and Zou, Z.-J. (2012). Wave interaction with a uniform porous cylinder of arbitrary shape. *Ocean Engineering*, 44:90–99.
- Moe, H., Fredheim, A., and Hopperstad, O. (2010). Structural analysis of aquaculture net cages in current. *Journal of Fluids and Structures*, 26:503–516.
- Molin, B. (2011). Hydrodynamic modeling of perforated structures. *Applied Ocean Research*, 33:1–11.
- Morison, J., Johnson, J., and Schaaf, S. (1950). The force exerted by surface waves on piles. *Journal of Petroleum Technology*, 2:149–154.

## References

---

- Morrisey, D. J., Inglis, G., Tait, L., Woods, C., Lewis, J., and Georgiades, E. (2015). *Procedures for evaluating in-water systems to remove or treat vessel biofouling*. Ministry for Primary Industries, Manatū Ahu Matua.
- Myrli, O. and Khawaja, H. (2019). Fluid-structure interaction (fsi) modelling of aquaculture net cage. *International Journal of Multiphysics*, 13:97–111.
- Méhauté, B. L. (1976). *Introduction to Hydrodynamics and Water Waves*. Springer Verlag.
- Nakayama, A. and Kuwahara, F. (1999). A macroscopic turbulence model for flow in a porous medium. *Journal of Fluids Engineering*, 121:427–433.
- NS9415, N. S. (2009). Marine fish farms-requirements for site survey, risk analyses, design, dimensioning, production, installation and operation. *Standards Norway*, 915:2009.
- Park, J. C. and Wang, C. (2022). Hydrodynamic behaviour of floating polygonal ring structures under wave action. *Ocean Engineering*, 249:110195.
- Park, M.-S. and Koo, W. (2015). Mathematical modeling of partial-porous circular cylinders with water waves. *Mathematical Problems in Engineering*, 2015:1–19.
- Park, M.-S., Koo, W., and Choi, Y. (2010). Hydrodynamic interaction with an array of porous circular cylinders. *International Journal of Naval Architecture and Ocean Engineering*, 2:146–154.
- Patursson, O. (2008). *Flow through and around fish farming nets (Ph. D. thesis)*. University of New Hampshire.
- Patursson, O., Swift, M. R., Tsukrov, I., Simonsen, K., Baldwin, K., Fredriksson, D. W., and Celikkol, B. (2010). Development of a porous media model with application to flow through and around a net panel. *Ocean Engineering*, 37:314–324.
- Pichot, G., Germain, G., and Priour, D. (2009). On the experimental study of the flow around a fishing net. *European Journal of Mechanics - B/Fluids*, 28:103–116.
- Qin, H., Yu, S., and Li, P. (2020). Dynamic response of floating collar and cage under waves and current. *Ocean Engineering*, 205:107330.
- Sankarbabu, K., Sannasiraj, S., and Sundar, V. (2007). Interaction of regular waves with a group of dual porous circular cylinders. *Applied Ocean Research*, 29:180–190.
- Sarpkaya, T. and Isaacson, M. (1981). *Mechanics of Wave Forces on Offshore Structure*. Van Nostrand Reinhold Company.
- Selvan, S. A., Gayathri, R., Behera, H., and Meylan, M. H. (2021). Surface wave scattering by multiple flexible fishing cage system. *Physics of Fluids*, 33:037119.
- Sheng, W., Tapoglou, E., Ma, X., Taylor, C., Dorrell, R., Parsons, D., and Aggidis, G. (2022). Hydrodynamic studies of floating structures: Comparison of wave-structure interaction modelling. *Ocean Engineering*, 249:110878.

- Shim, K., Klebert, P., and Fredheim, A. (2009). Numerical investigation of the flow through and around a net cage. In *International Conference on Offshore Mechanics and Arctic Engineering*, volume 43444, pages 581–587.
- Sommerfeld, A. (1949). *Partial Differential Equations in Physics*. Academic Press.
- Song, W., Liang, Z., Guan, C., Zhao, F., Huang, L., and Zhu, L. (2005). Application of two different wave theories to calculate the horizontal wave force of a square cage (in chinese). *Chinese Fisheries Science*, 12:91–98.
- Strand, I. M. and Faltinsen, O. M. (2017). Linear sloshing in a 2d rectangular tank with a flexible sidewall. *Journal of Fluids and Structures*, 73:70–81.
- Strand, I. M. and Faltinsen, O. M. (2019). Linear wave response of a 2d closed flexible fish cage. *Journal of Fluids and Structures*, 87:58–83.
- Strand, I. M. and Faltinsen, O. M. (2020). Linear wave-induced dynamic structural stress analysis of a 2d semi-flexible closed fish cage. *Journal of Fluids and Structures*, 94:102909.
- Su, W., min Zhan, J., and Huang, H. (2015). Analysis of a porous and flexible cylinder in waves. *China Ocean Engineering*, 29:357–368.
- Tang, H., Hu, F., Xu, L., Dong, S., Zhou, C., and Wang, X. (2017). The effect of netting solidity ratio and inclined angle on the hydrodynamic characteristics of knotless polyethylene netting. *Journal of Ocean University of China*, 16:814–822.
- Tang, M.-F., Dong, G.-H., Xu, T.-J., Zhao, Y.-P., Bi, C.-W., and Guo, W.-J. (2018). Experimental analysis of the hydrodynamic coefficients of net panels in current. *Applied Ocean Research*, 79:253–261.
- Tang, T., Yu, P., Yu, S., Shan, X., and Chen, H. (2020). Connection between pore-scale and macroscopic flow characteristics of recirculating wake behind a porous cylinder. *Physics of Fluids*, 32:083606.
- Thomassen, P. E. and Leira, B. J. (2012). Statistical analysis of stress histories for fatigue damage design of floating fish cages. *Journal of Waterway, Port, Coastal, and Ocean Engineering*, 138:30–41.
- Tsukrov, I., Eroshkin, O., Fredriksson, D., Swift, M., and Celikkol, B. (2003). Finite element modeling of net panels using a consistent net element. *Ocean Engineering*, 30:251–270.
- Tu, G., Liu, H., Ru, Z., Shao, D., Yang, W., Sun, T., Wang, H., and Gao, Y. (2020). Numerical analysis of the flows around fishing plane nets using the lattice boltzmann method. *Ocean Engineering*, 214:107623.
- Wang, C. and Wu, G. (2007). Time domain analysis of second-order wave diffraction by an array of vertical cylinders. *Journal of Fluids and Structures*, 23:605–631.

## References

---

- Wang, H., Zhang, X., Zhang, X., Li, X., Tian, X., Shen, Y., and Song, W. (2023). Experimental investigations on hydrodynamic interactions between the cylinder and nets of a typical offshore aquacultural structure in steady current. *Marine Structures*, 88:103367.
- Wang, S. and Liang, B. (2013). *Wave Mechanics for Ocean Engineering (In Chinese)*. China Ocean University Press.
- Wiegerink, J., Baldock, T., Callaghan, D., and Wang, C. (2022). Slosh suppression blocks - a concept for mitigating fluid motions in floating closed containment fish pen in high energy environments. *Applied Ocean Research*, 120:103068.
- Xu, T.-J., Dong, G.-H., Zhao, Y.-P., Li, Y.-C., and Gui, F.-K. (2011). Analysis of hydrodynamic behaviors of gravity net cage in irregular waves. *Ocean Engineering*, 38:1545–1554.
- Xu, T.-J., Zhao, Y.-P., Dong, G.-H., and Gui, F.-K. (2013a). Analysis of hydrodynamic behavior of a submersible net cage and mooring system in waves and current. *Applied Ocean Research*, 42:155–167.
- Xu, T.-J., Zhao, Y.-P., Dong, G.-H., Li, Y.-C., and Gui, F.-K. (2013b). Analysis of hydrodynamic behaviors of multiple net cages in combined wave–current flow. *Journal of Fluids and Structures*, 39:222–236.
- Yang, Y. and Wang, C. (2020). Finite element analysis of second order wave resonance by multiple cylinders in a uniform current. *Applied Ocean Research*, 100:102132.
- Yao, Y., Chen, Y., Zhou, H., and Yang, H. (2016). Numerical modeling of current loads on a net cage considering fluid–structure interaction. *Journal of Fluids and Structures*, 62:350–366.
- Yip, T., Sahoo, T., and Chwang, A. T. (2002). Trapping of surface waves by porous and flexible structures. *Wave Motion*, 35:41–54.
- Yu, X. and Chwang, A. T. (1994). Wave-induced oscillation in harbor with porous breakwaters. *Journal of Waterway, Port, Coastal, and Ocean Engineering*, 120:125–144.
- Zhan, J., Jia, X., Li, Y., Sun, M., Guo, G., and Hu, Y. (2006). Analytical and experimental investigation of drag on nets of fish cages. *Aquacultural Engineering*, 35:91–101.
- Zhang, D., Bai, Y., and Soares, C. G. (2021). Dynamic analysis of an array of semi-rigid “sea station” fish cages subjected to waves. *Aquacultural Engineering*, 94:102172.
- Zhao, F., Bao, W., Kinoshita, T., and Itakura, H. (2011). Theoretical and experimental study on a porous cylinder floating in waves. *Journal of Offshore Mechanics and Arctic Engineering*, 133.
- Zhao, Y.-P., Bai, X.-D., Dong, G.-H., and Bi, C.-W. (2019a). Deformation and stress distribution of floating collar of net cage in steady current. *Ships and Offshore Structures*, 14:371–383.



- Zhao, Y.-P., Bai, X.-D., Dong, G.-H., Bi, C.-W., and Gui, F.-K. (2015). Numerical analysis of the elastic response of a floating collar in waves. *Ocean Engineering*, 95:175–182.
- Zhao, Y.-P., Bi, C.-W., Dong, G.-H., Gui, F.-K., Cui, Y., Guan, C.-T., and Xu, T.-J. (2013). Numerical simulation of the flow around fishing plane nets using the porous media model. *Ocean Engineering*, 62:25–37.
- Zhao, Y.-P., Bi, C.-W., Sun, X.-X., and Dong, G.-H. (2019b). A prediction on structural stress and deformation of fish cage in waves using machine-learning method. *Aquacultural Engineering*, 85:15–21.
- Zhao, Y.-P., Li, Y.-C., Dong, G.-H., Gui, F.-K., and Teng, B. (2007). A numerical study on dynamic properties of the gravity cage in combined wave-current flow. *Ocean Engineering*, 34:2350–2363.
- Zhao, Y.-P., Li, Y.-C., Dong, G.-H., Gui, F.-K., and Wu, H. (2008). An experimental and numerical study of hydrodynamic characteristics of submerged flexible plane nets in waves. *Aquacultural Engineering*, 38:16–25.
- Zheng, S., Meylan, M. H., Greaves, D., and Iglesias, G. (2020a). Water-wave interaction with submerged porous elastic disks. *Physics of Fluids*, 32:047106. doi: 10.1063/5.0006119.
- Zheng, S., Meylan, M. H., Zhu, G., Greaves, D., and Iglesias, G. (2020b). Hydroelastic interaction between water waves and an array of circular floating porous elastic plates. *Journal of Fluid Mechanics*, 900:A20.
- Zheng, S., Zhang, Y., Liu, Y., and Iglesias, G. (2019). Wave radiation from multiple cylinders of arbitrary cross sections. *Ocean Engineering*, 184:11–22.
- Zhou, X. (2019). Brief overview of world aquaculture production: an update with latest available 2017 global production data. *FAO Aquaculture Newsletter*, pages 6–8.
- Zhu, S.-P. and Mitchell, L. (2009). Diffraction of ocean waves around a hollow cylindrical shell structure. *Wave Motion*, 46:78–88.